Linda Payerl, Bsc.

NUMERICAL STUDIES ON THE BEARING CAPACITY OF SHALLOW FOOTINGS

Masterarbeit
zum Erlagen des akademischen Grades
Diplom-Ingenieur
eingereicht an der
Technischen Universität Graz

Betreuer

Assoc. Prof. Dipl.- Ing. Dr. techn. Franz Tschuchnigg

Institut für Bodenmechanik, Grundbau und Numerische Geotechnik

Graz, Jänner 2021

Eidesstattliche Erklärung

Ich erkläre an Eides statt, dass ich die vorliegende Arbeit selbstständig verfasst, andere als die angegebenen Quellen/Hilfsmittel nicht benutzt, und die den benutzten Quellen wörtlich und inhaltlich entnommenen Stellen als solche kenntlich gemacht habe. Das in TUGRAZonline hochgeladene Textdokument ist mit der vorliegenden Arbeit identisch.

....
        Datum   Unterschrift

Affidavit

I declare that I have authored this thesis independently, that I have not used other than the declared sources/resources, and that I have explicitly indicated all material which has been quoted either literally or by content from the sources used. The text document uploaded to TUGRAZonline is identical to the present doctoral thesis.

....
        Datum   Unterschrift

Acknowledgment

Kurzfassung

Im Rahmen dieser Arbeit wird die Standsicherheit geotechnischer Bauwerke untersucht. Bezogen auf Stabilitätsprobleme im Falle von Tragfähigkeitsnachweisen bezieht sich der Stand der Technik auf zwei wichtige Sicherheitsanalysen. Das plastische Grenzgleichgewicht wird entweder durch die Erhöhung der Belastung (Bruchlastanalyse) oder die Reduktion der Festigkeitsparameter (Festigkeitsreduktionsanalyse) herbeigeführt. Das Hauptthema dieser Arbeit ist der Vergleich dieser beiden Vorgehensweisen, wobei sowohl analytische (ÖNORM B 4435, EC7, DIN 4017) als auch numerische Methoden (FEA, FELA) unter Berücksichtigung assoziierter, nicht assoziierter "Davis A" und nicht assoziierte Plastizität zur Anwendung kommen.

Die in dieser Arbeit vorgestellten Ergebnisse bestätigen, dass herkömmliche analytische Methoden gemäß Standards (ÖNORM B 4435, EC7, DIN 4017) als konservativ eingestuft werden können und im Vergleich zu numerischen Methoden für die Bruchlastanalyse zu geringeren Bruchlasten führen. Beim Vergleich der numerischen Bruchlastanalyse beider Programme wird gezeigt, dass die Bruchlast von Plaxis im Allgemeinen höher ist als die Bruchlast von Optum. Darüber hinaus wird gezeigt, dass der ursprüngliche Davis Ansatz A zu stark konservativen Ergebnissen bei der Belastung für beide Sicherheitsanalysen führt, während die verbesserten Davis Ansätze B und C zu einem genaueren Sicherheitsfaktor führen. Sowohl für beide Methoden als auch für die Sicherheitsanalysen liefert die nicht assoziierte Plastizität sowie die nicht assoziierte Plastizität nach Davis Ansatz A im Vergleich zu den Ergebnissen einer assoziierten Plastizität eine wesentlich geringere Bruchlast.

Ein weiterer Schwerpunkt dieser Arbeit besteht darin, die beiden Sicherheitsanalysen zu vergleichen und die Belastungsunterschiede aufzuzeigen, die dem jeweiligen Sicherheitsfaktor entsprechen, sowie den Sicherheitsfaktor zu vergleichen, der der aufgebrachten Last entspricht. Es wird gezeigt, dass in Bezug auf die Sicherheitsanalysen, ein höherer Sicherheitsfaktor zu größeren Differenzen in der Belastung führt.

Je geringer der Unterschied in der aufgebrachten Belastung ist (tatsächliche Belastung gegenüber Versagensbelastung), desto geringer ist der Unterschied hinsichtlich des resultierenden Sicherheitsfaktors bei Anwendung der Festigkeitsreduktionsanalyse. Die in dieser Arbeit vorgestellten Ergebnisse bestätigen, dass die Sicherheitsfaktoren beider Analysen für die untersuchten konstitutiven Modelle MC (Plaxis, Optum) und HS (Plaxis) / HMC (Optum) sowie numerischen Berechnungsverfahren FEA (Plaxis, Optum) und FELA (Optum) für drainierte Bedingungen gleich sind, sofern ein homogener Bodenaufbau vorliegt. Unter drainierten Bedingungen ist der resultierende Sicherheitsfaktor für beide Sicherheitsanalysen unabhängig von den Anfangsspannungen.

Die Durchführung einer automatischen Festigkeitsreduktionsanalyse im Falle eines FEA-codes (SRFEA) mit geringerer Fehlertoleranz führt zu geringeren Oszillationen und somit zu "glatteren" (stetig differenzierbar) Kurven, während eine höhere Fehlertoleranz zu stärkerer Oszillation führt, wodurch Spitzen in den Sicherheitsfaktoren auftreten. Es werden jedoch selten Unterschiede im Sicherheitsfaktor nachgewiesen, lediglich der Verlauf der Kurve ändert sich. Unter Berücksichtigung des MC-Versagenskriterium und Aufbringung der Bruchlast, kommt es zum Materialversagen. Die entsprechenden π-Ebenen zeigen den Spannungspfad in einem p'-q-Raum im Falle des Versagens für jeden Spannungspunkt (FoS$_{FL}$ 1.0). Es wird gezeigt, dass die Spannungspunkte (A bis F) in Richtung triaxialer Kompression verlaufen. Darüber hinaus bleibt der θ - Winkel nahezu konstant.

Im Fall von Plaxis SRFEA mit assoziierter Plastizität sowie nicht assoziierter Plastizität ist ersichtlich, dass der Sicherheitsfaktor bei 3D Berechnungen im Vergleich zu 2D Berechnungen zu etwas höheren Werten führt. Bei nicht assoziierter Plastizität führt der Sicherheitsfaktor zu einer höheren Oszillation im Vergleich zur assoziierten Plastizität, während beim Sicherheitsfaktor von 1.5 die Kurve im Vergleich zur assoziierten Plastizität glatter ist. Schlussendlich stimmen numerische 3D- und 2D-Ergebnisse hinsichtlich der Bruchlast sehr gut überein. Im Fall von einer Grenzwertanalyse (FELA) in Optum bei assoziierter wie auch nicht assoziierter Plastizität nach Davis A ist ersichtlich, dass eine beinahe zweifach so große "3D Bruchlast" resultiert, im Vergleich zur 2D Bruchlast. Unter der 3D Versagenslast ist zu sehen, dass das System stabil bleibt, bis der Festigkeitsparameter φ' um ~1° verringert wird (c'=0kPA). Während unter der 2D Versagenslast das System stabil bleibt, bis der Festigkeitsparameter φ' um ~7° reduziert wird (c'=0kPA). Dies lässt auf die geringeren Versagenslasten rückschließen.

Abstract

Within the scope of this thesis stability problems, especially bearing capacity, will be discussed. There are two important safety analyses, when it comes to stability problems, like bearing capacity. On the one hand, the loads are amplified until collapse occurs, and on the other hand the strength parameters are determined, which are necessary to prevent collapse, given a set of actual loads. The main issue of this thesis is to compare these two safety analyses by means of analytical methods (ÖNORM B 4435, EC7, DIN 4017), as well as numerical methods (FEA, FELA) considering associated, non-associated (after Davis A) and non-associated plasticity. The results presented in this thesis confirm that conventional analytical methods according to standard regulations (ÖNORM B 4435, EC7, DIN 4017) can be classified as conservative approach and lead to lower failure loads compared to numerical methods for the failure load analysis. Regarding the numerical failure load, the results show that the failure load obtained with Plaxis is generally higher compared to Optum. Furthermore, it is shown that the original Davis Approach A leads to strongly conservative results in the failure load for both safety analyses, whereas the enhanced Davis Approaches B and C are results in a more accurate factors of safety. For both methods, as well as for both safety analyses, non-associated plasticity and non-associated plasticity after Davis Approach A provides a substantially lower failure load when compared with results of an associated plasticity.

Another aim of this thesis is to compare the two safety analyses and show the differences in loading corresponding to the factor of safety, as well as to compare the factor of safety corresponding to the applying load. It is shown that, the higher the FoS, the greater the difference in the exposure related to the safety analysis. Furthermore, the less the difference in the applied loading (actual load vs. failure load) the less the difference in the resulting FoS_{SR} considering SRFEA. The results presented in this thesis confirm that the FoS for both analyses, as well as both numerical methods (FEA, FELA) using the constitutive models MC (Plaxis, Optum) and HS (Plaxis) / HMC (Optum) are the same for drained conditions of one homogenous soil body. Furthermore, under conditions where no excess pore pressures are generated (drained) the solution is independent of the initial stresses. Performing automatic strength reduction using a FEA-code (SRFEA), with lower tolerated errors lead to less oscillations and therefore smooth curves, whereas higher tolerated errors lead to more oscillations and therefore higher FoS_{SR}-peak values (amplitude). However, only slight differences were observed for the factor of safety at failure; only the graph changes. Under the MC failure criterion and the application of the failure load, the soil mass fails. The corresponding π-plane illustrates the stress path in a p'-q space at failure for different stress points. It is shown that each stress point tends to triaxial compression. Furthermore, the lode angle θ remains nearly constant.

In case of Plaxis SRFEA, associated plasticity as well as non-associated plasticity 3D calculations result in slightly higher FoS_{SR} values compared to 2D calculations. In case of non-associated plasticity, the FoS_{SR} at failure results in more oscillation compared to associated plasticity, whereas for the FoS_{SR} 1.5 the curve is smoother compared to associated plasticity. Nevertheless, results obtained with 3D- and 2D SRFEA are in good agreement and comply with the 2D failure load. In case of Optum limit analysis (FELA) associated plasticity and non-associated plasticity after Davis A, it is seen that the resulting 3D load is nearly twice the 2D load at failure. Under the 3D failure load, it is seen that the system remains stable until the strength parameter φ' is reduced by ~1° (c'=0kPA). Whereas under the 2D failure load the system remains stable until the strength parameter φ' is reduced by ~7° (c'=0kPA), relating to the lower failure loads compared to 3D.

Table of Content

List of symbols and abbreviations

Capital letters

A'	effective area of the footing
A_e	area of element
A_q	boundary area of soil mass subjected to unknown surface tractions
A_t	boundary area of soil mass subjected to fixed surface tractions
A_w	boundary area of soil mass subjected to fixed velocities
B	strain interpolation matrix
$\bar{B}$	global strain–displacement matrix for mesh multiplied by the element areas
B_e	strain–displacement matrix for element e
$\overline{B_e}$	strain–displacement matrix for element e multiplied by its area
B_j	strain–displacement matrix for node j of an element
$\bar{B_J}$	strain–displacement matrix for node j of an element multiplied by the element area
D	non-linear material stiffness matrix
D_e	elastic material stiffness matrix
E'	Young`s modulus
E_i	initial stiffness modulus
E_{50}	secant stiffness in standard drained triaxial test
E_{50}^{ref}	reference secant stiffness in standard drained triaxial test
E_{Oed}	tangent stiffness for primary oedometer loading
E_{Oed}^{ref}	reference tangent stiffness for primary oedometer loading
E_{ur}	unloading/reloading stiffness from triaxial test

E_{ur}^{ref} reference unloading/reloading stiffness from triaxial test

F_c compression cap yield function

H hardening parameter

J_1, J_2, J_3 deviatoric stress invariants

K global stiffness matrix

K_0^{NC} K_0-value for normal consolidation

K_c bulk modulus for primary isotropic compression

K^i stiffness matrix (step i)

K_s bulk modulus for isotropic swelling

K_s^{ref} reference bulk modulus for unloading, reloading

M Plaxis model parameter for cap point (chapter 2.1.2) Optum material parameter (chapter 2.1.3)

N dilation at ultimate limit state; shape function

N_j linear shape function for node j

N_c, N_q, N_x, N_γ bearing capacity factor

P_{ext}^i external force vector (step i)

P_{int}^{i-1} internal force vector (step i-1)

Q collapse load

Q_n, Q_s normal and tangential (shear) loads per unit thickness acting on element edge of length L

$Q_{f,k}$ characteristic value of bearing resistance

$R_{f,k}=R_n$ characteristic value of bearing resistance

R_f failure ratio

V volume of soil mass

$\dot{W}$ rate of internal energy dissipation less rate of work done by external loads

$\dot{W}$ rate of internal energy dissipation less rate of work done by external loads

$\dot{W}_{ext}$, P_{ext} rate of work expended by external forces

$\dot{W}_{int}$, P_{int} rate of internal energy dissipation

L   length of discontinuity; length of element edge

Small letters

a'	effective length of the footing
a_c	magnitude of triaxial compression at a specific stress state
a_e	magnitude of triaxial extension at a specific stress state
b'	effective width of the footing
b_x	factor considering the foundation base inclination
c	design effective value of cohesion
c'	effective cohesion
$c'_{failure}$	effective cohesion at failure
c'_{mob}	mobilized effective cohesion
c*	reduced effective cohesion according to Davis (1968)
c_c	cohesion at triaxial compression
c_d	design effective value of cohesion
c_e	cohesion at triaxial extension
d	effective depth of the footing
f	yield function
f^c	yield function cap point
f^s	yield function hardening
g	potential function (chapter 2.1.1) vector of fixed body forces at a point (chapter 2.2.2)
g^c	yield function cap point
g^e	vector of fixed body forces for element e
g^s	yield function hardening
g_x	factor considering the surface inclination
g_x, g_y	fixed body forces in x- and y-directions

g^e_x, g^e_y	fixed body forces in x- and y-directions for element e
h	global vector of unknown body forces
h^e	vector of unknown body forces for element e
h_x, h_y	unknown body forces in x- and y-directions
h^e_x, h^e_y	unknown body forces in x- and y-directions for element e
i_x	factor considering the load inclination
l'	effective length of the footing
m	power of stress-level dependency of stiffness
p	volumetric stress
p_0	confining initial pressure
p'	effective mean stress
p_P	isotropic pre-consolidation stress
p_u	confining pressure at q_u
$\dot{p}_p$	isotropic pre-consolidation stress rate
p^{ref}	reference stress for stiffness
q	deviatoric stress vector of unknown tractions acting on area A_q (chapter 2.2.2)
q'	design effective overburden pressure
$\bar{q}$	deviatoric stress
q_a	asymptotic deviatoric stress
q_f	ultimate deviatoric stress
q_n, q_s	unknown normal and tangential (shear) stresses acting on element edge
q_u	ultimate shear stress

q_{jn}, q_{js}	unknown normal and tangential (shear) stresses acting on element edge at node j
s	diameter of Mohr Coulomb circle
s_x	factor considering the foundation shape
t	radius of Mohr Coulomb circle (chapter 2.1.1) effective depth of the footing (chapter 2.3.2) vector of fixed surface tractions acting on area A_t (chapter 2.2.2)
t_{jn}, t_{js}	fixed surface tractions in normal and tangential (shear) directions at node j
t_x	factor considering the foundation base inclination
u	vector of displacement field (chapter 2.2.1) global vector of unknown nodal velocities (chapter 2.2.2)
u_e	vector of unknown nodal velocities for element e
u_j	vector of unknown velocities at node j
u_n, u_s	unknown velocities in normal and tangential (shear) directions
u_x, u_y	unknown velocities in x- and y-directions
u_{jn}, u_{js}	unknown velocities in normal and tangential (shear) directions for node j
u_{jx}, u_{jy}	unknown velocities in x- and y-directions for node j
Δu	displacement increment
Δu_n, Δu_s	velocity jumps across discontinuity in normal and tangential directions
$|u|$	total displacements
v	nodal values of displacements
w	fixed velocities on surface A_w
w_n, w_s	fixed velocities in normal and tangential (shear) directions

w_{jn}, w_{js} fixed velocities in normal and tangential (shear) directions for node j

x, y cartesian coordinates

Greek letters

β strength factor according to Davis (1968)

β_0 strength factor according to Davis (1968) at initial conditions

$\beta_{failure}$ strength factor according to Davis (1968) at failure

ε strain

$\Delta\varepsilon$ strain increment

$\Delta\varepsilon^p$ incremental plastic strains

ε^e elastic strain

ε^p plastic strains

$\dot{\varepsilon}$ strain rate

$\dot{\varepsilon}^e$ elastic strain rate

$\dot{\varepsilon}^p$ plastic strain rate

ε_1 total principal strain

$\varepsilon_{1,50}$ axial strain at half of the ultimate shear stress

ε_1^p total plastic principal strain

ε_{vol} total volumetric strain

ε_v^p total plastic volumetric strain

$\dot{\varepsilon}_v^p$ total plastic volumetric strain rate according to compression

$\dot{\varepsilon}_{v,c}^p$ total plastic volumetric strain rate

γ^p plastic shear strain

$\dot{\gamma}^p$ plastic shear strain rate

γ unit weight

γ_{sat} saturated unit weight

γ_{unsat}	unsaturated unit weight
γ'_o, γ'_1	buyoyant unit weight above foundation level
$\gamma'_u, \gamma'_2, \gamma'$	buyoyant unit weight below foundation level
φ'	effective friction angle
φ^*	reduced effective friction angle according to Davis (1968)
φ'_{mob}	mobilized effective friction angle
$\varphi'_{failure}$	effective friction angle at failure
φ'_{peak}	maximum effective friction angle
φ'_{pt}	effective friction angle on transition line between contraction and dilatancy
φ'_{cv}	critical state Effective friction angle
φ'_c	effective friction angle at triaxial compression
φ'_e	effective friction angle at triaxial extension
φ_c	inclination of the compression cone
κ_c	compressive strength
$\dot{\kappa}_c$	compressive strength
λ	plastic multiplier
$\dot{\lambda}$	plastic multiplier rate
$\dot{\lambda}^c$	plastic multiplier hardening state
$\dot{\lambda}^s$	plastic multiplier cap point
λ_x	factor considering the surface inclination
ν'	Poisson´s ratio
ν'_{UR}	Poisson´s ratio for unloading/reloading
ν_x	factor considering the foundation shape

Δv^i	incremental displacement vector (step i)
θ	lode angle
σ	stress
σ'	effective stress
$\dot{\sigma}'$	effective stress rate
$\sigma'_1, \sigma'_2, \sigma'_3$	principle effective stress
σ'_1	major effective principal stress
σ'_3	minor effective principal stress
σ	total stress
$\sigma_1, \sigma_2, \sigma_3$	principle total stress
σ'_f	effective normal stress at failure
σ_i	unknown actual stress state
σ^{i-1}	known stress state of the previous step
σ_m	effective mean stress
σ_n	normal stress
σ'_k	effective normal stress based on velocity characteristics
σ'_s	effective normal stress which defines failure criterion according to Coulomb
$\sigma_{jxx}, \sigma_{jyy}$	cartesian stresses at node j
σ_{xx}, σ_{yy}	cartesian stresses
σ_{nn}	normal stress at node j
$\Delta\sigma$	additional stress increment
τ	shear stress
τ_f	shear strength

τ'_f	effective shear strength
τ_k	shear stress based on velocity characteristics
τ_k	shear stress which defines failure criterion according to Coulomb
τ_{mob}	mobilized shear stress
τ_{jxy}	cartesian stresses
τ_{xy}	cartesian stresses at node j
τ_{jns}	shear stress at node j
ξ_x	factor considering the foundation base inclination
ψ'	effective dilatancy angle
ψ'_{mob}	mobilized effective friction angle
$\psi'_{failure}$	effective dilatancy angle at failure

Abbreviations

ULS	Ultimate limit state
SLS	Serviceability limit state
FEA	Finite element analysis
FELA	Finite element limit analysis
LB	lower boundary
UB	upper boundary
FoS	factor of safety
FL	failure load
SR	strength reduction
MC	Mohr Coulomb
HMC	Hardening Mohr Coulomb
HS	Hardening soil

Figures and tables declaration chapter 4 and 5 as well as in the appendix:

a.	associated
n.a.	non-associated
n.a. Davis A	non-associated Davis A
FEA, FELA	failure load analysis based on FEA/FELA
SRFEA, SRFELA	strength reduction analysis based on FEA/FELA
FoS_{FL}	factor of safety for failure load
FoS_{SR}	factor of safety for strength reduction

1 Introduction

In general, the design of geotechnical structures comprises ultimate and serviceability limit state considerations. Within the scope of this thesis stability problems, especially ground failure behaviour, will be discussed. There are two important safety analyses when it comes to stability problems such as bearing capacity. On the one hand, the loads are amplified until collapse occurs (failure load) and on the other hand the strength parameters (i.e. φ' and c') are determined, which are necessary to prevent collapse, given a set of actual loads. The main aim of this thesis is to compare these two safety analyses by analytical methods (ÖNORM B 4435, EC7, DIN 4017), as well as numerical methods (FEA, FELA).

Conventional analytical methods according to standard regulations are still used in daily engineering practice, despite many assumptions. However, the applicability of these methods is limited to certain boundary conditions. Hence, there is still need to find other, more efficient methods that provide more realistic solutions. Tools which are quite frequently used in the field of soil mechanics are finite element analysis (FEA) and finite element limit analysis (FELA). Generally, this thesis considers standard limit boundary problems, which allow to compare analytically derived results (DIN 4017, EC 1997, ÖNORM B 4435) with numerical results (FEA, FELA). The latter consider different orders of shape function (FEA: 6-noded, 10-noded, 15-noded) as well as lower and upper bound theorems of plasticity (FELA). In both analytical and numerical methods, characteristic values are used. It should be mentioned at this point that it is discussed, whether partial factors are appropriate or distort the characteristics of the soil body.

The variation of the friction angle has been used to evaluate differences between numerical and analytical methods. For the latter, several assumptions are made: neglection of the dilatancy angle (ψ'), constant friction angle (φ'). It is known that with non-associated flow rule the failure mechanism is not unique. Further, non-associated plasticity models yield lower bearing capacity values compared to the associated flow rule (Optum G2 Theory Manual, 2016). Due to the fact that for the case of finite element limit analysis only associated plasticity computes a rigorous solution, the approach by Davis (1968) is used. Therefore, reduced strength parameters in combination with an associated flow rule are used to simulate non-associated behaviour.

The comparison of these methods has been carried out for the Mohr Coulomb (MC) and Hardening Soil (HS) model. Both models use the MC failure criterion, thus the results for a homogenous soil body should be nearly the same. At last, only drained conditions are analyzed as well as one type of footing (strip foundation). All calculations were done in 2D and 3D.

2 Theoretical Part

2.1 Constitutive Model

The following contents in this chapter are based on [1], [2].

Analytical design approaches comprise both, serviceability limit state (SLS) and ultimate limit state (ULS) considerations. In addition, advanced numerical methods describe soil behaviour by means of constitutive models. In this way, inhomogeneous soil stratification and naturally grown material can be taken into account; further, different loading conditions are considered: primary loading, unloading / reloading. Constitutive models describe stress-strain behaviour and, thus, soil displacements as a consequence of different loading conditions. These models are used with finite element analyses (FEA), as well as finite element limit analysis (FELA) for soil bodies and soil/structure interaction issues under symmetric/axisymmetric, plane strain (2D) and three-dimensional conditions. A large quantity of constitutive models are input parameter based on laboratory tests, whereas each of them deals with uncertainties, inter alia due to the inhomogeneity of the soil body. In this thesis different constitutive models are used with finite element analyses (FEA), as well as finite element limit analysis (FELA) for plane strain (2D) and three-dimensional conditions, namely Mohr Coulomb (MC) and Hardening Soil (HS) for Plaxis 2D/3D and Mohr Coulomb (MC) and Hardening Mohr Coulomb (HMC) for Optum G2/G3. In this thesis compression is signed positive, and tension negative, as it is usual for geotechnical engineering.

2.1.1 Mohr Coulomb Model (MC)

The following contents in this chapter are based on [3], [4], [5].

It should be mentioned that the Mohr Coulomb model is used in both numerical programs (i.e. Plaxis and Optum). The Mohr Coulomb model is defined as a linear-elastic, perfectly plastic constitutive model with MC failure criterion. Based on the Young's modulus E and the Poisson's ratio ν the linear-elastic part, behaves based on Hooke's law of isotropic elasticity and yields reversible strains. The plastic part is described by means of the effective friction angle φ', cohesion c' and dilatancy angle ψ' and yields irreversible strains. To evaluate whether the material behaves plastically or not, a yield function f is established which accounts for the stress and strain history. Plastic yielding occurs as soon as f = 0. A perfectly plastic model is specified by a certain (= fixed) yield surface, which is not affected by the plastic strain, therefore only defined by the input parameters. For stress states represented by points within the yield surface, the material behaves elastically. As indicated in Eq. (1) and Eq. (2), the total strain (rate) are divided into an elastic and plastic portion.

$$\underline{\varepsilon} = \underline{\varepsilon}^e + \underline{\varepsilon}^p \tag{1}$$

$$\underline{\dot{\varepsilon}} = \underline{\dot{\varepsilon}}^e + \underline{\dot{\varepsilon}}^p \tag{2}$$

The relation between the stress rates and the elastic strain rates is described by Hook's law, shown in Eq. (3)

$$\underline{\dot{\sigma}'} = \underline{\underline{D}}^e \underline{\dot{\varepsilon}}^e = \underline{\underline{D}}^e (\underline{\dot{\varepsilon}} - \underline{\dot{\varepsilon}}^p) \tag{3}$$

According to the classical theory of plasticity (Hill, 1950), plastic strain rates are proportional to the derivative of the yield function with respect to the stresses (Plaxis Manual, 2018). This behaviour responds in a perpendicular vector of the plastic strain rate to the yield surface. This classical form of the theory relates to associated plasticity (φ'=ψ'). Since the Mohr Coulomb model overestimates dilatant effects due to associated plasticity, a plastic potential function g is established in case of non-associated plasticity (φ'> ψ'), whereas g ≠ f applies. Eq. (4) describes the plastic strain rate taking into account a plastic multiplier λ.

$$\underline{\dot{\varepsilon}}^p = \lambda \frac{\partial g}{\partial \underline{\sigma}'} \tag{4}$$

For linear elastic behaviour, the plastic multiplier λ equals zero, whereas at the onset of plastic behaviour the plastic multiplier λ gives in a positive value (Eq. (5), (6)).

$$\lambda = 0 \quad for: \quad f < 0 \quad or: \quad \frac{\partial f^T}{\partial \underline{\sigma'}} \, \underline{\underline{D^e}} \underline{\dot{\varepsilon}} \leq 0 \quad (elasticity) \tag{5}$$

$$\lambda > 0 \quad for: \quad f = 0 \quad and: \quad \frac{\partial f^T}{\partial \underline{\sigma'}} \, \underline{\underline{D^e}} \underline{\dot{\varepsilon}} > 0 \quad (plasticity) \tag{6}$$

Fig. 1 displays both, the reversible elastic stress-strain portion as well as the irreversible plastic strains in a stress-strain (σ'–ε) diagram.
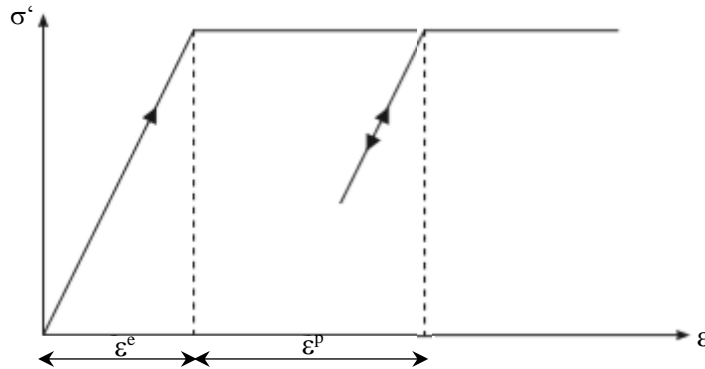
Fig. 1   Linear-elastic perfectly plastic model (according to Brinkgreve, 2018)

The Mohr Coulomb failure criterion defines the state of yielding, shown in Eq. (7):

$$\tau'_f = \sigma'_f \tan \varphi' + c' \tag{7}$$

Expressing the Mohr Coulomb failure criterion by means of principal effective stresses, Eq. (7) can be rewritten using a MC stress circle as shown in Eq. (8):

$$(\sigma'_1 - \sigma'_3) = (\sigma'_1 + \sigma'_3) \sin \varphi' + 2c' \cos \varphi' \tag{8}$$

Failure occurs as soon as the Mohr Coulomb's circle reaches the failure line (Fig. 2).
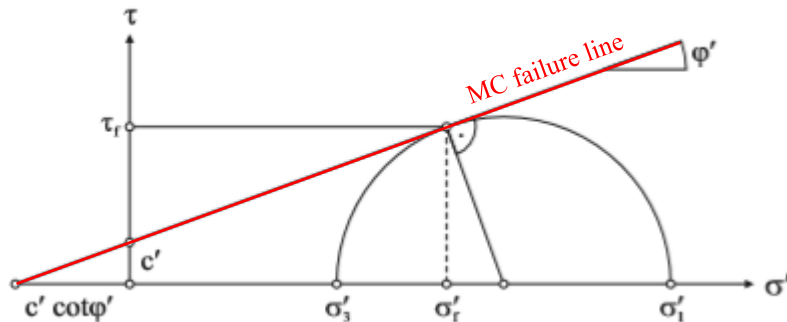
Fig. 2   Mohr Coulomb failure criterion in t'-s' plane (according to M. Wehnert, 2006)

Eq. (8) does not account for the intermediate effective principal stress σ'_2. However, in finite element analyses (FEA) as well as finite element limit analyses (FELA) a three-dimensional principal effective stress space is considered. *The Mohr Coulomb yield condition is an extension of the Coloumb`s friction law to general state of stress* (Plaxis Material Manual, 2016). To obtain full Mohr Coulomb yield conditions, six yield functions f, as well as six potential functions g, have to be applied. The yield function f consists of two parameters describing plastic behaviour, the friction angle φ' and the cohesion c'. Based on the major σ'_1 and the minor σ'_3 effective principal stress, both the yield function f (flow condition) and the potential function g are shown in Eq. (9), (10). For the case f = 0, all functions together give a fixed hexagonal cone in principal stress space (Fig. 3) (see for instance Smith&Griffiths, 1982).

$$f_{(\{\sigma'\})} = (\sigma'_1 - \sigma'_3) - (\sigma'_1 + \sigma'_3) \sin \varphi' - 2c \cos \varphi' \qquad (9)$$

$$g_{(\{\sigma'\})} = \tfrac{1}{2}(\sigma'_1 - \sigma'_3) + \tfrac{1}{2}(\sigma'_1 + \sigma'_3) \sin \psi' \qquad (10)$$
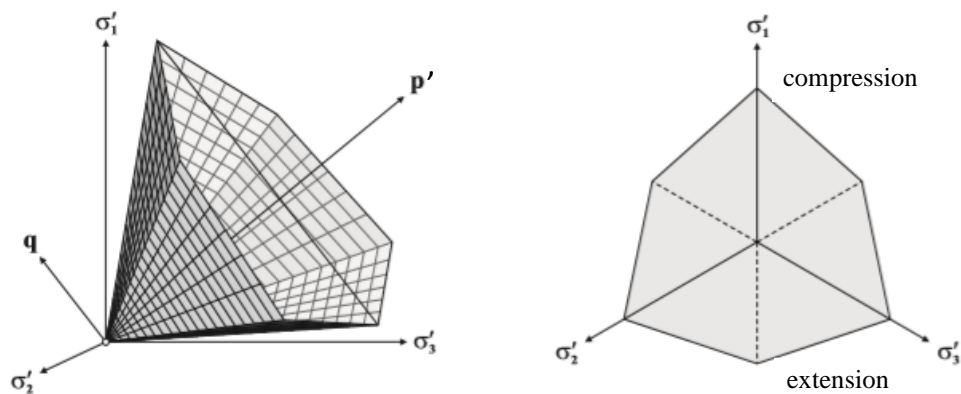
Fig. 3   MC yield function in the principal stress space for a coarse-grained soil (according to M. Wehnert, 2016)

The linear-elastic perfectly plastic Mohr Coulomb model requires a total of five soil parameters to describe soil behaviour, shown in Tab.1. Considering that the loading history (over- or normally consolidated) as well as the loading type (normal, un-and reloading) of the soil is not taken into account by this constitutive model, only one stress-independent stiffness parameter E' is applied.

Tab. 1   Required parameter for the Mohr Coulomb model

Young's modulus	E'	[kPa]
Poisson's ratio	ν'	[−]
Effective cohesion	c'	[kPa]
Effective friction angle	φ'	[°]
Effective dilatancy angle	ψ'	[°]

2.1.1.1 Interpretation of the Stress State

In Fig. 4 (a), the Mohr Coulomb failure criterion is displayed based on the relation between shear stress and normal stress.

(a)   (b)   (c)
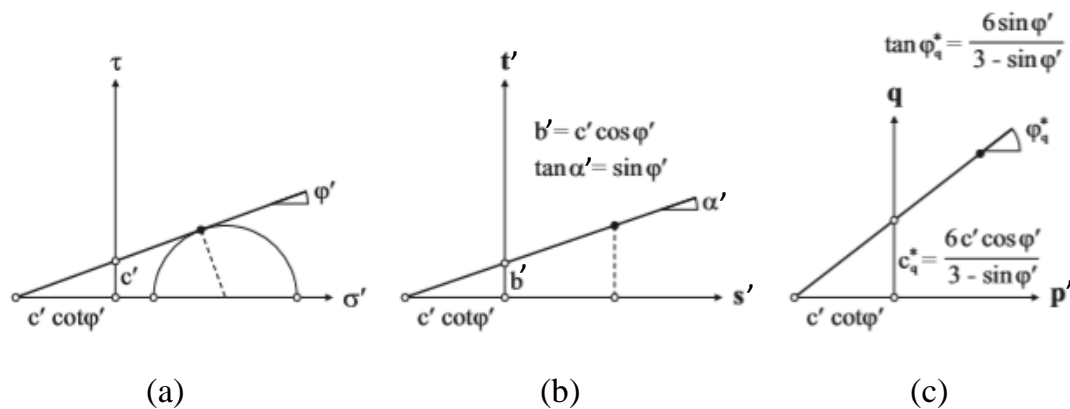
Fig. 4   Different types of presentation of the Mohr Coulomb failure criterion for compression (according to M. Wehnert, 2006)

Fig. 4 (b) presents the s'-t' diagram, where s' defines the center of the Mohr Coulomb´s circle and t' defines the radius.

$$s' = \frac{\sigma_1' + \sigma_3'}{2} \qquad (11)$$

$$t' = \frac{\sigma_1' - \sigma_3'}{2} \qquad (12)$$

Fig.4 (c) presents the p'-q diagram, which is generally used for the visualization of the stress paths; in this context, p' denotes the mean effective stress and q the deviatoric stress invariant. For the condition of a triaxial stress, state the overall formula can be reduced to Eq. (13), (14):

$$p' = \frac{\sigma_1' + 2\sigma_3'}{3} \qquad (13)$$

$$q = \sigma_1' - \sigma_3' \qquad (14)$$

2.1.1.2 Principal Effective Stress Space

In finite element analyses (FEA), as well as finite element limit analyses (FELA), a three-dimensional principal effective stress space is considered. Thus, representing the yield criterion in a principal stress space by means of a p'-q diagram, would be opportune (Fig.4). The diagonal space of the three-dimensional cone is defined by the mean effective stress axis (Fig.3). The distance between origin and current deviatoric plane along the space diagonal is given by the magnitude of p'. The shape of the π-plane (deviatoric plane) is defined by six yield functions, whereas the orientation of the π-plane is perpendicular to the space diagonal. The triaxial compression point C as well as the triaxial extension point E determine the cone opening. Fig.5 shows characteristic stress paths.
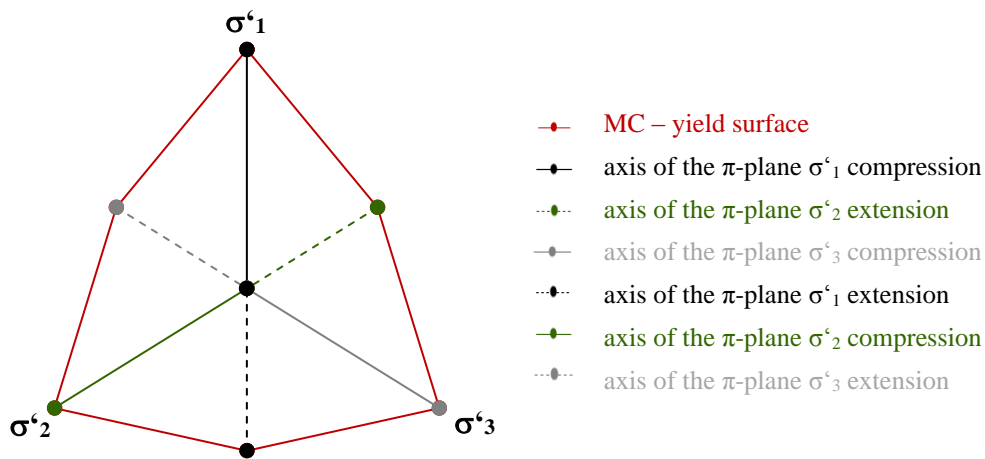
Fig. 5   MC yield function in the principal stress space for a cohesionless soil

The magnitude of triaxial compression / extension at a specific stress state is shown in Eq. (15), (16). The present investigations are restricted to coarse-grained soil conditions, which are herein also referred to as cohesionless soil conditions (c' = 0 kPa).

$$\frac{q}{p'} = \tan \varphi_c' \;\rightarrow\; a_c = p' \times \tan \varphi_c' + c_c' \tag{15}$$

$$\frac{q}{p'} = \tan \varphi_e' \;\rightarrow\; a_e = p' \times \tan \varphi_e' + c_e' \tag{16}$$

with:

$$\varphi_c' = \tan^{-1}\frac{6 \times \sin \varphi'}{3 - \sin \varphi'} \qquad\qquad \varphi_e' = \tan^{-1}\frac{6 \times \sin \varphi'}{3 + \sin \varphi'} \tag{17}$$

$$c_c' = \frac{6c' \times \cos \varphi'}{3 - \sin \varphi'} \qquad\qquad c_e' = \frac{6c' \times \cos \varphi'}{3 + \sin \varphi'} \tag{18}$$

In order to clarify the mathematical relations Eq. (15), (16), (17), (18) a graphic illustration for cohesionless soils is shown in Fig. 6.
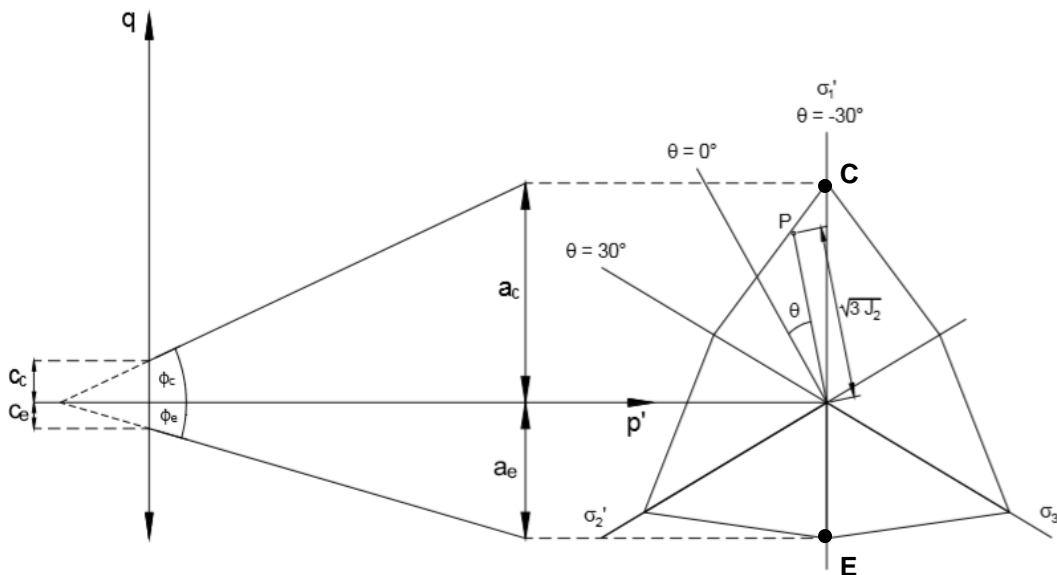
Fig. 6   MC yield function in the principal stress space for a cohesionless soil (according to MA Thesis Sallinger, 2017)

Additionally, the location of a random stress state P in the deviatoric plane can be established by using invariants. In this way, the actual stress state is unique and independent of the respective coordinate system. In addition to the mean effective stress p', the second as well as the third deviatoric stress invariant are necessary to define a stress state in the principal stress space. The deviatoric stress invariant is shown in Eq. (19), (20), (21).

$$J_1 = (\sigma_1' - \sigma_m') + (\sigma_2' - \sigma_m') + (\sigma_3' - \sigma_m') \tag{19}$$

$$J_2 = \frac{1}{6}\left[\left(\sigma_1' - \sigma_2'\right)^2 + \left(\sigma_2' - \sigma_3'\right)^2 + \left(\sigma_3' - \sigma_1'\right)^2\right] \tag{20}$$

$$J_3 = (\sigma_1' - \sigma_m') \times (\sigma_2' - \sigma_m') \times (\sigma_3' - \sigma_m') \tag{21}$$

The orientation within the deviatoric plane is given by the lode angle θ, which is formulated by Eq. (22). Conversely, the distance of a stress state perpendicular from the space diagonal is calculated as $\sqrt{3J_2}$.

$$\theta = \frac{1}{3}\sin^{-1}\left(-\frac{\sqrt{27}}{2} \times \frac{J_3}{\sqrt{J_2^3}}\right) \tag{22}$$

The lode angle spans a range from -30° (triaxial compression) to +30° (triaxial extension).

> θ = -30°   → triaxial compression   (Point C: σ'$_1 \geq$ σ'$_2 =$ σ'$_3$)
> θ = +30°   → triaxial extension   (Point E: σ'$_1 =$ σ'$_2 \geq$ σ'$_3$)

In summary, a random stress state P can be completely described by means of 3 components: p', $\sqrt{3J_2}$ and q, shown in Fig.6.

2.1.2 Hardening Soil Model (HS)

The following contents in this chapter are based on [6], [7].

Nevertheless, *the Mohr Coulomb model has a number of inherent limitations and cannot be expected to capture the entire spectrum of soil behaviour* (Optum G2 Material Manual, 2016). In addition, the predictions of any model strongly depend on the choice of the input material parameters. Indeed, there is no guarantee that a complex model represents reality better than a simple model. However, the advantages of the Hardening Soil model (Plaxis 2D) compared to MC are obvious:

- HS considers a hyperbolic stress-strain relation, which is more realistic compared to the bi-linear curve as is the case for MC.
- HS accounts for the stress-dependency of soil stiffness.

When using the Mohr Coulomb model, a fixed value of stiffness has to be entered, which is not reality.

The Hardening Soil model was developed by Schanz (1998) and Schanz (1999) based on Vermeer (1978). It is an advanced model for simulating the behaviour of different types of soil and applicable to both soft soils and stiff soils; further, it belongs to the family of double hardening models (shear and compression hardening). By introducing two additional flow conditions to the MC failure criterion, shear hardening as well as isotropic hardening, can be resembled for different loading conditions. The former is used to model irreversible plastic strains (shear distortion) due to deviatoric loading, whereas the latter is used to model irreversible plastic strains as a consequence of primarily isotropic compression (e.g. primary loading path in oedometer tests). In contrast to a linear-elastic, perfectly plastic models (e.g. MC), the yield surface of hardening plasticity models is not fixed in principal stress space. In contrast, the develop based on respective stress paths. The striking features of the model are the stress-dependent stiffness as well as a mobilized dilatancy angle and the strict separation between primary loading and unloading/reloading. In the case of a triaxial test for drained conditions, the observed relation between axial strain and deviatoric stress can be approximated by a hyperbola taking into account plastic behaviour, a dilatancy angle and a yield cap for volumetric hardening. To simulate this material behaviour, a hyperbolic stress-strain relationship is used in the model, first formulated by Konder and Zelasko (1963) and later expanded by Ducan and Chang (1970) (Fig. 7, Eq. (23)).
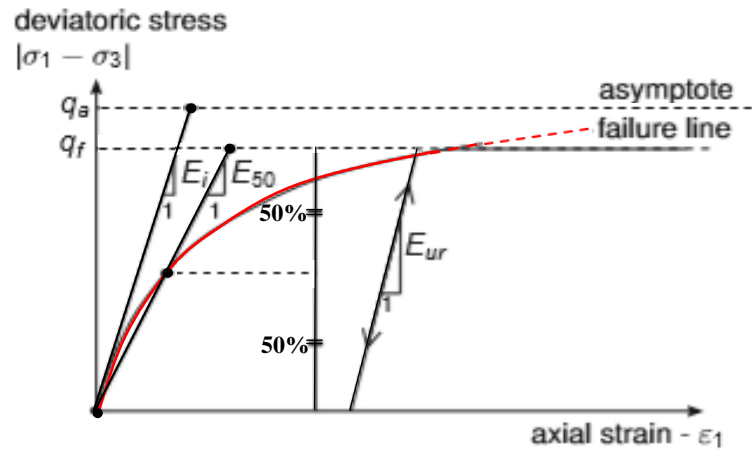
Fig. 7   Hyperbolic stress-strain relation in primary loading for a standard drained triaxial test (according to Brinkgreve, 2008)

2.1.2.1 Hyperbolic Stress-Strain Relationship

The asymptotic deviatoric stress q_a is linked to the ultimate deviatoric stress q_f according to the following equation:

$$q_a = \frac{q_f}{R_f} \qquad and \qquad q_f = (c' \cot \varphi' + \sigma_3') \times \frac{2 \sin \varphi'}{1 - \sin \varphi'} \qquad (23)$$

$$\varepsilon_1 = \frac{1}{E_i} \times \frac{q}{1 - \frac{q}{q_a}} \quad \rightarrow \quad with \; E_i = \frac{2E_{50}}{2 - R_f} \qquad (24)$$

The relationship for q_f (Eq. (24)) is derived from the Mohr Coulomb failure criterion and involves strength parameters φ' and c'. For the case that q equals q_f the failure criterion, as described by the Mohr Coulomb model, is satisfied and thus perfectly plastic yielding occurs. The proportion between q_a and q_f is defined by the failure ratio R_f, which should be smaller than 1 (Plaxis default setting 0.9). E_i defines the initial stiffness modulus according to E_{50}. In contrast to primary deviatoric loading, where both elastic and plastic strains occur, unloading/reloading processes are modeled as purely elastic processes using Hooke's law. The unloading/reloading modulus E_{ur} and the constant Poisson ratio ν_{ur} are required as elastic parameters. The secant modulus E_{50} (primary deviatoric loading) and the unloading/reloading modulus E_{ur} are both stress-dependent and inter alia described by means of the minor principal stress σ'_3 (i.e. confining pressure in triaxial test). E_{50}^{ref} is defined as the secant of the triaxial stress-strain curve at 50% of the ultimate deviatoric stress q_f at a reference confining stress level p^{ref} (Plaxis default setting 100 kPa). E_{ur}^{ref} is the reference stiffness modulus for unloading/reloading and is approximately 3 times larger than E_{50}^{ref} (Plaxis default setting).

The tangent stiffness modulus E_{oed} is also stress-dependent and obtained by the oedometer test. Compared to purely elastic constitutive models, the elastoplastic Hardening Soil model does not contain a fixed relationship between E_{50} and E_{oed}; as a consequence, E_{oed} can be specified independent of E_{50}. It should be noted that, in contrast to E_{50} and E_{ur}, the minor principal stress σ'_1 is used to describe the stress-dependency of E_{oed}. E_{oed}^{ref} is mainly used for primary loading with one-dimensional compression. Moreover, stress dependent soil behaviour is described by the power factor m ($0.5 < m < 1$).

$$E_{50} = E_{50}^{ref} \left(\frac{c' \cos \varphi' + \sigma'_3 \sin \varphi'}{c' \cos \varphi' + p^{ref} \sin \varphi'} \right)^m \tag{25}$$

$$E_{ur} = E_{ur}^{ref} \left(\frac{c' \cos \varphi' + \sigma'_3 \sin \varphi'}{c' \cos \varphi' + p^{ref} \sin \varphi'} \right)^m \tag{26}$$

$$E_{oed} = E_{oed}^{ref} \left(\frac{c' \cos \varphi' + \sigma'_1 \sin \varphi'}{c' \cos \varphi' + p^{ref} \sin \varphi'} \right)^m \tag{27}$$

2.1.2.2 Yield Surface of the Hardening Soil Model

Irreversible shear distortions from primary deviatoric loading paths are governed by the deviatoric yield surface f^s (Eq. (28)). Vermeer (1980) invented contour lines where γ^p (plastic shear strain) remains constant, which presumed as characteristic hardening parameter.

$$f^s = \frac{2}{E_i} \times \frac{q}{1 - \frac{q}{q_a}} - \frac{2q}{E_{ur}} - \gamma^p \quad with \quad \gamma^p = -(\varepsilon_1^p - \varepsilon_2^p - \varepsilon_3^p) \tag{28}$$

The definition of γ^p is reduced to $\gamma^p \sim -2\varepsilon_1^p$ for triaxial conditions, assuming that plastic volume expansion ε_v^p is negligible compared to the plastic shear distortion. Adding the elastic and the plastic part of the axial expansion results exactly in the value for ε_1 according to Eq. (24) from the formulation of the hyperbolic stress-strain relationship. However, this only applies, if $\varepsilon_v^p = 0$.

Considering a three-dimensional stress state, five additional flow conditions are required in addition to the flow condition depicted in Eq. (28). A non-associated flow rule ($g^s \neq f^s$) is used to describe the change in the plastic strains during hardening. The same function as in the Mohr Coulomb model (Eq. (10) is used for the plastic potential function in the Hardening Soil model. Instead of a constant dilatancy angle (ψ'), g^s considers the dilatancy angle as function of the mobilized friction angle (φ'_m). The mobilized dilatancy angle (ψ'_m) is calculated based on the well-known stress-dilatancy theory issued by Rowe (1962) and depends on the mobilized friction angle (φ'_m). In this case, slight modifications of Rowe's theory are applied:

$$\psi_m' = \begin{cases} 0 & \to 0 < \varphi_m' \leq \varphi_{pt}' \\ \vdots \\ \dfrac{\sin\varphi_m' - \sin\varphi_{pt}'}{1 - \sin\varphi_m' \sin\varphi_{pt}'} & \to \varphi_{pt}' < \varphi_m' \leq \varphi_{peak}' \end{cases} \qquad (29)$$

$$\sin\varphi_m' = \frac{\sigma_1' - \sigma_3'}{\sigma_1' + \sigma_3' - 2c'\cot\varphi'} \qquad (30)$$

$$\sin\varphi_{cv}' = \frac{\sin\varphi' - \sin\psi'}{1 - \sin\varphi'\sin\psi'} \qquad (31)$$

Where φ'_{cv} is the critical state friction angle, φ'_{pt} is the friction angle on the transition line between contraction and dilatancy and φ'_{peak} is the maximum friction angle. The material contracts for small stress ratios $\varphi'_m < \varphi'_{cv}$, whereas dilatancy appears for high-stress ratios $\varphi'_m > \varphi'_{cv}$, which is a significant characteristic of the stress-dilatancy relationship. For larger values of the mobilized friction angle φ'_m, the mobilized dilatancy angle ψ'_m is performed by Rowe's theory, as far as the results signed positive. If the results signed negative, or for very small mobilized friction angles φ'_m, ψ'_m is equal to zero. For all issues when φ' equals zero, ψ'_m is set to zero, too.

In addition to using the mobilized dilatancy angle to define the yield surface (deviatoric flow area), ψ_m is also used to calculate plastic volumetric strains under pure shear stress. Schanz et al. (1999) introduced the following relationship between $\dot{\varepsilon}_v^p$ and $\dot{\gamma}^p$; see Eq. (32) (shear hardening flow rule – linear form):

$$\dot{\varepsilon}_v^p = \dot{\gamma}^p \sin\psi_m \qquad (32)$$

Finally, the strain increments $\dot{\varepsilon}$ due to deviatoric loading are defined as (see also Eq. (2), (3)):

$$\dot{\varepsilon} = \dot{\varepsilon}^e + \varepsilon^{\dot{p}s} = (D^e)^{-1}\dot{\sigma}' + \dot{\lambda}^s \frac{\partial g^s}{\partial\sigma'} \qquad (33)$$

The plastic multiplier $\dot{\lambda}^s$ is again determined by using the consistency condition. In contrast to the Mohr Coulomb model, the consistency condition $\dot{f} = 0$ expands due to the hardening by a further term. This term contains the hardening parameter $\dot{\gamma}^p$. Mentioned that for the consistency condition the stress point cannot propagate beyond the yield surface.

$$\dot{f} = \frac{\partial f^{sT}}{\partial\sigma'}\dot{\sigma}' + \frac{\partial g^s}{\partial\gamma^p}\dot{\gamma}^p = 0 \qquad (34)$$

2.1.2.3 Cap Point of the Yield Surface of the Hardening Soil Model

The yield surface f^s can only be used to describe plastic strains under deviatoric loading. Plastic volume strains under isotropic loading, however, cannot be described with this yield surface. Therefore, a second yield surface f^c is introduced (Fig. 8), which closes the elastic cone region of the principal stress space. This so-called cap type yield surface governs isotropic hardening behaviour under isotropic loading and allows to formulate a model input independently of E_{50}^{ref} and E_{oed}^{ref}. E_{50}^{ref} mainly controls the magnitude of the plastic strains, which are related to the shear yield surface f^s. In contrast, E_{oed}^{ref} is used to control the magnitude of plastic strains, which develop in direction of the cap yield surface f^c. For triaxial conditions, the cap point f^c is defined as follows:

$$f^c = \frac{\bar{q}^2}{M^2} - \left(p'\right)^2 - p_p^2 \tag{35}$$

with

$$p' = \frac{\sigma_1' + \sigma_2' + \sigma_3'}{3} \tag{36}$$

$$\bar{q} = -(\sigma_1' - \sigma_3') \quad \rightarrow \textit{for triaxial compression} \tag{37}$$

The size and shape of the cap are determined by the parameter M and the isotropic pre-consolidation stress p_p, where M is an auxiliary model parameter that primarily depends on the earth pressure coefficient K_0^{NC} for normally consolidated soils and p_p governs the size / position of the cap-yield surface. In contrast to the deviatoric yield surface f^s, an associated flow rule ($g^c = f^c$) is available to determine plastic strain rates invoked by isotropic loading. Therefore, the ellipse could be used as a yield surface as well as a plastic potential. The plastic multiplier $\dot{\lambda}^c$ is again determined by using the consistency condition. In contrast to the Mohr Coulomb model, the consistency condition $\dot{f} = 0$ expands due to hardening by a further term (Eq. (38)). The hardening law linking $\dot{p}_p$ to volumetric cap strain $\dot{\varepsilon}_v^{pc}$ is shown in Eq. (39):

$$\dot{\varepsilon}_v^{pc} = \lambda^c \frac{\partial f^c}{\partial \sigma'} \tag{38}$$

$$\dot{\varepsilon}_v^{pc} = \frac{K_s/K_c - 1}{K_s^{ref}} \times \left[\left(\frac{p_p + c' \cot \varphi'}{p^{ref} + c' \cot \varphi'} \right)^{-m} \right] \times \dot{p}_p \tag{39}$$

K_s/K_c is the ratio of bulk moduli for isotropic swelling and primary isotropic compression, and represents another model constant in addition to m and p^{ref}. Furthermore, K_s^{ref} is the reference bulk modulus in unloading/reloading. There is a relationship between the ratio of bulk moduli K_s/K_c as well as the parameter M and K_0^{NC}, E_{ur}^{ref}, E_{oed}^{ref}, so that these three parameters togther (K_0^{NC}, E_{ur}^{ref}, E_{oed}^{ref}) can be used as input parameter to determine the magnitude of M and K_s/K_c, respectively. High values of M lead to steep caps below the Mohr Coulomb failure criterion and, thus, to small K_0^{NC} values. On the other hand, small M values responds into caps that are located around the p' axis, corresponding into large K_0^{NC} values.

To completely understand the two yield surfaces (f^s, f^c) of the Hardening Soil model, both Fig. 8 and Fig. 9 should be considered. Fig.8 shows a simple yield line in p'-q plane, whereas Fig.9 represents the yield surfaces in principal stress space. The cap yield surface f^c expands as a function of the pre-consolidation stress p_p, whereas the deviatoric yield surface f^s can expand up to the Mohr Coulomb failure surface.
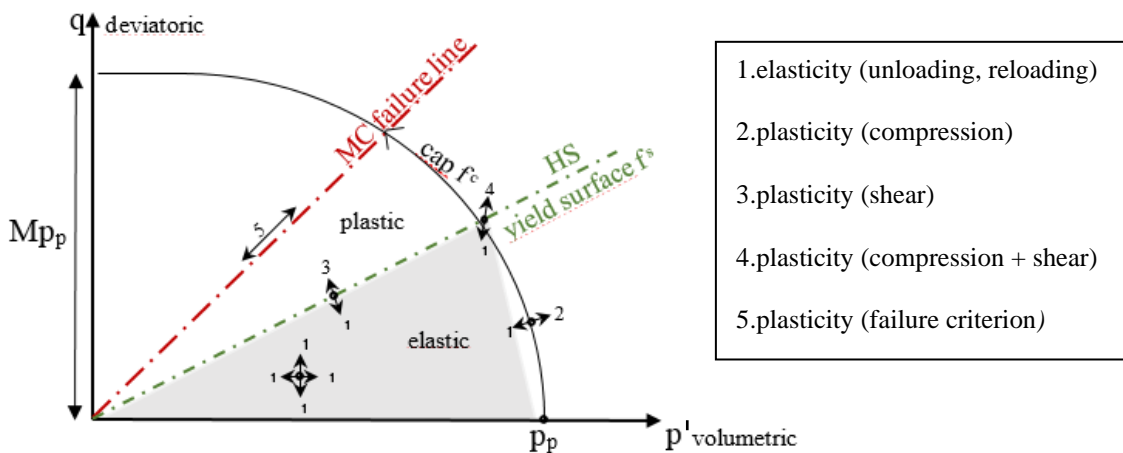
Fig. 8   Yield surfaces f ^{s} and f ^{c} of the HS Model in p'-q plane
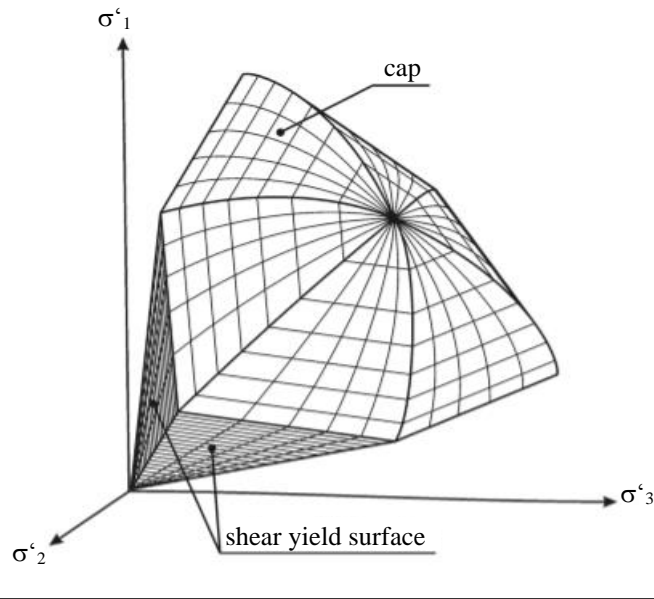
Fig. 9   Yield surfaces f^s and f^c for the HS Model in the principal stress space for a coarse-grained soil (according to M. Wehnert, 2006)

Tab. 2 shows the required parameter for the Hardening Soil model.

Tab. 2   Required parameter for the Hardening Soil model

Tangent stiffness for primary oedometer loading (plastic straining due to primary compression)	E^{ref}_{oed}	[kPa]
Secant Young's modulus in triaxial compression under confining pressure $\sigma_3 = p^{ref}$ (plastic straining due to primary deviatoric loading)	E^{ref}_{50}	[kPa]
Young's modulus in unloading/reloading at reference pressure p^{ref}	E^{ref}_{ur}	[kPa]
Poisson's ratio for unloading/reloading	ν'_{ur}	[−]
Power factor	m	[−]
Effective cohesion	c'	[kPa]
Effective friction angle	φ'	[°]
Effective dilatancy angle	ψ'	[°]

2.1.3 Hardening Mohr Coulomb Model (HMC)

The following contents in this chapter are based on [8].

The Hardening Mohr Coulomb model is used in Optum only and is herein used to resemble the Hardening Soil model in Plaxis, which was already explained in chapter 2.1.2. The basic idea of these two constitutive models is roughly the same: Both models use stress-dependent stiffness parameters and non-associated plasticity. Nevertheless, these two constitutive models are equal in results, for the boundary value problems in this thesis.

It should be mentioned that the user has the opportunity to use the MC model with an implemented hardening compression cap which is defined by:

$$F_c = |\sigma_1 - \sigma_3| - (\sigma_1 + \sigma_3)\sin\varphi_c - 2\kappa_c\sin\varphi_c \qquad (40)$$

$$\dot{\kappa}_c = -H\dot{\varepsilon}^p_{v,c} \qquad (41)$$

The cap hardens according to $\dot{\kappa}_c$ ($\kappa_{c,0}$ initial compressive strength); $\dot{\varepsilon}^p_{v,c}$ defines the part of the plastic volumetric strain associated with the compression cap. H is the corresponding hardening parameter and φ_c represents the inclination of the compression cone. Fig.10 shows the stress-strain response under drained confined compression.
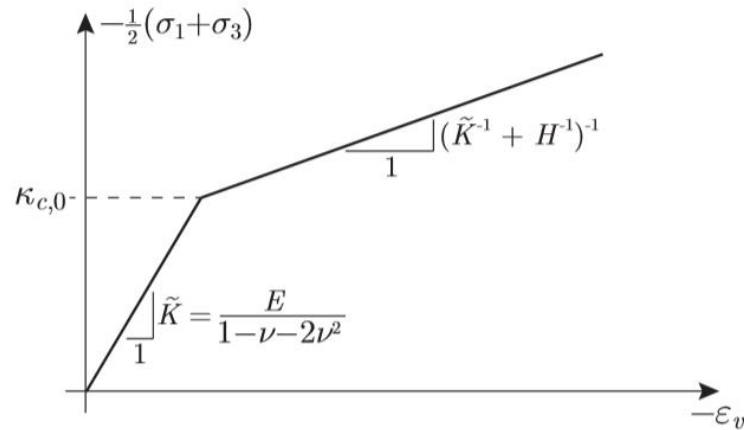
Fig. 10   Stress-strain response under drained confined compression (Optum G2 Material Manual, 2016)

Nevertheless, *the Mohr Coulomb model has a number of inherent limitations and cannot be expected to capture the entire spectrum of soil behaviour* (Optum G2 Material Manual, 2016). On the other hand, the predictions of any model are strongly depending on the choice of the input material parameters. Indeed, there is no guarantee that a complex model represents the reality better than a simple model. However, the Hardening Mohr Coulomb model (HMC) was generated to eliminate some of the drawbacks of the standard Mohr Coulomb model. The HMC model was first developed by Muir Wood (2004) considering a triaxial stress space, later extended by Doherty and Muir Wood (2013) considering a general stress space. In comparison to other non-granular materials, soil behaves differently in stiffness for initial loading and unloading/reloading processes. The apparent stiffness in initial loading is significantly less than the observed stiffness after unloading/reloading. To define the initial stiffness, the secant modulus E_{50} is used:

$$E_{50} = \frac{\frac{1}{2}q_u}{\varepsilon_{1,50}} \quad with \quad q_u = (\sigma_1 - \sigma_3)_u \qquad (42)$$

The ultimate shear stress is characterized by q_u and the axial strain at half the ultimate shear stress is defined as $\varepsilon_{1,50}$. For unloading/reloading conditions the stiffness modulus is defined by E_{ur}. It should be mentioned that E_{ur} is an elastic stiffness, whereas E_{50} is active in both, the elastic and plastic strain range. Thus, E_{ur}^{ref} (unloading/reloading) and the constant Poisson ratio ν_{ur} (transverse expansion factor) are required as elastic parameters, whereas the "elastoplastic" E_{50}^{ref} (primary loading) is not related in an obvious linear fashion. In general, both moduli E_{50}, and E_{ur}, are stress-dependent stiffness moduli, which grow with increasing confining pressure. E_{ur} is approximately 2-5 times higher compared to E_{50}. The amount of stress dependency is given by the power m (0.5< m <1). Fig. (11) compares real soil behaviour in primary loading and unloading/reloading with numerical results when applying the Mohr Coulomb model.
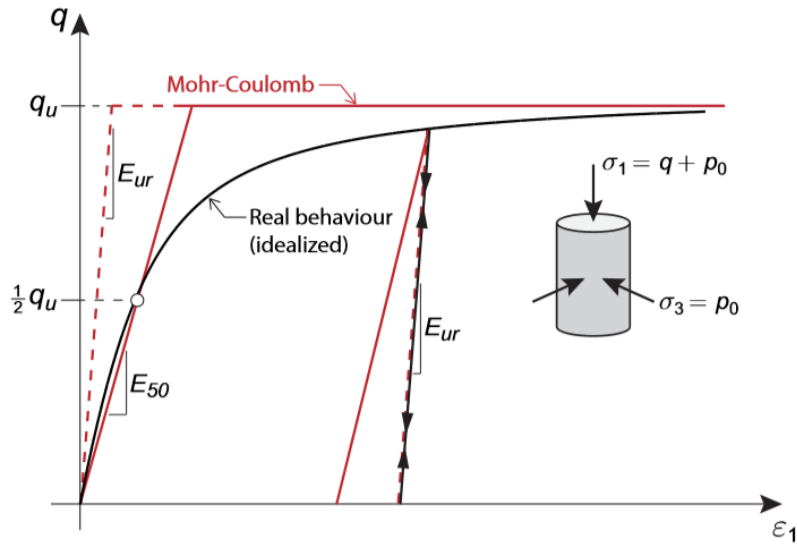
Fig. 11   Soil behaviour under primary and un/reloading conditions (Optum G2 Material Manual, 2016)

The ultimate shear stress is proportional to the pressure p', whereas p' is defined by $q_u = M p_u$. M characterizes a material parameter and p_u the confining pressure at the ultimate limit state (p_0 confining pressure). For conventional triaxial compression and a purely frictional material the ultimate shear stress is defined by Eq. (43).

$$q_u = \left(\frac{3M}{3-M}\right) p_0 \quad with \quad M = \frac{6\sin\varphi}{3-\sin\varphi} \quad (43)$$

Under an appreciable level of shear strains, the dilation is a function of the material density, which is therefore related to the strains. For dense soils under continuing shearing, the soil undergoes a significant amount of dilation, whereas loose soils tend to dilate less, up to a plastic contraction. The actual dilation observed in experiments is in fact quite variable compared to constitutive models that use constant dilation and thus are not representing the real soil behaviour. Tayler (1948) suggested to link the variability of the current dilation to the current stress ratio q/p'. Approaching ultimate limit state, the dilation increases, nevertheless soil undergoes compaction as well. N characterizes the dilation at the ultimate limit state and can be described by Eq.(45).

$$\frac{\dot{\varepsilon}_v^p}{\dot{\varepsilon}_s^p} = M - N - \frac{q}{p} \quad (44)$$

$$N = \frac{3\sin\psi}{\sqrt{3}\cos\theta + \sin\theta\sin\psi} \quad (45)$$

$$\theta = -30° \rightarrow \frac{\dot{\varepsilon}_v^p}{\dot{\varepsilon}_s^p} = \frac{6\sin\varphi}{3-\sin\varphi} - \frac{6\sin\psi}{3-\sin\psi} - \frac{q}{p} \quad (46)$$

The Hardening Mohr Coulomb model deals with three regions in p'-q stress space, contrary to the Mohr Coulomb model which consists of one elastic region only, which is limited by a failure criterion.
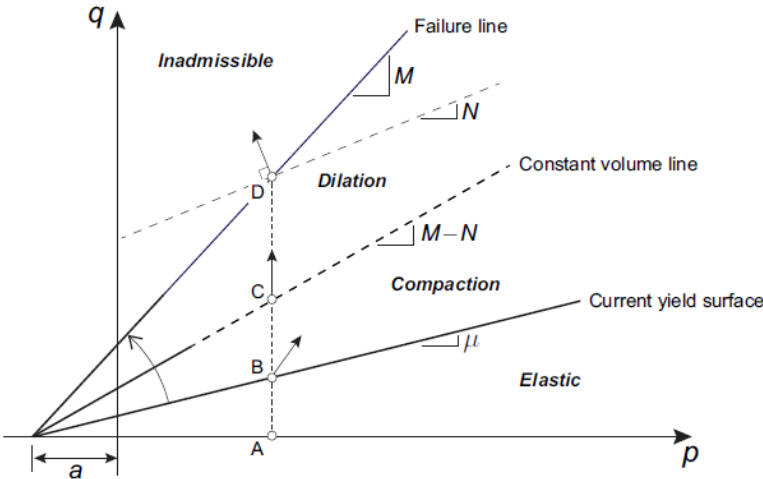
Fig. 12   Hardening, compaction and dilation procedure in the HMC model (Optum G2 Material Manual, 2016)

Tab. 3   Hardening, compaction and dilation procedure in the HMC model

1	Elastic region point A to B	no plastic/irreversible strains shear loading initial yield surface is reached
2	Compaction region point B to C	hardening of yield surface implying a decrease of stiffness compaction takes place
3	Dilation region point C to D	plastic dilation occurs → failure

In practice, the HMC model is initialized as follows:

Tab. 4   Practice initialization of the Hardening Mohr Coulomb model

1	Initial stress calculated by K_0 procedure (automatic or manual (via separate step))
2	μ_{min} is calculated based on the stress state at each point stress state satisfies the initial yield criterion → $F_0 = q_0 - \mu_{min}(p'_0 + a) = 0$
3	Finally, set $\mu_0 = \mu_{min} + \delta\mu$ $\delta\mu$ user defined, using $F = q - \mu_0(p'+a)$ as initial yield surface → initial point will be below yield

It should be mentioned that, as a consequence of point 3 Tab.4, soil behaves much stiffer at very low levels of strain (Small strain stiffness).
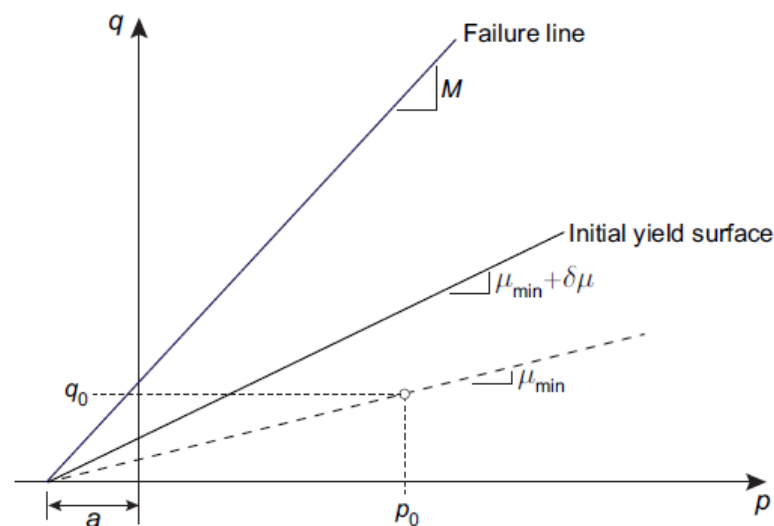
Fig. 13   Practice initialization of the Hardening Mohr Coulomb model (Optum G2 Material Manual, 2016)

The HMC model makes use of three stiffness parameters, which can be entered in two different ways: Set A and Set B. Set A is shown in Tab.5, which is used for all calculations (as well as Plaxis HS Model).

Tab. 5   Required parameter for the hardening Mohr Coulomb model

Set A	Secant Young's modulus in triaxial compression under confining pressure $\sigma_3 = p^{ref}$	E^{ref}_{50}	[MPa]
	Young's modulus in unloading/reloading at reference pressure p^{ref}	E^{ref}_{ur}	[MPa]
	Poisson's ratio in unloading/reloading at reference pressure p^{ref}	ν'_{ur}	[−]
	Power of stress-level dependency of stiffness	m	[−]
Strength parameter according to MC	Effective cohesion	c'	[kPa]
	Effective friction angle	φ'	[°]
	Effective dilatancy angle	ψ'	[°]

2.2 Numerical Methods

2.2.1 FEA

The following contents in this chapter are based on [9], [10].

It should be mentioned that Plaxis has only the opportunity to use FEA, whereas Optum has the opportunity to use FEA as well as FELA. FEA is known as displacement-based finite element analysis. For plane strain (2D) conditions the domain can get discretized by either 6-noded or 15-noded triangular elements, which are defined by the user itself, for both programs (Plaxis, Optum). The former is defined by second order (quadratic) interpolation functions based on nodal displacements and first-order (linear) interpolation based on the strains, whereas the numerical integration involves three Gauss points. The latter is defined by a fourth-order interpolation based on the displacements and third order (cubic) interpolation based on the strains, whereas the numerical integration involves twelve Gauss points. The 15-noded triangular element produces very accurate and high-quality stress results for difficult engineering problems, like bearing capacity. In comparison, the 6-noded triangular element produces good results for standard deformation analysis problems in engineering fields, as long as the number of elements is sufficient. Failure loads and safety factors of strength reduction are generally overestimated using 6-noded triangular elements. However, one 15-noded element is more powerful than four 6-noded elements, thus the total number of nodes and stress points is equal. The use of 15-node triangles leads to more storage consumption and slower calculation and, thus, to lower operational performance. In this thesis, all examples have been modeled using a 15-noded element. For three-dimensional (3D) conditions the domain can get discretized only by a 10-noded triangular (quadratic) element (Plaxis 3D only; Optum 3D → LB, UB).

o   displacement node   □   stress node (Gauss points)
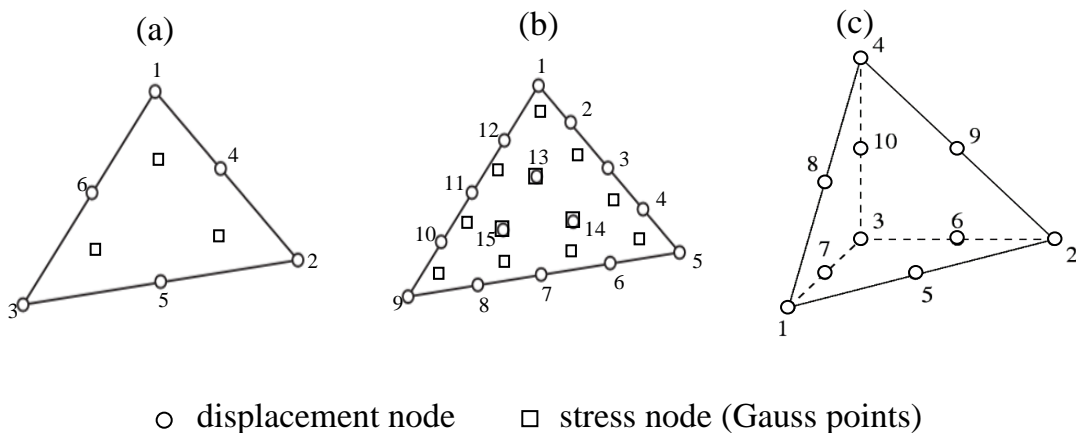
Fig. 14   (a)   6-noded   triangular   element,   (b)   15-noded   triangular   element, (c)   10-noded tetrahedral element (according to Optum G2 Theory Manual, 2016)

Each node is outlined by a specific number of degrees of freedom according to the unknown displacement component. The distribution of the displacement component within the element depends on the nodal values of displacements as well as the shape function N (Eq. (47)). The number of nodes determine the variation of the displacements within the elements and leads to the polynomial form of the distribution.

$$u = Nv \tag{47}$$

In order to calculate the strains from the nodal displacements, a strain interpolation matrix B is introduced. Matrix B contains derivatives of the shape functions (Eq. (48)).

$$\varepsilon = Bv \tag{48}$$

The formulation of the equilibrium equation (Eq. (49)) involves body forces h as well as tractions t imposed on the surface. An incremental process has to be introduced, due to the unknown actual stress state σi (Eq.(50)). σ^{i-1} represents the known stress state of the previous step and $\Delta\sigma$ is the sought additional stress increment. Equilibrium is reached as soon as the difference between external and internal forces falls below a specified threshold.

$$\int B^T \Delta\sigma dV \; = \; \int N^T h^i dV + \int N^T t^i dS - \int B^T \sigma^{i-1} dV \tag{49}$$

$$\sigma^i = \sigma^{i-1} + \Delta\sigma \tag{50}$$

For the preexisting conditions (i.e. elastoplastic behaviour) no linear correlation between strains and stresses is given, thus an iterative procedure has to be introduced to fulfill equilibrium within the domain. The elastoplastic material behaviour includes a non-linear material stiffness matrix D (Eq. (51)).

$$\sigma = D\varepsilon \tag{51}$$

The calculation procedure of displacement-based finite element analyses initiates by adopting a displacement increment Δu; next, the interpolation matrix B is used to obtain the strain increment $\Delta\varepsilon$. Eq. (52) is used to rate the stress increment, whereas D^e defines the elastic material stiffness. The vector of incremental plastic strains $\Delta\varepsilon^p$ depends on the material behaviour itself. In the elastic regime, $\Delta\varepsilon^p$ equals zero, whereas for elastoplastic conditions, it has to be determined as in Vermeer (1989).

$$\Delta\sigma = D^e(\Delta\varepsilon - \Delta\varepsilon^p) \tag{52}$$

Substituting the incremental stress-strain relation into the equilibrium Eq. (49), the resulting correlation can be written as follows:

$$K^i \Delta v^i = P_{ext}^i - P_{int}^{i-1} \qquad (53)$$

K^i stiffness matrix (step i)

Δv^i incremental displacement vector (step i)

P_{ext}^i external force vector (step i)

P_{int}^{i-1} internal force vector (step i-1)

The stiffness matrix is iteratively updated, whereas equilibrium and compatibility conditions are met (considering the non-linear relation of stress and strain increments). The global stiffness matrix K comprises the stiffness components of the entire model (Eq. (54)). *The incremental displacement vector Δv^i is defined as the sum of sub-incremental displacement vectors δv, applied to the domain* (MA Thesis Oberhollenzer, 2017).

$$K = \int B^T DB dV \qquad (54)$$

2.2.2 FELA

The following contents in this chapter are based on [11].

Finite element limit analysis (FELA) is based on the lower an upper bound theorem of plasticity. The gap between the two boundaries represents the range of admissible solutions. FELA requires an elastic-perfectly plastic material (MC failure criteria). Furthermore, only associated plasticity ($\psi' = \varphi'$) can be modeled; in order to resemble non-associated flow, the Davis Approach has to be applied. If the failure load is reached (MC failure criterion), infinite plastic strains occur at a constant stress level. On the other hand, elastic strain increments are set to zero because they have no effect on the failure load.

2.2.2.1 Lower-Bound Theorem of Plasticity

The lower-bound theorem requires a statically feasible stress field, which satisfies equilibrium conditions (body forces, surface tractions) for the whole system, as well as stress boundary conditions and yield criteria. In contrast, soil kinematics are not concerned. In respect to a lower-bound solution the failure criteria and therefore the actual collapse load, is not reached. Discontinuities in the stresses cause the division of the material into several stress zones, which do not violate the yield condition. Fig. (15) shows a soil mass with a volume V and a boundary area A, which is exposed to fixed surface stresses t and unknown tractions q. In practice, q might correspond to unknown bearing capacity, whereas t might correspond to a prescribed surcharge load (Sloan, 2013). Additionally, two body forces g (fixed) and h (unknown) are acting over the volume V. The former is generally defined as unit weight, whereas the latter is an unknown body force, which could be useful for calculating slope stability or excavations.
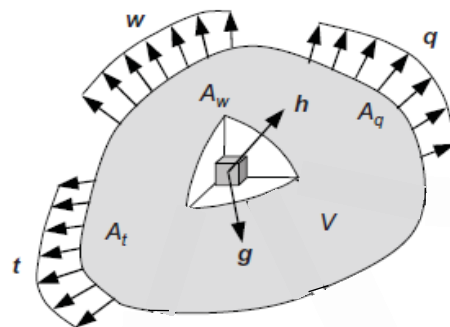
Fig. 15   Surface and body forces acting on soil mass (according to Sloan, 2013)

Referring to the collapse load (Eq. (55)) of a bearing capacity problem, Q_2 equals zero and Q_1 at least equals q_n, by maximizing the load carried by the tractions normal to the boundary edge.

$$Q = \int_{Aq} Q_1(\boldsymbol{q})dA + \int_V Q_2(\boldsymbol{h})dV \quad \rightarrow \quad Q = \int_{Aq} q_n dA \quad (55)$$

In the case of the lower-bound theorem, a non-linear optimization problem is modeled by discretizing the model in 3-noded elements. The nodes of each element consist of two vectors, one of three unknown stresses, and one of two unknown body forces. *The unknowns are subject to equilibrium equality constraints for each continuum element, equilibrium equality constraints for each discontinuity, stress boundary conditions, and a yield condition inequality constraint for each node* (MA Thesis Oberhollenzer, 2017).
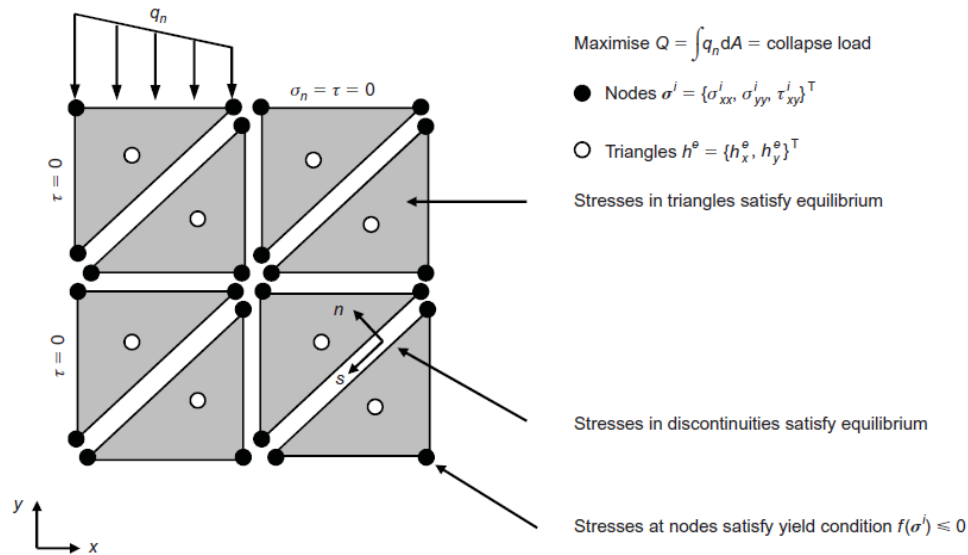
Fig. 16   Lower-bound mesh for strip footing problem (according to Sloan, 2013)

The object function, which has to be maximized up to failure, signifies the collapse load. In case of a bearing capacity problem, the external traction q is increased until failure occurs. The resulting forces acting in a normal and tangential direction are defined by Eq.(56), based on the linear variation of the stresses over the edge. The stresses q^1 and q^2 are acting at the nodes of the 3-noded triangular element.

$$\begin{Bmatrix} Q_n \\ Q_s \end{Bmatrix} = \frac{L}{2}\left(\begin{Bmatrix} q_n^1 \\ q_s^1 \end{Bmatrix} + \begin{Bmatrix} q_n^2 \\ q_s^2 \end{Bmatrix} \right) \qquad (56)$$

By summing up each load edges, and making use of a Cartesian coordinate system, the failure load can be formulated as $c_1{}^T\sigma$ in case of bearing capacity problems. On the contrary, for slope stability problems (body forces instead of external forces), $c_2{}^T\sigma$ is defining the critical condition at failure. In this context, c represents a vector of constants and σ represents the global vector of unknown nodal stresses.

To get statically admissible conditions, the stresses in each element have to satisfy continuum equilibrium. Based on the linear variation of the stresses over the edge, a relation between σ and the linear shape function N_i can be established. The shape function depends on x and y and the element nodal coordinates.

$$\frac{\partial \sigma_{xx}}{\partial x} + \frac{\partial \tau_{xy}}{\partial y} + h_x + g_x = 0 \quad (57)$$

$$\frac{\partial \sigma_{yy}}{\partial y} + \frac{\partial \tau_{xy}}{\partial x} + h_y + g_y = 0 \quad (58)$$

$$\boldsymbol{\sigma} = \sum_{i=1}^{3} N_i \boldsymbol{\sigma}^i \quad (59)$$

Inserting Eq.(59) into Eq.(57),(58) results in a pair of equilibrium where the B-matrices define the standard strain-displacement matrix and further consider compatibility constraints. For an elegant implementation of the stress discontinuities, both sides have to be multiplied by the element area A^e (Eq. (60)). Equilibrium at any point in the domain is satisfied as long as Eq.(60) is fulfilled.

$$[\overline{\boldsymbol{B}}_1^T \overline{\boldsymbol{B}}_2^T \overline{\boldsymbol{B}}_3^T]\boldsymbol{\sigma}^e = -(\boldsymbol{h}^e + \boldsymbol{g}^e)A^e \quad (60)$$

$$where \ \overline{\boldsymbol{B}}_j^T = A^e \boldsymbol{B}_1^T = \begin{bmatrix} b_j & 0 & c_j \\ 0 & c_j & b_j \end{bmatrix} \quad (61)$$

To obtain statically admissible stress fields, which are in equilibrium, the normal and shear stresses have to be the same on both sides of discontinuities; see Eq.(62). Consequently, each pair of nodes has to consider two equality limitations induced by two associated Cartesian stress components. Considering this limitation over all pairs of nodes gives the global set of conditions for satisfying discontinuity equilibrium. Across each stress discontinuity, the normal and shear stresses are continuous, while the tangential normal stress may differ at the same nodes.

$$\begin{Bmatrix} \sigma_{nn}^1 \\ \tau_{ns}^1 \end{Bmatrix} = \begin{Bmatrix} \sigma_{nn}^2 \\ \tau_{ns}^2 \end{Bmatrix}, \begin{Bmatrix} \sigma_{nn}^3 \\ \tau_{ns}^3 \end{Bmatrix} = \begin{Bmatrix} \sigma_{nn}^4 \\ \tau_{ns}^4 \end{Bmatrix} \quad (62)$$

Fig. 17, shows a zero-thickness interface element which is used to model areas of discontinuity; the latter helps to increase calculation accuracy of the collapse load.
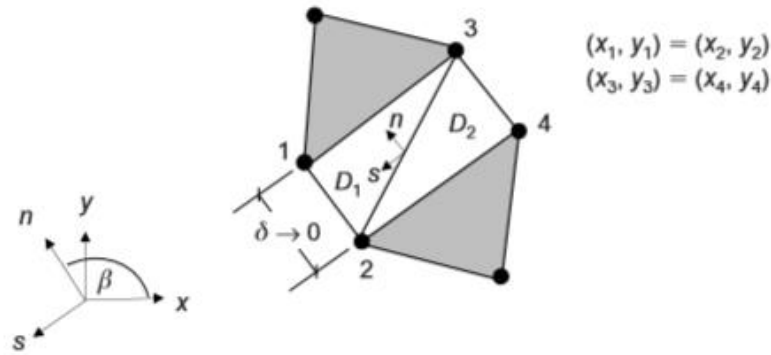
Fig. 17   Statically admissible stress discontinuity for zero thickness elements (Sloan, 2013)

Fig. 17 shows nodal pairs initially located at the same coordinates (x_1, $y_1 = x_2$, y_2 and x_3, $y_3 = x_4$, y_4), which leads to a change in Eq.(63) and provides the evidence that $\mathbf{B}_{1}^{T}\boldsymbol{\sigma}^1 = \mathbf{B}_{1}^{T}\boldsymbol{\sigma}^2$.

$$[\bar{\boldsymbol{B}}_1^T - \bar{\boldsymbol{B}}_1^T \quad 0]\boldsymbol{\sigma}^e = 0 \tag{63}$$

To fulfill the stress boundary conditions with respect to equilibrium conditions, the stresses for any boundary node have to correspond to the prescribed surface traction t. *These constraints must be applied to all edges where surface stresses are specified, and they ensure that the boundary conditions are satisfied exactly for a linear finite element model* (Sloan, 2013).

$$\begin{Bmatrix} \sigma_{nn}^1 \\ \tau_{ns}^1 \end{Bmatrix} = \begin{Bmatrix} t_n^1 \\ t_s^1 \end{Bmatrix}, \begin{Bmatrix} \sigma_{nn}^2 \\ \tau_{ns}^2 \end{Bmatrix} = \begin{Bmatrix} t_n^2 \\ t_s^2 \end{Bmatrix} \tag{64}$$
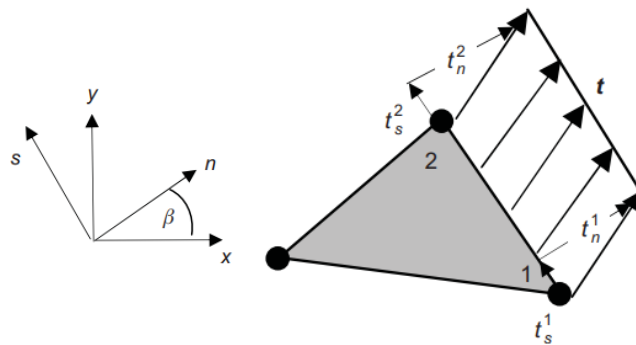
Fig. 18   Stress boundary conditions (Sloan, 2013)

Given that the linearly variation of the stresses over an element, as well as the convex behaviour of the yield function is provided, the yield condition is satisfied and the limitation f (σ^i) ≤ 0 is fulfilled at each node i.

2.2.2.2 Upper-Bound Theorem of Plasticity

In contrast to the lower-bound theorem, which represents the lower bound of possible failure loads, the upper-bound theorem marks the upper limits of possible failure loads. In simple terms, the upper bound theorem states that an upper bound to the true collapse load can be derived from an energy equation between the external work and the internal plastic power dissipation for any kinematically admissible failure mechanism (Yu, 2006: Plasticity and Geotechnics). Modifications in displacement within the soil body have to be kinematically admissible. Furthermore, no gaps as well as overlaps should occur (i.e. compatibility conditions). Notably, the stress distribution does not have to fulfill equilibrium compared to the lower-bound theorem. The upper-bound calculation procedure is formulated as a non-linear optimization problem by applying a velocity distribution u = {u_x, u_y, u_z}^{T} that satisfies compatibility, the flow rule as well as the velocity boundary conditions w. The mechanism which gives the least dissipated plastic power is used to compute the best upper bound of the limit load. Additionally, it leads to a minimizing of the internal power dissipation (plastic shearing) by the rate of work (fixed external forces), according to Eq.(65). Eq.(65) is also known as the object function.

$$\dot{W} = P_{int} - \int_{A_t} \boldsymbol{t}^T \boldsymbol{u} dA - \int_V \boldsymbol{g}^T \boldsymbol{u} dV \quad (65)$$

$$P_{int} = \int_V \boldsymbol{\sigma}^T \dot{\boldsymbol{\varepsilon}}^p dV \quad\quad (66)$$

The upper bound is specified by the enhanced value $\dot{W}$ to the rate of expended work caused by external forces P_{ext} (Eq.(66))

$$P_{ext} = \int_{A_q} \boldsymbol{q}^T \boldsymbol{u} dA - \int_V \boldsymbol{h}^T \boldsymbol{u} dV \quad\quad (67)$$

Similar to a lower-bound theorem linear elements are used to discretize the domain and investigate kinematic admissibility of the velocity field. The 3-noded elements adopt a linear velocity distribution u, which is associated with a constant stress field σ. *To satisfy the requirements of the upper-bound theorem, the unknowns are subject to constraints arising from the flow rule, the velocity boundary conditions, and the yield condition* (Sloan, 2013). The nodes of each element are described by means of two vectors; one comprises three unknown stresses, the other one two unknown velocities as well as an unknown non-negative plastic multiplier rate $\dot{\lambda}$. The unknowns are obtained by solving Eq.(65).

In each triangle, the plastic strains (velocities) are governed by the limitations attributed to associated plastic flow, and also have to fulfill the consistency requirement $\dot\lambda f(\sigma_e) = 0$. For modeling velocity discontinuities two multipliers are implemented to realize associated plasticity. Each corresponding node has to meet the velocity boundary conditions.

Summing up, all stresses in each element result in the yield condition $f(\sigma^e) \leq 0$ (Sloan, 2013).
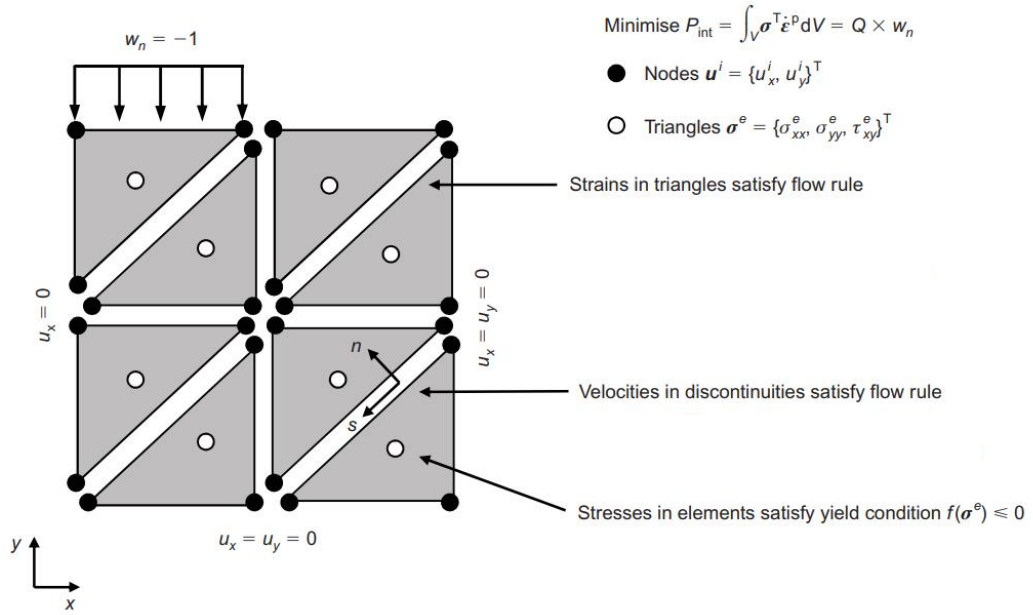
Fig. 19   Upper-bound mesh for strip footing problem (according to Sloan, 2013)

The stresses and plastic strain rates $\dot\varepsilon^p$ are constant over each element, and are resulting in an internal power dissipation P_{int} determined by Eq.(68), where σ^T is the global vector of element stresses and u^e is the global vector of nodal velocities.

$$P_{int} = \int_V \sigma^T \dot{\varepsilon}^p dV = \Sigma_e \left(\sigma^T \dot{\varepsilon}^p V\right)^e = \Sigma_e \sigma^T \bar{B}^e u^e = \sigma^T \bar{B} u^e \quad (68)$$

The residual integrals in Eq.(65) can be evaluated by using the linear expansions of velocities u, resulting in $c^T u$; in the latter, c is a vector of known constants (Sloan, 2013). The final correlation is shown in Eq.(69).

$$\dot{W} = \sigma^T \bar{B} u - c^T u \quad (69)$$

For a triangular element, the continuum flow rule conditions are given in Eq.(70). The plastic multiplier is denoted as $\dot\lambda$.

To ensure the occurrence of the plastic strain $\dot{\varepsilon}^p$ at the yield surface, $\dot{\lambda}\, f(\sigma^e)$ has to be zero.

$$\dot{\varepsilon}^p = \dot{\lambda}\nabla f(\boldsymbol{\sigma}^e),\ \dot{\lambda} \geq 0 \qquad (70)$$

Any 3-noded element has to fulfill the flow rule constraints, as shown in Eq. (71).

$$\overline{\boldsymbol{B}}^e \boldsymbol{u}^e = \dot{\alpha}\nabla f(\boldsymbol{\sigma}^e) \qquad (71)$$

$$\dot{\alpha} \geq 0,\quad \dot{\alpha}f(\boldsymbol{\sigma}^e) = 0 \ \rightarrow\ \dot{\alpha} = A^e\dot{\lambda}$$

Hence, in the case of two-dimension conditions, the continuum flow rule produces four resemble restrictions, as well as one inequality restriction on the element unknowns. Whenever the yield criterion represents a linear stress function, all resemble restrictions results in a non-linear shape.

For the discontinuity flow rule a similar procedure as for lower-bound theorems is used to describe velocity discontinuities for upper-bound theorems. Fig. (20) represents two triangles of zero thickness (six unknowns), both corresponding to the flow conditions expressed in Eq.(71). Along the discontinuity, velocity peaks can act in normal Δu_n as well as tangential Δu_s directions, which results in potential differences at nodes which initially had the same coordinates. These peaks are represented in Fig.(20) by means of two zero-thickness continuum elements with $(x_1, y_1) = (x_2, y_2)$ and $(x_3, y_3) = (x_4, y_4)$. It should be mentioned that for each triangle the flow rule constraints (Eq.(71)) have to be satisfied.
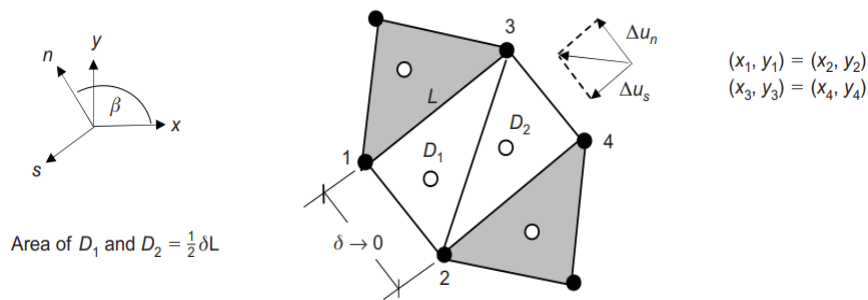
Fig. 20   Kinematically admissible velocity discontinuity (Sloan, 2013)

$$\Delta u_n = \frac{\dot{\alpha}\partial f}{\partial\sigma_n} \quad ; \quad \Delta u_s = \frac{\dot{\alpha}\partial f}{\partial\tau} \qquad (72)$$

$$\rightarrow with\ \dot{\alpha} \geq 0,\ \dot{\alpha}f(\sigma_n,\tau) = 0$$

In Eq. (72), $\dot{\alpha}$ is the product of an amount A^e equal to zero and an infinite amount $\dot{\lambda}$, also known as $\delta=0$. In the case of plane-strain discontinuity conditions, the common yield condition f (σ^e) can be substituted by its planar counterpart $f(\sigma_n,\tau)$. Whereby, σ_n declares σ_{nn} and τ declares τ_{ns}. The flow rule conditions (Eq. (70)) that define $(\Delta u_n, \Delta u_s)$ are then given by Eq.(72)

To fulfill the velocity boundary conditions with respect to kinematic admissibility, the velocity field must satisfy the prescribed boundary conditions. The limitations must be applied to all boundary nodes, where velocity is specified. Based on the linearly variation of the velocity over the edge, the boundary conditions can be expressed as Eq.(73).

$$\begin{Bmatrix} u_n^1 \\ u_s^1 \end{Bmatrix} = \begin{Bmatrix} w_n^1 \\ w_s^1 \end{Bmatrix} , \begin{Bmatrix} u_n^2 \\ u_s^2 \end{Bmatrix} = \begin{Bmatrix} w_n^2 \\ w_s^2 \end{Bmatrix} \qquad (73)$$
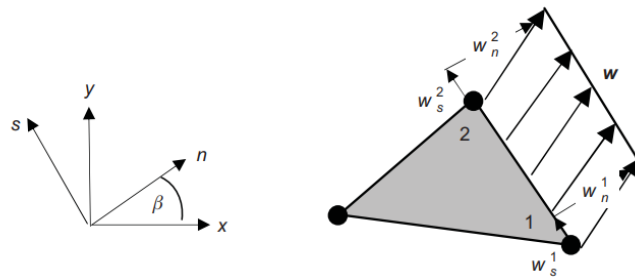
Fig. 21   Velocity boundary conditions (Sloan, 2013)

To implement an upper-bound theorem, supplementary restrictions are imposed on the velocity field, to correspond the type of loading. According to Fig.19, the velocity boundary conditions shown in Eq.(73) could be used to model loading under associated plasticity conditions by applying the normal velocities $w_n^1 = w_n^2 = -C$ along the convenient element edges, whereas C represents a constant value. In the case of bearing capacity problems, where a specific part of the soil body is loaded by an unknown uniform normal pressure q, (e.g. strip footing), the surface normal velocities are imposed by restrictions to match the type of loading. These restrictions on the surface normal velocities result in C as a prescribed rate of flow of material across the boundary.

$$(a) \int_{A_q} u_n dA = C \qquad\qquad (b) \int_V u_y dA = -C \qquad (74)$$

To ensure that kinematic admissibility conditions are met (including zero thickness discontinuities), the stresses must satisfy the following yield condition within each element: $f(\sigma^e) < 0$. By assuming the element stresses to be constant, results are given in one non-linear inequality restriction for each continuum and discontinuity triangle.

2.2.2.3 Davis Approach

The following contents in this chapter are based on [12].

Finite element limit analyses are restricted to an associated flow rule, whereas the SRFEA technique provides the opportunity of using a non-associated flow rule. The application of an associated flow rule presumes φ'=ψ'; as a consequence, soil dilatancy is generally overestimated. In order to overcome this limitation, Davis (1968) suggested to modify the strength parameters (c' → c*, φ' → φ*) to model non-associated plasticity (ψ'< φ'), shown in Eq. 75-77. The parameter β failure (Eq. (77)) is determined as a function of the effective friction angle φ' and the effective dilatancy angle ψ'.

$$c^* = \beta c' \tag{75}$$

$$\tan \varphi^* = \beta \tan \varphi' \tag{76}$$

$$\beta_{failure} = \beta = \frac{\cos \psi' \cos \varphi'}{1 - \sin \psi' \sin \varphi'} \tag{77}$$

Since the original Davis Approach A leads to strongly conservative results regarding the factor of safety, two further approaches (Davis B, Davis C) were developed by Tschuchnigg et al. (2015) in order to investigate the failure mechanism in more detail. In addition to generally reduced strength parameters according to Davis Approach A, the β_failure value applied in Davis Approach B (Eq.(78)) is determined based on an iterative procedure and varies throughout strength reduction procedures. β_failure is iteratively updated until the factor of safety remains constant.

$$\beta_{failure} = \frac{\cos\left(\tan^{-1}\left(\frac{\tan \varphi'}{FoS}\right)\right) \times \cos\left(\tan^{-1}\left(\frac{\tan \psi'}{FoS}\right)\right)}{1 - \sin \cos\left(\tan^{-1}\left(\frac{\tan \varphi'}{FoS}\right)\right) \times \sin\left(\tan^{-1}\left(\frac{\tan \psi'}{FoS}\right)\right)} \tag{78}$$

In much the same way, Davis Approach C resembles Davis Approach B; however, the effective dilatancy angle ψ' remains constant for Davis Approach C. The value β_failure (Eq.(79)) is again iteratively updated until the factor of safety remains constant. Consequently, Davis B and C lead to equal results in terms of the factor of safety, if ψ' equals zero.

$$\beta_{failure} = \frac{\cos\left(\tan^{-1}\left(\frac{\tan \varphi'}{FoS}\right)\right) \times \cos \psi'}{1 - \sin \cos\left(\tan^{-1}\left(\frac{\tan \varphi'}{FoS}\right)\right) \times \sin \psi'} \tag{79}$$

Tab. 6   Comparison of Davis Approach A, B, C (according to Tschuchnigg 2015a)

	Davis A	**Davis B**	**Davis C**
β	constant	varies	varies
ψ'	$\beta_{failure} = f(\varphi',\psi')$	$\beta_{failure} = f(\varphi'_{failure},\psi'_{failure})$	$\beta_{failure} = f(\varphi'_{failure},\psi')$
Note:	*φ^* could theoretically become smaller than ψ'*	*φ^* cannot be smaller than ψ'*	*φ^* could theoretically become smaller than ψ' limit $\beta \leq 1$*

2.2.3 Flow Rule

The following contents in this chapter are based on [13], [14], [15], [16], [17].

The flow rule is a key factor in finite element analyses as well as in finite element limit analyses and defines the direction of plastic strain increments, corresponding to the first derivative of the yield function for associated plasticity. As previously discussed, finite element limit analysis is restricted to associated flow, whereas the finite element analysis based on displacements provide the opportunity of using a non-associated flow rule. Considering the plasticity theory explored by Hill et al. (1998), one has clearly to distinguish between associated and non-associated plasticity. To illustrate the explanation, a linear-elastic perfectly-plastic MC model (chapter 2.1.1) is assumed. The strain increment can be calculated by Hooke's law, as far as the respective stress increment occurs in the elastic range. Stress increments occurring at the onset of plastic behaviour (failure criterion) cannot be carried by the material itself, resulting in plastic strains. As a result, the material undergoes a certain plastic deformation. However, the flow rule determines how the plastic strains develop at failure. An associated flow rule presumes a dilatancy angle ψ' equal to the friction angle φ'; consequently, the flow rule is assumed to be associated when the plastic strain increment is perpendicular to the yield function. This is convenient because it combines the yield surface with the flow rule. Laboratory tests documented in the literature (e.g. Schweiger et al, 1995) showed that the assumption of associated plasticity generally leads to an overestimation of plastic volumetric strains. In detail outcomes of laboratory tests show that the volume increase from a soil sample was less than the associated flow rule. For the case of shallow stress points, the dilatancy angle of granular, normally consolidated soils is usually in the range of less than 10°. Further, the dilatancy angle strongly depends on the friction angle as well as the soil density. Increasing depth leads to an increasing density of the soil body and, thus, decreasing dilatancy angles (MA Thesis Sallinger, 2017). However, it should be considered that the associated flow rule is by no means natural law. In the case of friction materials, the assumption of an associated flow rule usually does not match reality. Hence, non-associated flow rules may be adopted, which resemble soil behaviour in a more realistic way. To simulate non-associated behaviour ($\varphi' \neq \psi'$), a plastic potential g is added to the equations which represent the yield function. Thus, a non-associated flow rule presumes g≠f, which influences the direction of the plastic strain increment. *The approach of flow rule requires in general coaxiality between principal stress and strain rate* (B. De Saint Venant, 1870).

Fig. 22 represents the difference between associated and non-associated flow rule with respect to the direction of the plastic strain rate vector. γ^p describes the plastic deviatoric strain rate and ε^p describes the plastic volumetric strain rate. Notably, plastic volumetric strain rates ε^p are overestimated in the case of associated plasticity.
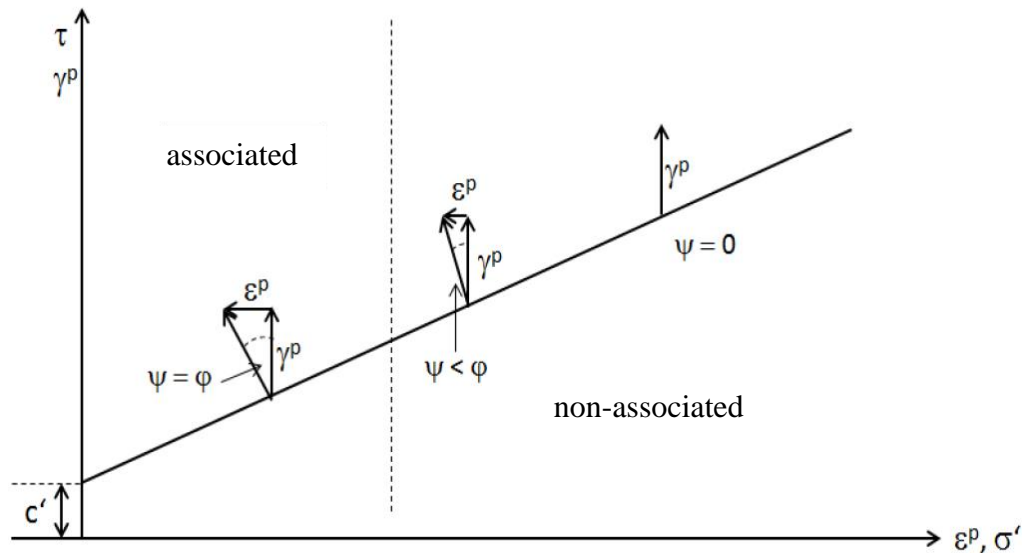
Fig. 22   Comparison of associated and non-associated flow rule (according to Egger, 2012)

To which extent plastic and elastoplastic boundary value problems are influenced by the flow rule type is still a matter of ongoing research. For a more realistic representation of the soil behaviour it is recommended to apply non-associated plasticity. Fig.23 concerns the stress-strain relation for associated as well as non-associated plasticity in combination with the Mohr Coulomb model based on a triaxial test. For loose sands and normally consolidated (NC) clays, the stress-strain relation causes a monotonically increasing up to the ultimate limit state is reached. It is shown that the deformations (volumetric vs. shear strain) are highly dependent on the flow rule. Most significantly, the resulting dilation is far too large for associated plasticity. On the other hand, non-associated plasticity specifies the amount of dilation directly and therefore the resulting can be described in more an accurate way. For dense sands and overconsolidated (OC) clays the situation is, qualitatively, nearly the same. It should be mentioned that the dilatant response of the soil ends at the onset of softening behaviour.
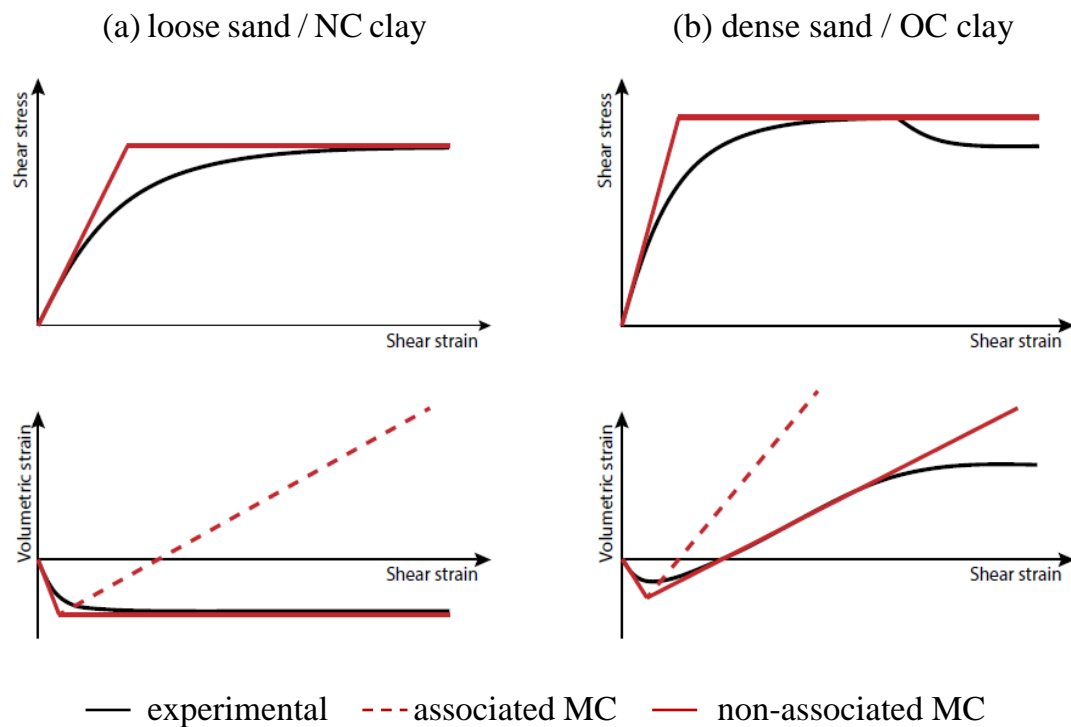
Fig. 23   Soil behaviour and capabilities of associated and non-associated Mohr Coulomb model (according to Optum G2 Theory Manual, 2016)

The effect of the flow rule on the deformations is clearly seen on lot of experiments, thus, the focus has been on how far the flow rule influences the failure load. Erickson and Drescher (2002), Loukidis and Salgado (2009), and Krabbenhoft et al. (2012) reported a reduction in bearing capacity of up to 45% for the case of a strip as well as a circular footing on sand when applying non-associated flow rule. Such reductions in bearing capacity are found in many theoretical documents and are caused by several aspects:

Matter the fact, a consequence of non-associated plasticity would result in the non-uniqueness of the limit load; while solving elastoplastic boundary value problems. The usual assumption that the limit load is unique applies only for associated plasticity. Thus, there may be multiple solutions that fulfill the governing equations, but each referring to a different limit load. This results in oscillations of the load-displacement curve beyond a certain level of displacement which is caused by switching between different modes of failure (beyond the point at which the load-carrying capacity of the structure first becomes exhausted). The level of non-uniqueness for non-associated plasticity is intimately related to the occurrence of shear bands representing localized areas of intensive deformation, which usually lead to oscillatory behaviour of the load-displacement curve (Fig.24).
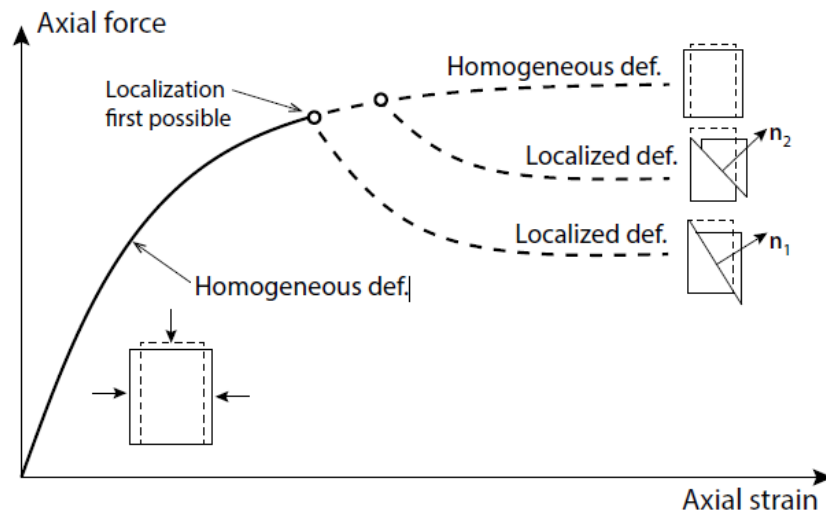
Fig. 24   Response of biaxial test prone to localization (Optum G2 Theory Manual, 2016)

Another consequence of non-associated plasticity is that the resulting limit load is significantly lower compared to the corresponding limit load under associated plasticity. The reduction of the limit load depends on the difference between friction and dilation angle and their magnitude. An increasing difference between friction and dilation angle leads to decreasing limit loads. This tendency can be attributed to localized states of increased stress and strain as well as to certain kinematic constraints of the shear bands.

As shown in many theses and papers, it has been often observed that numerical methods are depending on the finite element mesh.

2.3 Safety Analysis

2.3.1 Numerical Method

It should be mentioned that Plaxis has the opportunity to apply the strength reduction technique (SRFEA[1]) based on both, associated and non-associated plasticity. The failure load (FEA[2]) can only be calculated manually for the same conditions of plasticity. On the other hand, Optum has the opportunity to automatically calculate the failure load (FEA[2] and FELA[2]) for associated, non-associated plasticity conditions as well as Davis A, thereby taking into account non-associated plasticity conditions in combination with FELA[2]. In contrast, an automatic strength reduction is only possible for associated plasticity, by means of non-associated Davis A, either for SRFEA[1] and SRFELA[1]. Therefore, for non-associated plasticity, the strength reduction (SRFEA[1] and SRFELA[1]) can only be calculated manually.

2.3.1.1 Strength Reduction

The following contents in this chapter are based on [18].

A safety analysis by means of strength reduction corresponds to a simultaneously reduction of the strength parameter $\tan\varphi'$ and c' up to the onset, which defines the failure criteria and no more equilibrium is achieved (Eq.(80)). *It should be noted that as long as the reduced friction angle φ' is greater compared to the dilatancy angle ψ', the latter one is kept constant (Fig. 25a). At the point where $\varphi' = \psi'$, both get simultaneously reduced, as shown in Fig. 25b* (MA Thesis Oberhollenzer, 2017). In case of non-associated plasticity, a safety analysis by means of strength reduction leads to numerical instabilities without a clear failure mechanism. Since multiple solutions exist which fulfill the governing equations (due different strength parameters as mentioned in chapter 2.2.3), the factor of safety is generally lower compared to associated plasticity conditions.

$$\text{FoS}_{SR} = \frac{available\ soil\ resistance}{mobilized\ soil\ resistance} = \frac{\tan\varphi'}{\tan\varphi'_{mob}} = \frac{c'}{c'_{mob}} \quad (80)$$

---

[1] *SRFEA, SRFELA*   → *strength reduction anaylsis based on FEA / FELA*
[2] *FEA, FELA*   → *failure load analysis based on FEA / FELA*
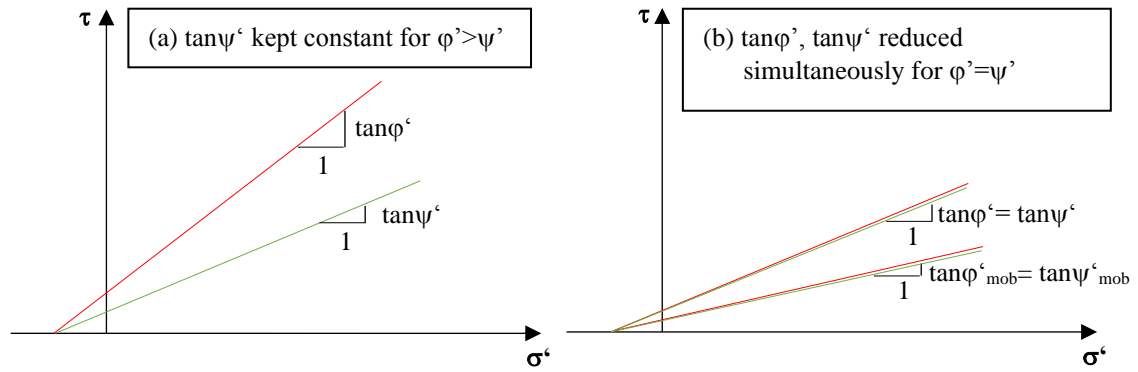
Fig. 25   Strength reduction (according to MA Thesis Oberhollenzer, 2017)

2.3.1.2 Failure Load

Safety analysis based on the consideration of applied failure loads requires a stepwise increase of the actual load until failure occurs.

$$\text{FoS}_{FL} = \frac{failure\ load}{working\ load} \qquad (81)$$

2.3.2 Analytical Method

The following contents in this chapter are based on [19], [20], [21].

The definition of a ground failure is described as collapse, which occurs, when the foundation is loaded until the failure appearance. This results in so called sliding areas between the subsoil, in which the shear resistance of the soil is overcoming, leading to a "laterally" displacement of the soil. (Fig. 26.)
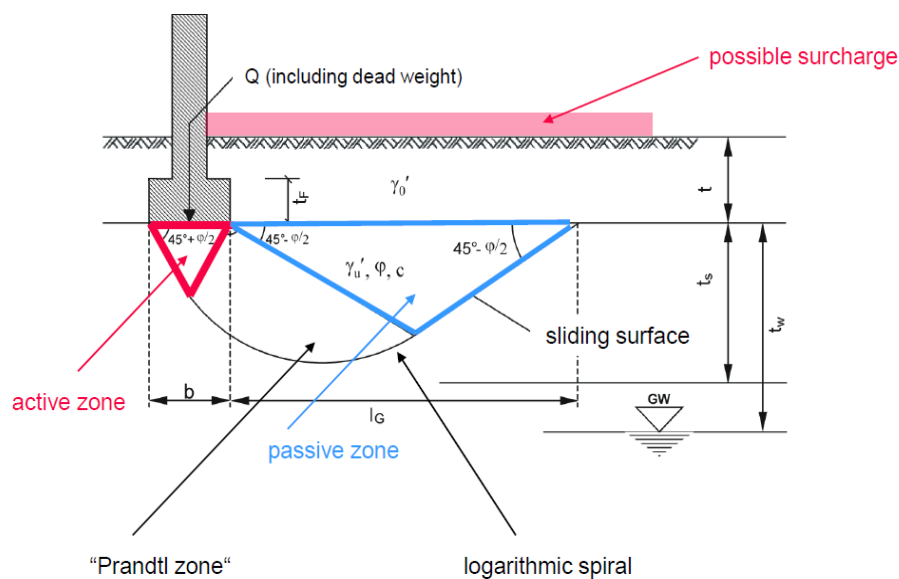
Fig. 26   Sliding surface according to bearing capacity (Lecture Nodes Advanced Soil Mechanics and Foundation Engineering (2018), Graz University of Technology)

2.3.2.1 Failure Load after DIN 4017

For the calculation of the failure load after DIN 4017 the program GGU FOOTING was used. The GGU-FOOTING program makes it possible to calculate the ground failure after DIN 4017 and settlements according to DIN 4019. The global safety concept can be used according to DIN 1054 (old) as well as the partial safety concept according to DIN 1054: 2005 and EC 7. In addition to the standard methods according to DIN 4017, the methods according to Terzaghi, Meyerhoff, Hansen, and Vesic can also be used.

Eq.(82) shows the definition of the failure load after DIN 4017 for drained conditions at final state.

$$R_n = a' \times b'[(\gamma_2 \times b' \times N_b) + (\gamma_1 \times d \times N_d) + (c \times N_c)] \quad (82)$$

influence of friction / foundation width	influence of overburden pressure / foundation depth	influence of cohesion

Eq. (83), (84), (85) represent the bearing capacity factor (N_x) according to DIN 4017, which considers five parameters:

- base values of the bearing capacity ($N_{x,0}$)
- coefficient of the load inclination (i_x)
- coefficient of the surface inclination (λ_x)
- coefficient of the foundation base inclination (ξ_x)
- foundation shape (ν_x).

$$N_b = N_{b,0} \times \nu_b \times i_b \times \lambda_b \times \xi_b \quad (83)$$

$$N_d = N_{d,0} \times \nu_d \times i_d \times \lambda_d \times \xi_d \quad (84)$$

$$N_c = N_{c,0} \times \nu_c \times i_c \times \lambda_c \times \xi_c \quad (85)$$

For the settings in GGU FOOTING the dead load of the strip foundation was considered. A study according to the influence of the depth coefficient (after Brinch Hansen) of the failure load was implemented.

2.3.2.2 Failure Load after EC7 (EN 1997-1)

The calculation of the failure load after EC7 was done manually for drained conditions in final state, shown in Eq.(86); the latter considers eight parameters:

- bearing capacity factor (N_x)
- coefficient of the load inclination (i_x)
- coefficient of the foundation base inclination (b_x)
- coefficient of the foundation shape (s_x)
- effective cohesion (c')
- overburden pressure including the foundation depth (q')
- buyoyant unit weight below foundation level (γ')
- foundation width (B').

$$
R_{f,k} = A' \times \Big[\underbrace{(c' \times N_c \times b_c \times s_c \times i_c)}_{\text{influence of cohesion}} + \underbrace{(q' \times N_q \times b_q \times s_q \times i_q)}_{\substack{\text{influence of overburden pressure} \\ \text{/ foundation depth}}} + \underbrace{0.5 \times (\gamma' \times B' \times N_\gamma \times b_\gamma \times s_\gamma \times i_\gamma)}_{\text{influence of friction / foundation width}} \Big] \tag{86}
$$

Eq. (87), (88), (89) represent the bearing capacity factor (N_x) according to EC7.

$$
N_q = e^{\pi \tan \varphi'} \times \tan\left(45 + {\varphi'}/{2}\right)^2 \tag{87}
$$

$$
N_c = \left(N_q - 1\right) \times \cot \varphi' \tag{88}
$$

$$
N_\gamma = 2 \times \left(N_q - 1\right) \times \tan \varphi' \tag{89}
$$

For the manual calculation of the failure load after EC7 a study according to the influence of the depth coefficient is not possible, because it is not considered in the formula. Compared to ÖNORM B4435, the EC7 is not considering the influence of the ground level inclination.

2.3.2.3 Failure Load after ÖNORM B 4435-2

The calculation of the failure load after ÖNORM B4435 was done manually for drained conditions in final state, shown in Eq.(90).

$$Q_{f,k} = A' \times \left[\left(\gamma'_u \times b' \times N_\gamma \right) + \left(\gamma'_o \times t \times N_q \right) + \left(c_d \times N_c \right) \right] \tag{90}$$

influence of friction / foundation	influence of overburden pressure / foundation depth	influence of cohesion

Eq. (91), (92), (93) represent the bearing capacity factors (N_x) according to ÖNORM B 4435-2, which consider seven parameters:

- base values of the bearing capacity ($N_{x,0}$)
- coefficient of the load inclination (i_x) / angle of the load inclination (δ_s)
- coefficient of the surface inclination (g_x)
- coefficient of the foundation base inclination (t_x) / angle of the foundation base (α)
- coefficient of the foundation shape (s_x).

$$N_\gamma = N_{\gamma,0} \times i_\gamma \times g_\gamma \times t_\gamma \times s_\gamma \tag{91}$$

$$N_q = N_{q,0} \times i_q \times g_q \times t_q \times s_q \tag{92}$$

$$N_c = \cot \varphi \times \left(N_{q,0} \times i_c \times g_c \times t_c - \frac{1}{\cos \alpha \times \cos \delta_s} \right) \times s_c \tag{93}$$

For the manual calculation of the failure load after ÖNORM B4435 a study concerning the influence of the depth coefficient is not possible; thus, it is not taken into account in the equation system.

3 Used Software

3.1 GGU FOOTING – 2D Analytical Calculation

For the calculation of the failure load after DIN 4017 the program GGU FOOTING was used. The GGU-FOOTING program makes it possible to calculate the bearing capacity after DIN 4017 and settlements according to DIN 4019. The global safety concept can be used according to DIN 1054 (old) as well as the partial safety concept according to DIN 1054: 2005 and EC 7. In addition to the standard methods according to DIN 4017, the methods according to Terzaghi, Meyerhoff, Hansen, and Vesic can also be used. All calculations were done taking into account characteristic values only, whereas the design situations and the partial safety factors were not considered.

3.1.1 Geometry and Loading

The simple homogeneous soil body includes one strip foundation (Fig. 27), with a depth t of 1m, a width b of 2m and a length l of 10,000m to simulate an infinite strip foundation ($>>$). Next to the strip foundation, the soil body is loaded by a constant distributed surface load of 10kPa (unfavorable, permanent) along 17m. For the failure load calculation one centrally concentrated load is imposed on the strip foundation (unfavorable, permanent), which is inclined by 8.5 degrees.
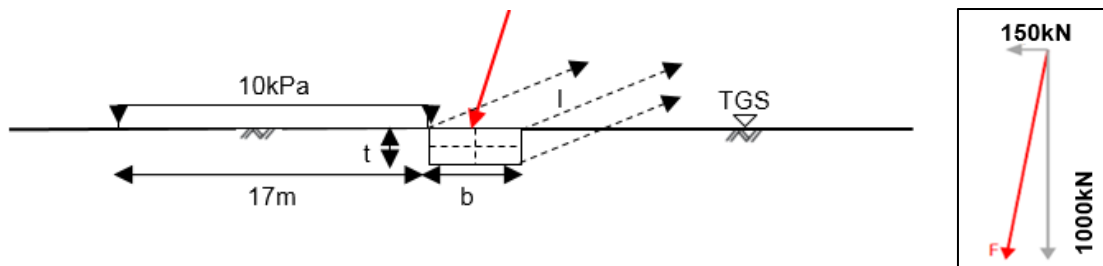
Fig. 27   Geometry and loading for analytical calculations of the failure load

3.1.2 Input Parameter

The input parameter of the strip foundation as well as the homogenous soil body are shown in Tab.7. For the homogenous soil body, a stiff sand under drained conditions was assumed. The calculations were executed with respect to the failure load (i.e. FoS = 1.0) for associated ($\varphi'=\psi'$), non-associated plasticity ($\psi'=0°$, 11.7°) and non-associated plasticity after Davis Approach A ($\varphi^*=\psi'$) considering a dilatancy angle of 0° and 11.7°; see Tab.8.

Tab. 7   Input parameter of the strip foundation and the soil body for analytical calculations of the failure load

input parameter			
strip foundation		soil body – final state drained	
b [m]	2.0	c' [kPa]	0
t [m]	1.0	φ' [°]	35
l [m] *	10,000	$\gamma = \gamma'$ [kN/m³]	20
γ [kN/m³]	20	E [MPa] *	37.3
		ν' [-]	0.3
* for the manual calculation after EC7 and ÖNORM B 4435-2 the length of the strip foundation (∞) assumed to be 1.0m for the effective area A'		** only for the calculation after DIN 4017* ** calculated by the program GGU*	

Tab. 8   Flow rule of the soil body for analytical calculations of the failure load

	ψ' [°]	φ' [°]	φ^* [°]
flow rule - plasticity			
associated	35	35	-
non-associated	0	35	32.44
after Davis A	11.7	35	29.84

For the manual analytical calculation after EC7 and ÖNORM B 4435 the same geometry and loading was used, as for the GGU FOOTING software (DIN 4017).

3.2 PLAXIS- 2D / 3D Calculations (FEA)

The following contents in this chapter are based on [22], [23], [26], [27].

Plaxis 2D / 3D is a displacement-based FEA code designed for geotechnical applications (2D 6-noded, 2D 15-noded, 3D 10-noded elements). The program includes different constitutive models, which allow the user to consider both, simple constitutive models like the linear-elastic perfectly plastic MC model (chapter 2.1.1) as well as more complex models like the HS model (chapter 2.1.2). Plaxis 2D / 3D enables the user to investigate deformation problems, stability problems, structural elements (anchors, retaining walls etc.) and flow analyses for various types of geotechnical applications. For both, Plaxis 2D as well as for Plaxis 3D, Version 2018 is used.

3.2.1 Numerical Control Parameter

There are specific numerical control parameters that are mainly used for the calculations discussed below. The setting *maximum number of steps* stored defines the number of steps during calculation phase to be stored. It is increased from only one (default setting) to 3 for the calculations of the stress paths, whereas the final step generally contains the most relevant results. The setting *maximum steps* specifies the maximum number of steps during each calculation phase. During calculations performed in the scope of this thesis, it was sometimes necessary to increase the default setting (i.e. 1000 steps) to reach stable results, which lead to an increase of the calculation time. The setting *maximum number of iterations* (default setting 60) describes the maximum number of iterations performed within each calculation step.

With respect to the numerical settings, *tolerated error* studies were conducted to define the influence on the factor of safety, discussed in the following chapter 4.2.3.1. Every non-linear numerical analysis represents an approximation of the exact solution; thus, deviations between the approximation and the exact solution occur, shown in Fig.28. These deviations are substantially controlled by the numerical control parameter *tolerated error* associated with the solution algorithm. The algorithm verifies that the error of equilibrium is confined to acceptable limits. Within the safety analysis, the program produces iterations until the calculated error is less than the pre-defined tolerated error.
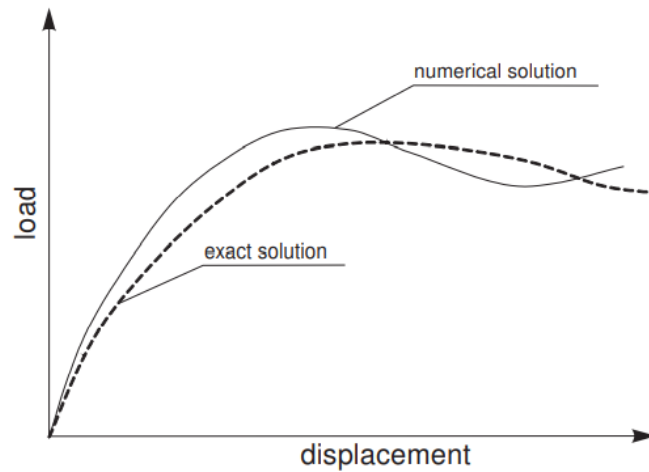
Fig. 28   Exact solution versus approximate (numeric) solution primarily governed by
             the tolerated error (Plaxis References Manual, 2018)

The use of the numerical control parameter *arc-length control* considers the application of an automatic failure detection technique. This application is described by a decrease of the applied load for the calculation to converge which leads to an assumed failure, hence stopping the calculation.
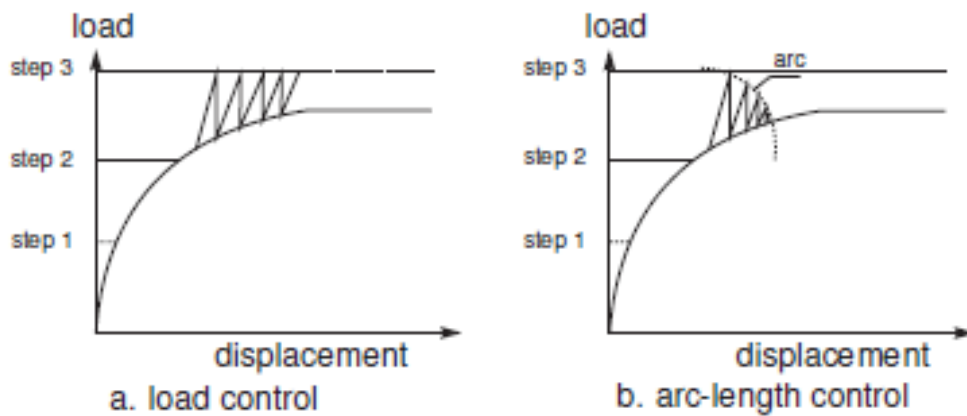
Fig. 29   Numerical controll parameter arc-length control (Plaxis References Manual,
             2018)

3.2.2 General Settings

There are general settings that are mainly used for the calculations discussed below. It should be mentioned that for all calculations the setting *design approach* is set to (none) indicating that only characteristic values are considered. In the calculations, the calculation type *Plastic* is used except for the safety analysis (*Safety*) as well as the initial phase (*K0 procedure*). For the general setting of the loading type, the *staged construction* loading type is used for the initial as well as the plastic phase. This setting allows the user to determine a new condition that is to be achieved at the end of the calculation phase. On the other hand, for the safety phase the loading type *incremental multiplier* is used. The *incremental multiplier* concerns a safety analysis using the load advancement number of steps process and is used to determine the increment of the strength reduction. The strength reduction technique is executed automatically until the value of the max. steps parameter is reached. Steady-state water pressure conditions were modelled by means of the *phreatic* option.

3.2.3 Deformation Control Parameter

There are specific deformation control parameters, that are mainly used for the calculations discussed below. The deformation control parameter *reset displacement and small strain to zero* is used (switch on) after the initial phase, so that the displacements are set to zero at the beginning of following calculation phase; in this way, displacements of the initial phase are not considered.

3.2.4 Geometry and Loading

The simple homogeneous soil body (10m times 36m) includes a one strip foundation, presented in Fig. 30, with a depth t of 1m and a width b of 2m for plane-strain conditions; in the three-dimensional case, lengths l from 1m to 4m are used. Beside the strip foundation the soil body is loaded by a constant distributed surface load of 10kPa (unfavorable, permanent) stretching a distance of 17m to reach higher plasticity. For the failure load analysis, as well as the strength reduction analysis, one centrally positioned single load on the strip foundation is considered (unfavorable, permanent), which is inclined by 8.5 degrees. This example corresponds to the MA Thesis of Knitter and Nowakoswki 2018 Ex.2 [26], [27].
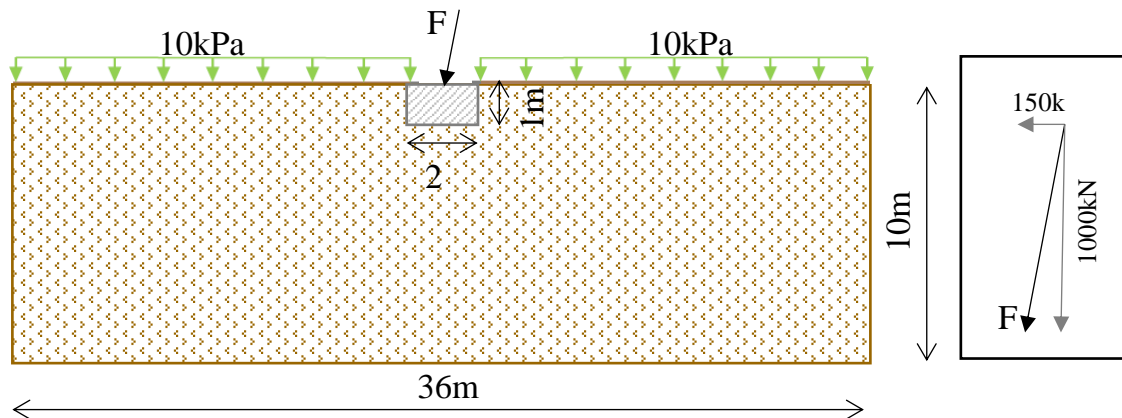
Fig. 30   Geometry and loading for numerical calculations

3.2.5 Input Parameter

The input parameter of the strip foundation as well as the homogenous soil body are shown in Tab.10. For the homogenous soil body, a stiff sand and drained conditions are assumed. The flow rule conditions are shown in Tab.9.

Tab. 9 Flow rule of the soil body for numerical calculations

	flow rule - plasticity		
	ψ' [°]	φ' [°]	φ^* [°]
associated	35	35	-
non-associated	0	35	-
	11.7	35	-
non-associated after Davis A	0	35	32.44
	11.7	35	29.84

Tab. 10 Input parameter of the strip foundation and the soil body for numerical calculations

	input parameter	soil body -drained stiff sand	strip foundation
	c'_{ref} [kPa]	0	-
	φ' [°]	35	-
	ψ' [°]	varied due to flow rule	-
	γ_{sat} [kN/m³]	20	24
	γ_{unsat} [kN/m³]	17	24
MC	E' [MPa]	50	30,000
	ν' [-]	0.3	0.2
	$E_{50}^{ref} = E_{oed}^{ref}$ [MPa]	69.06	-
HS	E_{ur}^{ref} [MPa]	207.2	-
	ν'_{ur} [-]	0.2	0.2
	K_0 [-]	varied due to flow rule	0.5
	p_{ref} [kPa]	100	-
	m [-]	0.5	-

3.3 Phases

3.3.1 Initial Phase

To perform the initial state (Tab.11, I) of the subsoil before construction, the K_0-procedure is used in the first calculation step. The major influence on the initial horizontal, as well as vertical stresses, equals the unit weight of the subsoil itself, including their loading history. In this context, in chapter 4.2.3.3 a study concerning the influence of the K_0-value on the factor of safety was done. At last the empirical equation by Jacky (Eq.(94)) is used to calculate the earth pressure coefficient K_0, which is calculated based on the effective friction angle φ' of the soil body.

$$K_0 = 1 - \sin \varphi' \qquad (94)$$
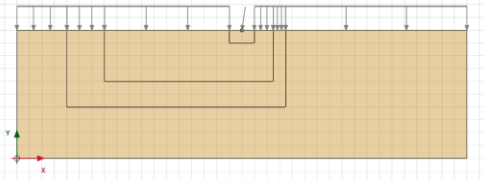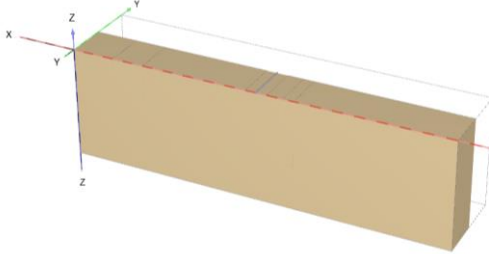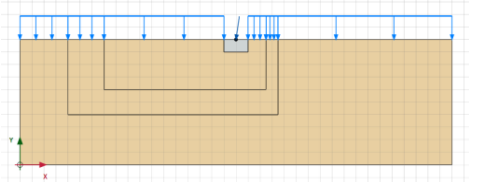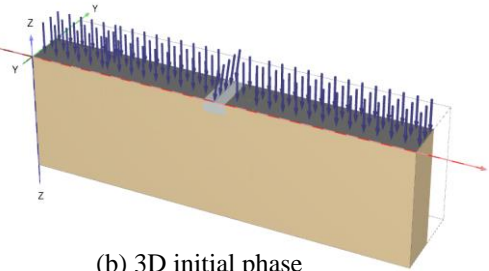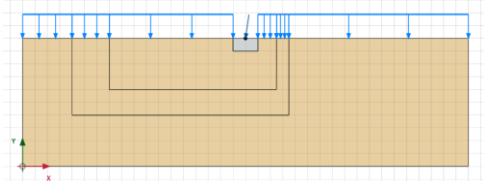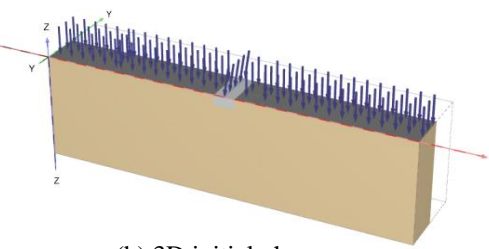
3.3.2 Plastic Phase - Loading

The second calculation phase (Tab.11, II) after the initial state is a plastic phase that calculates the elastic-plastic deformations of the soil body after construction due to dead load. This phase is used to calculate the failure load in Plaxis manually. In order to obtain the failure load, the total multiplier $\sum M_{stage}$ is used that starts at zero and incrementally increases to the value of 1.0 in the case equilibrium conditions are met. Note that the subsequent phase will not be started, unless $\sum M_{stage}$ criteria are satisfied. Thus, the failure load is reached if the plastic phase at a certain value of load does not satisfy the $\sum M_{stage}$ criteria. For example, in this thesis there is only one plastic phase applied, according to the MA Thesis of Knitter and Nowakoswki 2018 Ex.2. In this phase, the strip foundation, as well as the loading are activated. → *max. steps 1000-3000 (arc length on/off)*

3.3.3 Safety Analysis – Strength Reduction

The third and last calculation phase (Tab.11, II) after the plastic phase is the safety analysis (chapter 2.3.1.1). → *max. steps 300-500 (arc length on)*

Tab. 11   Plaxis – calculation phases

I.   Initial State

| (a) 2D initial phase | (b) 3D initial phase |

II.   Plastic Phase – failure load (manual)

| (a) 2D initial phase | (b) 3D initial phase |

III.   Safety analysis - strength reduction (automatic)

| (a) 2D initial phase | (b) 3D initial phase |

3.4 Mesh and Shape Functions

Several scientific investigations (e.g. Oberhollenzer 2017, Veigl 2020) show that the mesh discretization has a significant influence on the factor of safety. In this thesis the use of a mesh study was not implemented. Furthermore, a medium mesh discretization and 15-noded elements for the 2D calculations is used. For the 3D calculations, a fine mesh discretization and 10-noded elements were used. The use of higher order elements in combination with a fine mesh discretization gives reasonable calculation results, thereby leading to higher calculation times, especially for 3D calculations. Fig. 31 and 32 show the mesh distribution for 2D and 3D calculations in Plaxis.

3370 elements
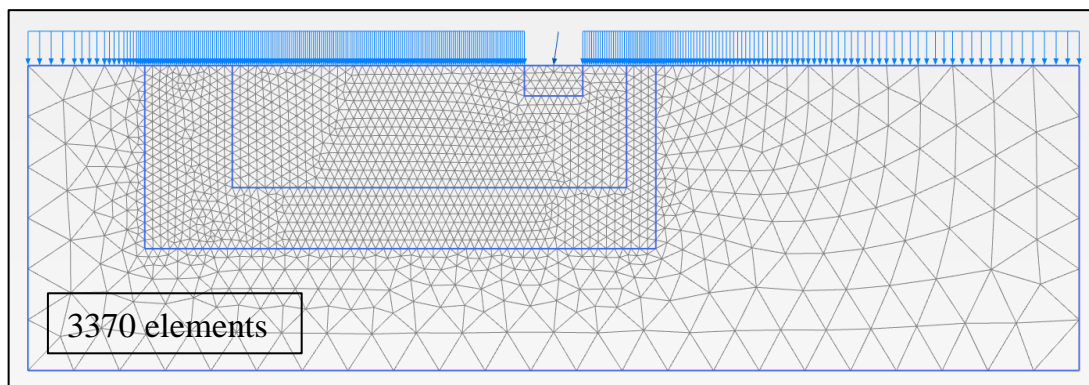
Fig. 31   2D mesh distribution – medium – 15-noded elements

700,952 elements → 1m thickness
862,508   elements   →   4m

1m
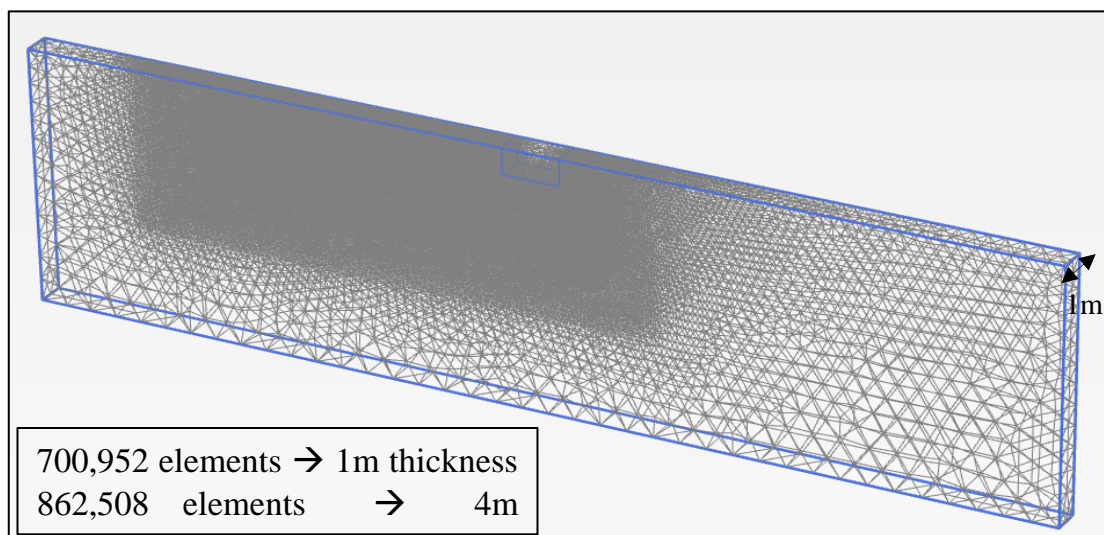
Fig. 32   3D mesh distribution – fine – 10-noded elements

3.5 OPTUM G2 / G3 – Calculations (FEA, FELA)

The following contents in this chapter are based on [24], [25], [26], [27].

Optum G2 is a two-dimensional and Optum 3D is a three-dimensional, finite element program that has the opportunity to use a displacement-based FEA code (2D 6-noded, 2D 15-noded, 3D 10-noded elements), as well as finite element limit analysis (LB, UB). The program includes different constitutive models that allow the user to model simple models like the linear-elastic perfectly plastic MC model (chapter 2.1.1) as well as more complex models like the HMC model (chapter 2.1.3). Optum G2/G3 enables the user to perform deformation and strength analysis of geotechnical boundary value problems. For Optum G2 Version 2018, for Optum G3 Version 2019 are used.

3.5.1 Numerical Settings

3.5.1.1 Element Type

For the setting *element type* there are four possibilities in plane-strain conditions: There are 6-noded, as well as 15-noded elements, for computing FEA code and on the other hand lower and upper "elements" for calculating limit analysis.

3.5.1.2 Mesh Adaptivity

The setting *mesh adaptivity* induces an automatic mesh discretization procedure at the position of the critical points in the subsoil.

3.5.1.3 Drainage Condition

In Optum the user has the opportunity to distinguish between three drainage conditions: drained/undrained, always drained and non-porous. For each drainage type characteristic drainage conditions have to be chosen, which can either be defined as long or short term. These setting determine whether the soil behaves drained or undrained. In this thesis, the options drained/undrained and long term are chosen. To model the strip foundation, the setting non-porous was chosen.

3.5.1.4 Design Approach

For all calculations the setting *design approach* is set to (none), thereby applying characteristic values. In this way, no design situations and partial safety factors are considered.

3.5.2 Geometry and Loading

The simple homogeneous soil body (10m times 36m) includes one strip foundation, presented in Fig. 33, with a depth t of 1m and a width b of 2m for plane-strain conditions. On both sides of the strip foundation, the soil body is loaded by a constant distributed surface load of 10kPa (unfavorable, permanent) along 17m to generate increased soil plasticity. For the failure load analysis, as well as the strength reduction analysis, one centrally concentrated load on the strip foundation is considered (unfavorable, permanent), which is inclined by 8.5 degrees. This example corresponds to the MA Thesis of Knitter and Nowakoswki 2018 Ex.2 [26], [27].
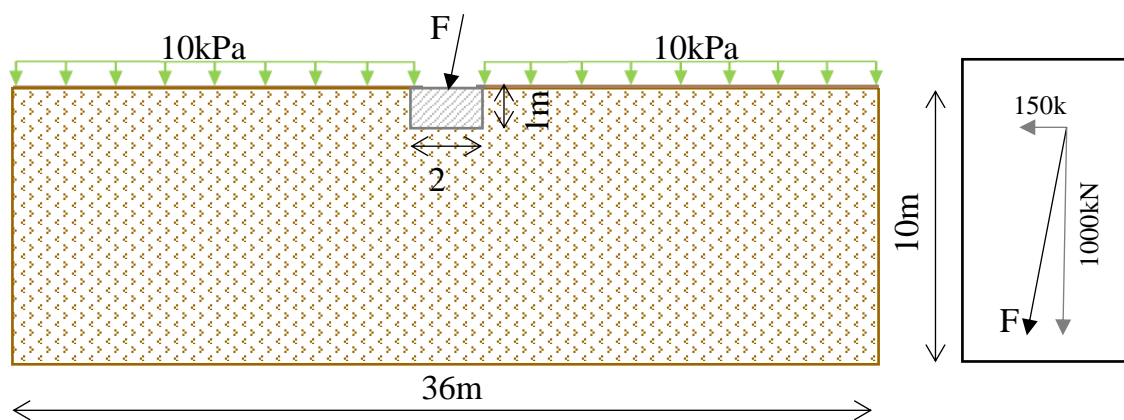
Fig. 33   Geometry and loading for numerical calculations

3.5.3 Input Parameter

The input parameters of the strip foundation as well as the homogenous soil body are shown in Tab.13. For the homogenous soil body, a stiff sand in combination with drained conditions was considered. The flow rule conditions (plasticity) are shown in Tab.12.

Tab. 12   Flow rule of the soil body for numerical calculations

flow rule - plasticity			
	ψ' [°]	φ' [°]	$\varphi*$ [°]
associated	35	35	-
non-associated	0	35	-
	11.7	35	-
non-associated after Davis A	0	35	32.44
	11.7	35	29.84

Tab. 13   Input parameter of the strip foundation and the soil body for numerical calculations

	input parameter	soil body -drained stiff sand	strip foundation
	c'_{ref} [kPa]	0	-
	φ' [°]	35	-
	ψ' [°]	varied due to flow rule	-
	γ_{sat} [kN/m³]	20	24
	γ_{unsat} [kN/m³]	17	24
MC	E' [MPa]	50	30,000
	ν' [-]	0.3	0.2
HMC	$E_{50}^{ref} = E_{oed}^{ref}$ [MPa]	69.06	-
	E_{ur}^{ref} [MPa]	207.2	-
	ν'_{ur} [-]	0.2	0.2
	K_0 [-]	varied due to flow rule	0.5
	p_{ref} [kPa]	100	-
	m [-]	0.5	-

3.5.4 Phases

Optum G2 has the opportunity to calculate an automatic failure load (FEA and FELA) considering associated and non-associated plasticity conditions as well as the Davis A approach for imitating non-associated plasticity in terms of limit analysis. In contrary, an automatic strength reduction is only possible for associated plasticity, in relation to non-associated Davis A, either for SRFEA or SRFELA. For non-associated plasticity, the strength reduction (SRFEA and SRFELA) can only be calculated manually. For the calculation of the automatic strength reduction, as well as the automatic failure load it is not necessary to perform an exhaustive step-by-step elastoplastic analysis (compared to Plaxis). Thus, under drained conditions, where no excess pore pressures are generated, the solution is independent of the initial stresses and only one phase has to be computed for the analysis.

Optum G3 has the opportunity to calculate an automatic failure load (FELA) for associated and non-associated plasticity after Davis A. In contrast to 2D calculations an automatic strength reduction is not possible, therefore a manual strength reduction for both associated plasticity, and non-associated plasticity after Davis A (SRFELA) was done.

Fig. 34 shows the calculation phase for the failure load (i.e. the strength reduction analysis phase).
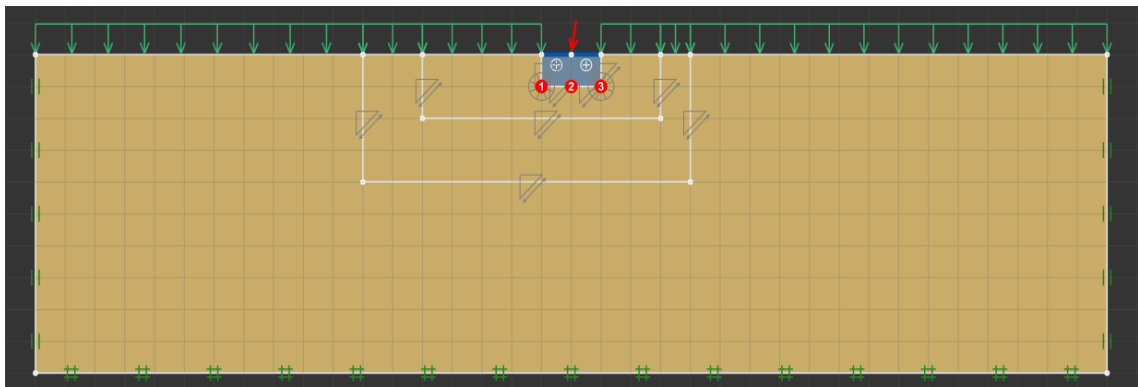
Fig. 34   Calculation phase for failure load and strength reduction analysis

3.5.4.1 Limit Analysis – Automatic Failure Load

The analysis type *limit analysis* yields an automatic collapse multiplier value, which describes to which extent the actual load has to be increased in order to invoke failure. Therefore, fixed loads are kept constant and multiplier loads are amplified until collapse is reached.

3.5.4.2 Multiplier Elastoplastic - Automatic Failure Load

In the same way, for *multiplier elastoplastic analysis* fixed loads are kept constant and multiplier loads are amplified until collapse is reached. With the resulting collapse multiplier the actual load has to be increased to obtain collapse. Tab.14 presents the notations for FEA and FELA calculations, as well as the definition of the analysis.

Tab. 14   Phases for automatic failure load analysis

	notation 2D	notation 3D*	analysis
associated	LB	failure load LB	Limit Analysis
	UB	failure load UB	
	15.noded	-	Multiplier Elastoplastic
non-associated	15.noded	-	Multiplier Elastoplastic
non-associated after Davis A	LB Davis A	failure load LB	Limit Analysis
	UB Davis A	failure load UB	
	15.noded Davis A	-	Multiplier Elastoplastic

* for 1m and 4m thickness

3.5.4.3 Strength Reduction – Automatic

The analysis *strength reduction* produces an automatic reduction of strength parameters, that is necessary to reach collapse at the actual load. For a factor higher than unity, the whole system is under stable conditions. Tab.15 presents the notations for SRFEA and SRFELA calculations as well as the definition of the analysis.

3.5.4.4 Elastoplastic - Manual Strength Reduction

An *Elastoplastic* analysis calculates the responding deformations either to a specific value of loading or to gravity loading (e.g. excavation, embankment). To check whether the corresponding failure load leads to failure for a given friction angle, feasibility analyses were conducted (output stable or unstable).

Notably, a feasibility analysis requires an initial phase (K_0-procedure). Thus, the failure load could lead to failure without reducing the strength parameter as well. Tab.15- 17 present the notations for SRFELA calculations as well as the definition of the analysis for 2D and 3D calculations.

Tab. 15   Phases for 2D automatic strength reduction analysis

	notation	analysis
associated	LB UB 15.noded	Strength Reduction
non-associated after Davis A	LB Davis A UB Davis A 15.noded Davis A	Strength Reduction

Tab. 16   Phases for 3D manual strength reduction analysis

	notation*	analysis
associated	manuel SR LB manuel SR UB	Elastoplastic
non-associated after Davis A	manuel SR LB manuel SR UB	
* for 1m and 4m thickness		

Tab. 17   Phases for 3D manual strength reduction analysis

	notation*	analysis
associated and non-associated after Davis A	3D failure load LB 1m 3D failure load LB 1m φ'_{red} 2D failure load LB 1m 2D failure load LB 1m φ'_{red}	Feasibility
* equal for 4m thickness as well as for UB		

3.5.5 Mesh and Shape Functions

Several scientific investigations (e.g. Oberhollenzer 2017, Veigl 2020) show that the mesh discretization has a significant influence on the factor of safety. In this thesis the use of a mesh study was not implemented. In contrary, an automatic mesh adaptivity for 2D and 3D calculations is used. Mesh adaptivities are realized by means of an automatic mesh discretization at critical points in the soil domain. Fig. 35, 36 show the mesh distribution for 2D and 3D calculations in Optum for 15-noded elements as well as limit analysis.
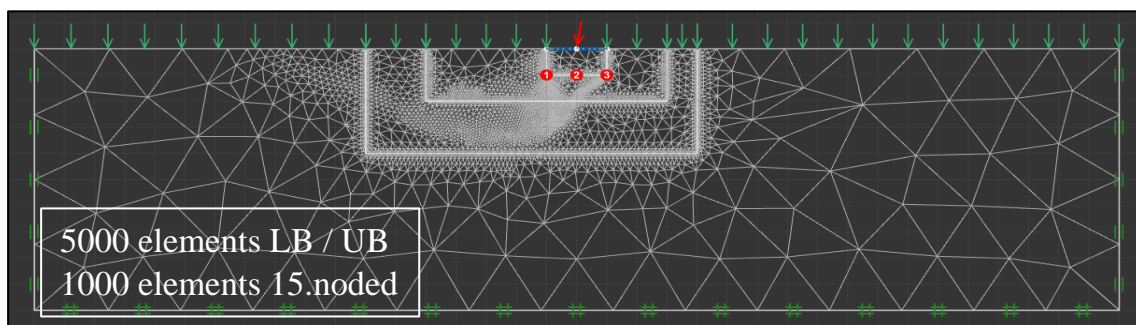
Fig. 35   2D mesh distribution – 3 mesh adaptivity
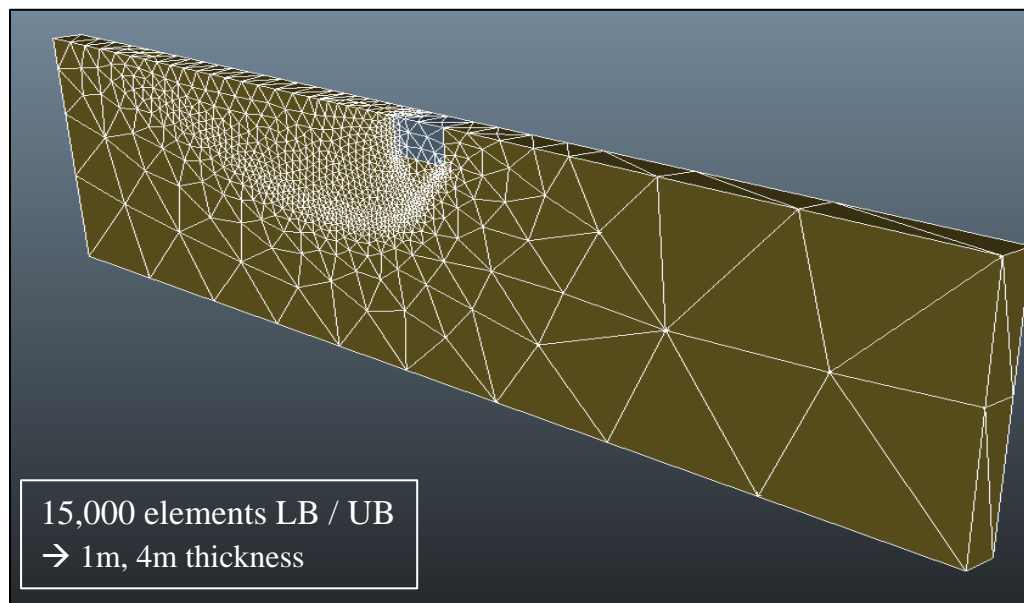
Fig. 36   3D mesh distribution – 5 mesh adaptivity

4 Calculation Results

All calculations are done for drained conditions. Both, the analytical and the numerical methods, use characteristic values.

4.1 Analytical Method

4.1.1 2D: Failure load

Conventional analytical methods according to standards are still used in daily engineering practice, despite many – at least in part – spurious assumptions. Even so, analytical methods do not consider the impact of the dilatancy angle (ψ') and the friction angle (φ') is presumed to be evenly distributed, which does not correspond to reality. This fact represents the main differences compared to FEA.

Fig.37 shows the difference between analytical and numerical methods. The markers (–✗–) at the vertical axis describe the failure loads after standard regulations (Tab.18), whereas the load-displacement curve presents the numerical method (FEA 15-nod.). It has been noted that for associated plasticity and non-associated plasticity after Davis Approach A ($\psi'=0°$), the difference between FEA and conventional methods is in a range spanning from ~300kN/m to 1100kN/m relating to the failure load. Notably, that the lower the friction angle is, the lower the differences become. For both methods, analytical and numerical, non-associated plasticity after Davis Approach A provides a substantially lower bearing capacity when compared with results of an associated flow rule.

Tab.18 shows the resulting failure loads for associated plasticity, as well as non-associated plasticity after Davis Approach A ($(\psi'=0°)$ for both methods, analytical and numerical. Differences in the bearing capacity of the analytical method arising from different design standards, namely DIN 4017, EC7 and ÖNORM B 4435, are caused by different declarations of the coefficient concerning the load inclination. Nevertheless, for the investigated coarse-grained soil, in case of zero cohesion, the analytical methods show differences up to 350kN/m. Comparing each standard regulations DIN4017, EC 7 and ÖNORM B 4435, the results are indicating a decrease in the range spanning of bearing capacity, with a decreasing friction angle (non-associated plasticity after Davis Approach A). *However, due to remarkably lower values of the failure load, it has to be considered as a conservative method* (MA Thesis Nowakoswki, 2018).
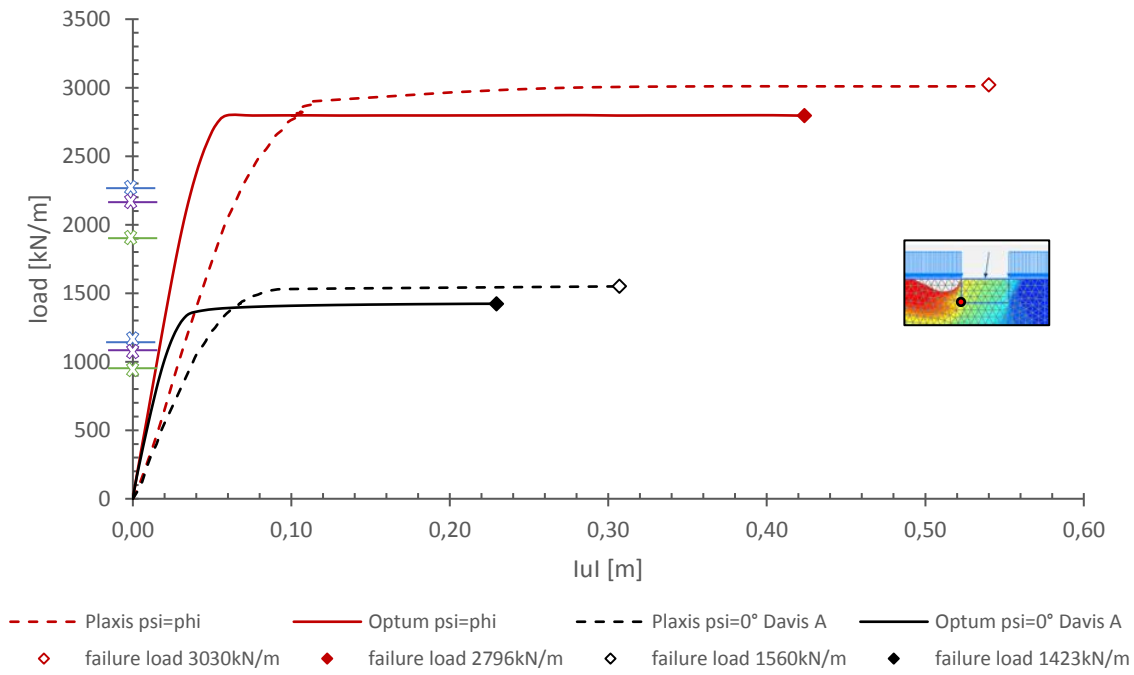
Fig. 37   Load-displacement curve analytical vs. numerical method (FEA 15-nod.) for a. φ'=ψ'=35° and n.a. Davis A φ*=ψ'=29.84°

Tab. 18   Analytical method failure load

failure load [kN/m]			
		φ'=35°	φ*=29.84° (Davis A ψ'=0°)
analytic —⋇—	DIN 4017 (consideration depth coeffcient) (consideration dead load foundation)	1895.46	961.48
	EC 7	2244.75	1113.82
	ÖNORM B 4435	2152.74	1078.26
numeric	Plaxis FEA 15-nod.	3030.00	1560.00
	Optum FEA 15-nod.	2796.00	1423.00
→ *failure load ~ Δ300-1100kN/m*			

A study on the influence of the depth coefficient after Brinch Hansen as well as on the depth of the foundation base (FB) at the failure load were conducted with GGU FOOTING, thereby taking into account DIN 4017. Without consideration of the depth coefficient, the difference in failure load is in a range between ~ 140kN/m and 375kN/m, whereas the same foundation base depth is used; see Tab.19. However, considering the depth coefficient as well as a deeper foundation base (FB) leads to higher failure loads and smaller differences compared to FEA results. Furthermore, with decreasing friction angle the differences become smaller.

Tab. 19   Analytical method failure load
           - influence of depth coefficient and foundation base

failure load [kN/m]		
DIN 4017 (consideration dead load foundation)	$\psi'=\varphi'=35°$	$\psi'=\varphi*=29.84°$ (Davis A $\psi'=0°$)
1m FB*	1895.46	961.48
1m FB	1666.65	820.26
2m FB*	2606.20	1357.92
2m FB	2233.21	1127.70
with depth coefficient by Brinch Hansen		

In addition, a goal was to investigate the influence of the dead load of the foundation and the depth coefficient after Brinch Hansen. Both parameters are implemented in GGU FOOTING, using the conventional approach after DIN 4017. The study is done for the case of 1m foundation base (FB). Ignoring both, the dead load of the foundation as well as the depth coefficient, the difference in failure load according to DIN 4017 is in a range between 405 kN/m and 775 kN/m as shown in Tab.20. However, considering the dead load of the foundation leads to higher failure loads and smaller differences compared to FEA results.

Tab. 20   Analytical method failure load - influence of dead load of the foundation

failure load [kN/m]		
DIN 4017	$\psi'=\varphi'=35°$	$\psi'=\varphi*=29.84°$ (Davis A $\psi'=0°$)
1m FB*	1895.46	961.48
1m FB	1121.79	557.02
with consideration of the dead load of the foundation, as *well as the depth coefficient by Brinch Hansen*		

Further calculations concerning non-associated plasticity after Davis Approach A with a dilatancy angle of 11.7° ($\varphi/3$) are documented in the Appendix. Detailed studies of the influence of the dilatancy angle as well as the cohesion on the bearing capacity / failure load are listed in the MA Thesis of Nowakoswki, 2018 (Ex.2).

4.2 Numerical Method

The validity of conventional approaches (analytical methods) is limited to certain conditions. Tools quite frequently used in the field of soil mechanics are finite element analysis (FEA) and finite element limit analysis (FELA). Therefore, the differences of numerical methods have been studied, using displacement-based finite element analyses (FEA 10-noded, 15-noded) and finite element limit analyses (FELA LB/UB). Furthermore, in numerical methods, the flow rule can be studied in more detail. Due to the fact that in the case of finite element limit analysis only associated plastic flow is applicable, the approach by Davis (1968) is used. Therefore, reduced strength parameters in combination with an associated flow rule are performed to simulate non-associated behaviour. Finally, both programs, Plaxis 2D and Optum G2, are compared for finite element analysis (FEA) calculations, also by means of the constitutive models. In the following two chapters 4.2.1, 4.2.2 and 4.2.3, the results concern associated plasticity and non-associated plasticity, as well as non-associated plasticity after Davis A ($\psi' = 0°$). Further calculations with non-associated plasticity after Davis Approach A with a dilatancy angle of 11.7° ($\varphi'/3$) as well as non-associated plasticity with a dilatancy angle of 11.7° ($\varphi'/3$) are documented in the Appendix. Detailed studies of the influence of the dilatancy angle as well as the cohesion on the bearing capacity represented by the failure load can be found in the MA Thesis of Nowakoswki, 2018 (Ex.2).

4.2.1 2D: Failure Load vs. Strength Reduction

The main aim of this thesis is to compare these two analyses and show the differences in loading corresponding to the factor of safety of 1.0, 1.5, 2.0, 3.0, as well as to compare the factor of safety corresponding to the applied load. This means applying the failure load for FoS_{FL} 1.0 up to 3.0 and calculate with these loads the FoS_{SR} for the strength reduction analysis and, on the other hand, applying the actual load for FoS 1.0 up to 3.0 for the strength reduction analysis and the failure load analysis. Eq.(95) shows the definition of the differences in loading for the failure load analysis and the strength reduction analysis. Eq.(96) shows the definition of the difference of the resulting strength reduction FoS_{SR} applying the failure load and the actual load. Eq.(97) shows the definition of the difference of the resulting FoS for both analyses, applying a specific load.

$$\Delta\% = \left(\frac{failure\ load - SR\ load}{failure\ load}\right) \times 100 \qquad (95)$$

$$\Delta\% = \left(\frac{FoS_{SR\_}failure\ load - FoS_{SR\_}load}{FoS_{SR\_}failure\ load}\right) \times 100 \qquad (96)$$

$$\Delta\% = \left(\frac{FoS_{FL} - FoS_{SR}}{FoS_{FL}}\right) \times 100 \qquad (97)$$

Fig.38 shows the load-displacement curve for the failure load analysis obtained with both, Plaxis and Optum FEA (15-noded), as well as Optum FELA (LB, UB) for associated plasticity and non-associated plasticity after Davis A ($\psi' = 0°$). The lower and upper bounds are marked as bars above and below the load-displacement curve, whereas the failure loads relating to FEA are marked as square icon. In this case, finite element limit analysis is confined to an associated flow rule only. It should be mentioned that the failure load for Plaxis FEA (15-noded) is calculated manually, whereas in Optum FEA (15-noded) and FELA (LB, UB) an automatic failure load analysis is possible. In the case of Plaxis calculations, special attention has to be drawn to the numerical control parameter *arc-length control* when obtaining the failure load of FoS_{FL} 1.0 (see 3.2.1).

Comparing the failure loads obtained with Plaxis and Optum, the differences are in a range spanning of ~7.8% (~200 kN/m; associated plasticity) and ~8.8% (~150 kN/m; non-associated plasticity after Davis A). Furthermore, comparing associated plasticity with non-associated plasticity after Davis A, it can be shown that smaller friction angles lead to decreasing failure loads; a reduction of 5° of the friction angle (associated $\varphi'=35°$, Davis A $\varphi*=29.84°$) reduce the failure load to 50%. As discussed in chapter 2.2.2 for the lower-bound solution, the actual failure load is not reached, whereas for the upper-bound solution the failure load overruns the actual failure load.
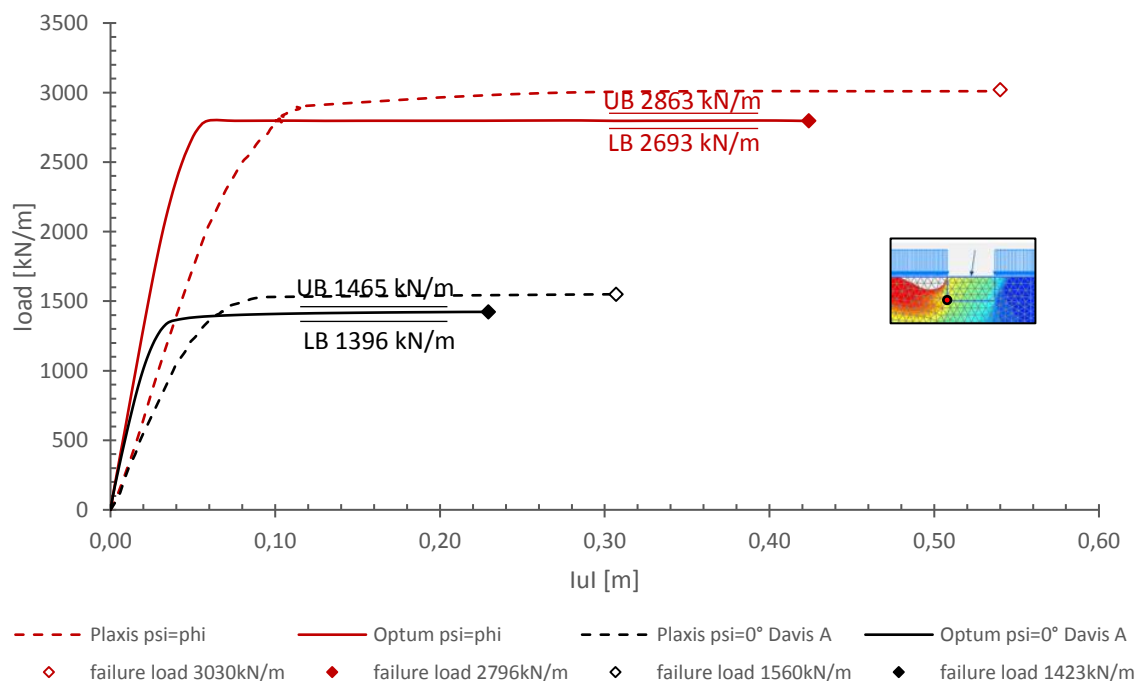
Fig. 38   Load-displacement curve numerical method Plaxis, Optum FEA 15-nod. and Optum FELA for a. $\varphi'=\psi'=35°$ and n.a. Davis A $\varphi*=\psi'=29.84°$

Fig.39 shows the load-displacement curve for the failure load analysis obtained with both, Plaxis FEA (15-noded) and Optum FEA (15-noded) for non-associated plasticity and non-associated plasticity after Davis A ($(\psi' = 0°)$. The failure loads relating to FEA are marked as square icon. It should be mentioned that the failure load for Plaxis FEA (15-noded) is calculated manually, whereas in Optum FEA (15-noded) an automatic failure load analysis is possible. Therefore, in Plaxis the numerical control parameter *arc-length control* is an issue for the resulting failure load of FoS_{FL} 1.0.

Comparing the failure loads obtained with Plaxis and Optum for non-associated plasticity, the differences lie within a range spanning of ~7.8% (~150 kN/m), whereas for non-associated plasticity after Davis A the differences are in a range spanning of ~8.8% (~150 kN/m). Furthermore, the result show that the original Davis Approach A leads to conservative results in the failure load compared to non-associated plasticity. As mentioned in chapter 2.2.3, a consequence of non-associated plasticity is that the resulting failure load is significantly lower compared to associated plasticity conditions. Furthermore, a consequence is that the failure mechanism is generally non-unique, resulting in oscillations of the load-displacement curve, which can be attributed to switching modes of failure. This phenomenon results in the peaks in the load-displacement curve. It should be mentioned that the second peak value of Optum fits well with the failure load according to Plaxis as the resulting failure load according to Optum.
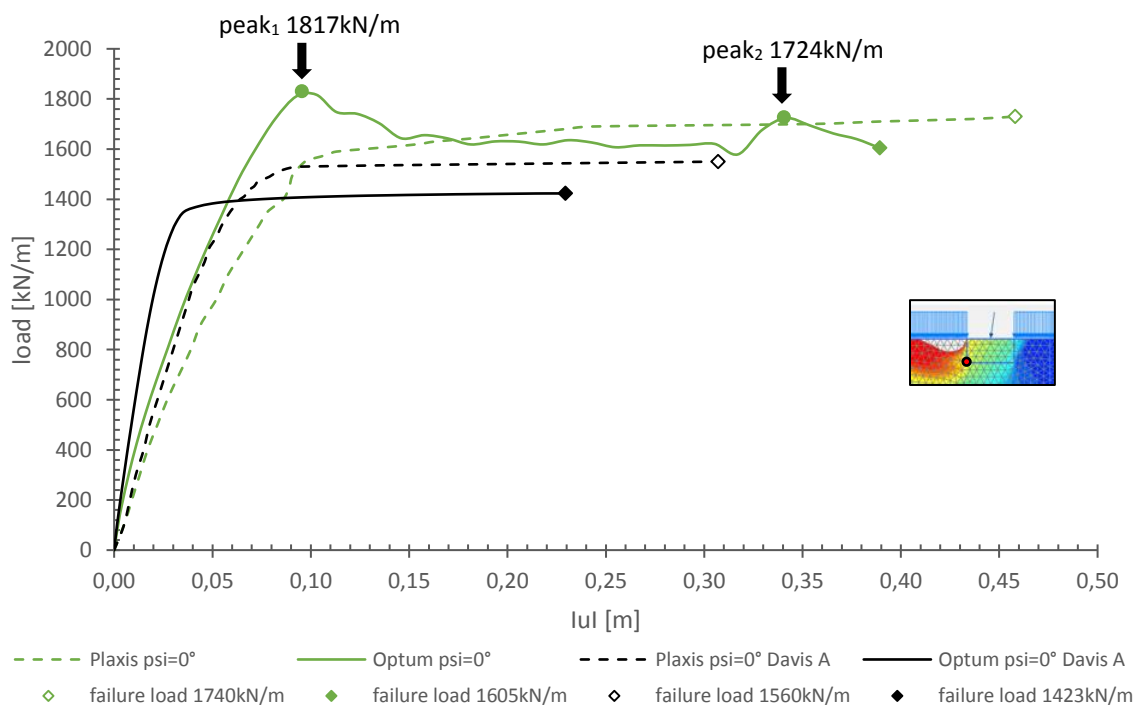
Fig. 39   Load-displacement curve numerical method Plaxis, Optum FEA 15-nod.
for n.a. $\psi'=0°$ and n.a. Davis A $\varphi^*=\psi'=29.84°$

Fig.40, 41 and 42 represent the total displacement │u│ for each analysis.
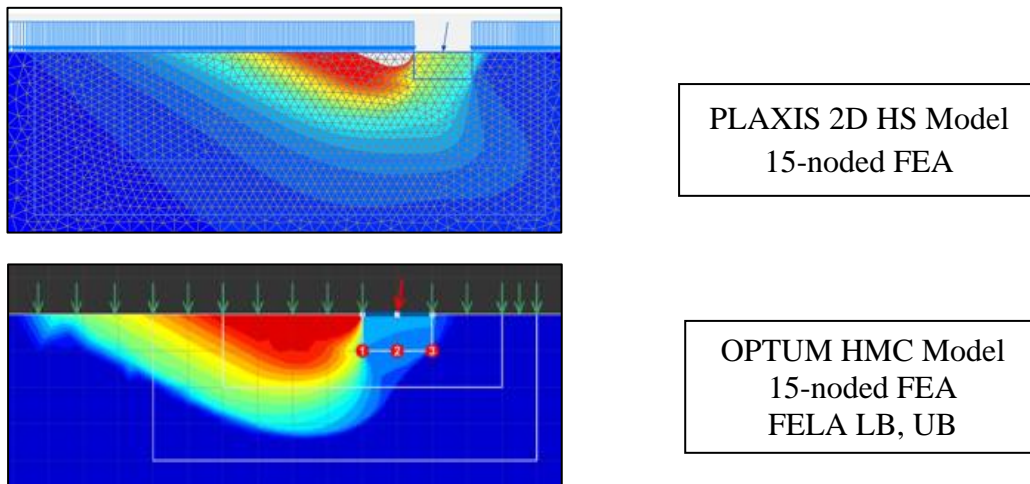
Fig. 40   Total displacement for the corresponding failure load a. φ'=ψ'=35°
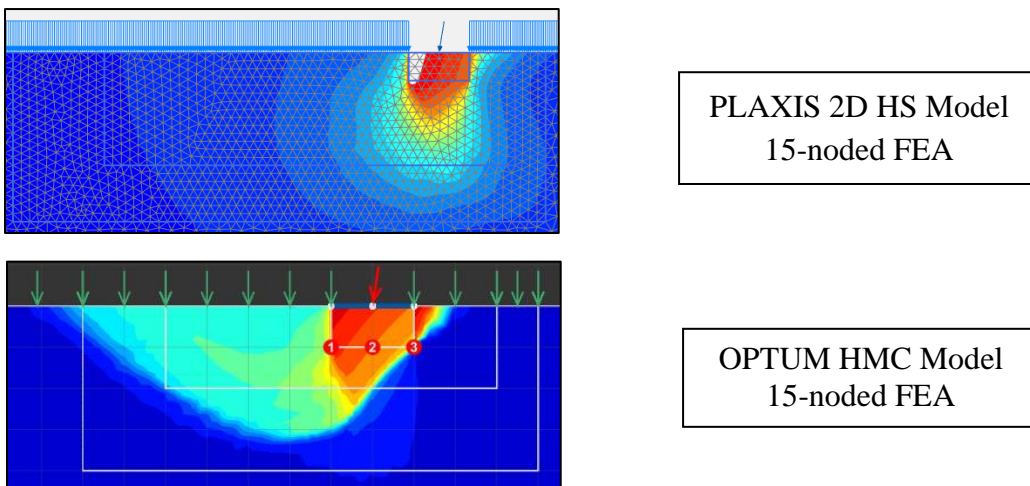
Fig. 41   Total displacement for the corresponding failure load n.a. ψ'=0°
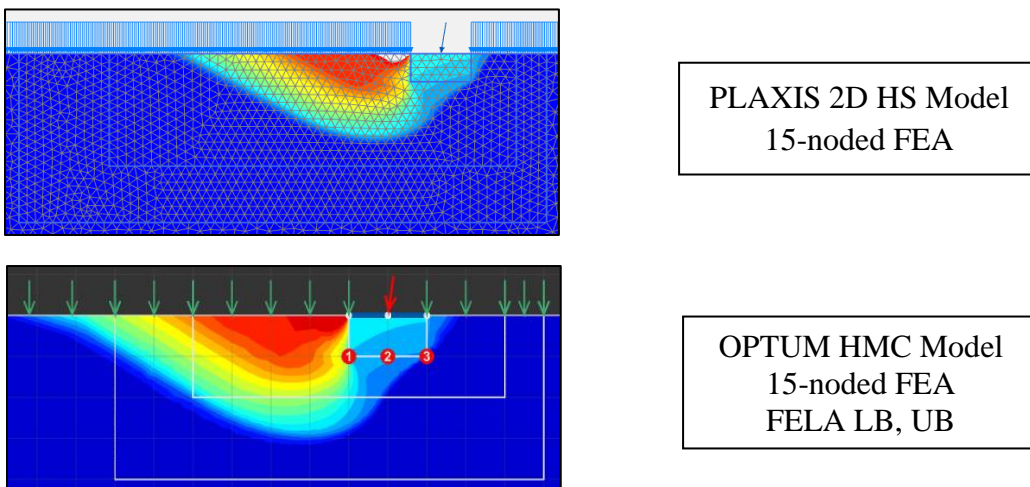
Fig. 42   Total displacement for the corresponding failure load
n.a. Davis A φ*=ψ'=29.84°

Fig.43, 44 and 45 represent the shear strains for each analysis.
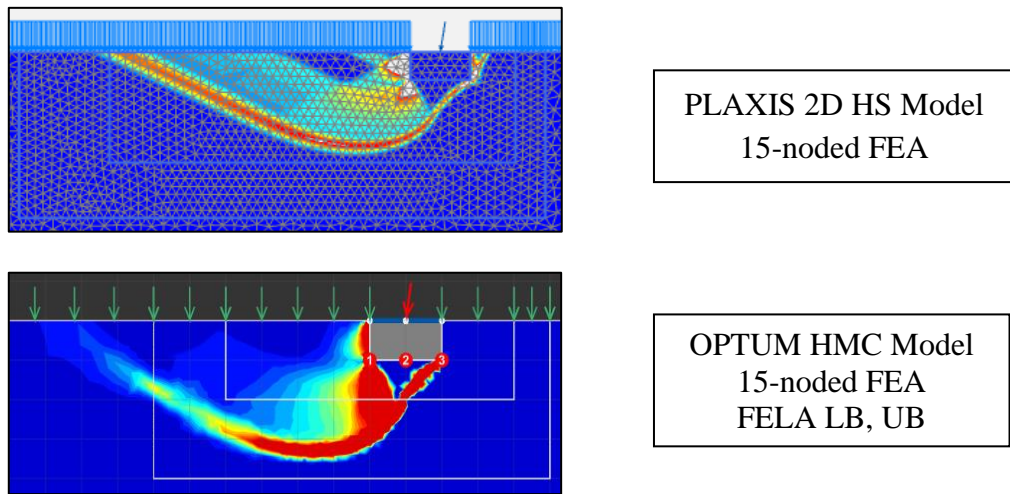
PLAXIS 2D HS Model
15-noded FEA

OPTUM HMC Model
15-noded FEA
FELA LB, UB

Fig. 43   Shear strains for the corresponding failure load a. φ'=ψ'=35°

PLAXIS 2D HS Model
15-noded FEA

OPTUM HMC Model
15-noded FEA

Fig. 44   Shear strains for the corresponding failure load n.a. ψ'=0°

PLAXIS 2D HS Model
15-noded FEA

OPTUM HMC Model
15-noded FEA
FELA LB, UB
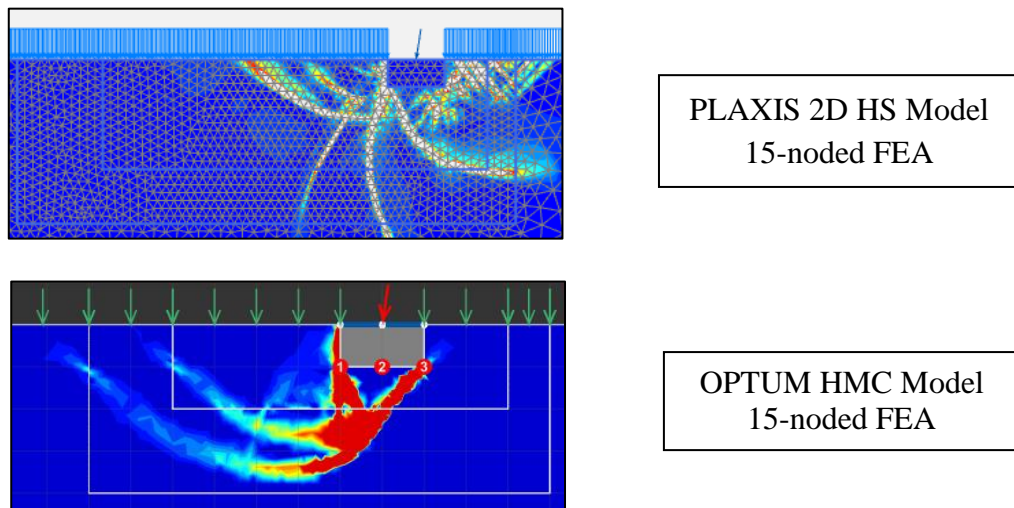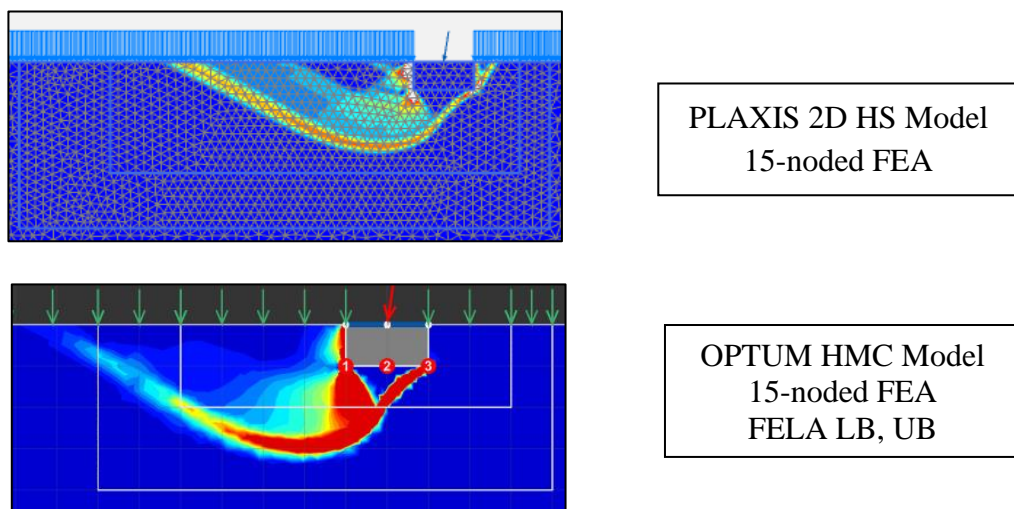
Fig. 45   Shear strains for the corresponding failure load n.a. Davis A φ*=ψ'=29.84°

For associated plasticity, non-associated plasticity as well as for non-associated plasticity after Davis A it has been noted that the failure load obtained with Plaxis is generally higher compared to Optum (according to MA Thesis Nowakoswki, 2018). The reason therefore is the mesh adaptivity used in Optum G2.

To study the influence of the Davis Approach on the strength reduction FoS_{SR}, the original Davis Approach A (Davis A 1968), as well as the enhanced Davis Approach B and C (Tschuchnigg et al 2015) are used to imitate non-associated plasticity for a dilatancy angle of 11.7°. It is also shown by Simon Oberhollenzer (MA Thesis "numerical studies on slope stability studies") that the original Davis Approach A leads to conservative results in the factor of safety, whereas the enhanced Davis Approach B and C give more accurate results regarding the factor of safety. Tab. 21 and 22 show the resulting strength reduction FoS_{SR} according to Davis Approach A, B, C (ψ'=11.7°). Therefore, the loads according to Davis Approach A are used to calculate the FoS_{SR} according to Davis Approach B and C, resulting in higher FoS_{SR}. The study of the influence of the Davis Approach is done for Optum SRFELA (LB, UB) and Plaxis SRFEA (15-nod.).

Tab. 21   Comparison of Davis Approach A, B, C for non-associated ψ'=11.7°

Optum HMC model SRFELA - φ'=35° =ψ'=11.7°							
	Davis A			Davis B*		Davis C*	
	LB	UB	(LB+UB)/2				
FoS_{SR}	load [kN/m]	load [kN/m]	load [kN/m]	FoS_{SR}	$\varphi^*=\psi'$ [°]	FoS_{SR}	$\varphi^*=\psi'$ [°]
3.0	163.5	171	167.25	3.25	34.79	3.30	34.99
2.0	333	345	339.00	2.15	34.51	2.20	34.92
1.5	620	655	637.50	1.60	34.08	1.65	34.57
* according to Davis A (LB+UB)/2							

Tab. 22   Comparison of Davis Approach A, B, C for non-associated ψ'=11.7°

Plaxis HS model SRFEA 15-noded - φ'=35° =ψ'=11.7°						
	Davis A		Davis B		Davis C	
load* [kN]	FoS_{SR}	$\varphi^*=\psi'$ [°]	FoS_{SR}	$\varphi^*=\psi'$ [°]	FoS_{SR}	$\varphi^*=\psi'$ [°]
174	2.99	32.44	3.30	34.79	3.30	34.99
360	1.99	32.44	2.20	34.50	2.20	34.92
670	1.49	32.44	1.60	34.06	1.60	34.56
according to Davis Approach A						

Fig.46 demonstrates both analyses, the failure load (FEA) as well as the strength reduction (SRFEA), for Plaxis and Optum. The figure shows the relation of the applied load, which is required to reach the FoS 3.0, 2.0, 1.5 and 1.0, in case of associated plasticity. The resulting FoS at 1000kN/m differs within a range of 51% and 10% for 2000kN/m (Eq.(97)). Thus, the higher the loading the less the difference in the resulting FoS, comparing both analyses.
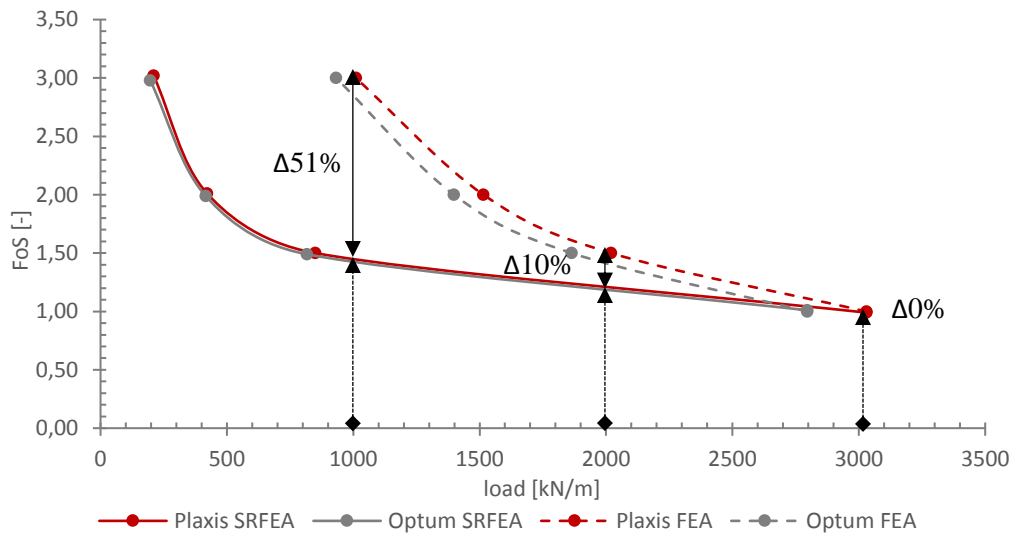
Fig. 46   FEA 15-nod. vs. SRFEA 15-nod. for a. φ'=ψ'=35°
               (Plaxis HS model and Optum HMC model)

Tab.23 shows the applied loads corresponding to FoS-values 3.0, 2.0, 1.5, 1.0 for different safety analysis considerations as depicted in Fig.46. The applying load differs within a range of 0% for FoS = 1.0 and 7 % for FoS = 3.0 (Eq.(95)). Thus, the higher the FoS the higher the difference regarding the corresponding load. Furthermore, it is shown that the required loading for the strength reduction analysis at FoS_{SR} 3.0 to 1.5 for Plaxis and Optum fits well, whereas for the FoS 1.0 at collapse the applied load in Plaxis results in generally higher loads compared to Optum (relating to the failure load analysis).

Tab. 23   FEA 15-nod. vs. SRFEA 15-nod. for a. φ'=ψ'=35°
               (Plaxis HS model and Optum HMC model)

	Plaxis – HS model		Optum – HMC model	
	FEA	SRFEA	FEA	SRFEA
FoS	failure load [kN/m]	SR load [kN/m]	failure load [kN/m]	SR load [kN/m]
3.0	1010	210	932	196.5
2.0	1515	422	1398	416
1.5	2020	850	1864	816
1.0	3030	3030	2796	2796

Tab.24 refers to Plaxis SRFEA and Tab.25 refers to Optum SRFEA, in case of associated plasticity. It demonstrates the strength reduction analysis, applying the failure load compared to the actual load, that is necessary to reach the FoS 3.0, 2.0, 1.5 and 1.0. The results in the strength reduction FoS_{SR} differ within a range of 0% for $FoS_{SR} = 1.0$ and 53% for $FoS_{SR} = 3.0$ (Eq.(96)). Thus, the smaller the difference in the applied loads the smaller the difference in the resulting FoS_{SR} with respect to the strength reduction analysis.

Tab. 24   SRFEA 15-nod. for a. φ'=ψ'=35° (Plaxis HS model)
                applying failure load vs. applying actual load for FoS 1.0-3.0

SRFEA 15-noded - φ'=ψ'=35°			
Plaxis – HS model			
failure load [kN/m] → FoS_{SR}		SR load [kN/m] → FoS_{SR}	
1010 → 1.40		210 → 3.02	
1515 → 1.22		422 → 2.01	
2020 → 1.12		850 → 1.50	
3030 → 0.99		3030 → 0.99	

Tab. 25   SRFEA 15-nod. for a. φ'=ψ'=35° (Optum HMC model)
                applying failure load vs. applying actual load for FoS 1.0-3.0

SRFEA 15-noded - φ'=ψ'=35°			
Optum – HMC model			
failure load [kN/m] → FoS_{SR}		SR load [kN/m] → FoS_{SR}	
932 → 1.43		196.5 → 2.98	
1398 → 1.24		416 → 1.99	
1864 → 1.13		816 → 1.49	
2796 → 1.01		2796 → 1.01	

Fig.47-51 represent the failure mechanism obtained using the strength reduction technique (associated plasticity) and FEA according to Plaxis and Optum. In this case, the applied failure loads corresponding to FoS_{FL}-values from 1.0 to 3.0 are used to calculate the FoS_{SR} for the strength reduction approach and vice versa (Tab.24, 25).

Fig. 47   Plaxis HS model SRFEA 15-nod. incremental deviatoric strain
            a. $\varphi'= \psi'= 35°$ for the corresponding actual load FoS_{SR} 3.0-1.5

Fig. 48   Plaxis HS model SRFEA 15-nod. incremental deviatoric strain
            a. $\varphi'= \psi'= 35°$ for the corresponding failure load FoS_{FL} 3.0-1.5

Fig. 49   Optum HMC model SRFEA 15-nod. shear dissipation
            a. $\varphi'= \psi'= 35°$ for the corresponding actual load FoS_{SR} 3.0-1.5

Fig. 50   Optum HMC model SRFEA 15-nod. shear dissipation
            a. $\varphi'= \psi'= 35°$ for the corresponding failure load FoS_{FL} 3.0-1.5

| Plaxis HS model | ← → | Optum HMC model |

Fig. 51   Sliding surface at collapse SRFEA 15-nod. a. $\varphi'= \psi' = 35°$

Fig.52 demonstrates both analyses, the failure load (FELA) as well as the strength reduction (SRFELA) for Optum. The figure shows the relation of the applied load, which is required to reach the FoS 3.0, 2.0, 1.5 and 1.0, in case of associated plasticity. The resulting FoS at 1000kN/m vary within a range of 49% and 14% for 2000kN/m (Eq.(97)). Thus, the higher the loading the less the difference in the resulting FoS, comparing both analyses.
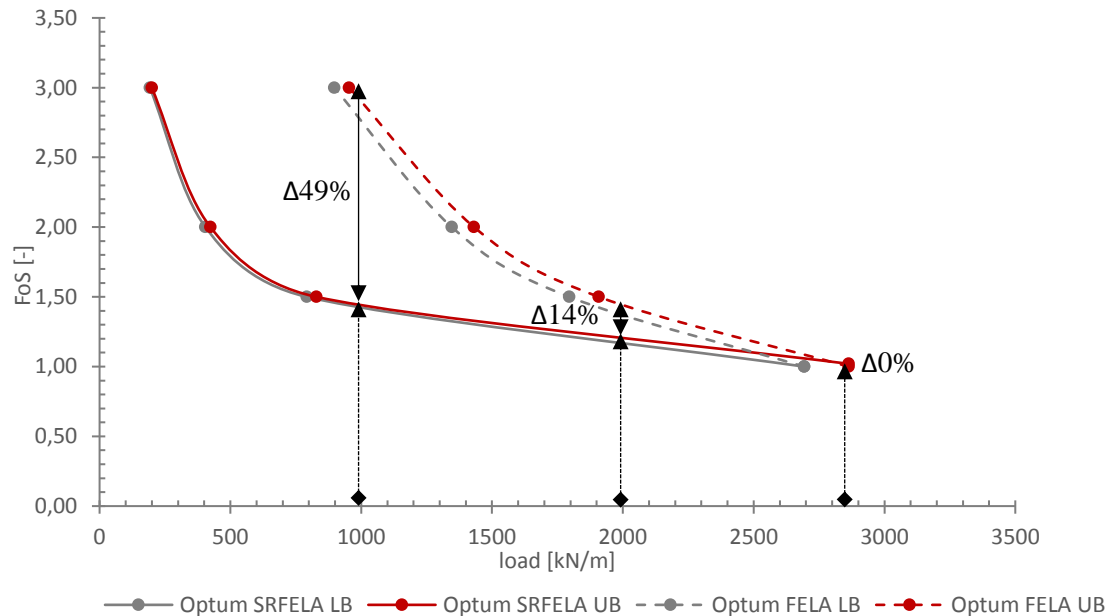
Fig. 52   FELA vs. SRFELA for a. $\varphi'=\psi'=35°$ (Optum HMC model LB, UB)

Tab.26 shows the applied loads corresponding to FoS-values 3.0, 2.0, 1.5, 1.0. for different safety analysis considerations as depicted in Fig.52. The results vary within a range of 0% for FoS = 1.0 and 79% for FoS = 3.0 (Eq.(95)). Thus, the higher the FoS the higher the difference regarding the corresponding load. As mentioned before, the loading for the strength reduction analysis at collapse has to be the same as for the failure load analysis, shown in Tab.26.

Tab. 26   FELA vs. SRFELA for a. $\varphi'=\psi'=35°$ (Optum HMC model LB, UB)

Optum HMC model – $\varphi'=\psi'=35°$				
	FELA LB	SRFELA LB	FELA UB	SRFELA UB
FoS	failure load [kN/m]	SR load [kN/m]	failure load [kN/m]	SR load [kN/m]
3.0	897.67	192	954.33	200
2.0	1346.50	405	1431.50	424
1.5	1795.33	792	1908.67	829
1.0	2693	2693	2863	2863

Tab.27 (LB) and 28 (UB) represent the strength reduction FoS$_{SR}$ for the applied failure load as well as the actual load reaching the FoS 3.0, 2.0, 1.5, 1.0, in case of associated plasticity. The results in the strength reduction FoS$_{SR}$ vary within a range of 0% for FoS$_{SR}$ = 1.0 and 52% for FoS$_{SR}$ = 3.0 (Eq.(96)). Thus, the smaller the difference in the applied loads the smaller the difference in the resulting FoS$_{SR}$ with respect to the strength reduction analysis.

Tab. 27   SRFELA LB for a. φ'=ψ'=35° (Optum HMC model)
           applying failure load vs. applying actual load for FoS 1.0-3.0

SRFELA LB - φ'=ψ'=35°					
Optum – HMC model					
failure load [kN/m]	→	FoS$_{SR}$	SR load [kN/m]	→	FoS$_{SR}$
897.67	→	1.43	192	→	3.00
1346.50	→	1.24	405	→	2.00
1795.33	→	1.13	792	→	1.50
2693	→	1.00	2693	→	1.00

Tab. 28   SRFELA UB for a. φ'=ψ'=35° (Optum HMC model)
           applying failure load vs. applying actual load for FoS 1.0-3.0

SRFELA UB - φ'=ψ'=35°					
Optum – HMC model					
failure load [kN/m]	→	FoS$_{SR}$	SR load [kN/m]	→	FoS$_{SR}$
954.33	→	1.42	200	→	3.00
1431.50	→	1.24	424	→	2.00
1908.67	→	1.13	829	→	1.50
2863	→	1.02	2863	→	1.02

Fig.53-57 represent the failure mechanism obtained using the strength reduction technique (associated plasticity) and the limit analysis according to Optum. In this case, the applied failure loads corresponding to FoS_{FL}-values from 1.0 to 3.0 are used to calculate the FoS_{SR} for the strength reduction approach and vice versa (Tab.27, 28).
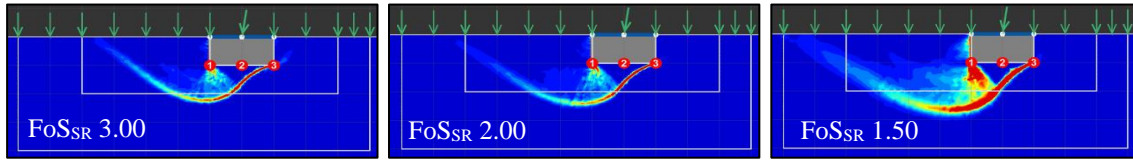
Fig. 53   Optum HMC model SRFELA LB shear dissipation a. $\varphi'= \psi'= 35°$
            for the corresponding actual load FoS_{SR} 3.0-1.5
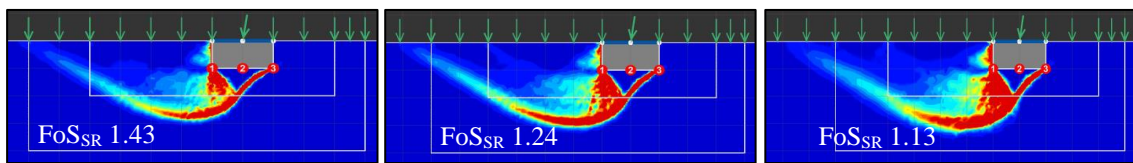
Fig. 54   Optum HMC model SRFELA LB shear dissipation a. $\varphi'= \psi'= 35°$
            for the corresponding failure load FoS_{FL} 3.0-1.5
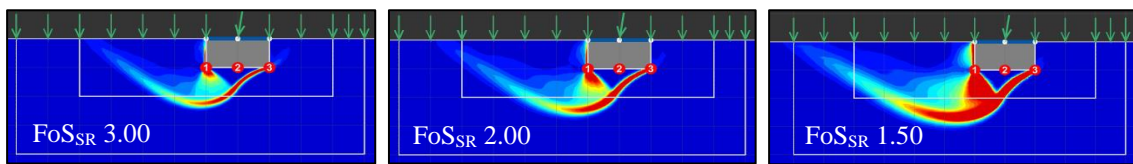
Fig. 55   Optum HMC model SRFELA UB shear dissipation a. $\varphi'= \psi'= 35°$
            for the corresponding actual load FoS_{SR} 3.0-1.5

Fig. 56   Optum HMC model SRFELA UB shear dissipation a. $\varphi'= \psi'= 35°$
            for the corresponding failure load FoS_{FL} 3.0-1.5
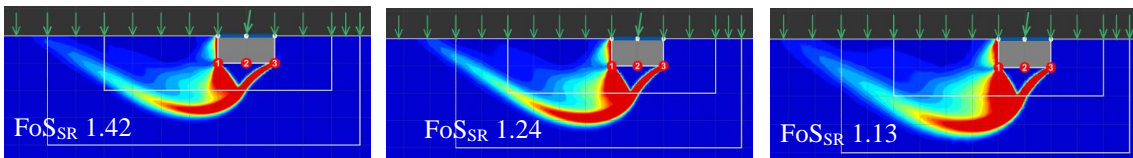
| Optum HMC model LB | ← → | Optum HMC model UB |
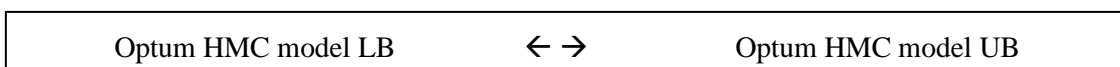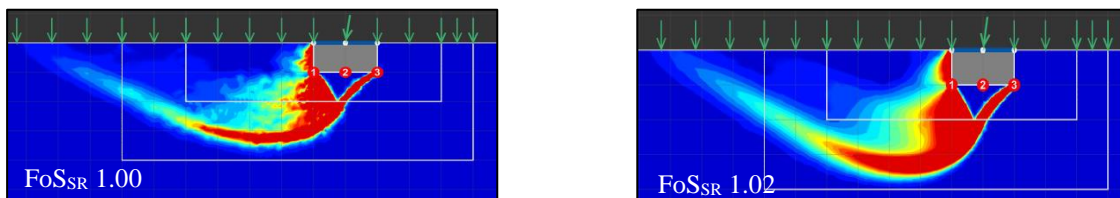
Fig. 57   Sliding surface at collapse SRFELA (LB, UB) a. $\varphi'=\psi'= 35°$

Fig.58 demonstrates both analyses, the failure load (FEA) as well as the strength reduction (SRFEA) for Plaxis. The figure shows the relation of the applied load, which is required to reach the FoS 3.0, 2.0, 1.5 and 1.0, in terms of non-associated plasticity versus non-associated plasticity after Davis A. The resulting FoS at 500kN/m differs within a range of 43 % and 21 % for 1000kN/m (Eq.(97)). Thus, the higher the loading the less the difference in the resulting FoS, comparing both analyses.
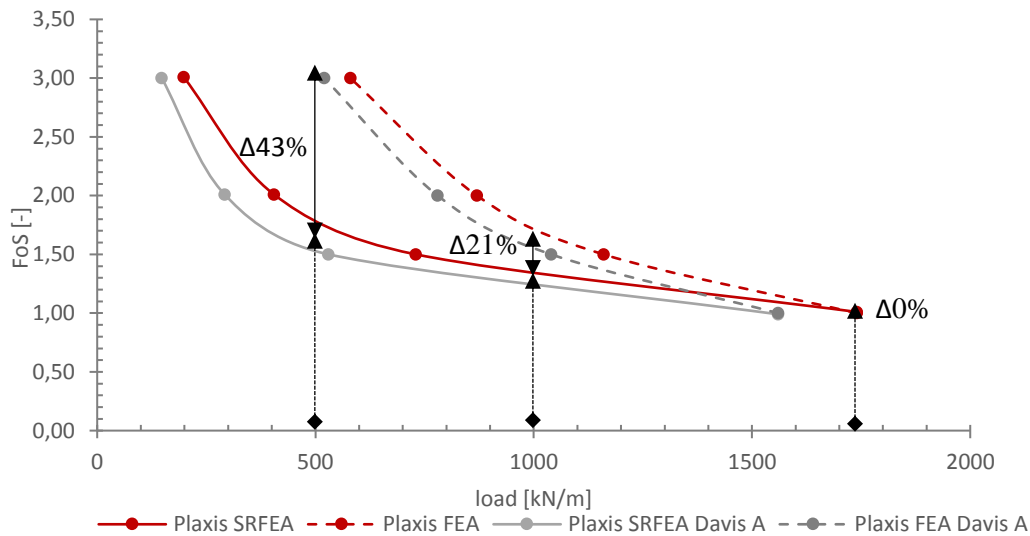
Fig. 58   FEA 15-nod. Vs. SRFEA 15-nod. for n.a. ψ'=0° and
               n.a. Davis A φ*=ψ'=29.84° (Plaxis HS model)

Tab.29 shows the obtained loads that correspond to the FoS-values 3.0, 2.0, 1.5, 1.0. for each safety analysis, failure load and strength reduction as depicted in Fig. 58. The results differ within a range of 0% for FoS = 1.0 and 70% for FoS = 3.0 for n.a. Davis A (Eq.(95)). On the opposite the results vary within a range of 0% for FoS = 1.0 and 66% for FoS = 3.0 (Eq.(95)), in terms of non-associated plasticity. Consequently, the higher the FoS the higher the difference regarding the corresponding load. It should be mentioned that the original Davis Approach A leads to conservative results regarding the factor of safety compared to non-associated plasticity. Furthermore, as mentioned before, the original Davis Approach A leads to conservative results with respect to the factor of safety compared to non-associated plasticity.

Tab. 29   FEA 15-nod. vs. SRFEA 15-nod. for n.a. ψ'=0° and
           n.a. Davis A φ*=ψ'=29.84° (Plaxis HS model)

	Plaxis – HS model ψ'=0°		Plaxis – HS model φ*=ψ'=28.94°	
	FEA	SRFEA	FEA	SRFEA
FoS	failure load [kN/m]	SR load [kN/m]	failure load [kN/m]	SR load [kN/m]
3.0	580	198	520	148
2.0	870	405	780	292
1.5	1160	730	1040	530
1.0	1740	1740	1560	1560

Tab.30 (non-associated) and Tab.31 (non-associated after Davis A) highlights the
results of the strength reduction analysis, applying the failure load compared to the
actual load, that is necessary to reach the FoS 3.0, 2.0, 1.5 and 1.0 considering non-
associated plasticity and non-associated plasticity after Davis A. The results differ
within a range of 0% for $FoS_{SR} = 1.0$ and 50% for $FoS_{SR} = 3.0$ for n.a. Davis A
(Eq.(96)). On the opposite the results vary within a range of 0% for $FoS_{SR} = 1.0$
and 45% for $FoS_{SR} = 3.0$ (Eq.(96)), in terms of non-associated plasticity.
Consequently, the less the FoS the less the difference regarding the corresponding
load.

Tab. 30   SRFEA 15-nod. for n.a. ψ'=0° (Plaxis HS model)
           applying failure load vs. applying actual load for FoS 1.0-3.0

SRFEA 15-noded - ψ'=0°			
Plaxis – HS model			
failure load [kN/m]	→ FoS_{SR}	SR load [kN/m]	→ FoS_{SR}
580	→ 1.67	198	→ 3.01
870	→ 1.39	405	→ 2.01
1160	→ 1.23	730	→ 1.50
1740	→ 1.01	1740	→ 1.01

Tab. 31   SRFEA 15-nod. for n.a. Davis A φ*=ψ'=29.84° (Plaxis HS model)
           applying failure load vs. applying actual load for FoS 1.0-3.0

SRFEA 15-noded - φ*=ψ'=28.94°			
Plaxis – HS model			
failure load [kN/m]	→ FoS_{SR}	SR load [kN/m]	→ FoS_{SR}
520	→ 1.51	148	→ 3.00
780	→ 1.26	292	→ 2.01
1040	→ 1.14	530	→ 1.50
1560	→ 0.99	1560	→ 0.99

Fig.59-63 represent the SRFEA failure mechanisms obtained with Plaxis considering both, non-associated plasticity and non-associated plasticity after Davis A. In this case, the applied failure loads corresponding to FoS_{FL}-values from 1.0 to 3.0 are used to calculate the FoS_{SR} for the strength reduction approach and vice versa (Tab.30, 31).
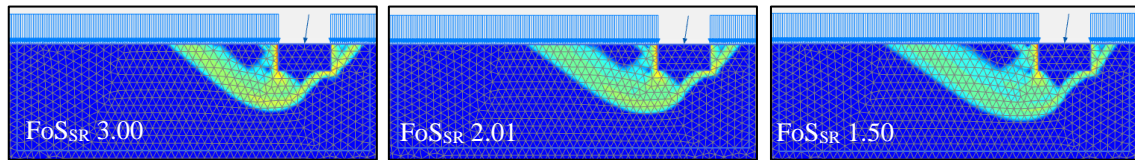
Fig. 59   Plaxis HS model SRFEA 15-nod. incremental deviatoric strain
            n.a. Davis A $\varphi^*=\psi'=29.84°$ for the corresponding actual load FoS_{SR} 3.0-1.5
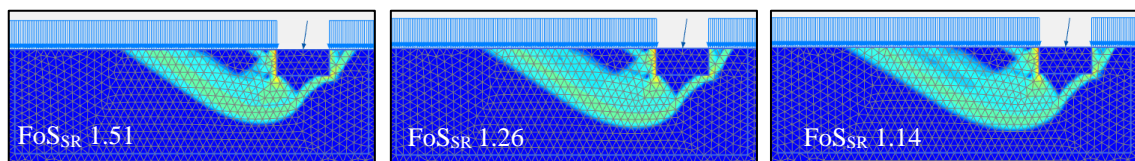
Fig. 60   Plaxis HS model SRFEA 15-nod. incremental deviatoric strain
            n.a. Davis A $\varphi^*=\psi'=29.84°$ for the corresponding failure load FoS_{FL} 3.0-1.5
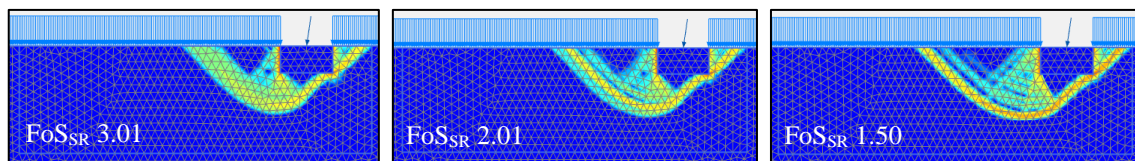
Fig. 61   Plaxis HS model SRFEA 15-nod. incremental deviatoric strain n.a. $\psi' = 0°$
            for the corresponding actual load FoS_{SR} 3.0-1.5
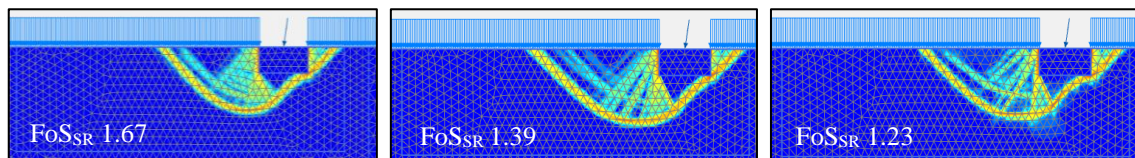
Fig. 62   Plaxis HS model SRFEA 15-nod. incremental deviatoric strain n.a. $\psi' = 0°$
            for the corresponding failure load FoS_{FL} 3.0-1.5
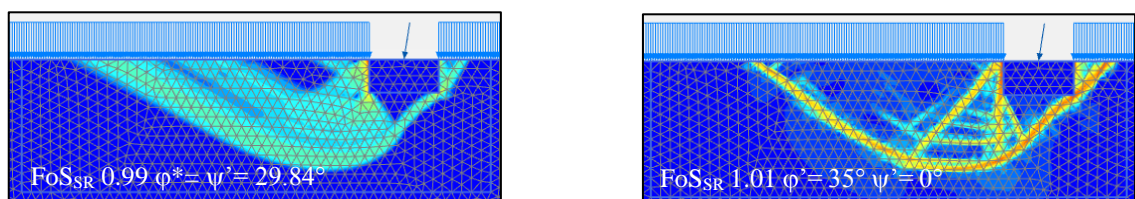
Fig. 63   Sliding surface at collapse
            Plaxis HS model SRFEA 15-nod. incremental deviatoric strain

Fig.64 demonstrates both analyses, the failure load (FELA) as well as the strength reduction (SRFELA) for Optum. The figure shows the relation of the applied load, which is required to reach the FoS 3.0, 2.0, 1.5 and 1.0, in case of non-associated plasticity after Davis A. The resulting FoS at 500kN/m vary within a range of 50% and 14% for 1000kN/m (Eq.(97)). Thus, the higher the loading the less the difference in the resulting FoS, comparing both analyses.
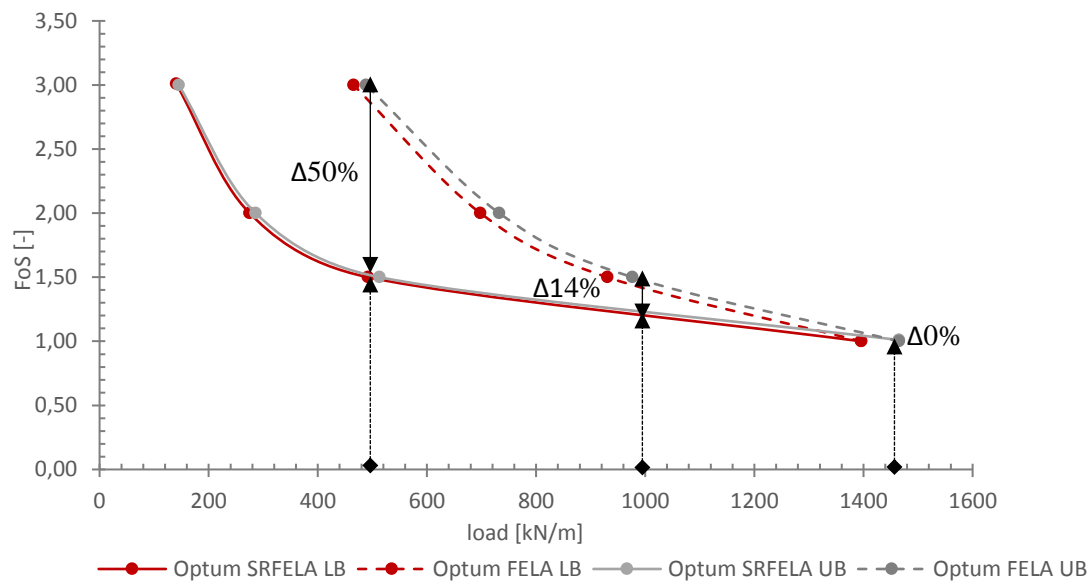
Fig. 64   FELA vs. SRFELA for n.a. Davis A $\varphi^*=\psi'=29.84°$
            (Optum HMC model LB, UB)

Tab.32 shows the applied loads corresponding to FoS-values 3.0, 2.0, 1.5, 1.0. for different safety analysis considerations as depicted in Fig.64. The results vary within a range of 0% for FoS = 1.0 and 70% for FoS = 3.0. Thus, the higher the FoS the higher the difference regarding the corresponding load. As mentioned before, the loading for the strength reduction analysis at collapse has to be the same as for the failure load analysis, shown in Tab.32.

Tab. 32   FELA vs. SRFELA for n.a. Davis A $\varphi^*=\psi'=29.84°$
            (Optum HMC model LB, UB)

Optum HMC model – $\varphi^*=\psi'=29.84°$				
	FELA LB	SRFELA LB	FELA UB	SRFELA UB
FoS	failure load [kN/m]	SR load [kN/m]	failure load [kN/m]	SR load [kN/m]
3.0	465.33	141	488.33	145
2.0	698	275	732.50	286
1.5	930.67	492	976.67	513
1.0	1396	1396	1465	1465

Tab.33 (LB) and 34 (UB) represent the strength reduction FoS_{SR} for the applied failure load as well as the actual load reaching the FoS 3.0, 2.0, 1.5, 1.0, in case of non-associated plasticity after Davis A. The results in the strength reduction FoS vary within a range of 0% for $FoS_{SR} = 1.0$ and 50% for $FoS_{SR} = 3.0$ (Eq.(96)). Thus, the smaller the difference in the applied loads the smaller the difference in the resulting FoS_{SR} with respect to the strength reduction analysis.

Tab. 33   SRFELA LB for n.a. Davis A $\varphi^*=\psi'=29.84°$ (Optum HMC model) applying failure load vs. applying actual load for FoS 1.0-3.0

SRFELA LB - $\varphi^*=\psi'=29.84°$					
Optum – HMC model					
failure load [kN/m]	→	FoS_{SR}	SR load [kN/m]	→	FoS_{SR}
465.33	→	1.54	141	→	3.01
698	→	1.30	275	→	2.00
930.67	→	1.16	492	→	1.50
1396	→	1.00	1396	→	1.00

Tab. 34   SRFELA UB for n.a. Davis A $\varphi^*=\psi'=29.84°$ (Optum HMC model) applying failure load vs. applying actual load for FoS 1.0-3.0

SRFELA UB - $\varphi^*=\psi'=29.84°$					
Optum – HMC model					
failure load [kN/m]	→	FoS_{SR}	SR load [kN/m]	→	FoS_{SR}
488.33	→	1.54	145	→	3.00
732.50	→	1.30	286	→	2.00
976.67	→	1.16	513	→	1.50
1465	→	1.01	1465	→	1.01

Fig.65-69 represent the failure mechanism obtained using the strength reduction technique (non-associated plasticity after Davis) and the limit analysis according to Optum. In this case, the applied failure loads corresponding to FoS_{FL}-values from 1.0 to 3.0 are used to calculate the FoS_{SR} for the strength reduction approach and vice versa (Tab.33, 34).
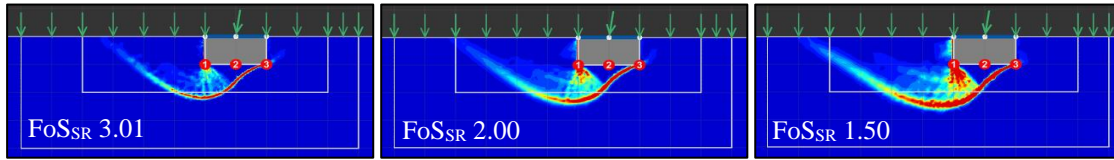
Fig. 65 Optum HMC model SRFELA LB shear dissipation
     n.a. Davis A $\varphi^*=\psi'= 29.84°$ for the corresponding actual load FoS_{SR} 3.0-1.5
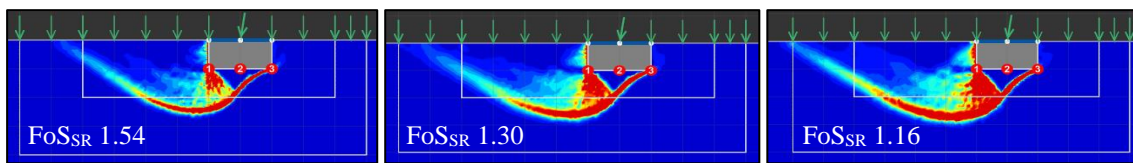
Fig. 66 Optum HMC model SRFELA LB shear dissipation
     n.a. Davis A $\varphi^* =\psi'=29.84°$ for the corresponding failure load FoS_{FL} 3.0-1.5
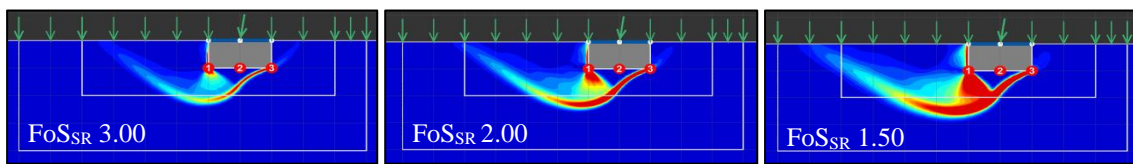
Fig. 67 Optum HMC model SRFELA UB shear dissipation
     n.a. Davis A $\varphi^*=\psi'=29.84°$ for the corresponding actual load FoS_{SR} 3.0-1.5
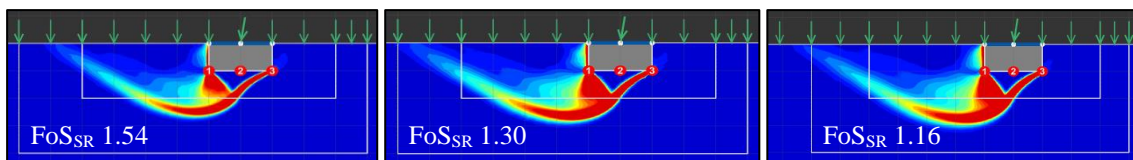
Fig. 68 Optum HMC model SRFELA UB shear dissipation
     n.a. Davis A $\varphi^*=\psi'=29.84°$ for the corresponding failure load FoS_{FL} 3.0-1.5
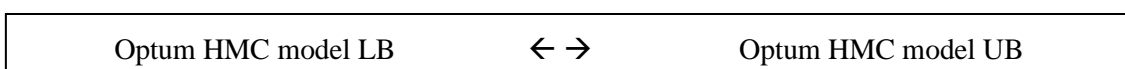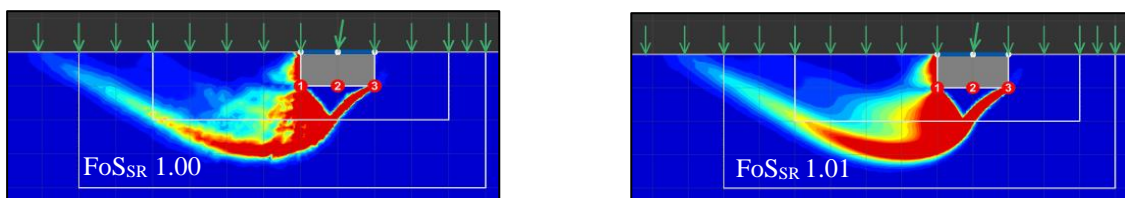
Fig. 69 Sliding surface at collapse SRFELA (LB, UB) n.a. Davis A $\varphi^*=\psi'=29.84°$

4.2.2 2D: Influence of the Constitutive Model

To evaluate the influence of the constitutive model on the obtained collapse loads and corresponding factors of safety, for both safety analyses (failure load, strength reduction) selected studies considering different flow rules and constitutive models (MC, HS, HMC) are performed. The HS (Plaxis) and HMC (Optum) model are both using the MC failure criterion, thus the results for a homogenous soil body should be nearly the same as for the MC Model and no differences in the factor of safety are expected to occur. For both models, strength reduction analyses (SRFEA 15-nod., SRFELA LB, UB) as well as failure load analyses (FEA 15-nod., FELA LB, UB) are performed, but only for associated plasticity. Tab. 35-38 show the required loading, that has to be applied to reach the FoS 3.0 to 1.0. for each safety analysis. This referred to both programs, Plaxis and Optum.

Tab. 35   Influence of the Plaxis constitutive model on the FoS for the failure load and strength reduction analysis (a. φ'=ψ'=35° 15-nod. element)

Plaxis 15-noded element - φ'=ψ'=35°				
	HS model		MC model	
	FEA	SRFEA	FEA	SRFEA
FoS	failure load [kN/m]	SR load [kN/m]	failure load [kN/m]	SR load [kN/m]
3.0	1010	210	1006.67	204
2.0	1515	422	1510	427
1.5	2020	850	2013.33	850
1.0	3030	3030	3020	3020

Tab. 36   Influence of the Optum constitutive model on the FoS for the failure load and strength reduction analysis (a. φ'=ψ'=35° 15-nod. element)

Optum 15-noded element- φ'=ψ'=35°				
	HMC model		MC model	
	FEA	SRFEA	FEA	SRFEA
FoS	failure load [kN/m]	SR load [kN/m]	failure load [kN/m]	SR load [kN/m]
3.0	932	196.5	933.33	195
2.0	1398	416	1400	415
1.5	1864	816	1866.67	815
1.0	2796	2796	2800	2800

Tab. 37   Influence of the Optum constitutive model on the FoS for the failure load and
           strength reduction analysis (a. φ'=ψ'=35° LB)

Optum LB - φ'=ψ'=35°				
	HMC model		MC model	
	FELA	SRFELA	FELA	SRFELA
FoS	failure load [kN/m]	SR load [kN/m]	failure load [kN/m]	SR load [kN/m]
3.0	897.67	192	896.67	192
2.0	1346.50	405	1345	400
1.5	1795.33	792	1793.33	790
1.0	2693	2693	2690	2690

Tab. 38   Influence of the Optum constitutive model on the FoS for the failure load and
           strength reduction analysis (a. φ'=ψ'=35° UB)

Optum UB - φ'=ψ'=35°				
	HMC model		MC model	
	FELA	SRFELA	FELA	SRFELA
FoS	failure load [kN/m]	SR load [kN/m]	failure load [kN/m]	SR load [kN/m]
3.0	954.33	200	954.67	202
2.0	1431.50	424	1432	420
1.5	1908.67	829	1909.33	830
1.0	2863	2863	2864	2864

The FoS results are almost identical for both constitutive models MC (Plaxis, Optum) and HS (Plaxis) / HMC (Optum) as well as FE codes (Plaxis, Optum). There is hardly any difference regarding the applied loads corresponding to FoS$_{SR}$ values from 3.0 to 1.0 as well as the applied loads required in order to reach the failure loads corresponding to FoS$_{FL}$ values from 3.0 to 1.0. At last, whether using the MC or the HS/HMC model, the constitutive model has hardly any effect on drained conditions of a homogenous soil body. Therefore, the 3D calculations according to Plaxis 3D and Optum G3 were done for the Mohr Coulomb model only.

In case of Plaxis, it should be taken into account that the mesh should be sufficiently fine to receive accurate numerical results. In contrast, too fine meshes should be avoided, since they lead to excessive calculation times. On the other hand, Optum involves an automatic mesh adaptivity function, which involves an iterative process that automatically refines the mesh at regions with large strain gradients. As a consequence, the mesh dependency of calculations results is significantly reduced, thereby reducing the calculation times.

4.2.2.1 p'-q stress path and corresponding π-plane

p'-q stress paths as well as corresponding π-planes are obtained for Plaxis calculations (15-noded elements) considering both, MC and HS. Considering the failure load analysis, the calculations were performed with associated ($\varphi'=\psi'$), non-associated plasticity ($\psi'=0°$, $11.7°$) and non-associated plasticity after Davis Approach A ($\varphi^*=\psi'$). The failure load analysis is done by stepwise loading according to FoS_{FL} 3.0, 2.0, 1.5 until collapse occurs (FoS_{FL} 1.0). Fig.70 shows the considered stress points, which are located at characteristic points of the failure body. Stress points A and B were positioned inside and on the edge of the active zone, whereas C and D were on the failure surface confining the passive zone; E was specified inside the passive zone (according to Fig.26). Stress point F was randomly specified outside the failure body. Subsequent results are restricted to MC; in addition, results obtained with HS are documented in the Appendix.
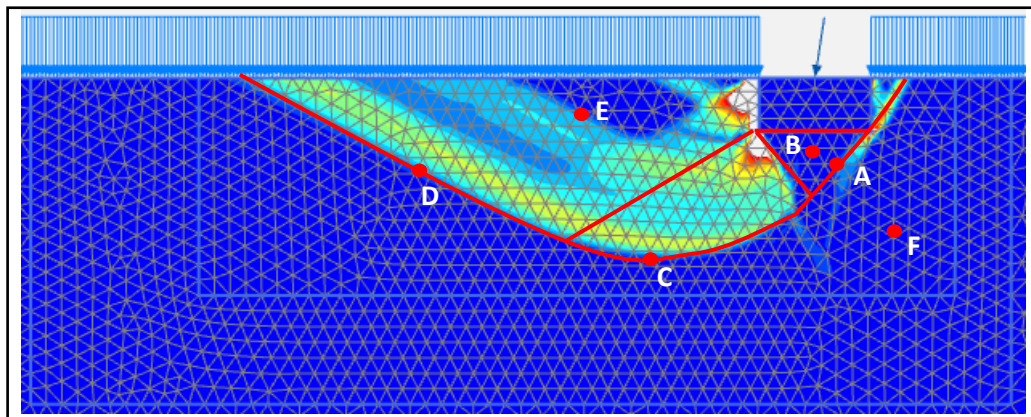
Fig. 70   Stress points on an in between the sliding surface
(failure mechanism incremental deviatoric strain Δy_s)

As a starting point, a brief introduction to the plots of the p'-q stress paths and the corresponding π-planes is given. π-planes cover starting and end points of respective phases (initial, FoS_{FL} 3.0, 2.0, 1.5,1.0), whereas p'-q stress paths involve all points of respective phases (initial, FoS_{FL} 3.0, 2.0, 1.5,1.0). Furthermore, the π-plane for each stress point is plotted at failure, and not for each FoS_{FL} (3.0, 2.0, 1.5). The yield surface for the π-plane is drawn in red solid lines and concerns the maximum isotropic effective stress. On the other hand, the grey dot-dashed lines represent the triaxial compression and triaxial extension MC failure lines in the π-plane and the p'-q stress paths. If the last point of the plastic phase at failure has reached the yield surface in π-plane, the current stress point is plastic, otherwise it is an elastic point.
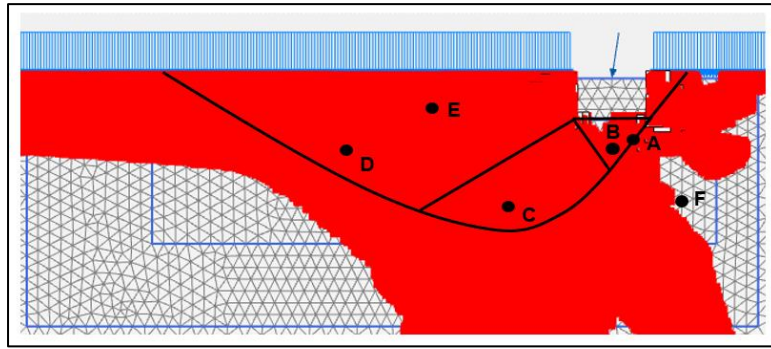
Fig. 71   MC model FEA 15-nod. plastic points for a. φ'=ψ'=35° stress point A-F
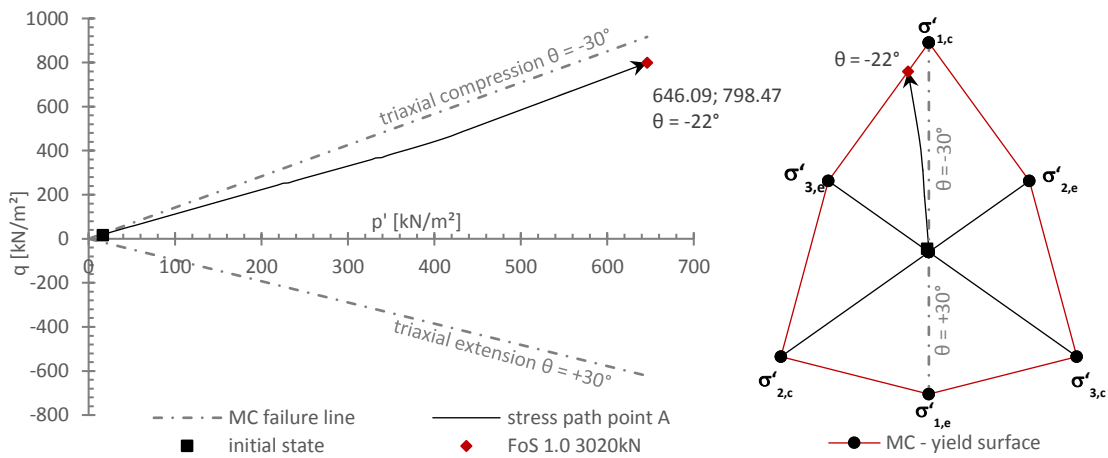
Fig. 72   p'-q stress path and corresponding π-plane
            for a. φ'=ψ'=35° and plastic stress point A (MC model FEA 15-nod.)
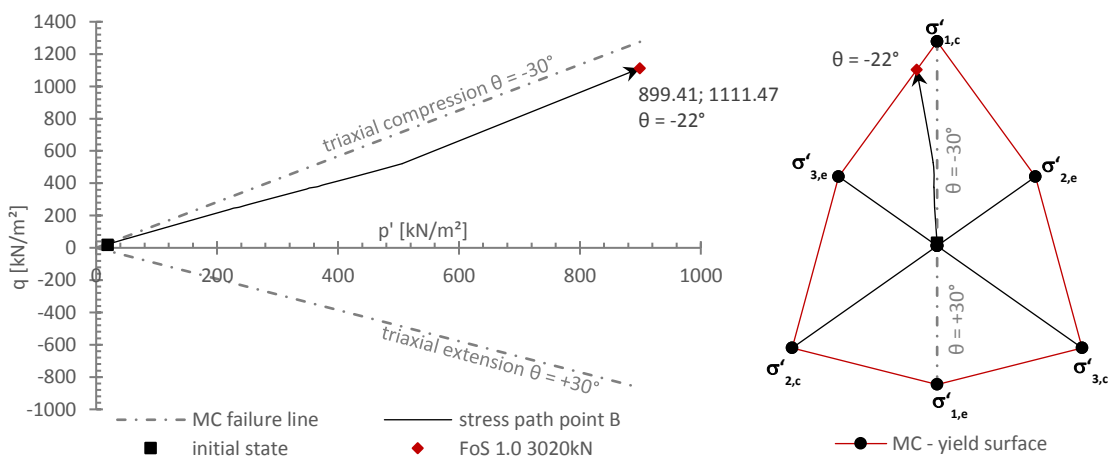
Fig. 73   p'-q stress path and corresponding π-plane
            for a. φ'=ψ'=35° and plastic stress point B (MC model FEA 15-nod.)

Fig. 72, 73 show stress points A and B (i.e. active zone; associated plasticity). As soon as stress paths coincide with the MC failure line, the stress points become plastic. The corresponding π-plane illustrates the stress path in a p'-q' space at failure for each stress point (FoS$_{FL}$ 1.0). Furthermore, Tab.39 shows that the lode angle θ is almost the same (i.e. -22°) except for the elastic stress point F (θ = −24°).

Tab. 39   Resulting stresses and lode angle for stress point A-F
           for a. φ'=ψ'=35° at failure (MC model FEA 15-nod.)

φ'=ψ'=35° - FoS$_{FL}$ 1.0 at failure			
stress point	σ'$_1$ [kN/m²]	σ'$_2$ [kN/m²]	σ'$_3$ [kN/m²]	θ [°]
A - plastic	1173.12	447.27	317.90	**-21.934**
B -plastic	1633.06	622.64	442.54	**-21.934**
C - plastic	438.93	167.29	118.95	**-21.945**
D - plastic	145.05	55.26	39.31	**-21.955**
E - plastic	87.42	33.31	23.69	**-21.950**
F - elastic	381.48	151.07	122.35	**-24.197**

The remaining stress points C,D,E and F for associated plasticity are shown in the Appendix.
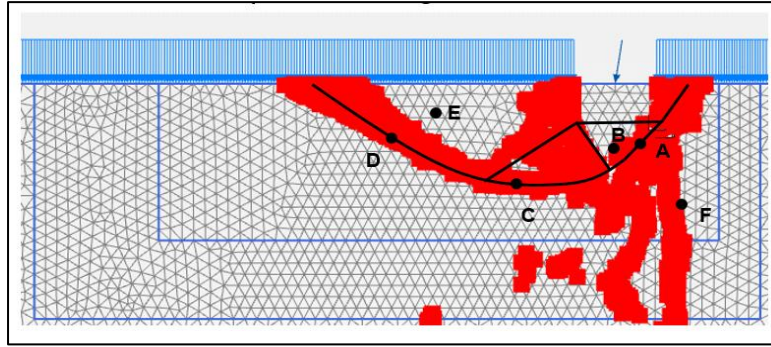
Fig. 74   MC model FEA 15-nod. plastic points for n.a. ψ'=0° stress point A-F
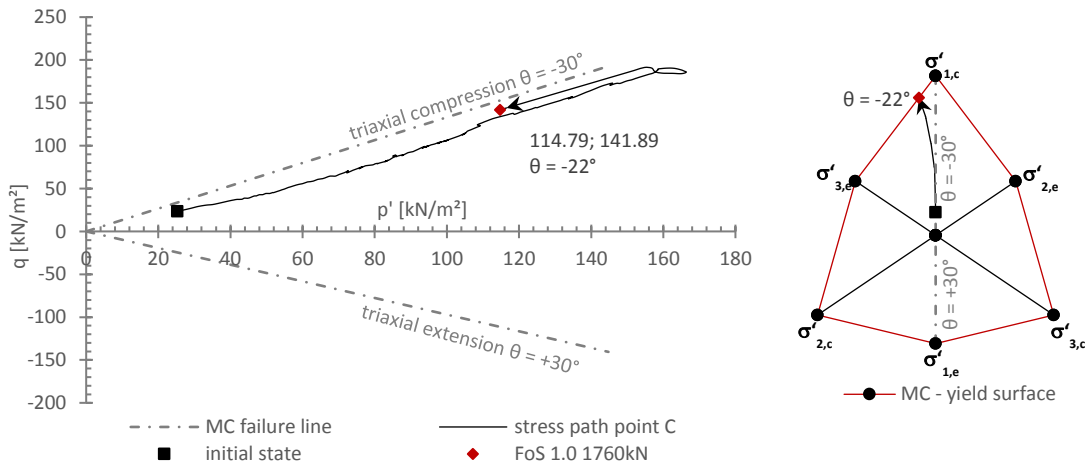
Fig. 75   p'-q stress path and corresponding π-plane
             for n.a. ψ'=0° and plastic stress point C (MC model FEA 15-nod.)
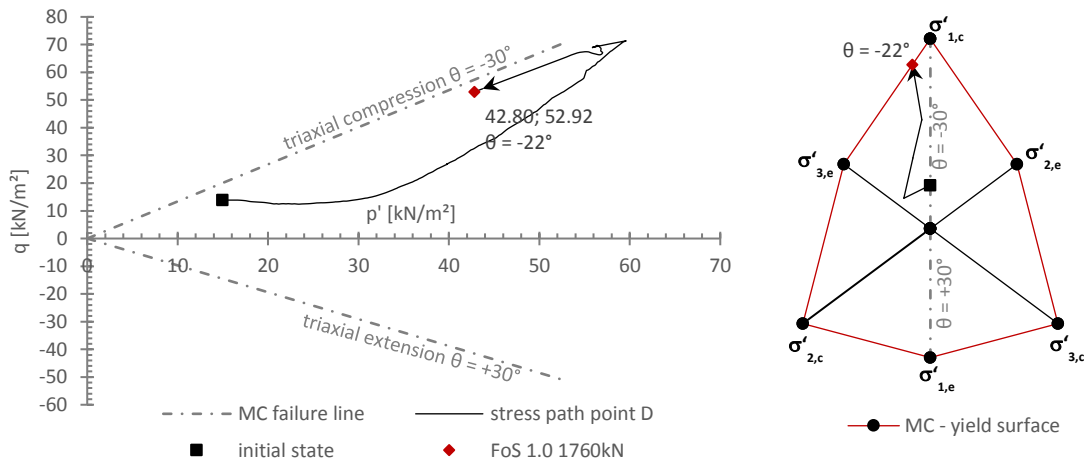
Fig. 76   p'-q stress path and corresponding π-plane
             for n.a. ψ'=0° and plastic stress point D (MC model FEA 15-nod.)

Fig. 75, 76 show stress points C and D (passive zone at sliding surface) for non-associated plasticity. The corresponding π-plane illustrates the stress path in a p'-q space until failure for each stress point (FoS$_{FL}$ 1.0). Furthermore, Tab. 40 illustrates that the lode angle θ remains nearly constant at -22° except for the elastic stress points E and F (θ = -23°). As mentioned in chapter 2.2.3, a consequence of non-associated plasticity is the non-unique failure load resulting in oscillations of the FoS$_{FL}$ beyond a threshold value linked to the bearing capacity.

Tab. 40   Resulting stresses and lode angle for stress point A-F
           for n.a. ψ'=0° at failure (MC model FEA 15-nod.)

ψ'=0° - FoS$_{FL}$ 1.0 at failure				
stress point	σ'_1 [kN/m²]	σ'_2 [kN/m²]	σ'_3 [kN/m²]	θ [°]
A - plastic	557.98	212.72	151.21	**-21.937**
B - plastic	1081.81	412.44	293.16	**-21.935**
C - plastic	208.45	79.42	56.49	**-21.954**
D - plastic	77.73	29.60	21.06	**-21.968**
E - elastic	77.46	30.01	22.64	**-22.884**
F - elastic	299.92	116.35	88.17	**-22.963**

Results concerning the remaining stress points A,B,E and F for non-associated plasticity are shown in the Appendix. In this context, the same conclusions can be drawn for a dilatancy angle of 11.7° ($\varphi'/3$).
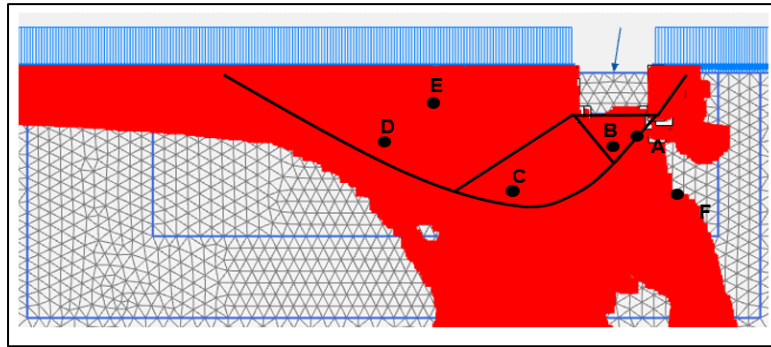
Fig. 77   MC model FEA 15-nod. plastic points
               for n.a. Davis A φ*=ψ'=29.84° stress point A-F
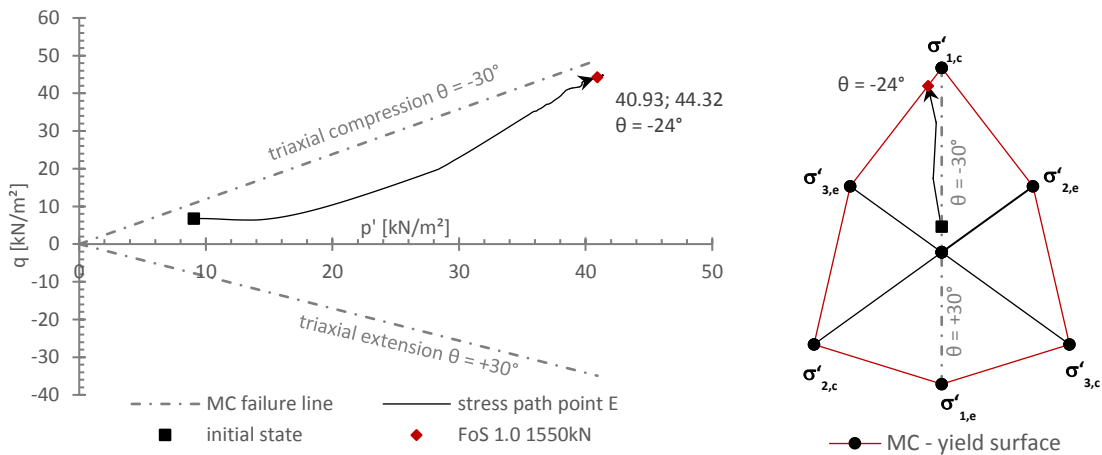
Fig. 78   p'-q stress path and corresponding π-plane (MC model FEA 15-nod.)
               for n.a. Davis A φ*=ψ'=29.84° and plastic stress point E
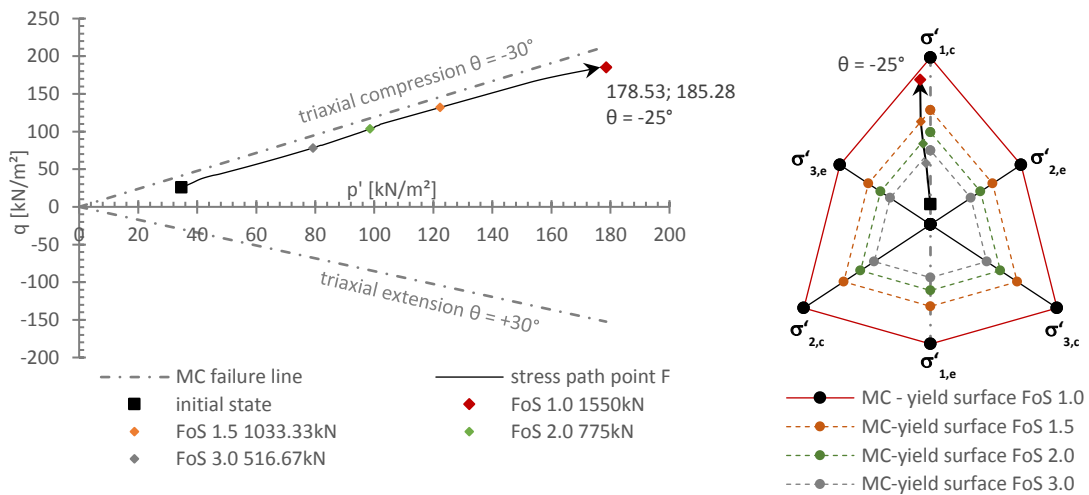
Fig. 79   p'-q stress path and corresponding π-plane (MC model FEA 15-nod.)
               for n.a. Davis A φ*=ψ'=29.84° and elastic stress point F

Fig. 78, 79 show stress points E and F, which are either located inside the passive zone or outside the failure body, for non-associated plasticity after Davis A. At the position of the MC failure criterion, the stress point becomes plastic. The corresponding π-plane illustrates the stress path in a p'-q space at failure for each stress point (FoS$_{FL}$ 1.0). As seen in Fig 78 and Fig. 79, both stress points (E, F) tend to trixial compression. Furthermore, Tab. 41 shows that the lode angle θ gives almost identical values ranging from -24° to -25°. It should be mentioned, that since the last point of the stress path remains in between the yield surface (at failure), stress point F functions as an elastic point. Comparing the FoS$_{FL}$ 3.0, 2.0 and 1.5, the last point of each phase lies on the corresponding yield surface.

Tab. 41   Resulting stresses and lode angle for stress point A-F
            for n.a. Davis A $\varphi^*=\psi'=29.84°$ at failure (MC model FEA 15-nod.)

	$\varphi^*=\psi'=29.84°$ - FoS$_{FL}$ 1.0 at failure			
	σ'_1 [kN/m²]	σ'_2 [kN/m²]	σ'_3 [kN/m²]	θ [°]
A - plastic	776.02	312.31	260.35	**-24.749**
B -plastic	884.24	355.88	296.65	**-24.748**
C - plastic	292.31	119.67	98.07	**-24.176**
D - plastic	116.49	48.18	39.08	**-23.830**
E - plastic	70.32	28.88	23.59	**-24.074**
F - elastic	301.64	125.66	108.28	**-25.341**

Results concerning the remaining stress points A,B,C and D for non-associated plasticity after Davis A are shown in the Appendix. In this context, the same conclusions can be drawn for a dilatancy angle of 11.7° ($\varphi'/3$).

4.2.3 2D: Influence of Numerical Settings

4.2.3.1 Tolerated error

To study the influence of numerical control parameters on safety analyses, SRFEA is performed with altered tolerated error values (0.1%, 1% = default setting, 3%, 5%). The numerical study concerning the tolerated error is done using Plaxis (15-noded elements, HS model). The calculations were executed for the FoS_{SR} 1.0, 1.5, 2.0 for associated ($\varphi'=\psi'$), non-associated plasticity ($\psi'=0°$, 11.7°) as well as non-associated plasticity after Davis Approach A ($\varphi^*=\psi'$), by applying the failure load (FoS_{FL} 1.0) from Optum and calculating the according strength reduction FoS_{SR}. Therefore, there should be no more reduction of the strength parameter. For FoS_{SR}-values 1.5 and 2.0, "real" loads according to Plaxis strength reduction were considered. In addition, failure loads obtained with Optum for FoS_{FL} 1.0 were applied for this study to compare both FE codes.

Fig.80 demonstrates the influence of the tolerated error (1% = default setting, 3%, 5%) on the oscillation behaviour with respect to the factor of safety at failure (FoS_{SR} 1.0). Performing automatic SRFEA with a tolerated error of 3% and 5% result in a higher amplitude of oscillation and therefore higher FoS_{SR}-peaks compared to the default setting of 1%. Thus, in case of associated plasticity, the higher the tolerated error (inaccurate), the more oscillations of the FoS_{SR}-value occur, for closer observation (zoomed in). Generally, associated plasticity results in less oscillations (smoother curve) compared to non-associated plasticity.
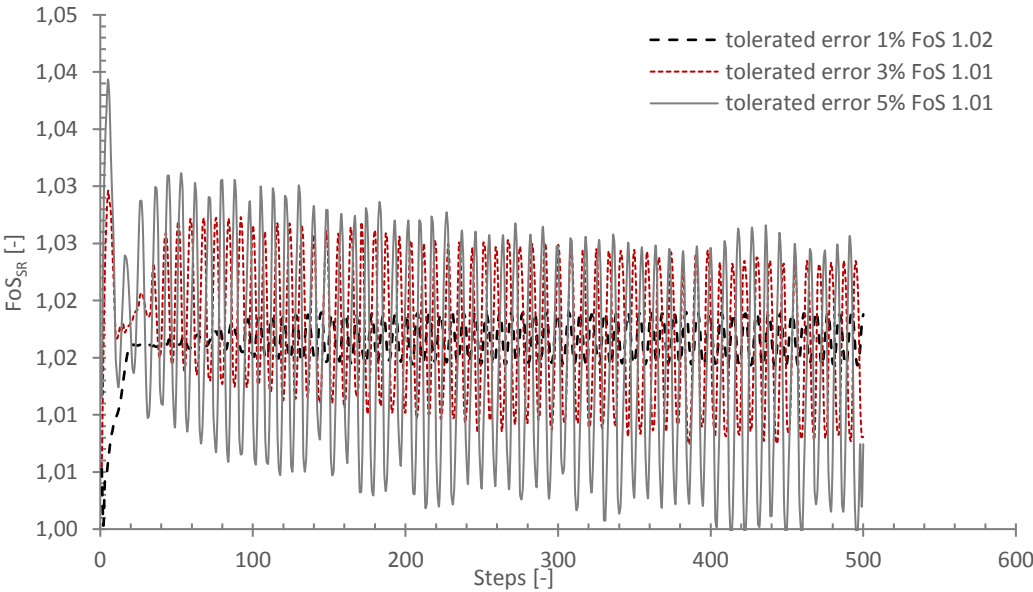
Fig. 80   Influence of tolerated error 1%, 3%, 5% for a. $\varphi'=\psi'=35°$ at failure (HS model SRFEA 15-nod.)

Given the same boundary conditions (i.e. associated plasticity, $FoS_{SR} = 1.0$), Fig.81 demonstrates the influence of a tolerated error equal 0.1%, which means less than the default setting of 1. Performing automatic SRFEA with a tolerated error of 0.1% results in less oscillations and therefore lower FoS_{SR}-peaks leading to a smoother curve. Thus, in case of associated plasticity, the lower the tolerated error, the less FoS_{SR}-oscillations occur. Furthermore, it is shown that the gradient of the first branch is lower compared to tolerated errors of 1% and 5%. Additionally, the horizontal branch is yet to be reached. However, when more steps are used, the graph converges towards the result obtained with tolerated errors 1% and 5%.
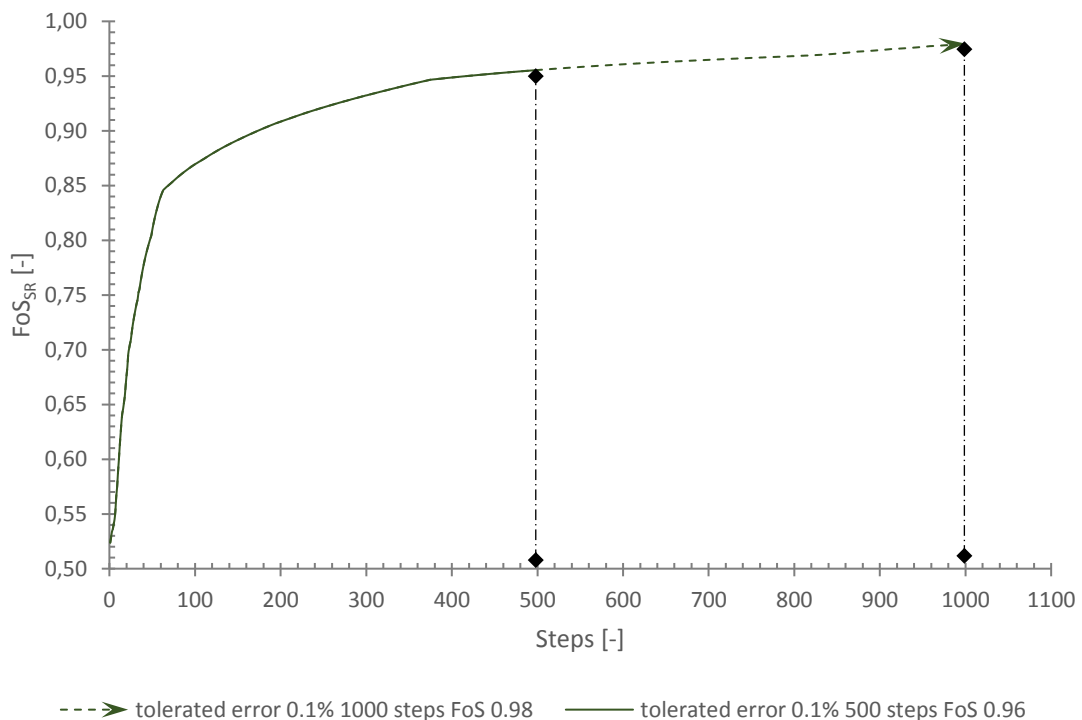
Fig. 81   Influence of tolerated error 0.1% for a. φ'=ψ'=35° at failure
              (HS model SRFEA 15-nod.)

Given the same number of load steps, Tab.42 demonstrates that the FoS_{SR}-values obtained with a tolerated error of 0.1 % are smaller compared to FoS_{SR} obtained with tolerated errors of 1% and 5%. However, when more steps are used, the graph is approximating towards the same value (i.e. 1.0).

Tab. 42   Comparison of the tolerated error 0.1%, 1%, 3%, 5% and the resulting FoS$_{SR}$
             at failure for a. φ'=ψ'=35° (HS model SRFEA 15-nod.)

steps	tolerated error			
	0.1%	1%	3%	5%
500	FoS$_{SR}$ 0.96	FoS$_{SR}$ 1.02	FoS$_{SR}$ 1.01	FoS$_{SR}$ 1.01
1000	FoS$_{SR}$ 0.98	-	-	-

Fig.82 demonstrates the influence of the tolerated error for ψ'=0° (1% default
setting, 3%, 5%) on the oscillation behavior with respect to the factor of safety at
failure (FoS$_{SR}$ 1.0). Performing automatic SRFEA with a tolerated error of 3% and
5% results in lower amplitudes of oscillation and therefore lower FoS$_{SR}$-peaks,
compared to the default setting of 1%. Thus, in case of non-associated plasticity
(ψ'=0°), the higher the tolerated error (inaccurate), the less FoS$_{SR}$-oscillation
(smooth curve) occurs, relating to 1%, 3%, 5%. As mentioned in chapter 2.2.3, a
consequence of non-associated plasticity is that the response of the collapse load
will generally be non-unique when solving elastoplastic boundary value problems.
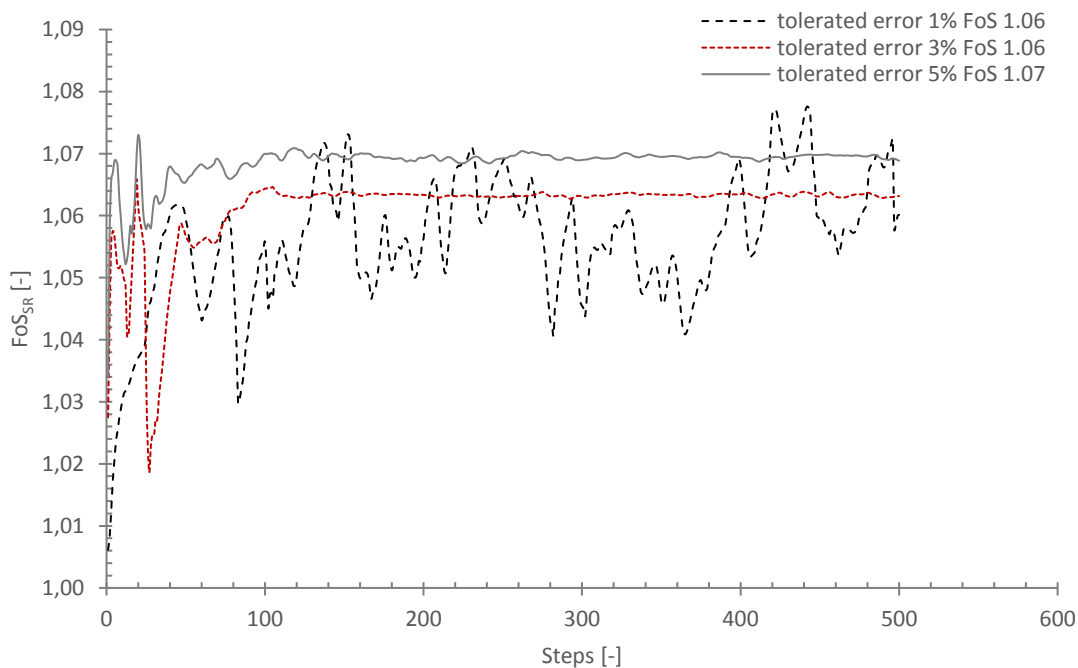
Fig. 82   Influence of tolerated error 1%, 3%, 5% for n.a. ψ'=0° at failure
             (HS model SRFEA 15-nod.)

Fig.83 demonstrates the influence of the tolerated error 0.1% in terms of non-associated plasticity (ψ'=0°) at failure (FoS$_{SR}$ 1.0). Performing automatic SRFEA with a tolerated error 0.1%. results in lower amplitudes of oscillation and therefore lower FoS$_{SR}$-peaks (smooth curve). Thus, in case of non-associated plasticity (ψ'=0°), the lower the tolerated error (more accurate), the less the FoS$_{SR}$-oscillation (smooth curve), relating to 0.1% and 1%. Furthermore, it is shown, that the gradient of the first branch is not as steep, compared to tolerated error of 1% up to 5%. It should be noted that the horizontal branch is yet not reached. However, when more steps are used, the graph is approximating towards the range of tolerated error 1% up to 5%.
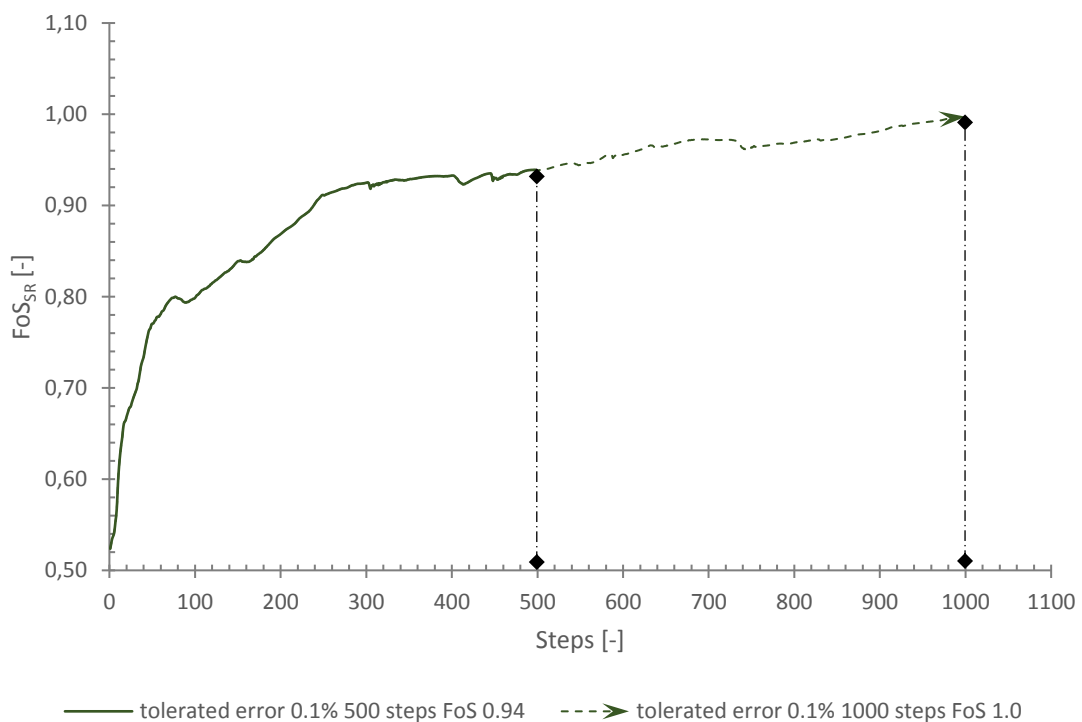
Fig. 83   Influence of tolerated error 0.1% for n.a. ψ'=0° at failure
               (HS model SRFEA 15-nod.)

Given the same number of load steps, Tab.43 demonstrates that the FoS$_{SR}$-values obtained with a tolerated error of 1 % up to 5% % the FoS$_{SR}$ for a tolerated error of 0.1% is less than 1.0. However, when more steps are used, the graph is approximating towards 1.0.

Tab. 43   Comparison of the tolerated error 0.1%, 1%, 3%, 5% and the resulting FoS$_{SR}$ at failure for n.a. ψ'=0° (HS model SRFEA 15-nod.)

	tolerated error			
steps	0.1%	1%	3%	5%
500	FoS$_{SR}$ 0.94	FoS$_{SR}$ 1.06	FoS$_{SR}$ 1.06	FoS$_{SR}$ 1.07
1000	FoS$_{SR}$ 1.00	-	-	-

Fig.84 demonstrates the influence of the tolerated error (1% default setting, 3%, 5%) on the oscillation behavior with respect to the factor of safety at failure (FoS$_{SR}$ 1.0). Performing automatic SRFEA with a tolerated error of 3% and 5% results in higher amplitudes of oscillation and therefore higher FoS$_{SR}$-peaks, compared to the default setting of 1%. Thus, in case of non-associated plasticity after Davis A (φ*=ψ'=29.84°), the higher the tolerated error (inaccurate), the more oscillations of the FoS$_{SR}$-value occur, for closer observation (zoomed in). On the opposite the tolerated error of 0.1% results in lower amplitudes of oscillation and therefore in lower FoS$_{SR}$-peaks. Consequently, the lower the tolerated error (more accurate), the less oscillations (smooth curve) of the FoS$_{SR}$-value occur, for closer observation (zoomed in). Furthermore, it is shown, that the gradient of the first branch is not as steep, compared to tolerated error of 1% up to 5%. It should be noted that the horizontal branch is yet not reached. However, when more steps are used, the graph is approximating towards the range of tolerated error 1% up to 5%.
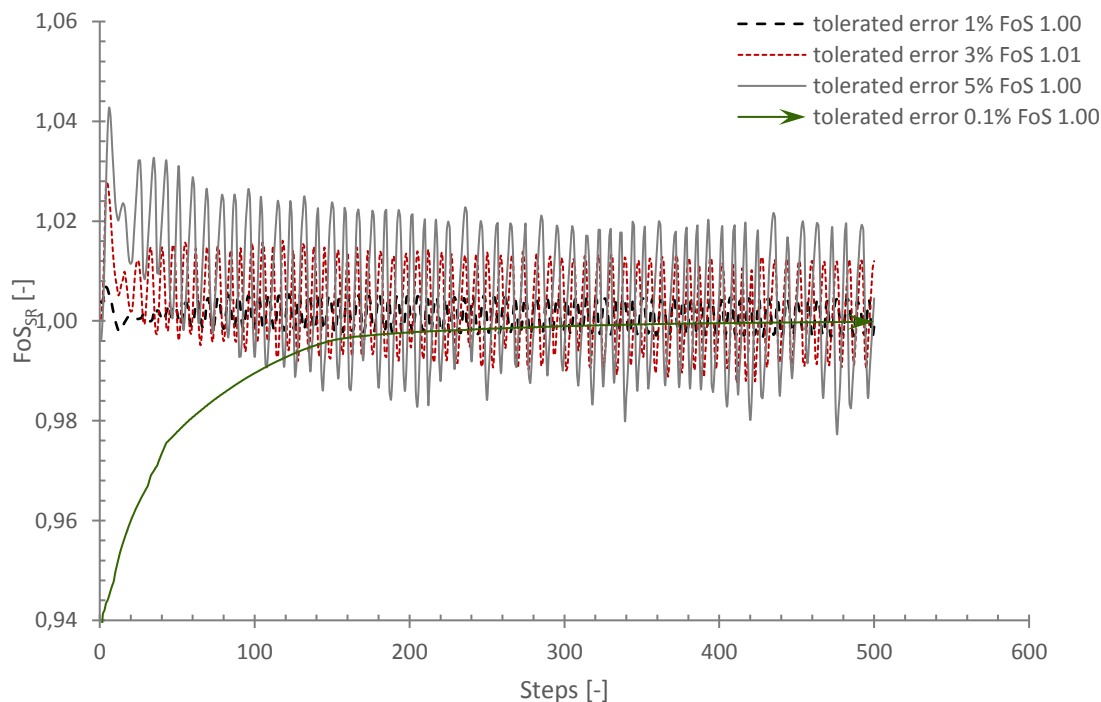
Fig. 84   Influence of tolerated error 0.1%, 1%, 3%, 5% for n.a. Davis A φ*=ψ'=29.84° at failure (HS model SRFEA 15-nod.)

Tab. 44   Comparison of the tolerated error 0.1%, 1%, 3%, 5% and the resulting
           FoS_{SR} at failure n.a. Davis A $\varphi*=\psi'=29.84°$ (HS model SRFEA 15-nod.)

	tolerated error			
steps	0.1%	1%	3%	5%
500	FoS_{SR} 1.00	FoS_{SR} 1.00	FoS_{SR} 1.01	FoS_{SR} 1.00
1000	FoS_{SR} 1.00	-	-	-

However, there are hardly difference observed in the factor of safety at failure, besides the changing of the graph (oscillation). Further calculations for non-associated plasticity as well as after Davis Approach A with a dilatancy angle of 11.7° ($\varphi'/3$) have been done, representing the same conclusions as for $\psi'=0°$ and shown in the Appendix. Additionally, all the conditions are calculated for the FoS_{SR} 1.5 and 2.0, shown in the Appendix. Notably, with decreasing FoS_{SR}-oscillation the tolerated error 1% up to 5% are in good agreement. Compared to tolerated error 0.1% the results and their conclusions are always the same. At last, studies according to the mesh discretization influence of the tolerated error and therefore on the resulting FoS_{SR} have been done in the MA Thesis of Dipl.-Ing. Veigl, Bsc "Numerical studies on slope stability analysis for drained and undrained material behaviour", 2020. The reason of the discrepancy between associated and non-associated plasticity according to the oscillation behavior at higher tolerated errors (3%, 5%) is part of ongoing research.

4.2.3.2 K_0 value

To study the influence of K_0 on both FE-codes (FEA, FELA) and the resulting FoS for each analysis, different values are considered (0.3, 1.0) and further compared to the original one (dependent on the friction angle). The numerical study of the K_0 parameter has been done for Plaxis MC model and for Optum HMC model. The calculations are done for the failure load and strength reduction FoS 1.0, 1.5, 2.0, 3.0 for associated and non-associated plasticity, as well as non-associated plasticity after Davis Approach A

$$K_0 = \frac{\sigma'_{xx}}{\sigma'_{yy}} \quad with \;\rightarrow\; \sigma'_{yy} = \gamma \times z \quad and \quad \sigma'_{xx} = K_0 \times \sigma'_{yy} \qquad (98)$$

Generally, the initial stress state is an important aspect in finite element analysis and significantly governed by the earth pressure coefficient at rest (but also from soil surface, soil stratigraphy and so on). The vertical effective stresses σ_v' satisfy equilibrium is relating to the dead load of the soil body. It should be noted, that the K_0 procedure does not guarantee failure criteria in the stress field, whereas complete equilibrium is satisfied only for a horizontal soil surface, soil layers and phreatic levels. The horizontal effective stress is defined by σ_h'. The K_0 value is generally calculated by Eq.(98), whereas the default setting in Plaxis corresponds to $K_0 = 1 - \sin\varphi'$.

Tab.45-53 show the resulting FoS and the applied loads obtained during failure load (FEA, FELA), as well as strength reduction analysis (SRFEA, SRFELA) for the Optum HMC model

Tab. 45 Influence of the K_0-value at the FoS_{FL} for Optum HMC model FEA 15-nod.
a. $\varphi'=\psi'=35°$, n. $\psi'=0°$ and n.a. Davis A $\varphi^*=\psi'=29.84°$

Optum HMC model – FEA 15-noded failure load [kN/m]			
ψ defining the flow rule	$K_0 = 0.3$	$K_0 = 0.426$ $K_0^* = 0.502$	$K_0 = 1.0$
$\varphi'= \psi'= 35°$	2797	2796	2759
$\psi'= 0°$	1634	1605	1631
$\varphi^*= \psi'= 29.84°$	1436	1423	1417

Tab. 46   Influence of the K_0-value at the FoS_{FL} for Optum HMC model FELA LB
           a. $\varphi'=\psi'=35°$ and n.a. Davis A $\varphi*=\psi'=29.84°$

Optum HMC model – FELA LB failure load [kN/m]			
ψ defining the flow rule	$K_0 = 0.3$	$K_0 = 0.426$ $K_0* = 0.502$	$K_0 = 1.0$
$\varphi'= \psi'= 35°$	2692	2693	2693
$\varphi*= \psi'= 29.84°$	1396	1396	1395

Tab. 47   Influence of the K_0-value at the FoS_{FL} for Optum HMC model FELA UB
           a. $\varphi'=\psi'=35°$ and n.a. Davis A $\varphi*=\psi'=29.84°$

Optum HMC model – FELA UB failure load [kN/m]			
ψ defining the flow rule	$K_0 = 0.3$	$K_0 = 0.426$ $K_0* = 0.502$	$K_0 = 1.0$
$\varphi'= \psi'= 35°$	2864	2863	2864
$\varphi*= \psi'= 29.84°$	1464	1465	1464

Tab. 48   Influence of the K_0-value at FoS_{SR} for Optum HMC model SRFEA 15-nod.
           a. $\varphi'=\psi'=35°$

Optum HMC model SRFEA 15-noded $\varphi'=\psi'=35°$					
$K_0 = 0.3$		$K_0 = 0.426$		$K_0 = 1.0$	
FoS_{SR}	load [kN/m]	FoS_{SR}	load [kN/m]	FoS_{SR}	load [kN/m]
3.00	197	2.99	197	3.00	197
2.00	415	1.99	416	2.01	415
1.50	810	1.49	816	1.51	805
1.00	2797	1.01	2796	1.01	2759

Tab. 49   Influence of the K_0-value at the FoS_{SR} for Optum HMC model SRFEA
           15-nod. n.a. Davis A $\varphi*=\psi'=29.84°$

Optum HMC model SRFEA 15-noded $\varphi*=\psi'=29.84°$					
$K_0 = 0.3$		$K_0* = 0.502$		$K_0 = 1.0$	
FoS_{SR}	load [kN/m]	FoS_{SR}	load [kN/m]	FoS_{SR}	load [kN/m]
3.01	144	3.01	143	3.01	143
2.01	280	2.01	280	2.01	280
1.51	501	1.51	501	1.51	501
1.01	1436	1.01	1423	1.01	1417

Tab. 50   Influence of the K_0-value at the FoS_{SR} for Optum HMC model SRFELA LB
                 a. φ'=ψ'=35°

Optum HMC model SRFELA LB φ'=ψ'=35°					
$K_0 = 0.3$		$K_0 = 0.426$		$K_0 = 1.0$	
FoS_{SR}	load [kN/m]	FoS_{SR}	load [kN/m]	FoS_{SR}	load [kN/m]
3.00	192.5	3.00	192	3.00	192.5
2.00	405	2.00	405	2.00	405
1.50	792	1.50	792	1.50	792
1.00	2692	1.00	2693	1.00	2693

Tab. 51   Influence of the K_0-value at the FoS_{SR} for Optum HMC model SRFELA LB
                 n.a. Davis A φ*=ψ'=29.84°

Optum HMC model SRFELA LB φ*=ψ'=29.84°					
$K_0 = 0.3$		$K_0* = 0.502$		$K_0 = 1.0$	
FoS_{SR}	load [kN/m]	FoS_{SR}	load [kN/m]	FoS_{SR}	load [kN/m]
3.00	140.5	3.01	140.5	3.00	140.5
2.00	275	2.00	275	2.00	275
1.50	492	1.50	492	1.50	492
1.00	1396	1.00	1396	1.00	1395

Tab. 52   Influence of the K_0-value at the FoS_{SR} for Optum HMC model SRFELA UB
                 a. φ'=ψ'=35°

Optum HMC model SRFELA UB φ'=ψ'=35°					
$K_0 = 0.3$		$K_0 = 0.426$		$K_0 = 1.0$	
FoS_{SR}	load [kN/m]	FoS_{SR}	load [kN/m]	FoS_{SR}	load [kN/m]
3.00	198.5	3.00	200	3.00	197
2.00	420	2.00	424	2.01	415
1.50	827	1.50	829	1.51	805
1.00	2864	1.01	2863	1.01	2864

Tab. 53   Influence of the K_0-value at the FoS_{SR} for Optum HMC model SRFELA LB n.a. Davis A $\varphi^*=\psi'=29.84°$

Optum HMC model SRFELA UB $\varphi^*=\psi'=29.84°$					
$K_0 = 0.3$		$K_0^* = 0.502$		$K_0 = 1.0$	
FoS_{SR}	load [kN/m]	FoS_{SR}	load [kN/m]	FoS_{SR}	load [kN/m]
3.00	144	3.01	145	3.00	145
2.01	280	2.00	286	2.00	286
1.51	501	1.50	513	1.50	513
1.01	1464	1.00	1465	1.01	1464

Nevertheless, in the case of drained conditions, the solution is independent of the initial stresses (K_0-procedure) and therefore the K_0 (according to MA Thesis Oberhollenzer, 2017). In contrast, K_0 has an impact on the safety calculation results when undrained conditions are considered. As shown in the Appendix, the results for the MC Model/Plaxis for the strength reduction analysis shows no difference in the resulting FoS_{SR}, as well as the loading.

4.2.4 2D vs. 3D: Effect on FoS

4.2.4.1 PLAXIS

2D and 3D results were compared using Plaxis 3D (SRFEA 10-noded elements, MC). The calculations are done for the strength reduction FoS_{SR} 1.0, 1.5, 2.0 for associated ($\varphi'=\psi'$) as well as non-associated plasticity ($\psi'=0°$, 11.7°). For this the two-dimensional SR_load for the FoS_{SR} 2.0, 1.5.,1.0 is applied and the three-dimensional FoS_{SR} for the strength reduction analysis is calculated.

To study the influence of the thickness of the model, different model extensions in the third direction (i.e. 1m and 4m) are applied. Fig.85 and 86 represent the total displacement for 1m and 4m thickness of the model, whereas an associated flow rule is applied.
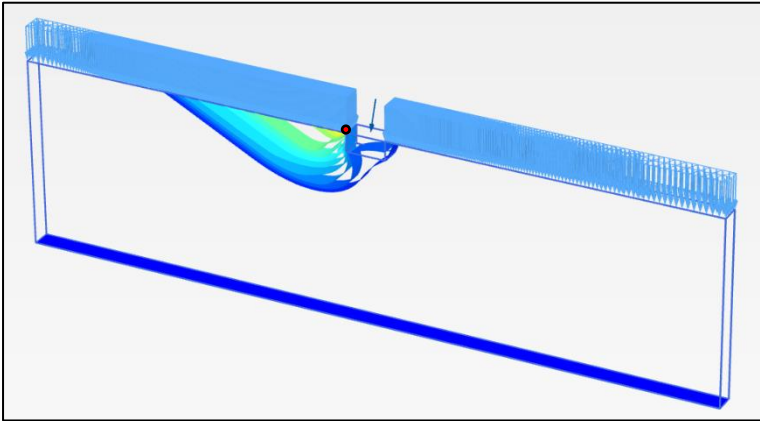
max. |u| at the left upper front corner of the strip foundation

Fig. 85   3D Plaxis MC model SRFEA 10-nod. 1m thickness for a. $\varphi'=\psi'=35°$
             sliding surface at failure
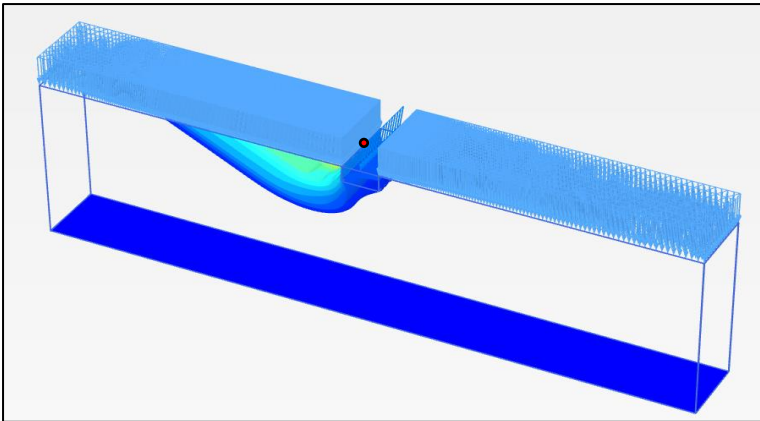
max. |u| at the left upper middle edge of the strip foundation

Fig. 86   3D Plaxis MC model SRFEA 10-nod.   4m thickness for a. $\varphi'=\psi'=35°$
             sliding surface at failure

Fig.87 compares 2D with 3D results using SRFEA and associated plasticity. The results show that for both 3D calculations, the FoS_{SR} gives slightly higher values compared to 2D calculations. Accordingly, 3D and 2D SRFEA are in good agreement (Δ0.02-0.03), which is also the case regarding the 2D failure load.
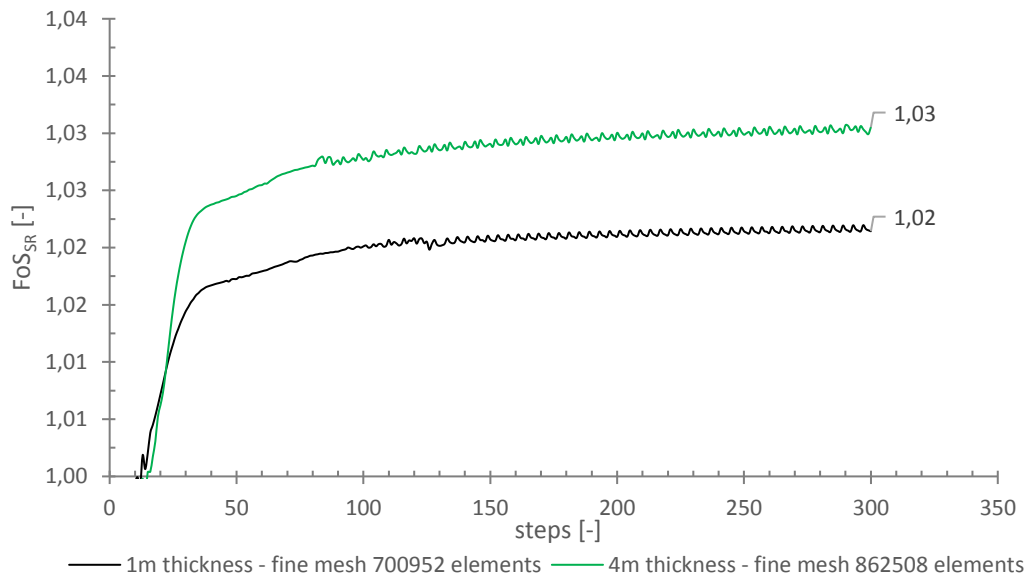
Fig. 87   3D Plaxis MC model SRFEA 10-nod.at failure for a. φ'=ψ'=35°

Fig.88 shows the 3D strength reduction analysis relating to the 2D load for the FoS_{SR} 1.5 in terms of associated plasticity. It is seen that for 3D calculations the peak FoS_{SR} results in the same values as in 2D calculations. Furthermore, the FoS_{SR} 1.5 induces higher amplitudes of oscillation in the resulting FoS_{SR}, therefore a manual curve (red dashed line) was plotted approximating towards the peak values. Thus, 3D strength reduction analysis, relating to the peak values of the FoS_{SR}, fits very well with 2D strength reduction analysis, both corresponding to the 2D load for the FoS_{SR} 1.5. The reason of the large oscillation is part of ongoing research.
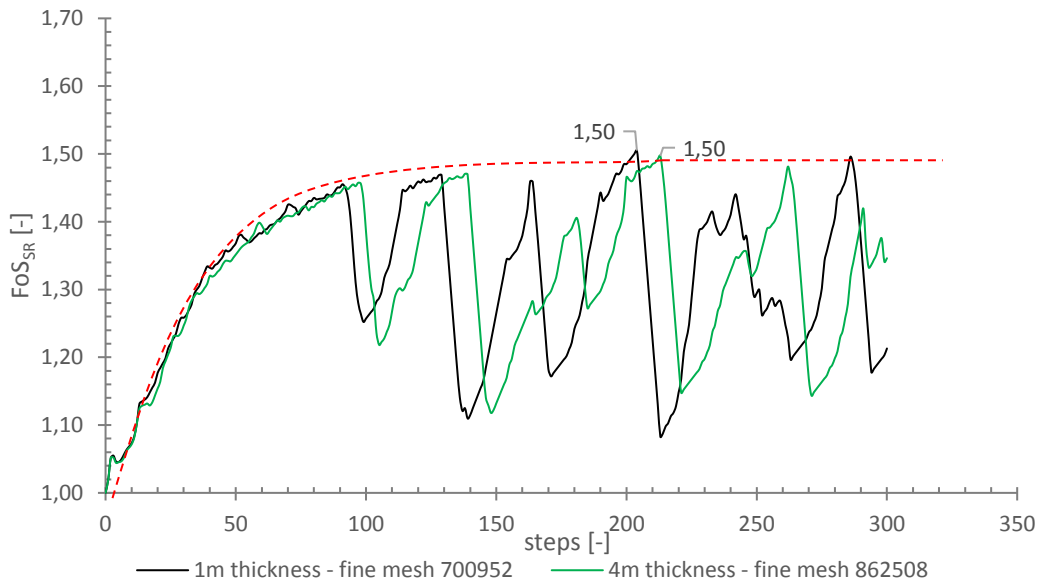
Fig. 88   3D Plaxis MC model SRFEA 10-nod. at FoS$_{SR}$ 1.5 for a. φ'=ψ'=35°

Fig. 89 demonstrate the influence of the tolerated error of 0.1%, which means less than the default setting of 1% (1m thickness) regarding to Fig 88. Performing automatic SRFEA with a tolerated error of 0.1% results in a smooth curve that converges to the desired FoS$_{SR}$ of 1.5. Furthermore, it is shown that the gradient of the first branch for a tolerated error of 0.1% is lower compared to the tolerated error of 1%; furthermore, the horizontal branch at the end was not reached within the specified number of allowable steps. Comparing both tolerated errors after step ~300, the peak FoS$_{SR}$ for 1% tolerated error results in 1.5 and the FoS$_{SR}$ for 0.1% tolerated error results in 1.17, thus showing a difference in the FoS$_{SR}$ of Δ0.33.
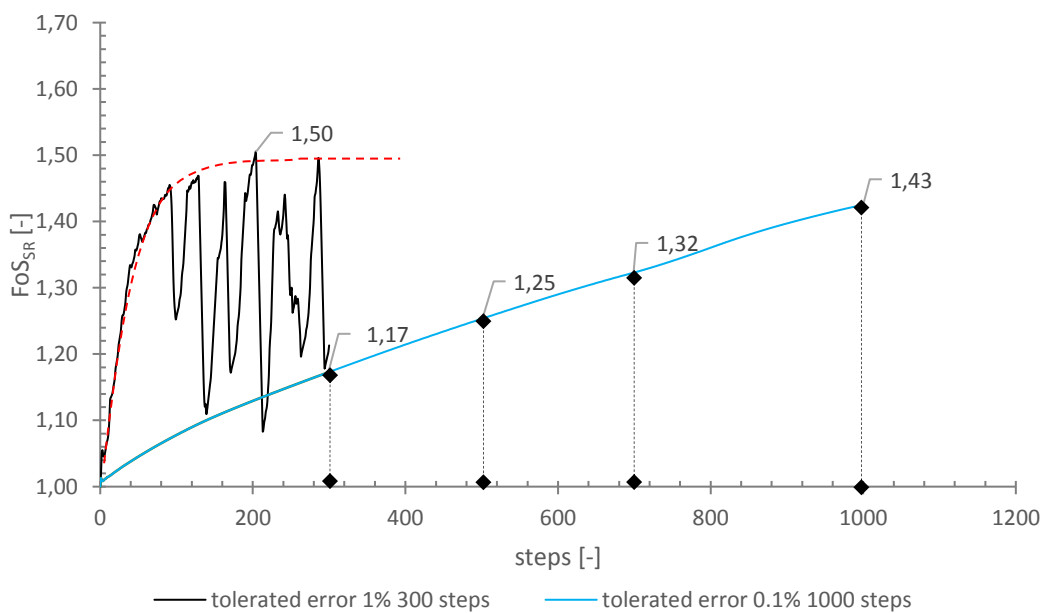
Fig. 89   3D Plaxis MC model SRFEA 10-nod. at FoS$_{SR}$ 1.5 for a. φ'=ψ'=35°
            influence of tolerated error 1% vs. 0.1%

Further calculations according to the FoS$_{SR}$ 2.0 in terms of associated plasticity are done and shown in the Appendix.

Fig.90 and 91 represent the total displacement for 1m and 4m thickness of the model, considering non-associated plasticity.
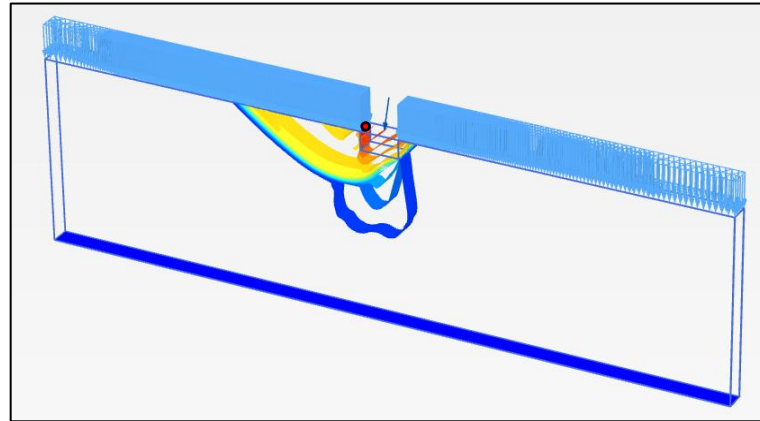
> max. |u| at the left upper middle edge of the strip foundation

Fig. 90   3D Plaxis MC model SRFEA 10-nod. 1m thickness for n.a. ψ'=0°
           sliding surface at failure for strength reduction analysis
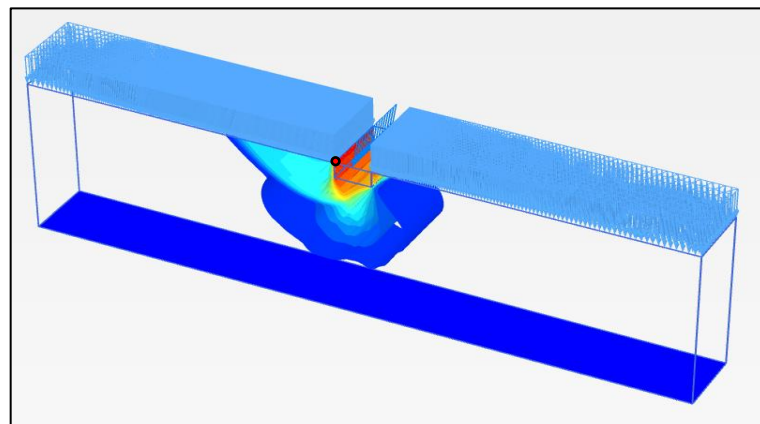
> max. |u| at the left upper front corner of the strip foundation

Fig. 91   3D Plaxis MC model SRFEA 10-nod. 4m thickness for n.a. ψ'=0°
           sliding surface at failure for strength reduction analysis

Fig.92 shows the 3D strength reduction analysis relating to the 2D failure load using a non-associated flow rule. It is seen that for 3D calculations the peak FoS_{SR} results in slightly higher values compared to 2D calculations. Furthermore, the FoS_{SR} 1.0 induces more oscillation in the resulting graph. Therefore, a manual smoothed curve (red dashed line) was plotted, which approximate towards the peak values. Nevertheless, peak values of the 3D SRFEA are in reasonable agreement with 2D SRFEA results (Δ0.08-0.12), whereas both correspond to the 2D failure load.
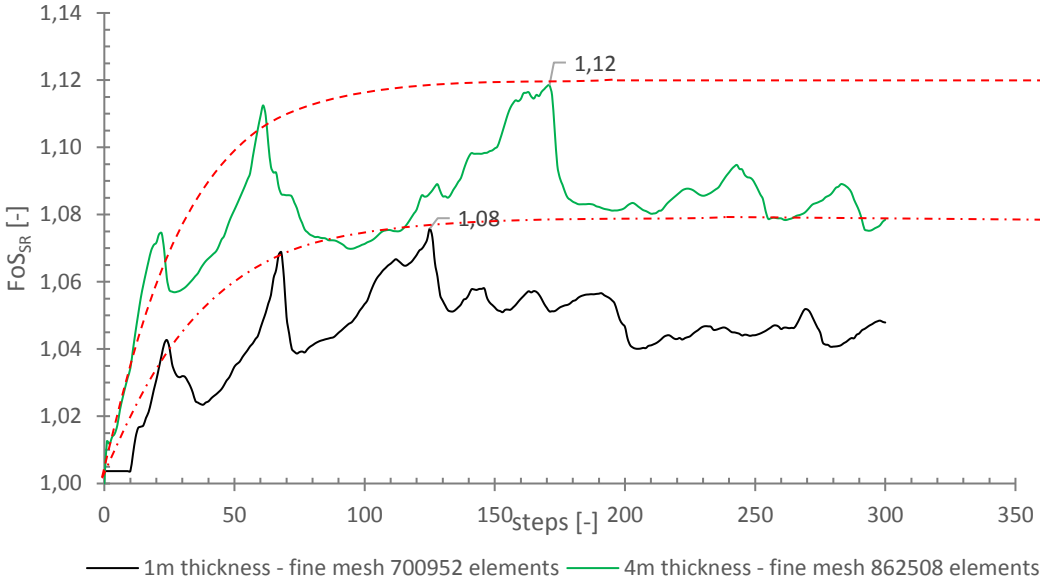
Fig. 92   3D Plaxis MC model SRFEA 10-nod. at failure for n.a. $\psi'=0°$

Fig.93 shows the 3D strength reduction analysis relating to the 2D load at FoS_{SR} 1.5 in terms of non-associated plasticity. It demonstrates higher values comparing 3D to 2D strength reduction analysis. Nevertheless, 3D analysis fits very well (Δ0.02-0.05) with 2D analysis at FoS_{SR} 1.5.
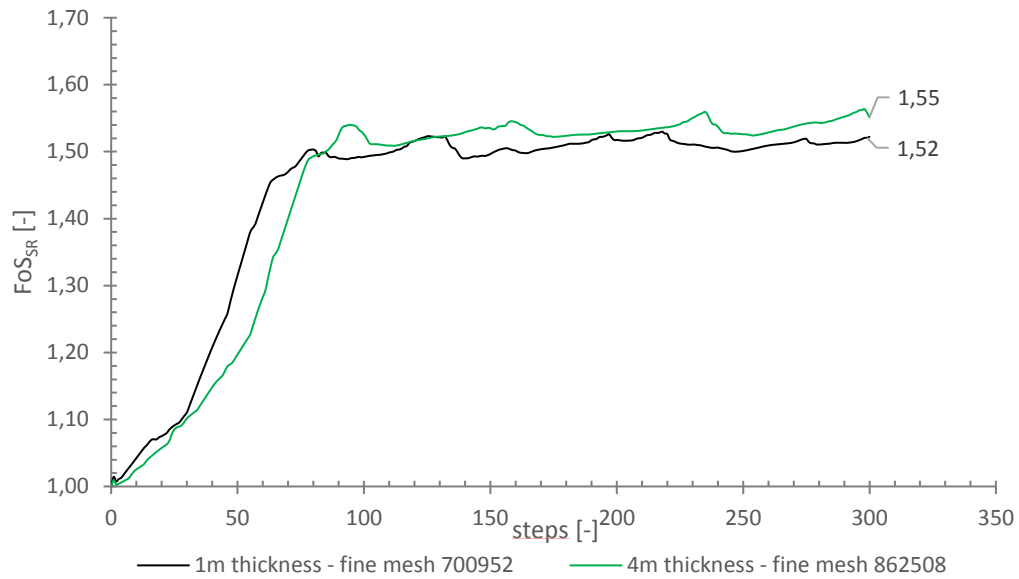
Fig. 93   3D Plaxis MC model SRFEA 10-nod. at FoS 1.5 for n.a. $\psi'=0°$

Further calculations according to the FoS_{SR} 2.0 in term of non-associated plasticity after Davis A are shown in the Appendix. Also listed are calculation made for non-associated plasticity in regards to the dilatancy angle of $11.7°(\varphi'/3)$. Notably those calculations equal the same conclusion as for $\psi'=0°$.

4.2.4.2 OPTUM

The comparison of two-dimensional systems versus three-dimensional systems done for Optum G3 for a FELA and SRFELA (LB, UB) MC model. The calculations are done for the failure load analysis (FELA) as well as the strength reduction analysis (SRFELA) at failure for FoS 1.0, in terms of associated ($\varphi'= \psi'$), as well as non-associated plasticity after Davis A ($\psi'=0°$, 11.7°). For the applied load for the failure load analysis at collapse (FoS_{FL} 1.0), no more strength reduction should occur. This means calculating the three-dimensional, as well as two-dimensional failure load analysis, and applying both loads for calculating the three-dimensional FoS_{SR} for the strength reduction analysis. To study the influence of the thickness of the soil body, 1m and 4m thick models were considered. Tab.54 and 55 show the resulting failure load analysis in terms of three-dimensional and two-dimensional space. It is seen that the resulting three-dimensional load is nearly twice the two-dimensional load at failure. The reason of the large discrepancy between 2D and 3D is part of ongoing research.

Tab. 54   Optum 3D MC model FELA for a. and n.a. Davis A

Optum 3D MC model – FELA failure load [kN/m]				
flow rule	LB 1m	LB 4m	UB 1m	UB 4m
$\varphi'= \psi'= 35°$	5130	4341	5500	4999
$\varphi^*= \psi'= 32.44°$	3808	3262	4069	3682
$\varphi^*= \psi'= 29.84°$	2856	2485	3031	2735

Tab. 55   Optum 2D MC model FELA a. and n.a. Davis A

Optum 2D MC model – FELA failure load [kN/m]		
flow rule	LB	UB
$\varphi'= \psi'= 35°$	2690	2864
$\varphi^*= \psi'= 32.44°$	1932	2036
$\varphi^*= \psi'= 29.84°$	1396	1464

Tab.56 shows the results of the 3D manual strength reduction according to the 3D failure load. It is seen that the system remains stable until the strength parameter is reduced by ~1°, thus nearly no more strength reduction occurs, hence collapse takes place at a almost unchanged strength parameter. Tab.57 shows the results of the 3D manual strength reduction according to the 2D failure load. It is seen that the system remains stable until the strength parameter is reduced by ~7°, relating to the lower loads compared to 3D failure load.

Tab. 56   3D manual SRFELA at 3D failure load for Optum MC model
           a. and n.a. Davis A

Optum MC model – manual SRFELA FoS → 3D loading at failure				
flow rule	LB 1m	LB 4m	UB 1m	UB 4m
φ'= ψ'= 35°	stable			
φ*= ψ'= 32.44°				
φ*= ψ'= 29.84°				
failure at φ'=34°, φ*=31.5°, φ*=29°				

Fig. 94   3D sliding surface at failure for manual SRFELA
           for 3D failure load a. φ'$_{red}$= ψ'= 34° Optum MC model
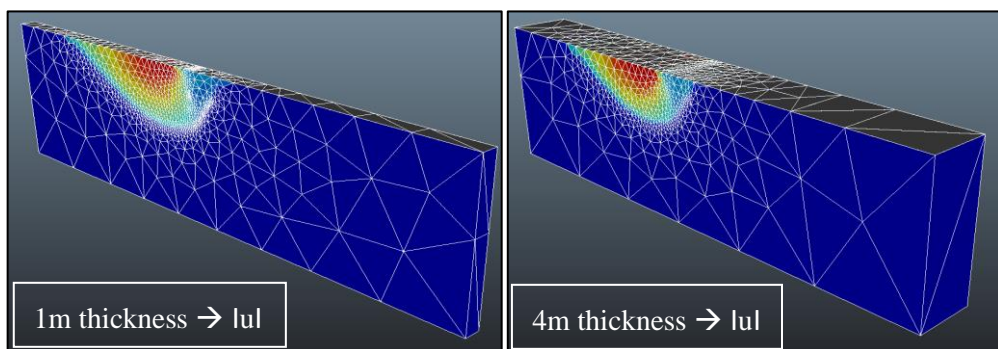
Fig. 95   3D sliding surface at failure for manual SRFELA
           for 3D failure load n.a. Davis A φ*$_{red}$= ψ'= 29° Optum MC model
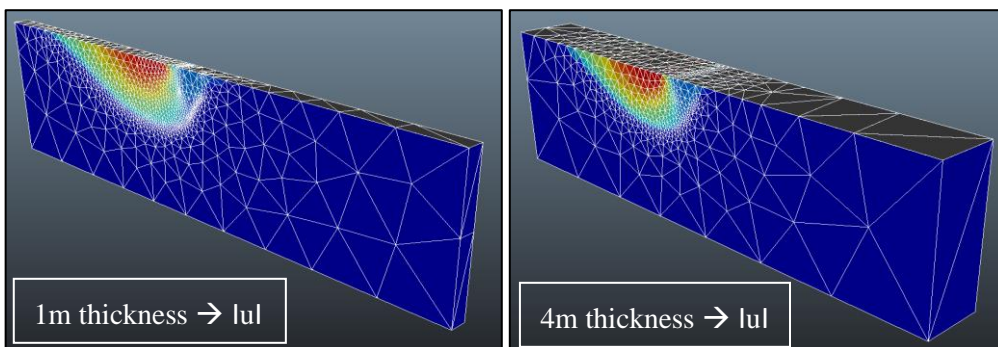
Fig. 96   3D sliding surface at failure for manual SRFELA
           for 3D failure load n.a. Davis A φ*$_{red}$= ψ'= 25.5° Optum MC model

Tab. 57   3D manual SRFELA at 2D failure load for Optum MC model
a. and n.a. Davis A

Optum MC model – manual SRFELA → 2D loading at failure				
flow rule	LB 1m	LB 4m	UB 1m	UB 4m
φ'= ψ'= 35°	stable			
φ*= ψ'= 32.44°				
φ*= ψ'= 29.84°				
failure at φ'=28°, φ=25.5°, φ*=22.5°*				

1m thickness → |u| 4m thickness → |u|

Fig. 97   3D sliding surface at failure for manual SRFELA
for 2D failure load a. $φ'_{red}= ψ'= 28°$ Optum MC model
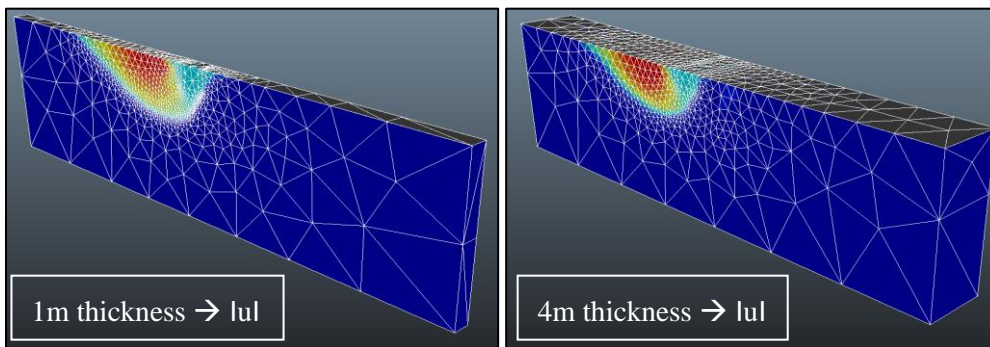
1m thickness → |u| 4m thickness → |u|

Fig. 98   3D sliding surface at failure for manual SRFELA
for 2D failure load n.a. Davis A $φ*_{red}= ψ'= 22.5°$ Optum MC model

1m thickness → |u| 4m thickness → |u|
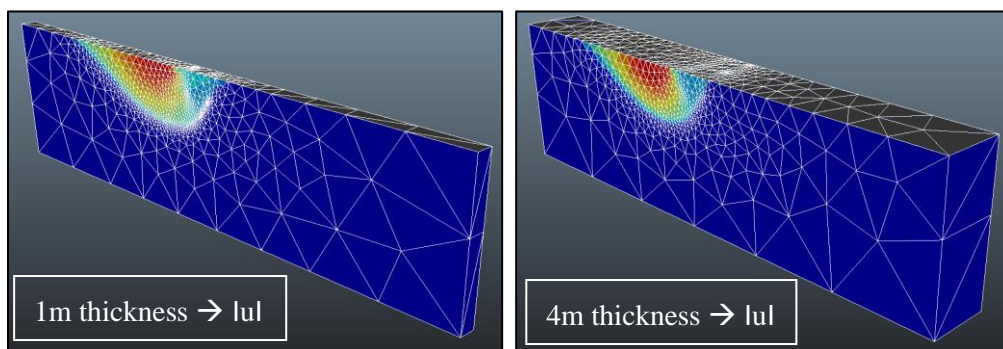
Fig. 99   3D sliding surface at failure for manual SRFELA
for 2D failure load n.a. Davis A $φ*_{red}= ψ'= 25.5°$ Optum MC model

5 Conclusion

The results presented in this thesis confirm that conventional analytical methods documented in standard regulations (DIN 4017, EC 7 and ÖNORM B 4435) are limited to certain conditions (e.g. associated plasticity) and can be classified as conservative. This can be attributed to the fact that analytical solutions ignore dilatancy effects and presume fully mobilized friction angles. This fact represents the main difference compared to numerical methods; furthermore, only failure load analyses can be considered. For the investigated coarse-grained soils the differences in failure load between analytical and numerical methods are in a range of ~300kN/m up to 1100kN/m. Notably, the lower the friction angle (e.g. non-associated plasticity Approach after Davis A) is, the less differences become, according to the standard regulations (e.g.: DIN4017, EC7, ÖNORM B4435) versus FEA.

Comparing the numerical failure load analysis (FEA) of both programs it is shown for associated plasticity and non-associated plasticity, as well as for non-associated plasticity after Davis A, that the failure load obtained with Plaxis is generally higher compared to Optum. Furthermore, it is shown that the original Davis Approach A leads to conservative results regarding the failure load for both safety analyses (failure load, strength reduction) compared to non-associated plasticity, whereas the enhanced Davis Approach B and C are in good agreement. Regardless of the calculation type (analytical and numerical) and the safety analysis type (failure load vs. strength reduction approach), non-associated plasticity as well as non-associated plasticity after Davis Approach A give lower FoS-values compared to associated plasticity calculations. In accordance with previous studies, the consequence of non-associated plasticity is the oscillation of the load-displacement curve, which can be attributed to switching between different modes of failure. This phenomenon as well explains the peaks in the load-displacement curve.

Another aim of this thesis is to compare the two safety analyses when it comes to bearing capacity problems; namely, failure load analysis and strength reduction analysis, which consider different definitions of the FoS. Comparing the FoS 1.0 to 3.0 for each analysis represents a difference in actual loading in a range of 0% corresponding to the FoS 1.0 up to ~79% corresponding to the FoS 3.0 for associated plasticity (~70% Davis A, 66% non-associated). Thus, higher FoS values lead to higher differences. It should be mentioned, that for the applied load at failure (FoS 1.0), no more strength reduction is required, since collapse takes place. Comparing the resulting strength reduction FoS_{SR}, the differences are in a range of 0% corresponding to the loading at collapse up to ~53%, corresponding to the actual load that is necessary to reach the FoS 3.0 for both analyses for associated plasticity (~50% Davis A, 45% non-associated). Thus, the smaller the difference in the applied loading the smaller the difference in the resulting FoS_{SR} relating to strength reduction analysis.

The results presented in this thesis confirm that the FoS for both constitutive models MC (Plaxis, Optum) and HS (Plaxis) / HMC (Optum), as well as FEA, SRFEA (Plaxis, Optum) and FELA, SRFELA (Optum), are the same. There is hardly any difference in the applying load for FoS_{SR}-values ranging from 3.0 to 1.0 as well as in the applying failure load required to obtain FoS_{FL}-values from 3.0 to 1.0.

In this thesis, the calculations for the stress paths and π-plane were done for the failure load analysis by gradually increasing the load to corresponding FoS_{FL}-values (i.e. 3.0, 2.0, 1.5 and 1.0 at failure). Stress points become plastic as soon as they coincide with the MC failure criterion at collapse. It is shown that each of the stress points A to F, which are located at characteristic position of the failure body, develops in direction of triaxial compression. Furthermore, the lode angle θ remains nearly constant at -22° for associated plasticity (-24° Davis A, -22° non-associated).

To study the influence of numerical control parameters on the automatic strength reduction for displacement based finite element, SRFEA has been performed with altered values of tolerated error (0.1%, 1% default setting, 3%, 5%). Performing automatic SRFEA with a tolerated error of 3% and 5% compared to the default setting of 1%, results in more oscillation and therefore higher peaks of the FoS_{SR}. Thus, in case of associated plasticity and non-associated plasticity after Davis, the higher the tolerated error, the more oscillation occurs in the FoS_{SR}. Performing automatic SRFEA with a tolerated error of 0.1% results in less oscillation and therefore lower peaks in the FoS_{SR}, thereby yielding smooth curves. Thus, in case of on associated plasticity and non-associated plasticity after Davis Approach A, the lower the tolerated error (more accurate), the less oscillation (smooth curve) occurs in the FoS_{SR}. Furthermore, it is shown, that the gradient of the first branch is lower compared to tolerated error of 1% up to 5%. Additionally, the horizontal branch (final FoS_{SR}) is yet not reached. However, when more steps are used, the graph converges towards the range of results marked by results obtained with tolerated errors of 1% and 5%.

Generally, associated plasticity results in less oscillation (smooth curve) compared to non-associated plasticity. For lower tolerated error and non-associated plasticity, less oscillation in the amplitude (smooth curve) occurs in the FoS_{SR} as well as for associated plasticity. The reason of the discrepancy between associated and non-associated plasticity according to the oscillation behavior at higher tolerated errors (3%, 5%) is part of ongoing research. However, there has hardly any differences been observed in the factor of safety at failure, only the graph changes (higher amplitudes of oscillation).

The results presented in this thesis confirm that under drained conditions (i.e. no excess pore water pressure) the solution is independent of the initial stresses (K_0-procedure) and therefore the K_0 has no influence.

Using Plaxis SRFEA and associated plasticity, it is seen that for 3D calculations the FoS_{SR} results in slightly higher values compared to 2D calculations. For $FoS_{SR} = 1.5$, it is shown that 3D-FoS_{SR}-peak-values are almost identical to 2D results. Performing automatic SRFEA with a tolerated error of 0.1% results in a smooth curve that converges towards the desired FoS_{SR} of 1.5. In simple terms, 3D strength reduction FoS_{SR}-peak-values are in good agreement with 2D strength reduction analysis, both corresponding to the 2D loading at $FoS_{SR} = 1.5$. In case of non-associated plasticity, the FoS_{SR} at failure results in more oscillation compared to associated plasticity, whereas for the FoS_{SR} 1.5 the curve is smoother compared to associated plasticity. Nevertheless, 3D strength reduction analysis fits very well with 2D strength reduction analysis. In case of Optum FELA associated and non-associated after Davis A plasticity, it is seen that the resulting three-dimensional load is nearly twice the two-dimensional load at failure. Under the 3D failure load, it is seen that the 3D system remains stable until the strength parameter φ' is reduced by ~1° (c'=0kPA). Whereas under the 2D failure load the 3D system remains stable until the strength parameter φ' is reduced by ~7° (c'=0kPA), relating to the lower failure loads compared to 3D. The reason of the large discrepancy between 2D and 3D is part of ongoing research.

6 List of Tables

7 List of Figures

8 References

8.1 Constitutive Models

[1] Lade, P.V. (2005), "Overview of Constitutive Models for Soils," ASCE Geotechnical Special Publication No:128, Soil Constitutive Models: Evaluation, Selection, and Calibration, Edited by J.A. Yamamuro and V.N. Kaliakin, pp. 1-34

[2] Veigl, I. (2020), "Numerical studies on slope stability analysis for drained and undrained material behaviour", Master´s thesis, Institute of Soil Mechanics, Foundation Engineering and Computational Geotechnics, Graz University of

8.2 Mohr Coulomb

[3] Optum G2 Materials Manual (2016), K Krabbenhoft, AV Lymain, J Krabbenhoft (Editors), pp. 28-41

[4] Plaxis 2D Material Models Manual (2018), pp. 33-44

- Brinkgreve R.B.J., Kumarswamy S., Swolfs W.M., Plaxis 3D 2018-User Manual, Delft, The Netherlands: Plaxis bv; 2018
- Hill, R. (1950), "The Mathematical Theory of Plasticity", Oxford University Press, London, U.K.
- Smith, I.M., Griffiths, D.V. (1982), "Programming the Finite Element Method" John Wiley&Sons, Chisester, U.K., second edition

[5] Sallinger M. (2017), "Slope stability analysis by means of strength reduction technique", Master's thesis, Institute of Soil Mechanics, Foundation Engineering and Computational Geotechnics, Graz University of Technology

- Brinkgreve R.B.J., Kumarswamy S. and S. W. M., Plaxis 2D 2016 – Material Models Manual, Delft, Netherlands: Plaxis bv., 2016.
- Potts D.M. and Z. L. (1999), "Finite element analysis in geotechnical engineering: theory", London: Thomas Telford
- Schofield A.N. and Wroth P. (1968), "Critical State Soil Mechanics", McGraw-Hill
- Wehnert, M. (2006), „Ein Beitrag zur drainierten und undrainierten Analyse in der Geotechnik", Habilitation, Mitteilung 53 des Instituts für Geotechnik, Universität Stuttgart

8.3 Hardening Soil Model

[6] Plaxis 2D Material Models Manual 2018, pp. 39-83

- Duncan, J.M.; Chang, C.-Y. (1970), "Nonlinear analysis of stress and strain in soil", ASCE J. of the Soil Mech. and Found. Div., 96
- Janbu, N. (1963), "Soil compressibility as determinded by oedometer and triaxial tests", Proc. ECSMFE Wiesbaden, 1, 19-25
- Kondner, R.L. (1963), "A hyperbolic stress strain formulation for sands", 2. Pan. Am. ICOSFE Brazil, 1, 289-394
- Rowe, P.W. (1962), "The stress-dilatancy relation for static equilibrium of an assembly of particles in contact", In Proc. Roy. Soc. A., No. 269., 500-527
- Schanz, T. (1998), "Zur Modellierung des mechanischen Verhaltens von Reibungsmaterialien", Habilitation, Universität Stuttgart
- Schanz, T., Vermeer, P.A. (1996), „Angles of friction and dilatancy of sand"
- Schanz, T., Vermeer, P.A., Bonnier, P.G. (1999), "The hardening-soil model", Formulation and verification. In R.B.J. Brinkregeve, Beyond 2000 in Computational Geotechnics, Balkema, Rotterdam, 281-290
- Von Soos, P. (1990), "Properties of soil and rock (in german)", Grindbautaschenbuch Part 4. Ernst&Sohn, Berlin

[7] Wehnert, M. (2006), „Ein Beitrag zur drainierten und undrainierten Analyse in der Geotechnik", Habilitation, Mitteilung 53 des Instituts für Geotechnik, Universität Stuttgart

- Duncan, J.M.; Chang, C.-Y., (1970), "Nonlinear analysis of stress and strain in soils", Journal of the Soil Mechanics and Foundations Division 96 No.SM5, S. 1629-1653
- Kondner, R.L.; Zelasko, J.S (1963), "A hyperbolic stress strain formulation for sands", Proceedings 2nd Pan. Am. Int. Conference on Soil Mechanics and Foundation Engineering Bd. 1. Brazil, 1963, S. 289-394
- Rowe, P.W. (1962), "The stress-dilatancy relation for static equilibrium of an assembly of particles in contact", Proceedings of the Royal Society of London Series A, Mathematical and Physical Sciences Bd. 269, S.500-527
- Schanz, T. (1998), „Zur Modellierung des mechanischen Verhaltens von Reibungsmaterialien", Universität Stuttgart, Habilitation, Mitteilung des Instituts für Geotechnik, Heft 45
- Schanz, T.: Vermeer, P.A.; Bonnier, P.G. (1999), "The hardening soil model- formulation and verification", Brinkgreve (Hrsg.): Beyond 2000 in Computational Geotechnics, A.A: Balkema, S.281-296

- Vermeer, P.A. (1978), "A double hardening model for sand", Geotechnique 28 No.4, S.413-433
- Vermeer, P.A. (1978), "Formulation and analysis of sand deformation problems", Delft University of Science and Technology, PhD Thesis, 198

8.4 Hardening Mohr Coulomb

[8] Optum G2 Materials Manual (2016), K Krabbenhoft, AV Lymain, J Krabbenhoft (Editors), pp. 94-105

8.5 FEA

[9] Oberhollenzer, S. (2017), "Numerical studies on slope stability analysis", Master´s thesis, Institute of Soil Mechanics, Foundation Engineering and Computational Geotechnics, Graz University of Technology

- Brinkgreve, R.B.J.; Kumarswamy, S.; Swolfs. W.M. (2016), PLAXIS 2D 2016 - User Manual. Delft, The Netherlands: Plaxis bv.

[10]   Plaxis 2D Reference Manual (2018), pp. 22

8.6 FELA

[11] Oberhollenzer, S. (2017), "Numerical studies on slope stability analysis", Master´s thesis, Institute of Soil Mechanics, Foundation Engineering and Computational Geotechnics, Graz University of Technology

- Chen, W.F. (2007), "Limit Analysis and Soil Plasticity", pp. 1-122, J.Ross publishing
- Lyamin, A. V. & Sloan, S. W. (2002a), "Lower bound limit analysis using nonlinear programming", Int. J. Numer. Methods Engng 55, No. 5, 573–611
- Lyamin, A. V. & Sloan, S. W. (2002b), "Upper bound limit analysis using linear finite elements and nonlinear programming", Int. J. Numer. Analyt. Methods Geomech. 26, No. 2, 181–216.
- Lyamin, A. V., Krabbenhøft, K., Abbo, A. J. & Sloan, S. W. (2005a), "General approach for modelling discontinuities in limit analysis", Proc. 11th Int. Conf. Int. Assoc. Computer Methods Adv. Geomech., Torino 1, 95–102

- Sloan, S. W. (2013), 51st Rankine lecture, "geotechnical stability analysis", Géotechnique 63, No. 7, 531- 572

8.7 Davis Approach

[12]   Oberhollenzer, S. (2017), "Numerical studies on slope stability analysis", Master´s thesis, Institute of Soil Mechanics, Foundation Engineering and Computational Geotechnics, Graz University of Technology

- Tschuchnigg, F.; Schweiger, H.F.; Sloan, S.W. (2015a), "Slope stability analysis by menas of finite element limit analysis and finite element strength reduction techniques", Part I: Numerical studies considering non-associated plasticity, Computers and Geotechnics 70, 169-177

8.8 Flow Rule

[13]   Egger, D. (2012), "Untersuchungen zur Böschungsstabilität mittels FE-Methode", Master´s thesis, Institute of Soil Mechanics, Foundation Engineering and Computational Geotechnics, Graz University of Technology

[14]   Knitter, D. (2018), "Finite Element Analysis of Footings", Master's thesis, Institute of Soil Mechanics, Foundation Engineering and Computational Geotechnics, Graz University of Technology

- Schweiger H. F. (2017), Computational Geotechnics: Lecture notes. Institute of Soil Mechanics, Foundation Engineering and Computational Geotechnics, Graz University of Technology

[15]   Oberhollenzer, S. (2017), "Numerical studies on slope stability analysis", Master´s thesis, Institute of Soil Mechanics, Foundation Engineering and Computational Geotechnics, Graz University of Technology

- Nordal, S. (2014), Advanced Course geotechnical Engineering: Lecture notes and background material, Institutt for bygg, anlegg og transport, Norwegian University of Science and Technology

[16]   Optum G2 Theory Model Manual (2016), K Krabbenhoft, AV Lymain, J Krabbenhoft (Editors), pp. 41-57

- Carter, J. P., Poon, M. S. B., and Airey, D. W. (2005), "Numerical and semi-analytical techniques for footings subjected to combined loading", Proc. IACMAG 11, Turin, pages 163–176

- Clausen, J. and Krabbenhoft, K. (2008), "Existence and uniqueness of solutions in non-associated Mohr-Coulomb elasto-plasticity", Proc. WCCM VIII, Venice
- Erickson, H. L. and Drescher, A. (2002), „Bearing capacity of circular footings", Journal of Geotechnical and Geoenvironmental Engineering, 128:38–43
- Krabbenhoft, K., Karim, M. R., Lyamin, A. V., and Sloan, S. W. (2012), "Associated computational plasticity schemes for non-associated frictional materials", International Journal for Numerical Methods in Engineering, 89:1089–1117
- Loukidis, D. and Salgado, R. (2009), "Bearing capacity of strip and circular footings in sand using finite elements", Computers and Geotechnics, 36:871–879
- Manzari, M. T. and Nour, M. A. (2000), "Significance of soil dilatancy in slope stability analysis", Journal of Geotechnical and Geoenvironnemental Engineering, 126:75–80
- Rice, J. R. (1976), "The localization of plastic deformation", Koiter, W., editor, Theoretical and Applied Mechanics, pp. 239–264. North-Holland

[17] Sallinger M. (2017), "Slope stability analysis by means of strength reduction technique", Master's thesis, Institute of Soil Mechanics, Foundation Engineering and Computational Geotechnics, Graz University of Technology

- De Saint Venant, B. (1870), Journal de mathématiques pures et applicquées
- Hill, R. (1998), "The Mathematical Theory of Plasticity", Clarendon Press
- Schweiger, H. F. (1995), „Ein Beitrag zur Anwendung der Finite-Elemente-Methode in der Geotechnik", Habilitation, Graz University of Technology

8.9 Numerical Method Failure Load

[18] Oberhollenzer, S. (2017), "Numerical studies on slope stability analysis", Master´s thesis, Institute of Soil Mechanics, Foundation Engineering and Computational Geotechnics, Graz University of Technology

- Brinkgreve, R.B.J.; Kumarswamy, S.; Swolfs. W.M. (2016) PLAXIS 2D 2016 - User Manual. Delft, The Netherlands: Plaxis bv.
- Tschuchnigg, F.; Schweiger, H.F.; Sloan, S.W. (2015a), „Slope stability analysis by means of finite element limit analysis and finite element strength reduction techniques", Part 1: Numerical studies considering non-associated plasticity. Computers and Geotechnics 70, 169-177

8.10 Analytical Method Strength Reduction

[19] DIN 4017

[20] EN 1997-1 (EC 7)

[21] ÖNORM B-4435-2

8.11 Used Software

[22] Plaxis 2D References Manual (2018) (numerical control parameter, deformation control parameter, general settings)

[23] Van der Sloot, M. (2020), "Iterative settings Influence of Arc length control", https://communities.bentley.com/products/geotech-analysis/w/plaxis-soilvision-wiki/45924/iterative-settings-influence-of-arc-length-control

[24] Optum G2 Analysis Manual (2016), K Krabbenhoft, AV Lymain, J Krabbenhoft (Editors) (Limit Analysis, Multiplier Elastoplastic, Strength Reduction, Elastoplastic)

[25] Optum G2 Materials Manual (2016), K Krabbenhoft, AV Lymain, J Krabbenhoft (Editors) (Numerical Settings)

[26] Knitter D. (2018), "Finite element limit analyses of footings", Master's thesis, Institute of Soil Mechanics, Foundation Engineering and Computational Geotechnics, Graz University of Technology

[27] Nowakowski P. (2018), "Numerical analyses of bearing capacity equations", Master's thesis, Institute of Soil Mechanics, Foundation Engineering and Computational Geotechnics, Graz University of Technology

9 Appendix

9.1 A – Analytical Method 2D Failure Load
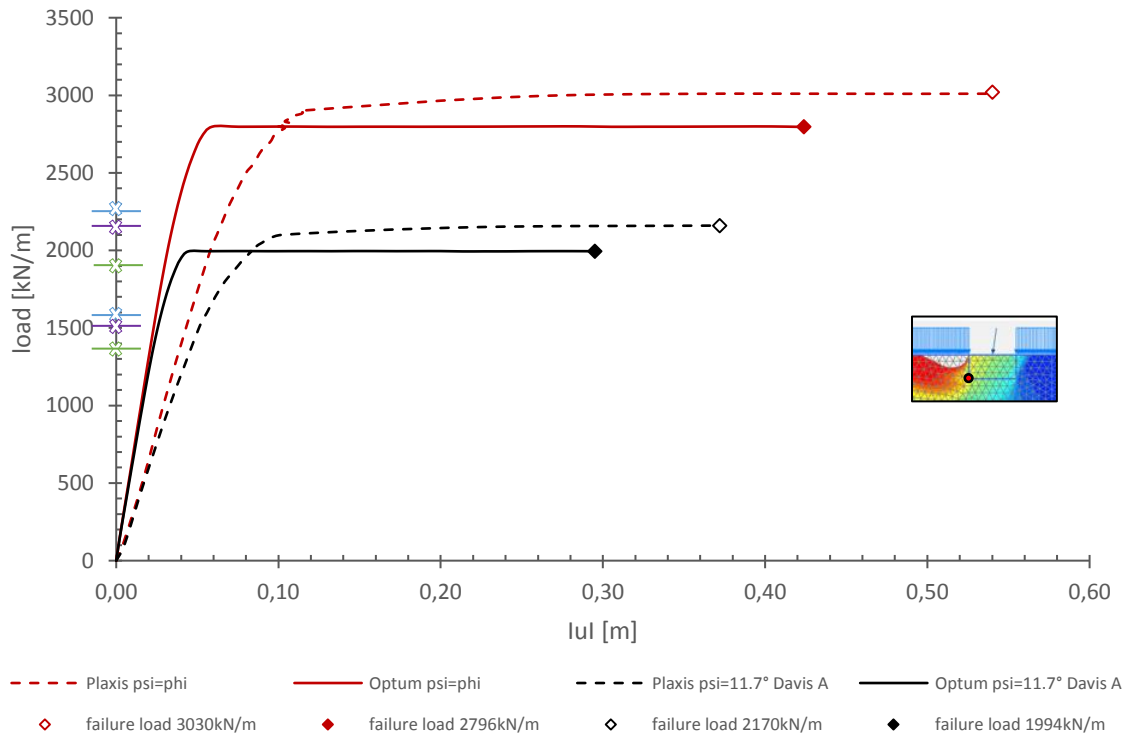
Fig. 100   Load-displacement curve analytical vs. numerical method (FEA 15-nod.)
for a. φ'=ψ'=35° and n.a. Davis A φ*=ψ'=32.44°

Tab. 58   Analytical method failure load

failure load [kN/m]				
		φ'=35°	φ*=32.44° (Davis A ψ'=11.7°)	
analytic —✕—	DIN 4017 (consideration depth coeffcient) (consideration dead load foundation)	1895.46	1344.11	
	EC 7	2244.75	1573.73	
	ÖNORM B 4435	2152.74	1515.84	
numeric	Plaxis FEA 15-nod.	3030.00	2170.00	
	Optum FEA 15-nod.	2796.00	1994.00	
→ *failure load ~ Δ425-1100kN/m*				

Tab. 59   Analytical method failure load
            - influence of depth coefficient and foundation base

failure load [kN/m]		
DIN 4017 (consideration dead load foundation)	φ'=35°	φ*=32.44° (Davis A ψ'=11.7°)
1m FB*	1895.46	1344.11
1m FB	1666.65	1164.15
2m FB*	2606.20	1872.85
2m FB	2233.21	1579.48

* with depth coefficient by Brinch Hansen

Tab. 60   Analytical method failure load – influence of the dead load of the foundation

failure load [kN/m]		
DIN 4017	φ'=35°	φ*=32.44° (Davis A ψ'=11.7°)
1m FB*	1895.46	1344.11
1m FB	1121.79	786.94

* with consideration of the dead load of the foundation, as well
as the depth coefficient by Brinch Hansen

9.2 B – Numerical Method
2D Failure Load vs. Strength Reduction
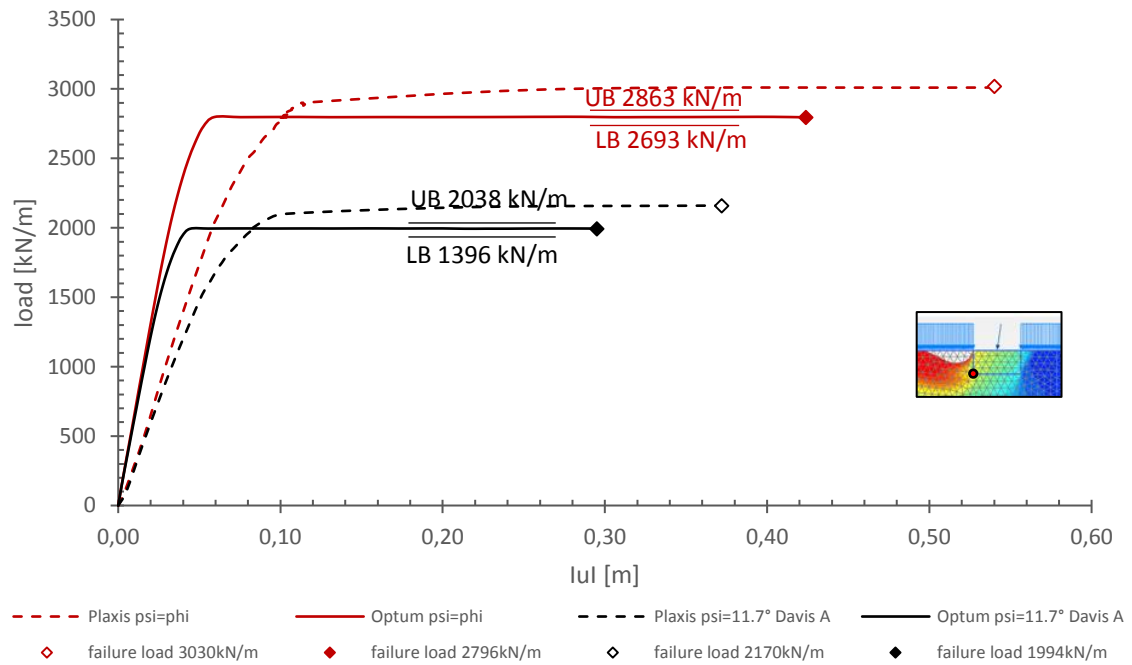
Fig. 101 Load-displacement curve numerical method Plaxis, Optum FEA 15-nod. and Optum FELA for a. φ'=ψ'=35° and n.a. Davis A φ*=ψ'=32.44°
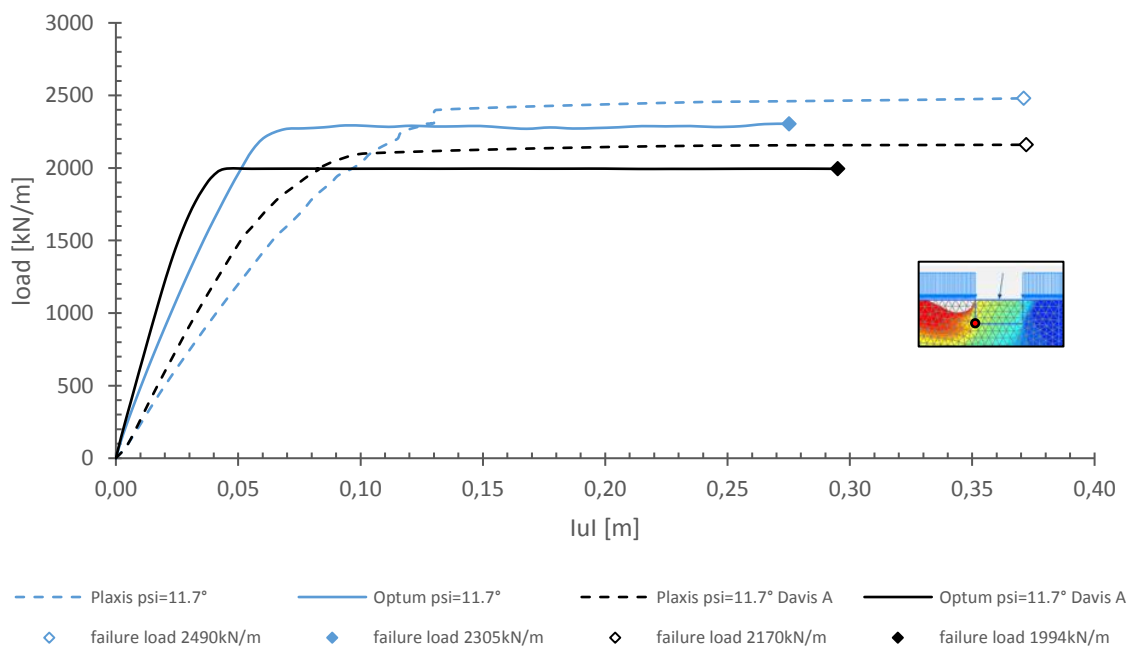
Fig. 102 Load-displacement curve numerical method Plaxis, Optum FEA 15-nod. for n.a. ψ'=11.7° and n.a. Davis A φ*=ψ'=32.44°
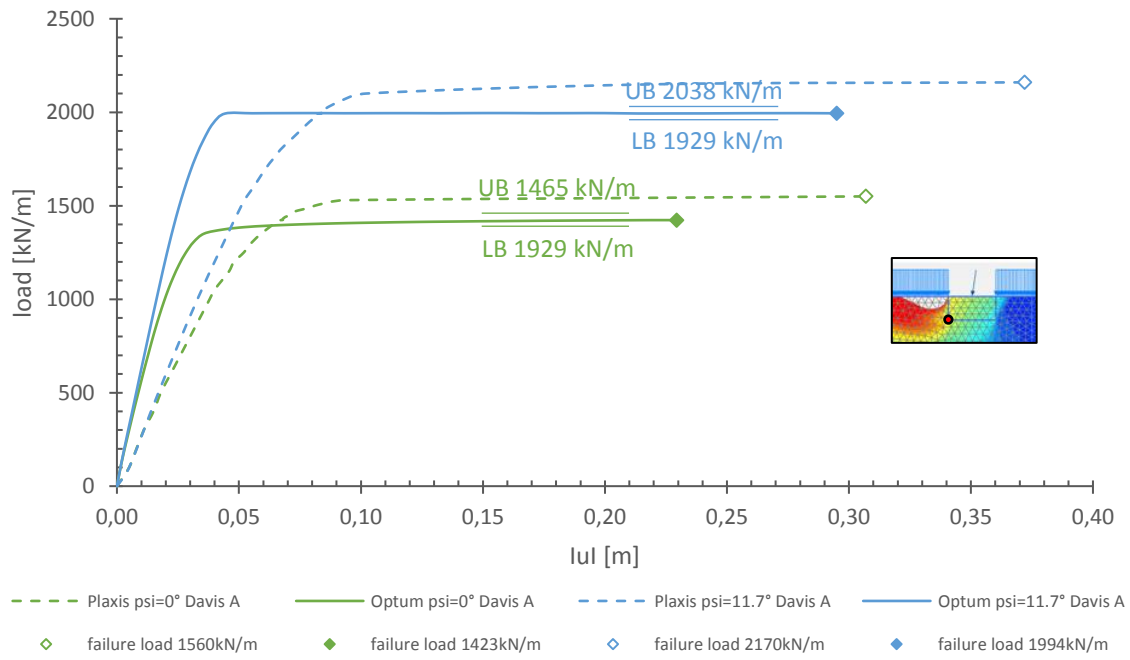
Fig. 103   Load-displacement curve numerical method Plaxis, Optum FEA 15-nod. and Optum FELA for n.a. Davis A $\varphi^*=\psi'=29.84°$ and n.a. Davis A $\varphi^*=\psi'=32.44°$
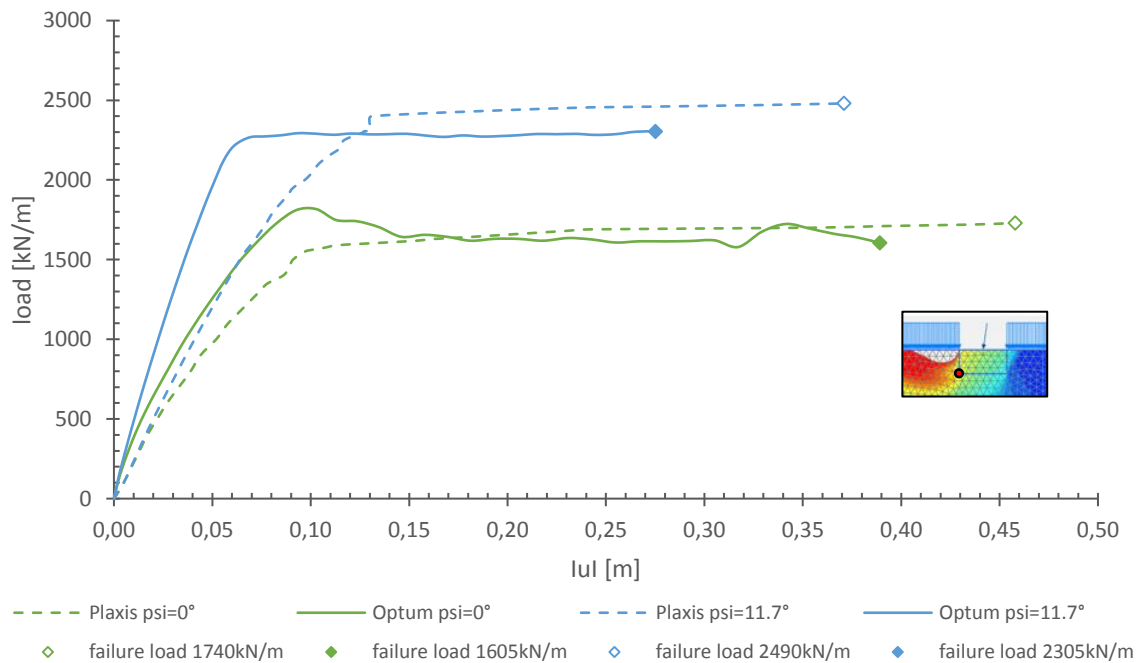
Fig. 104   Load-displacement curve numerical method Plaxis, Optum FEA 15-nod. for n.a. $\psi'=0°$ and n.a. $\psi'=11.7°$
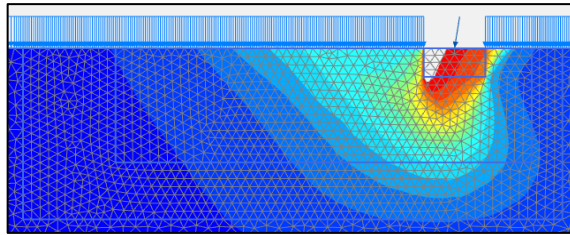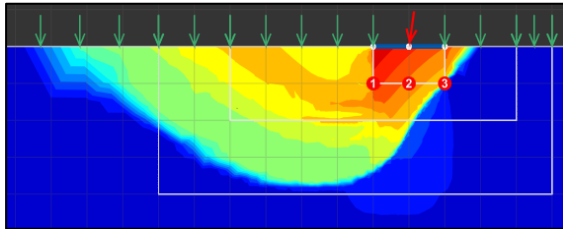
| | PLAXIS 2D HS Model 15-noded FEA |
| | OPTUM HMC Model 15-noded FEA |

Fig. 105   Total displacement for the corresponding failure load n.a. ψ'=11.7°
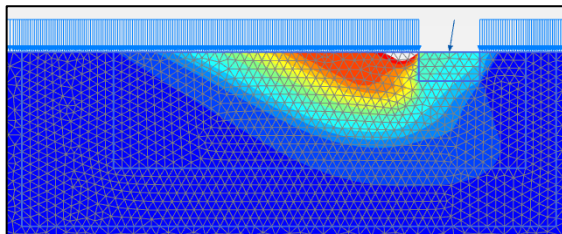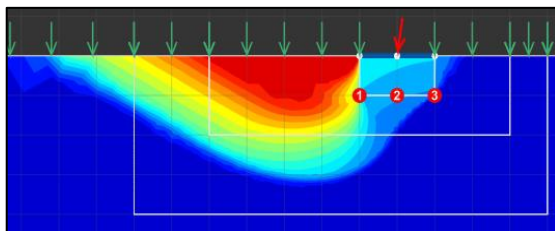
| | PLAXIS 2D HS Model 15-noded FEA |
| | OPTUM HMC Model 15-noded FEA FELA LB, UB |

Fig. 106   Total displacement for the corresponding failure load
                    n.a. Davis A φ*= ψ'= 32.44°
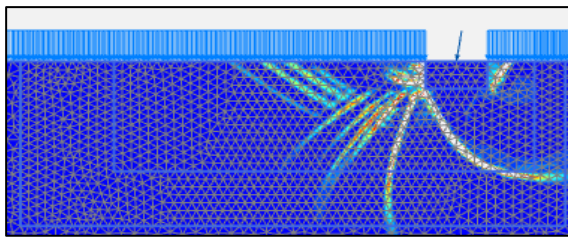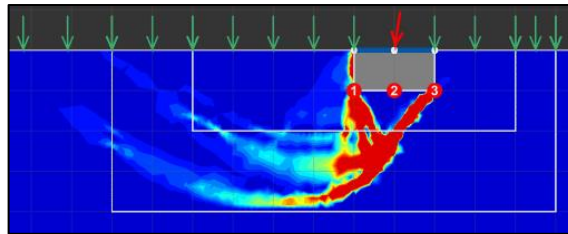
Fig. 107   Shear strains for the corresponding failure load n.a. ψ'=11.7°
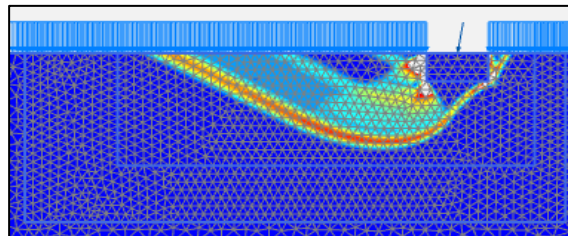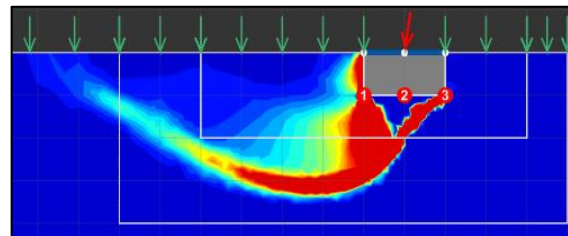
Fig. 108   Shear strains for the corresponding failure load n.a. Davis A φ*=ψ'=32.44°
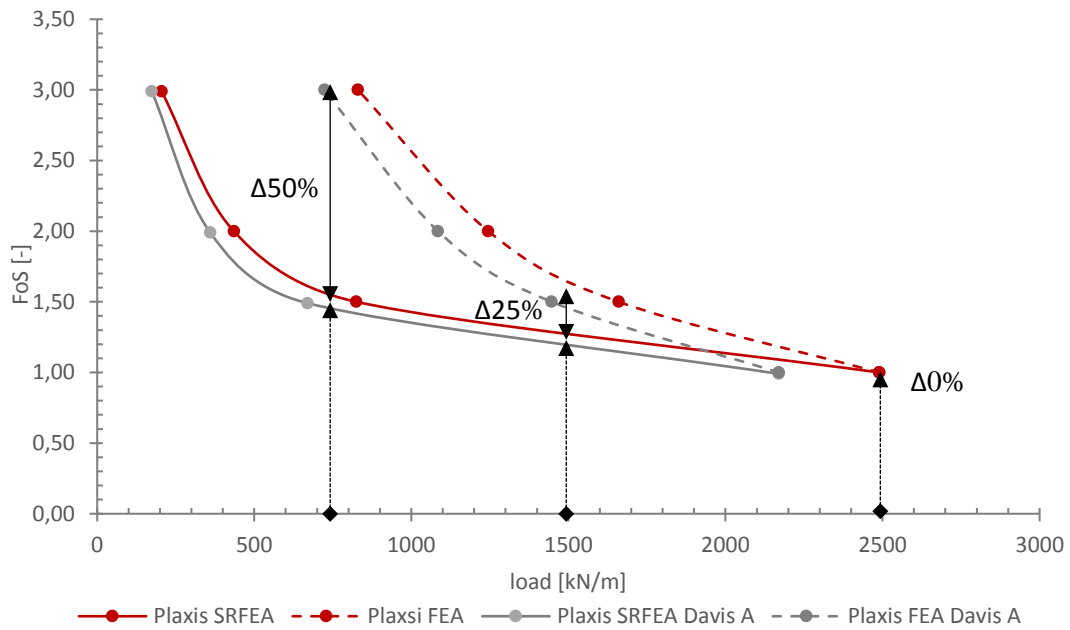
Fig. 109   FEA 15-nod. vs. SRFEA 15-nod. (Plaxis HS model)
for n.a. ψ'=11.7° and n.a. Davis A φ*=ψ'=32.44°

Tab. 61   FEA 15-nod. vs. SRFEA 15-nod. (Plaxis HS model)
for n.a. ψ'=11.7° and n.a. Davis A φ*=ψ'=32.44°

	Plaxis HS model - ψ'=11.7°		Plaxis HS model - φ*=ψ'=32.44°	
	FEA	SRFEA	FEA	SRFEA
FoS	failure load [kN/m]	SR load [kN/m]	failure load [kN/m]	SR load [kN/m]
3.0	830	205	723.33	174
2.0	1245	435	1085	360
1.5	1660	825	1446.67	670
1.0	2490	2490	2170	2170

Tab. 62   SRFEA 15-nod. for n.a. ψ'=11.7° (Plaxis HS model)
           applying failure load vs. applying actual load for FoS 1.0-3.0

SRFEA 15-noded - ψ'=11.7°					
Plaxis – HS model					
failure load [kN/m]	→	FoS_{SR}	SR load [kN/m]	→	FoS_{SR}
830	→	1.49	205	→	2.99
1245	→	1.27	435	→	2.00
1660	→	1.14	825	→	1.50
2490	→	1.00	2490	→	1.00

Tab. 63   SRFEA 15-nod. for n.a. Davis A φ*= ψ'=32.44° (Plaxis HS model)
           applying failure load vs. applying actual load for FoS 1.0-3.0

SRFEA 15-noded - φ*=ψ'=32.44°					
Plaxis – HS model					
failure load [kN/m]	→	FoS_{SR}	SR load [kN/m]	→	FoS_{SR}
723.33	→	1.51	174	→	2.99
1085	→	1.26	360	→	1.99
1446.67	→	1.14	670	→	1.49
2170	→	0.99	2170	→	0.99
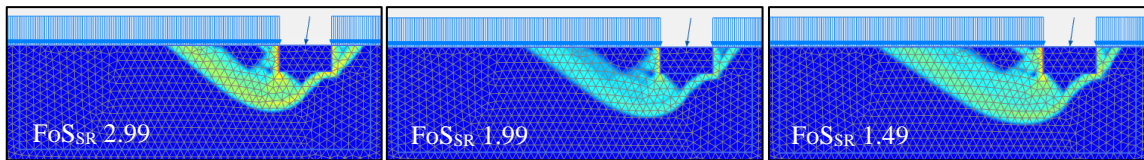
Fig. 110   Plaxis HS model SRFEA 15-noded incremental deviatoric strain
            n.a. Davis A $\varphi^*=\psi'=32.44°$ for the corresponding actual load FoS_{SR} 3.0-1.5
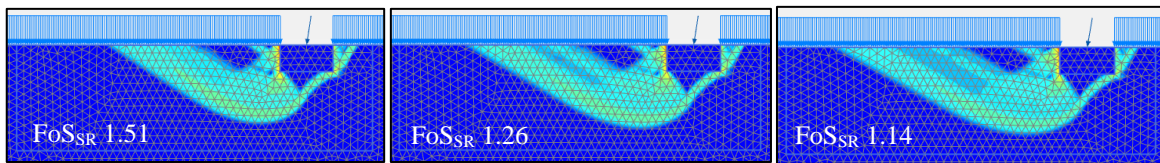
Fig. 111   Plaxis HS model SRFEA 15-noded incremental deviatoric strain
            n.a. Davis A $\varphi^*=\psi'=32.44°$ for the corresponding failure load FoS_{FL} 3.0-1.5
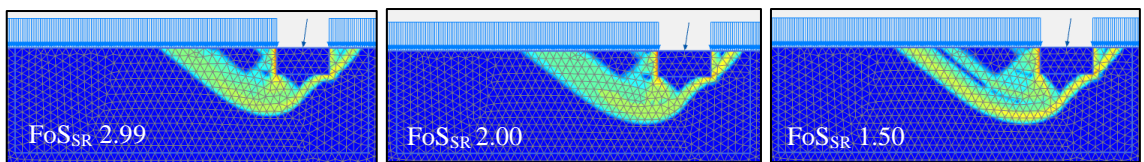
Fig. 112   Plaxis HS model SRFEA 15-noded incremental deviatoric strain
            n.a. $\psi'=11.7°$ for the corresponding actual load FoS_{SR} 3.0-1.5
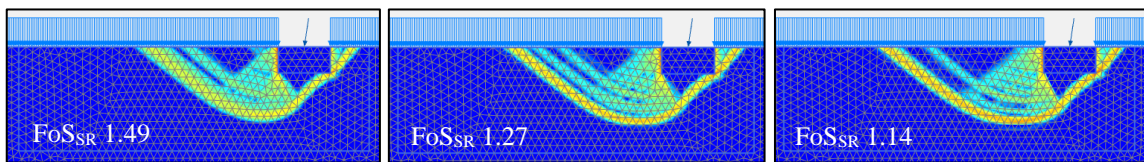
Fig. 113   Plaxis HS model SRFEA 15-noded incremental deviatoric strain
            n.a. $\psi'=11.7°$ for the corresponding failure load FoS_{FL} 3.0-1.5
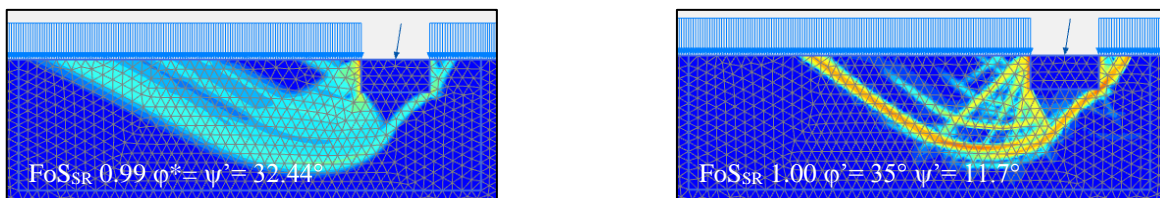
Fig. 114   Sliding surface at collapse
            Plaxis HS model SRFEA 15-noded incremental deviatoric strain
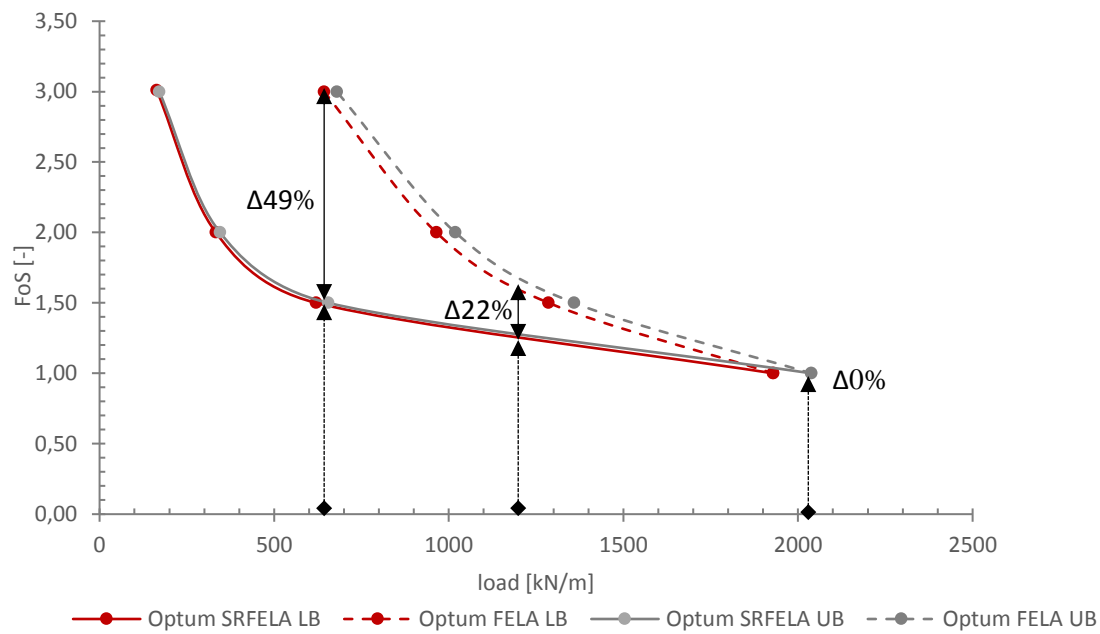
Fig. 115   FELA vs. SRFELA (Optum HMC model LB, UB)
            for n.a. Davis A φ*=ψ'=32.44°

Tab. 64   FELA vs. SRFELA (Optum HMC model LB, UB)
            for n.a. Davis A φ*=ψ'=32.44°

Optum HMC model – φ*=ψ'=32.44°				
	FELA LB	SRFELA LB	FELA UB	SRFELA UB
FoS	failure load [kN/m]	SR load [kN/m]	failure load [kN/m]	SR load [kN/m]
3.0	643	163.50	679.33	171
2.0	964.50	333	1019	345
1.5	1286	620	1358.67	655
1.0	1929	1929	2038	2038

Tab. 65   SRFELA LB for n.a. Davis A φ*=ψ'=32.44° (Optum HMC model)
applying failure load vs. applying actual load for FoS 1.0-3.0

SRFELA LB - φ*=ψ'=32.44°					
Optum – HMC model					
failure load [kN/m]	→	FoS$_{SR}$	SR load [kN/m]	→	FoS$_{SR}$
643	→	1.48	163.50	→	3.01
964.50	→	1.26	333	→	2.00
1286	→	1.14	620	→	1.50
1929	→	1.00	1929	→	1.00

Tab. 66   SRFELA for n.a. Davis A φ*=ψ'=32.44° (Optum HMC model)
applying failure load vs. applying actual load for FoS 1.0-3.0

SRFELA UB - φ*=ψ'=32.44°					
Optum – HMC model					
failure load [kN/m]	→	FoS$_{SR}$	SR load [kN/m]	→	FoS$_{SR}$
679.33	→	1.48	171	→	3.00
1019	→	1.26	345	→	2.00
1358.67	→	1.14	655	→	1.50
2038	→	1.00	2038	→	1.00
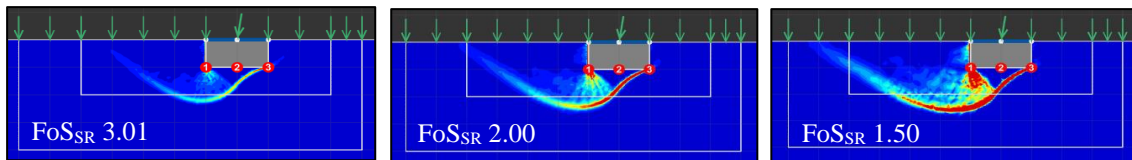
Fig. 116   Optum HMC model SRFELA LB shear dissipation
n.a. Davis A φ*=ψ'= 32.44° for the corresponding actual load FoS$_{SR}$ 3.0-1.5
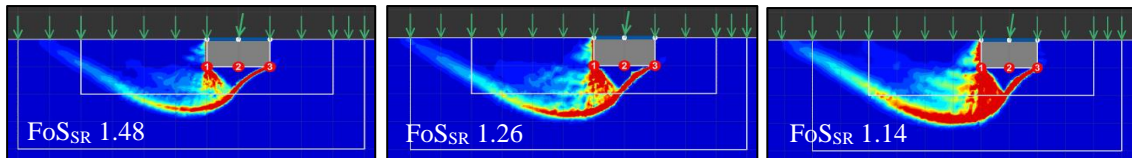
Fig. 117   Optum HMC model SRFELA LB shear dissipation
n.a. Davis A φ*=ψ'=32.44° for the corresponding failure load FoS$_{FL}$ 3.0-1.5
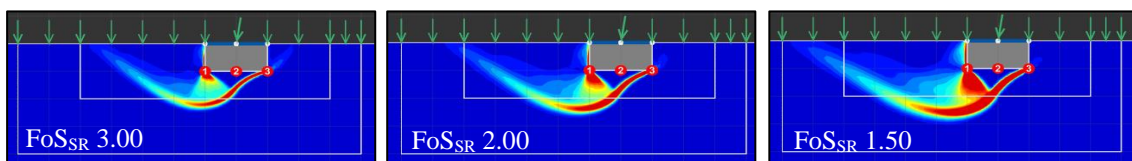
Fig. 118   Optum HMC model SRFELA UB shear dissipation
n.a. Davis A φ*=ψ'=32.44° for the corresponding actual load FoS$_{SR}$ 3.0-1.5

Fig. 119   Optum HMC model SRFELA UB shear dissipation
n.a. Davis A φ*=ψ'=32.44° for the corresponding failure load FoS$_{FL}$ 3.0-1.5
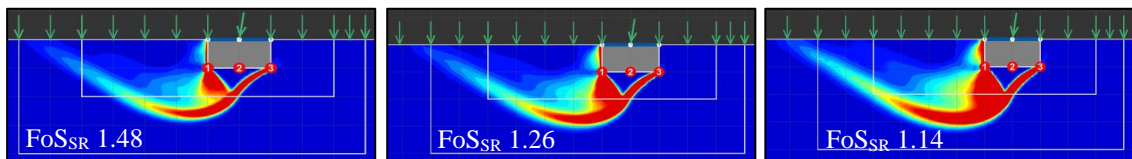
| Optum HMC model LB | ← → | Optum HMC model UB |
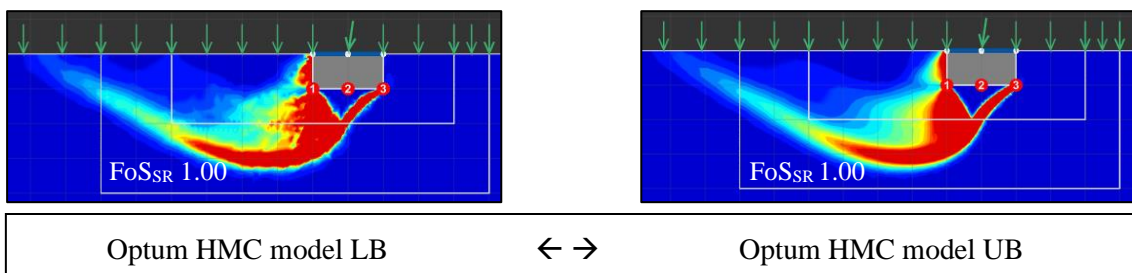
Fig. 120   Sliding surface at collapse – SRFELA n.a. Davis A φ*=ψ'=32.44°

9.3 C – 2D Constitutive Models

9.3.1 Plaxis MC Model Stress Path & π-Plane
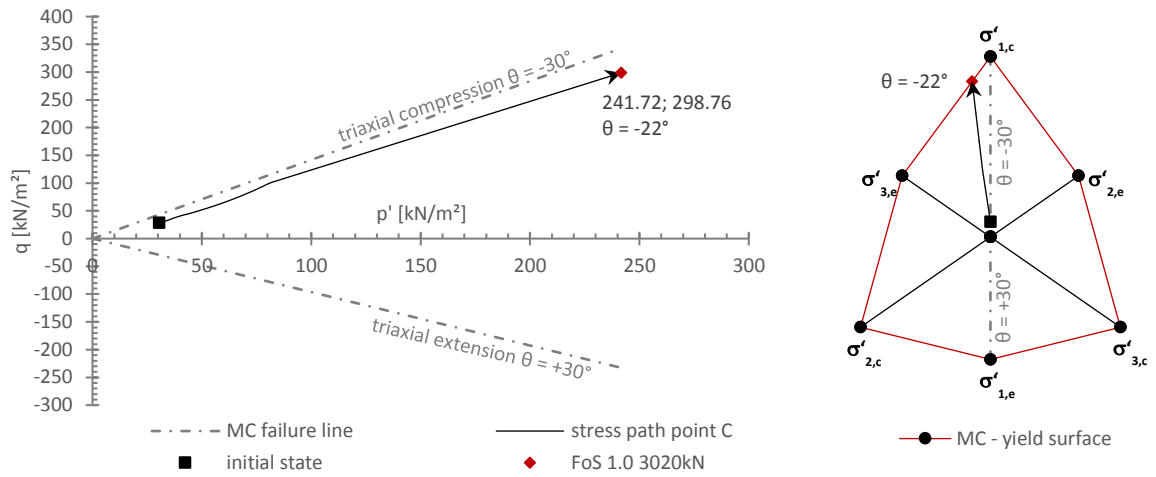
Fig. 121   p'-q stress path and corresponding π-plane
for a. φ'=ψ'=35° and plastic stress point C (MC model FEA 15-nod.)
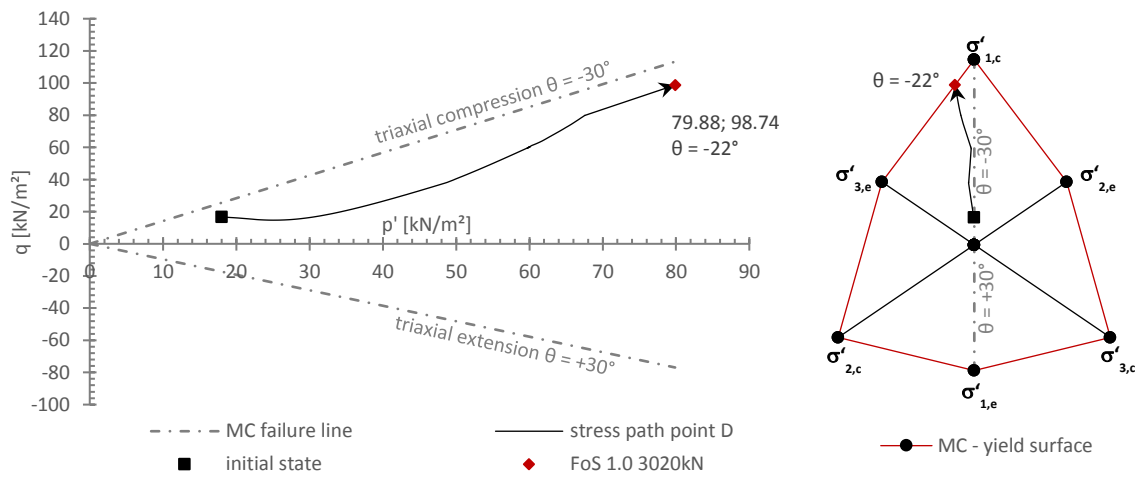
Fig. 122   p'-q stress path and corresponding π-plane
for a. φ'=ψ'=35° and plastic stress point D (MC model FEA 15-nod.)
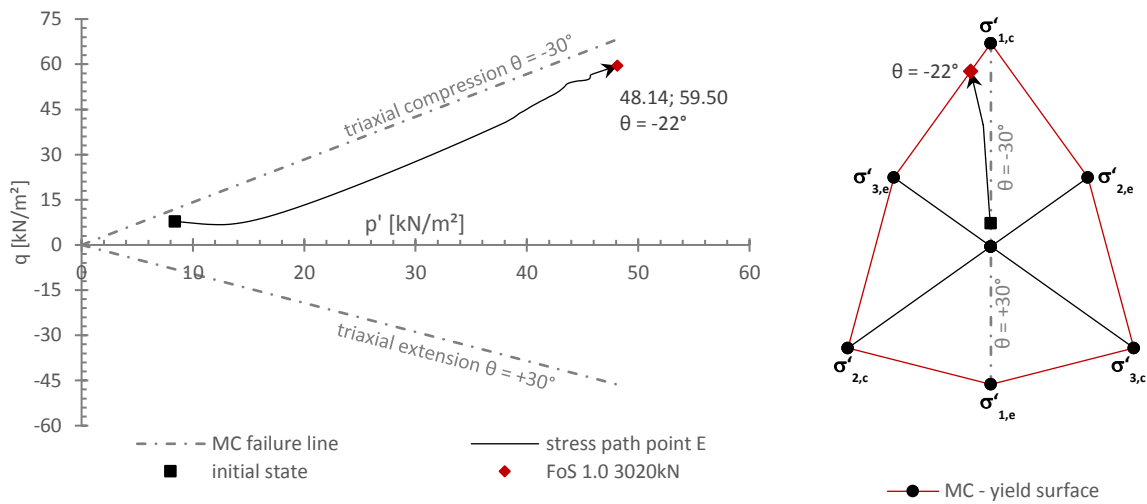
Fig. 123   p'-q stress path and corresponding π-plane
            for a. φ'=ψ'=35° and plastic stress point E (MC model FEA 15-nod.)
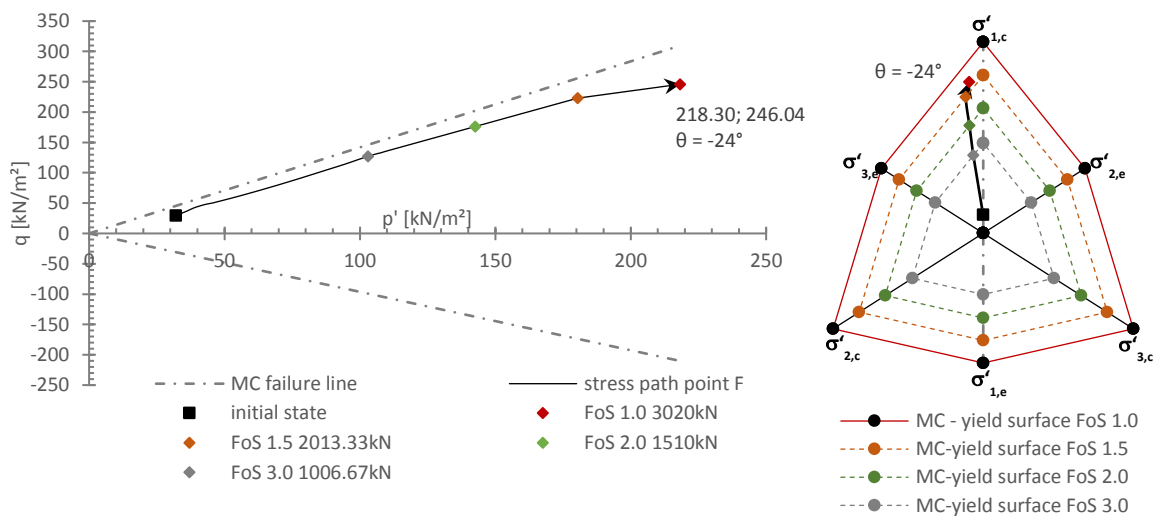
Fig. 124   p'-q stress path and corresponding π-plane
            for a. φ'=ψ'=35° and elastic stress point F (MC model FEA 15-nod.)
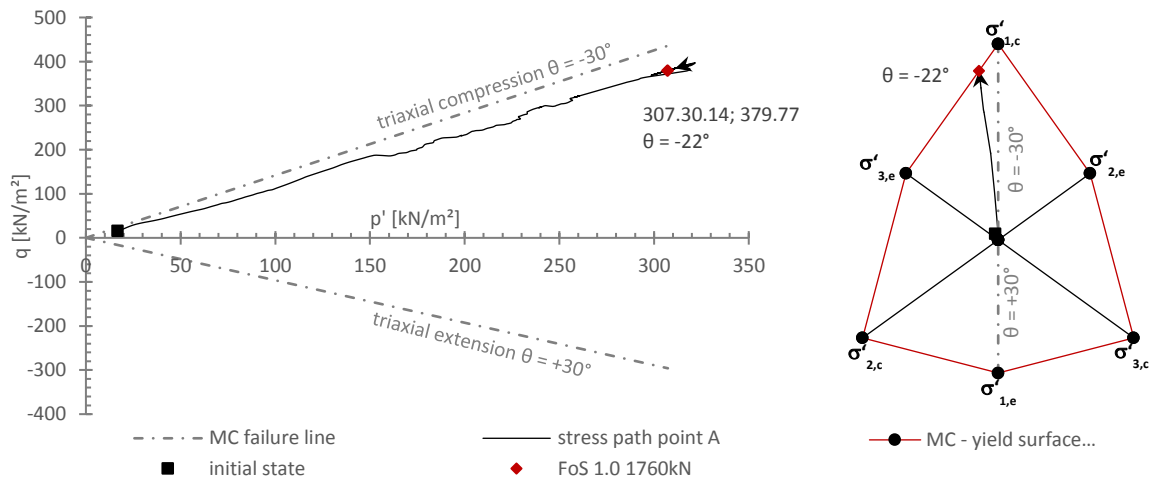
Fig. 125   p'-q stress path and corresponding π-plane
            for n.a. ψ'=0° and plastic stress point A (MC model FEA 15-nod.)
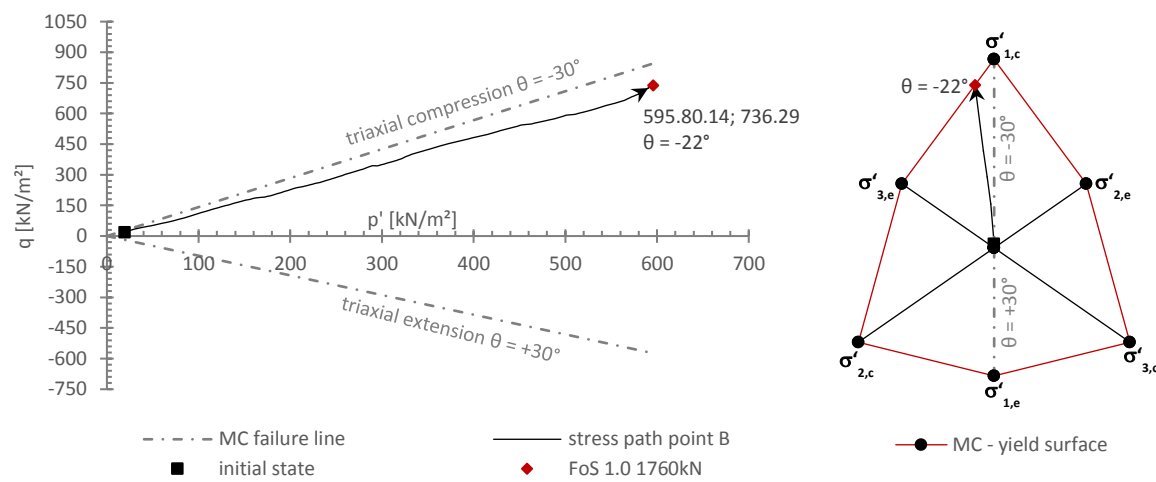
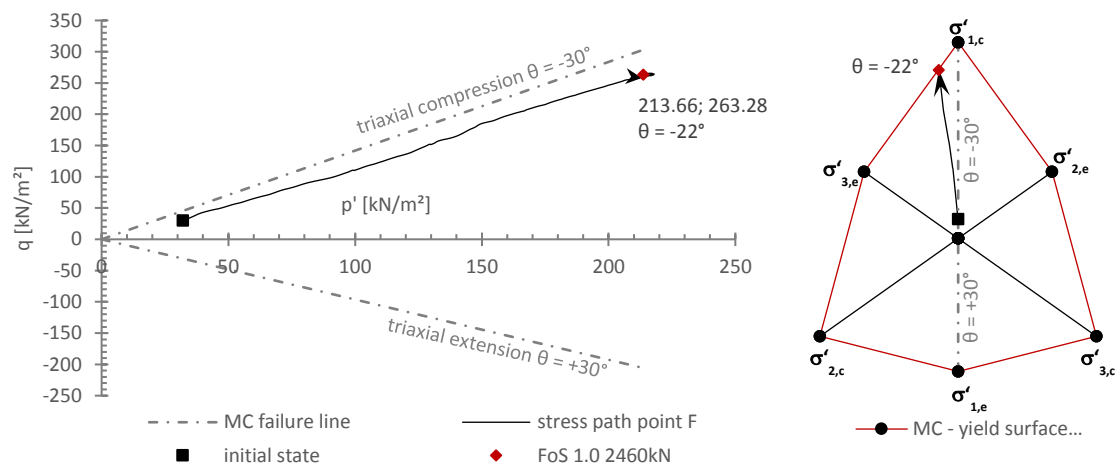Fig. 126   p'-q stress path and corresponding π-plane
            for n.a. ψ'=0° and plastic stress point B (MC model FEA 15-nod.)
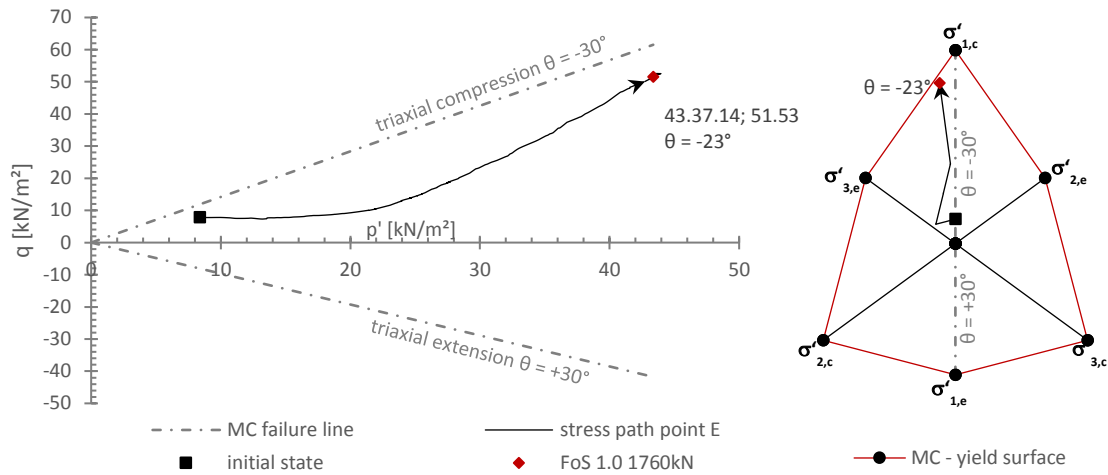
Fig. 127   p'-q stress path and corresponding π-plane
            for n.a. ψ'=0° and elastic stress point E (MC model FEA 15-nod.)
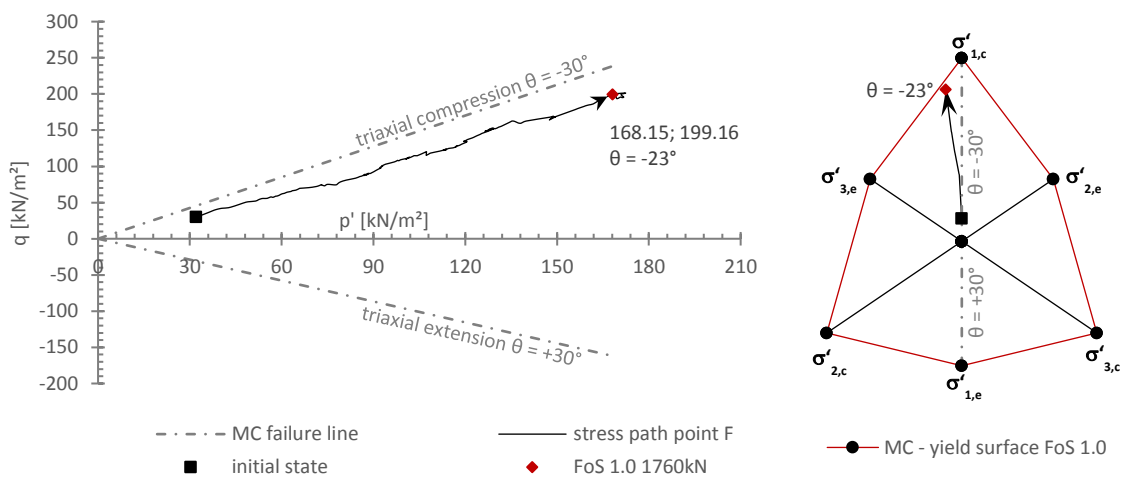
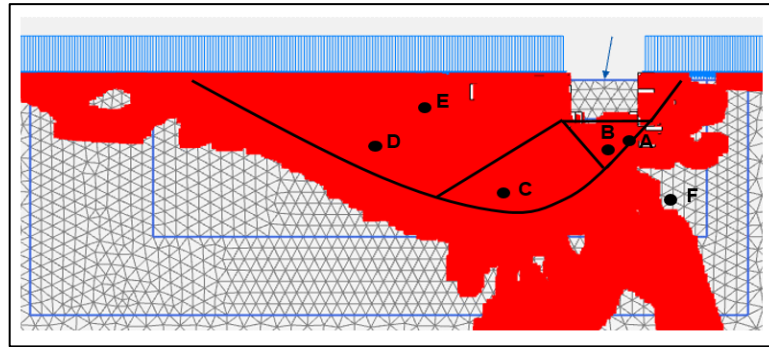Fig. 128   p'-q stress path and corresponding π-plane
            for n.a. ψ'=0° and elastic stress point F (MC model FEA 15-nod.)
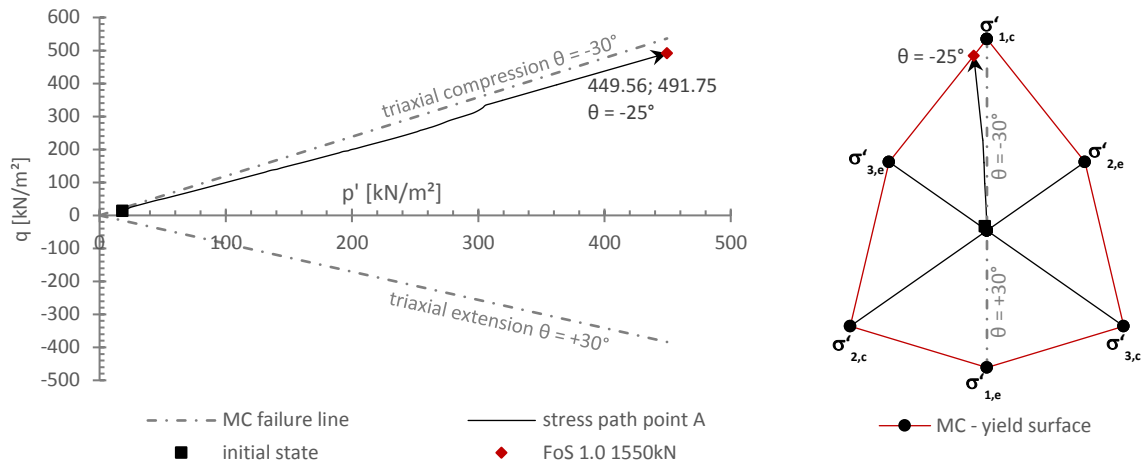
Fig. 129   p'-q stress path and corresponding π-plane (MC model FEA 15-nod.)
for n.a. Davis A φ*=ψ'=29.84° and plastic stress point A
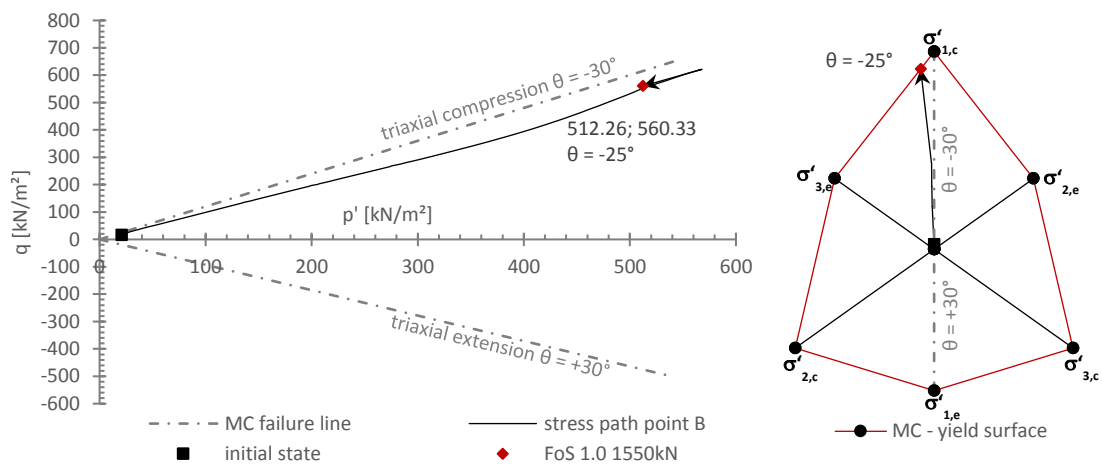
Fig. 130   p'-q stress path and corresponding π-plane (MC model FEA 15-nod.)
for n.a. Davis A φ*=ψ'=29.84° and plastic stress point B
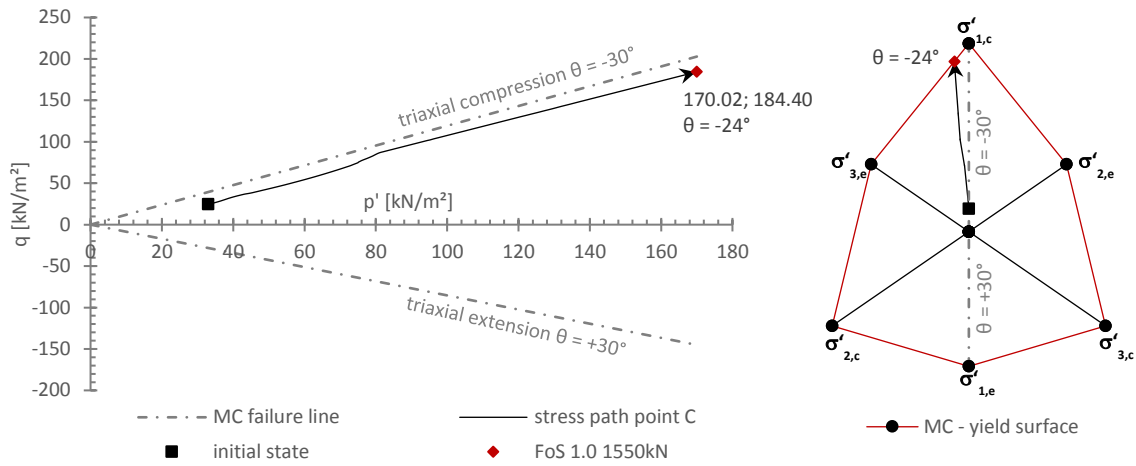
Fig. 131   p'-q stress path and corresponding π-plane (MC model FEA 15-nod.)
             for n.a. Davis A φ*=ψ'=29.84° and plastic stress point C
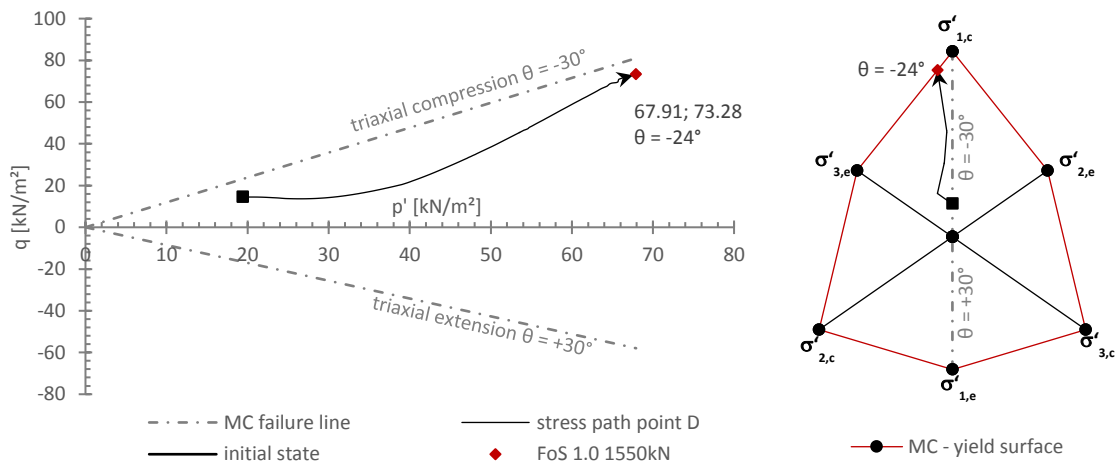
Fig. 132   p'-q stress path and corresponding π-plane (MC model FEA 15-nod.)
             for n.a. Davis A φ*=ψ'=29.84° and plastic stress point D
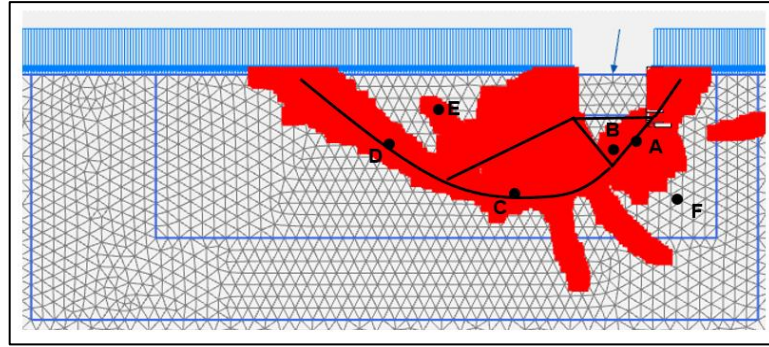
Fig. 133   MC model FEA 15-nod. plastic points
for n.a. ψ'=11.7° stress point A-F

Tab. 67   Resulting stresses and lode angle for stress point A-F
for n.a. ψ'=11.7° at failure (MC model FEA 15-nod.)

ψ'=11.7° - FoS$_{FL}$ 1.0 at failure				
stress point	σ'$_1$ [kN/m²]	σ'$_2$ [kN/m²]	σ'$_3$ [kN/m²]	θ [°]
A - plastic	748.09	285.20	202.72	**-21.936**
B -plastic	1475.49	562.55	399.84	**-21.934**
C - plastic	286.62	109.21	77.67	**-21.952**
D - plastic	116.00	44.19	31.43	**-21.961**
E - plastic	77.02	29.35	20.87	**-21.952**
F - elastic	387.48	147.86	105.64	**-22.018**
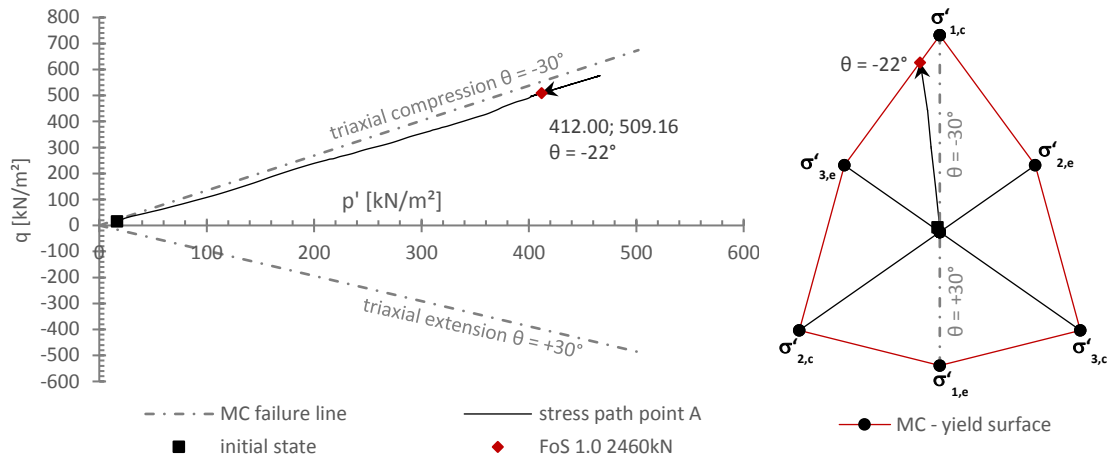
Fig. 134 p'-q stress path and corresponding π-plane
for n.a. ψ'=11.7° and plastic stress point A (MC model FEA 15-nod.)
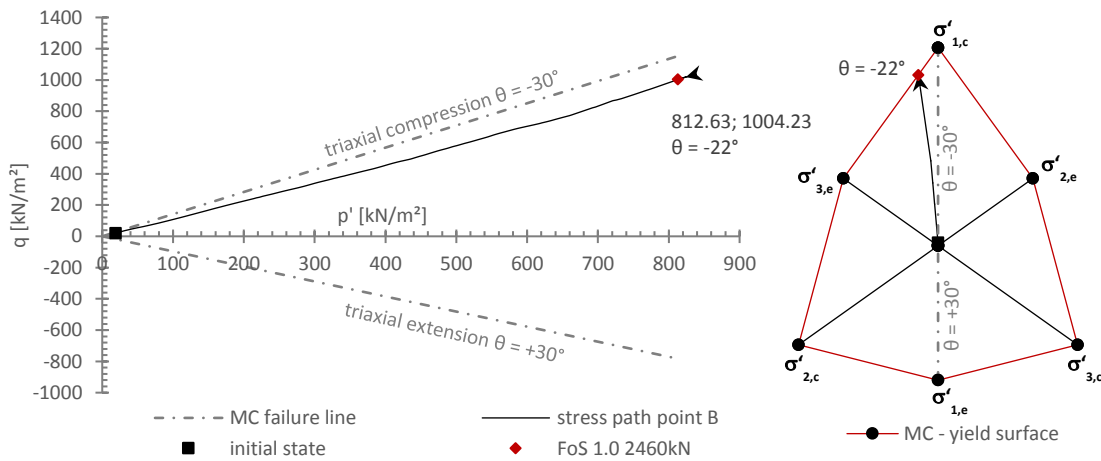
Fig. 135 p'-q stress path and corresponding π-plane
for n.a. ψ'=11.7° and plastic stress point B (MC model FEA 15-nod.)
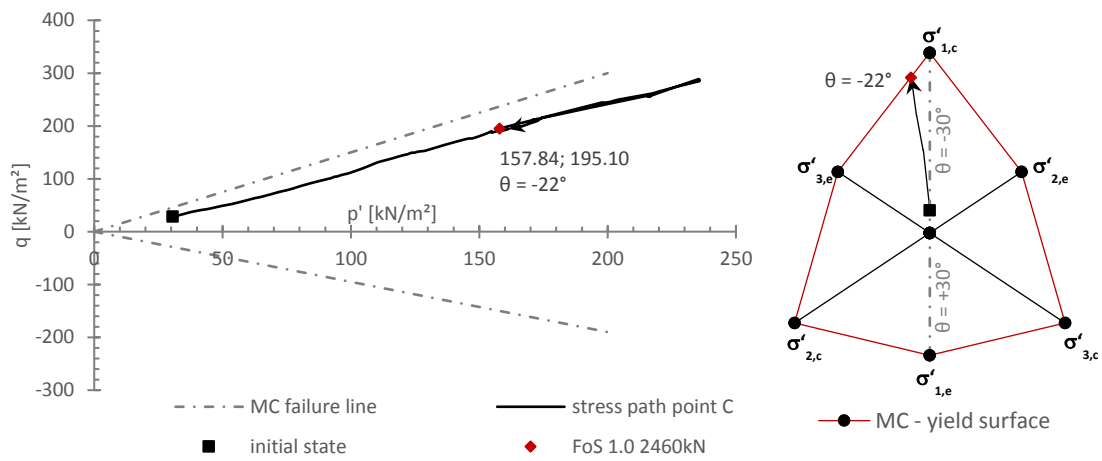
Fig. 136   p'-q stress path and corresponding π-plane
            for n.a. ψ'=11.7° and plastic stress point C (MC model FEA 15-nod.)
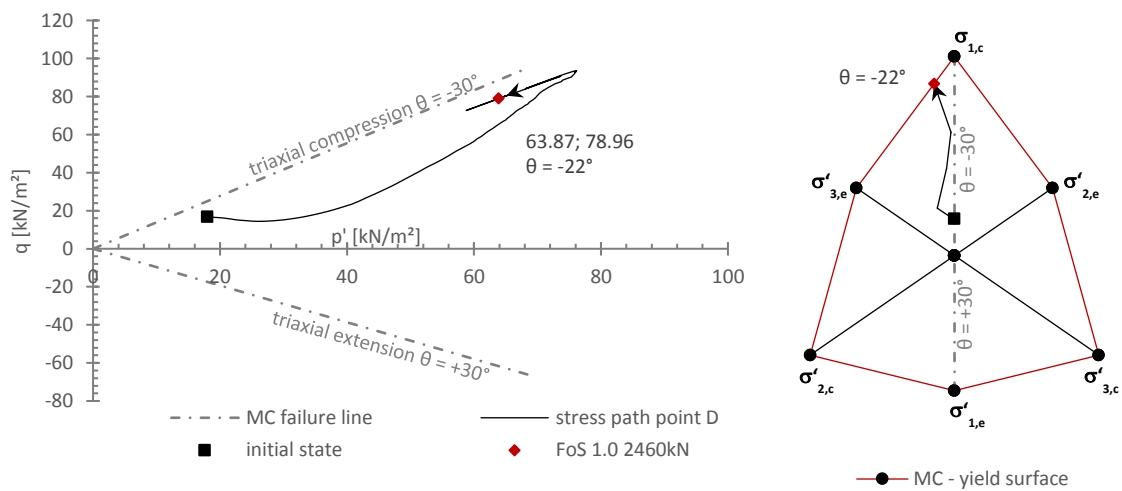
Fig. 137   p'-q stress path and corresponding π-plane
            for n.a. ψ'=11.7° and plastic stress point D (MC model FEA 15-nod.)
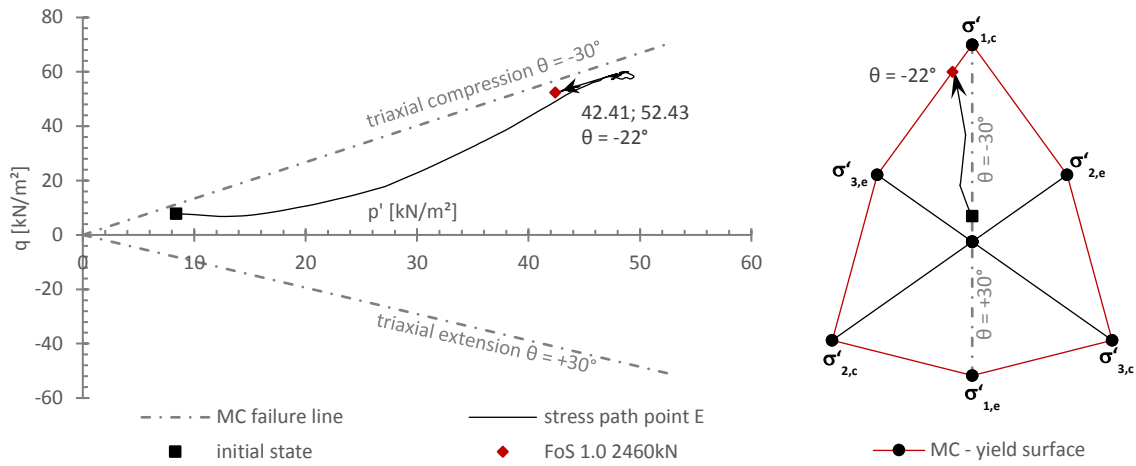
Fig. 138   p'-q stress path and corresponding π-plane
             for n.a. ψ'=11.7° and plastic stress point E (MC model FEA 15-nod.)

Fig. 139   p'-q stress path and corresponding π-plane
             for n.a. ψ'=11.7° and elastic stress point F (MC model FEA 15-nod.)
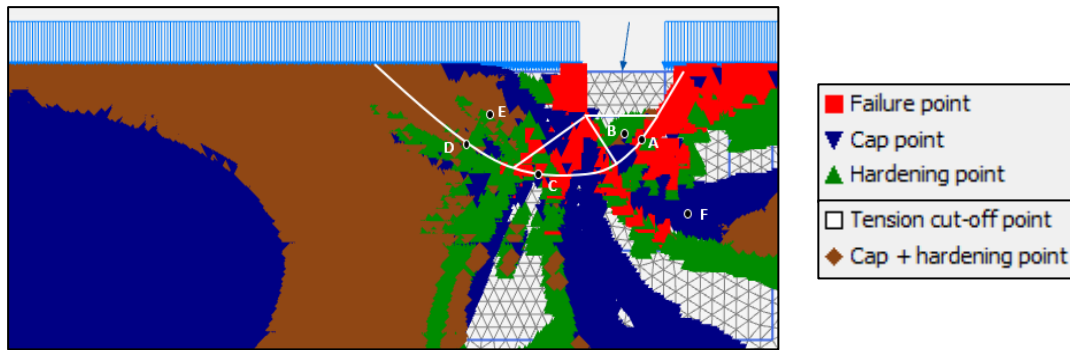
Fig. 140   MC model FEA 15-nod. plastic points
            for n.a. Davis A φ*=ψ'=32.44° stress point A-F

Tab. 68   Resulting stresses and lode angle for stress point A-F
            for n.a. Davis A φ*=ψ'=32.44° at failure (MC model FEA 15-nod.)

	σ'₁ [kN/m²]	σ'₂ [kN/m²]	σ'₃ [kN/m²]	θ [°]
φ*=ψ'=32.44° - FoS_FL 1.0 at failure				
A - plastic	999.44	390.97	301.56	**-23.240**
B -plastic	1232.59	482.12	371.91	**-23.244**
C - plastic	353.29	139.18	106.60	**-23.018**
D - plastic	129.06	51.11	38.94	**-22.850**
E - plastic	77.72	30.68	23.45	**-22.950**
F - elastic	301.18	124.08	108.19	**-25.747**
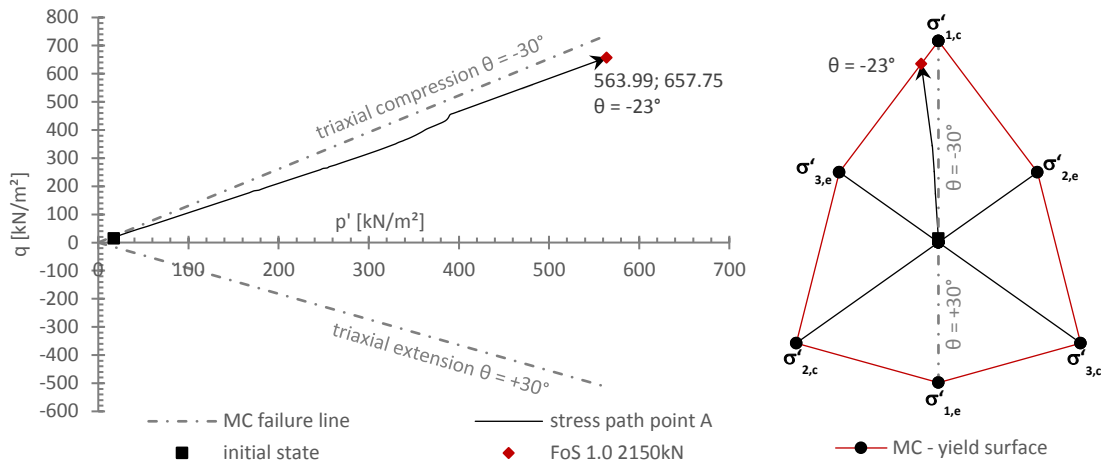
Fig. 141   p'-q stress path and corresponding π-plane (MC model FEA 15-nod.) for n.a. Davis A φ*=ψ'=32.44° and plastic stress point A
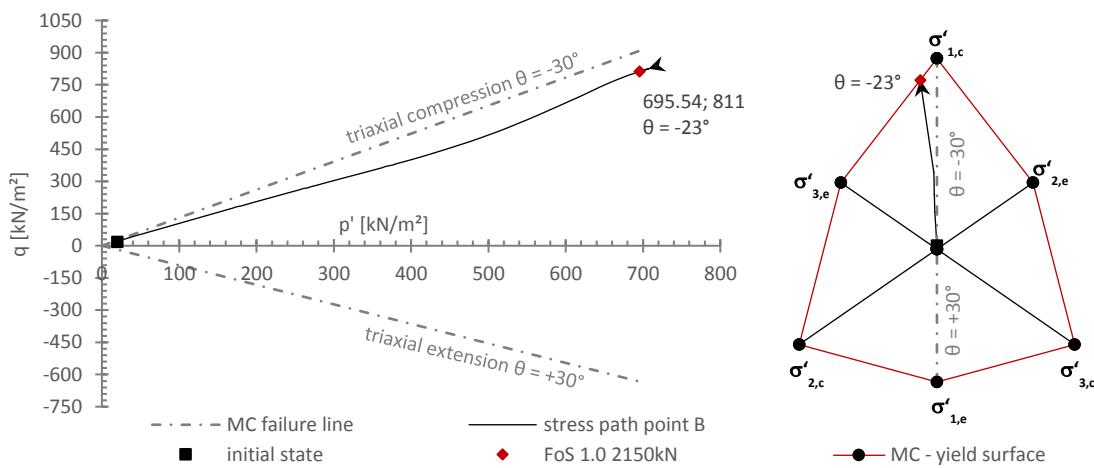
Fig. 142   p'-q stress path and corresponding π-plane (MC model FEA 15-nod.) for n.a. Davis A φ*=ψ'=32.44° and plastic stress point B
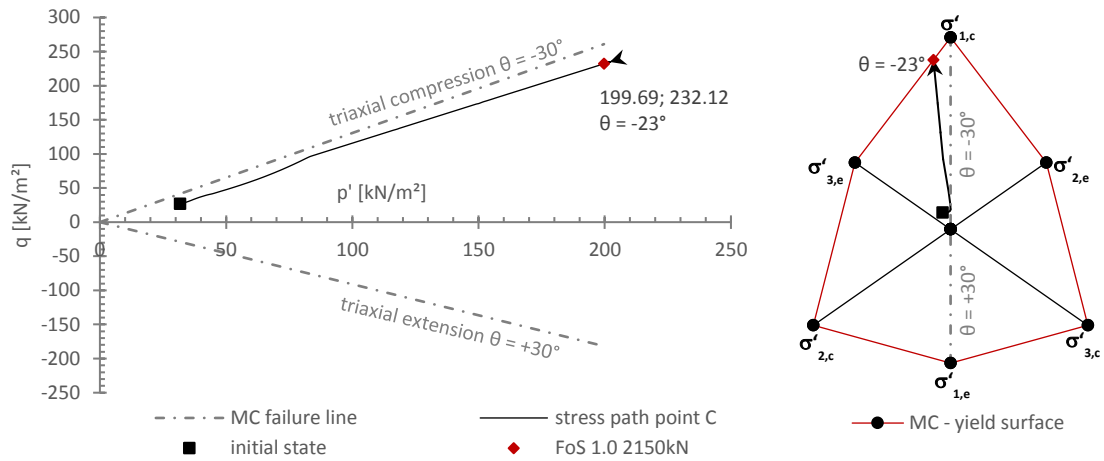
Fig. 143   p'-q stress path and corresponding π-plane (MC model FEA 15-nod.)
            for n.a. Davis A φ*=ψ'=32.44° and plastic stress point C
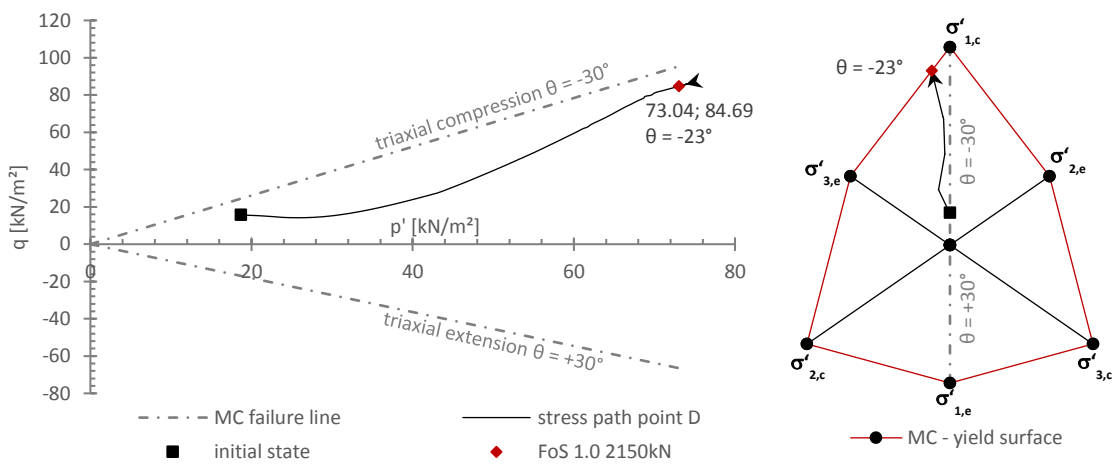
Fig. 144   p'-q stress path and corresponding π-plane (MC model FEA 15-nod.)
            for n.a. Davis A φ*=ψ'=32.44° and plastic stress point D
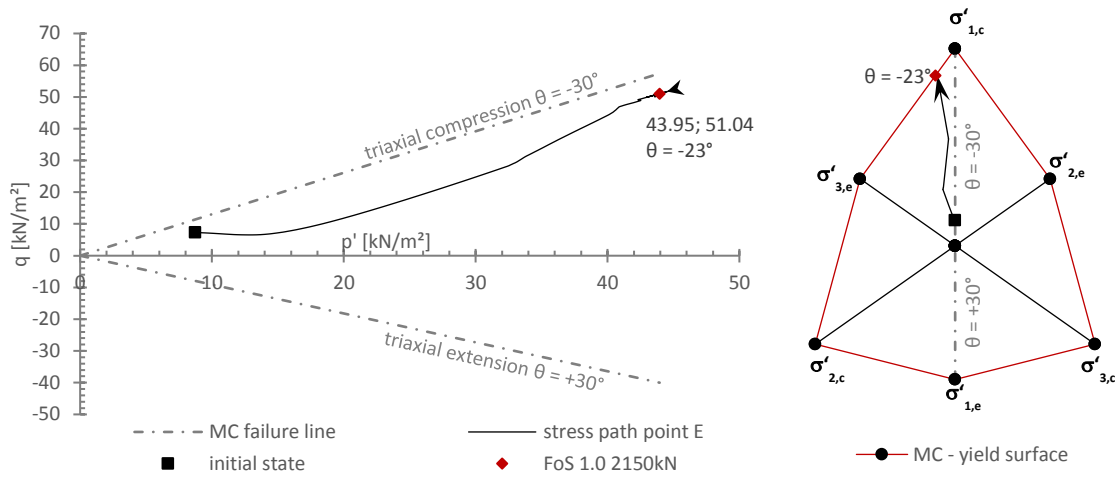
Fig. 145 p'-q stress path and corresponding π-plane (MC model FEA 15-nod.) for n.a. Davis A φ*=ψ'=32.44° and plastic stress point E
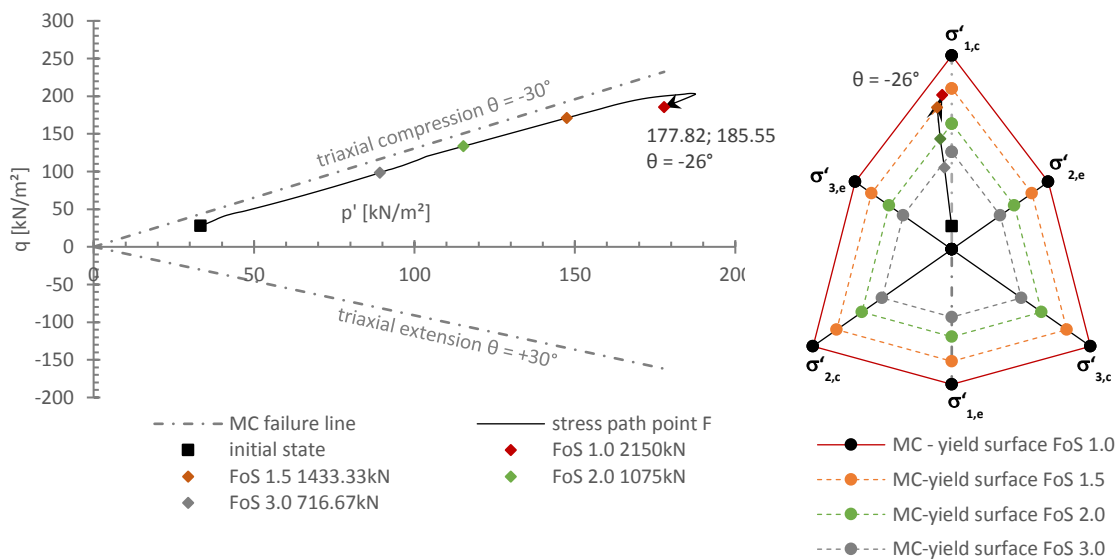
Fig. 146 p'-q stress path and corresponding π-plane (MC model FEA 15-nod.) for n.a. Davis A φ*=ψ'=32.44° and elastic stress point F

9.3.2 Plaxis HS Model Stress Path & π-Plane
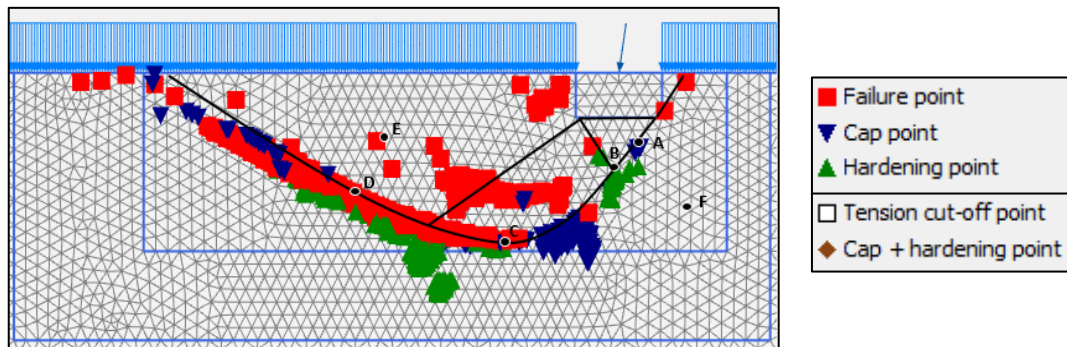
Fig. 147   HS model FEA 15-nod. plastic points for a. φ'= ψ'=35° stress point A-F

Tab. 69   Resulting stresses and lode angle for stress point A-F
for a. φ'=ψ'=35° at failure (HS model FEA 15-nod.)

|	σ'_1 [kN/m²]	σ'_2 [kN/m²]	σ'_3 [kN/m²]	θ [°]
φ'=ψ'=35° - FoS_FL 1.0 at failure				
A - cap	1087.63	295.65	295.17	**-29.970**
B - hardening	1978.99	553.45	551.42	**-29.929**
C - plastic	513.58	139.23	139.17	**-29.992**
D - plastic	202.62	54.92	54.91	**-29.997**
E - plastic	127.10	34.47	33.87	**-29.677**
F - elastic	440.76	142.40	142.23	**-29.972**

Fig. 148   HS model FEA 15-nod. plastic points for n.a. ψ'=0° stress point A-F

Tab. 70   Resulting stresses and lode angle for stress point A-F for n.a. ψ'=0° at failure
(HS model FEA 15-nod.)

ψ'=0° - FoS$_{FL}$ 1.0 at failure				
stress point	σ'$_1$ [kN/m²]	σ'$_2$ [kN/m²]	σ'$_3$ [kN/m²]	θ [°]
A - plastic	574.67	169.66	155.73	**-28.323**
B - hardening	882.48	315.76	313.85	**-29.833**
C - plastic	169.45	51.77	45.92	**-27.595**
D - hardening	96.98	32.86	28.39	**-26.658**
E - hardening	71.35	25.52	23.61	**-27.978**
F - elastic	305.99	95.12	91.12	**-29.766**

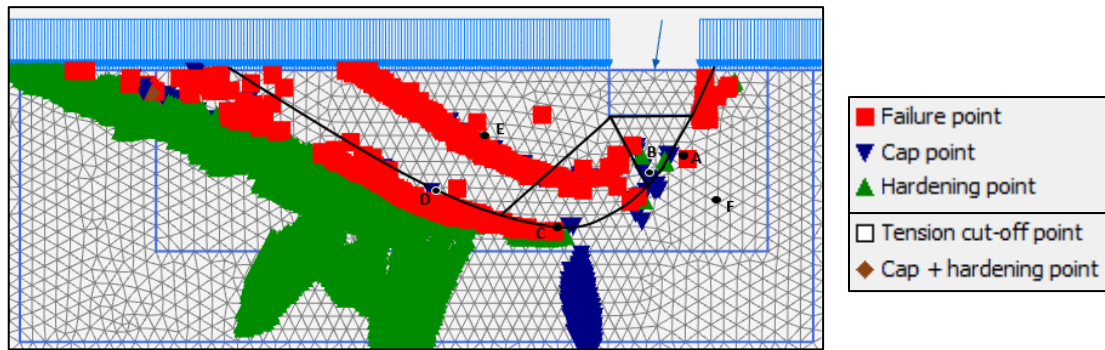Fig. 149　HS model FEA 15-nod. plastic points
　　　　　for n.a. Davis A φ*=ψ'=29.84° stress point A-F

Tab. 71　Resulting stresses and lode angle for stress point A-F
　　　　　for n.a. Davis A φ*=ψ'=29.84° at failure (HS model FEA 15-nod.)

φ*=ψ'=29.84° - FoS$_{FL}$ 1.0 at failure				
	σ'$_1$ [kN/m²]	σ'$_2$ [kN/m²]	σ'$_3$ [kN/m²]	θ [°]
A - hardening	576.16	194.11	193.66	**-29.942**
B - hardening	877.52	305.11	305.09	**-29.999**
C - plastic	352.92	118.49	118.40	**-29.982**
D - plastic	137.46	46.15	46.12	**-29.985**
E - plastic	88.37	29.75	29.38	**-29.840**
F - elastic	301.56	115.31	115.31	**-30.000**
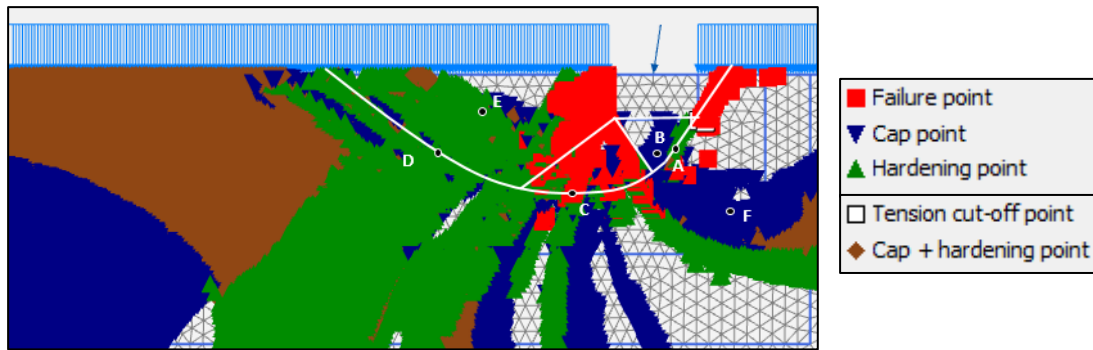
Fig. 150   HS model FEA 15-nod. plastic points for n.a. ψ'=11.7° stress point A-F

Tab. 72   Resulting stresses and lode angle for stress point A-F
for n.a. ψ'=11.7° at failure (HS model FEA 15-nod.)

ψ'=11.7° - FoS$_{FL}$ 1.0 at failure				
stress point	σ'$_1$ [kN/m²]	σ'$_2$ [kN/m²]	σ'$_3$ [kN/m²]	θ [°]
A - plastic	870.01	236.53	235.76	**-29.940**
B - cap	1250.77	388.86	388.86	**-30.000**
C - plastic	412.38	112.33	111.75	**-29.904**
D - hardening	138.35	40.31	40.25	**-29.970**
E - hardening	90.75	25.97	25.88	**-29.930**
F - cap	362.66	111.13	11.13	**-30.000**

Fig. 151   HS model FEA 15-nod. plastic points
for n.a. Davis A $\varphi^*=\psi'=32.44°$ stress point A-F

Tab. 73   Resulting stresses and lode angle for stress point A-F
for n.a. Davis A $\varphi^*=\psi'=32.44°$ at failure (HS model FEA 15-nod.)

	σ'_1 [kN/m²]	σ'_2 [kN/m²]	σ'_3 [kN/m²]	θ [°]
		$\varphi^*=\psi'=32.44°$ - FoS$_{FL}$ 1.0 at failure		
A - plastci	470.72	145.82	142.03	**-29.424**
B - cap	999.13	306.39	306.37	**-29.998**
C - plastic	471.03	142.31	142.12	**-29.973**
D - plastic	200.58	60.73	60.52	**-29.926**
E - plastic	119.94	36.19	36.19	**-30.000**
F - elastic	376.50	132.34	132.25	**-29.982**

9.4 D – 2D Numerical Settings Studies

9.4.1 D – Tolerated Error
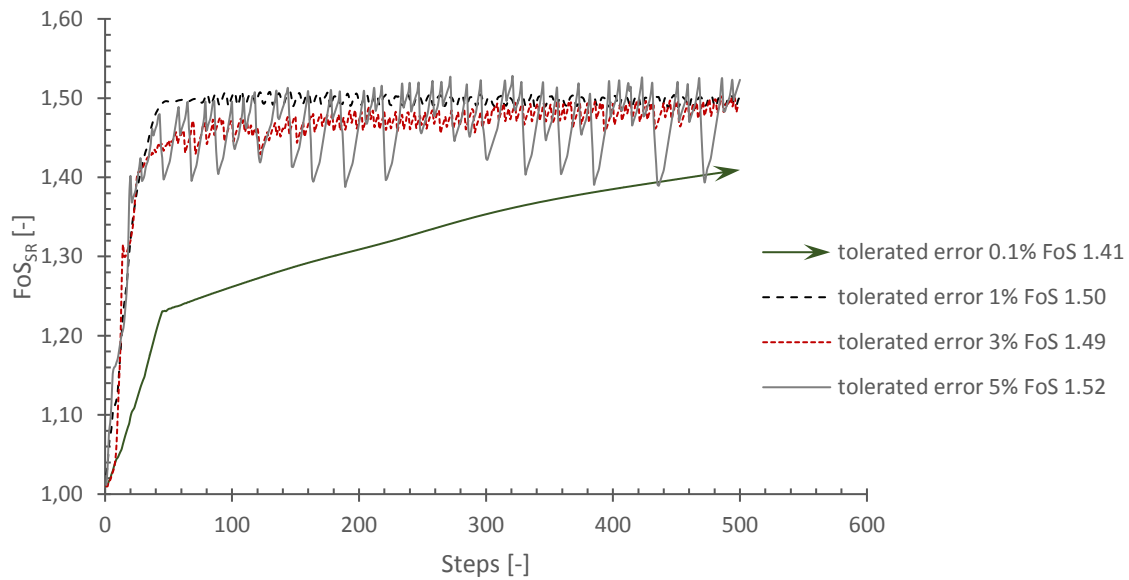
Fig. 152   Influence of tolerated error 0.1%, 1%, 3%, 5% for a. φ'=ψ'=35° at FoS$_{SR}$ 1.50
(HS model SRFEA 15-nod.)
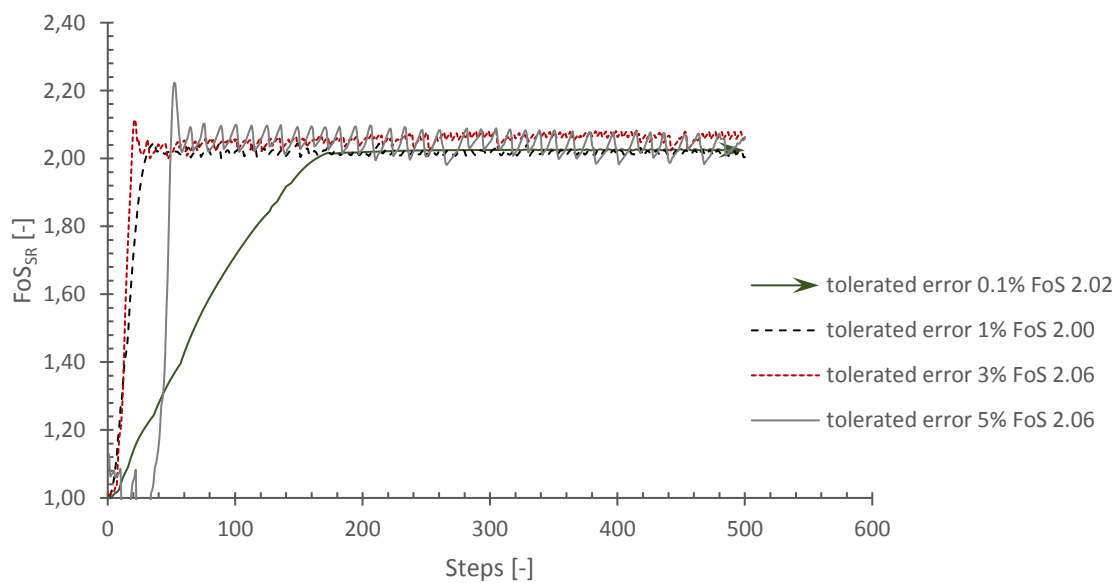
Fig. 153   Influence of tolerated error 0.1%, 1%, 3%, 5% for a. φ'=ψ'=35° at FoS$_{SR}$ 2.00
(HS model SRFEA 15-nod.)
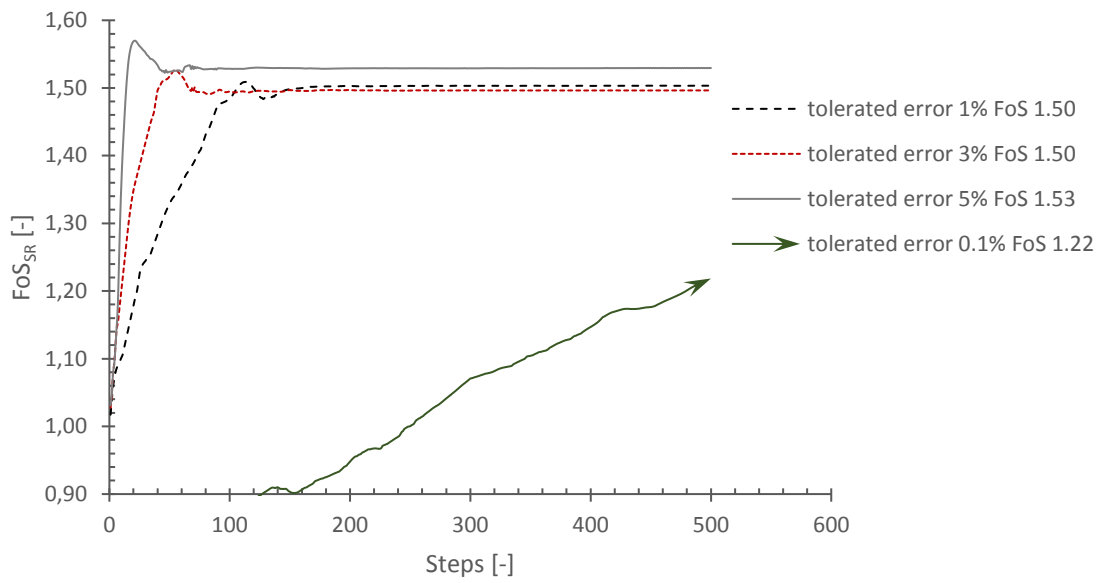
Fig. 154   Influence of tolerated error 0.1%, 1%, 3%, 5% for n.a. $\psi'=0°$ at FoS$_{SR}$ 1.50
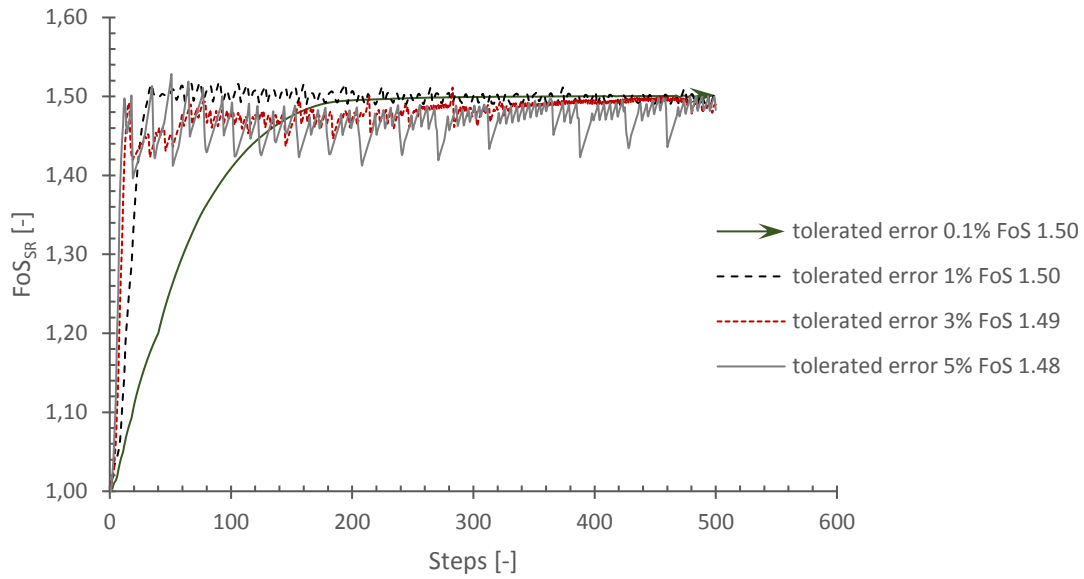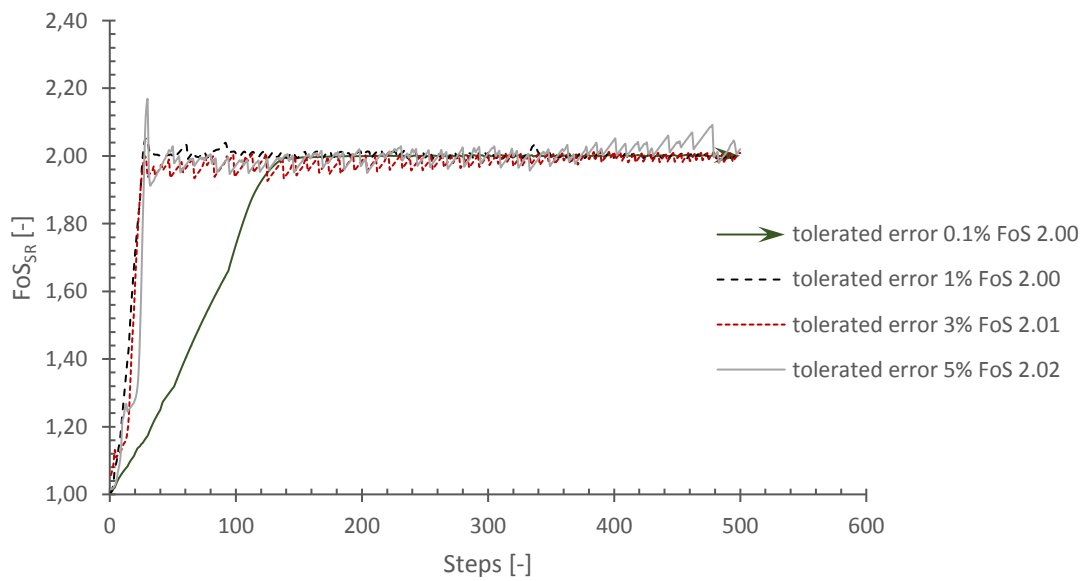(HS model SRFEA 15-nod.)
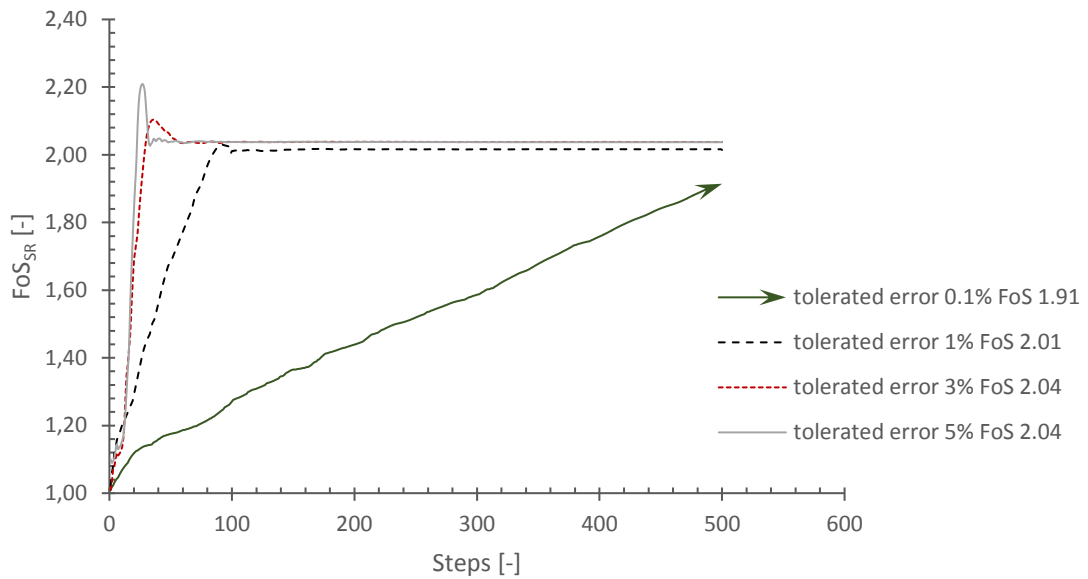
Fig. 155   Influence of tolerated error 0.1%, 1%, 3%, 5% for n.a. $\psi'=0°$ at FoS$_{SR}$ 2.00
(HS model SRFEA 15-nod.)

Fig. 156   Influence of tolerated error 0.1%, 1%, 3%, 5% for n.a. Davis A φ*=ψ'=29.84°
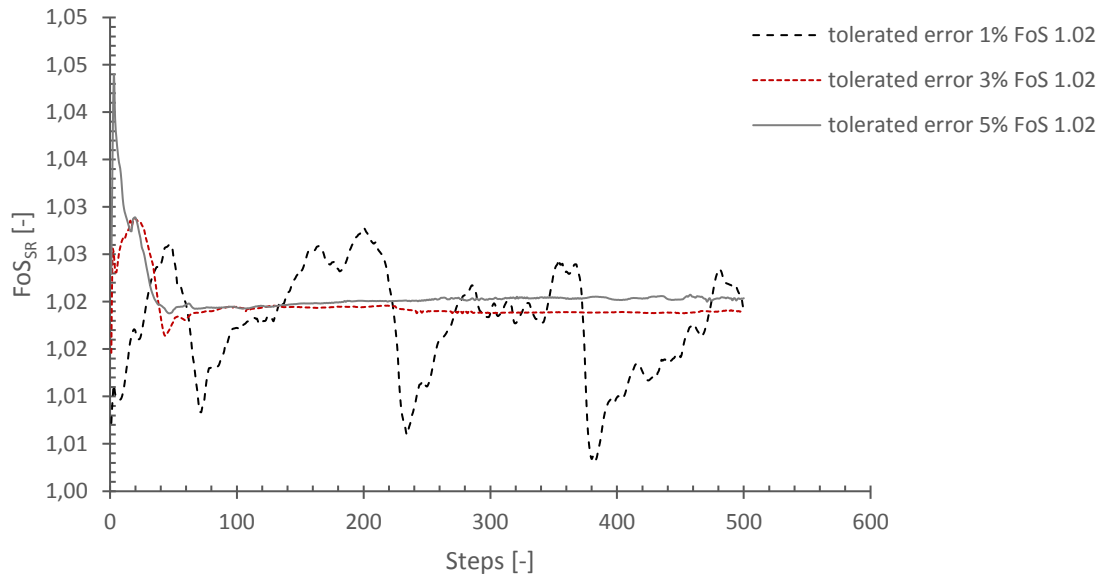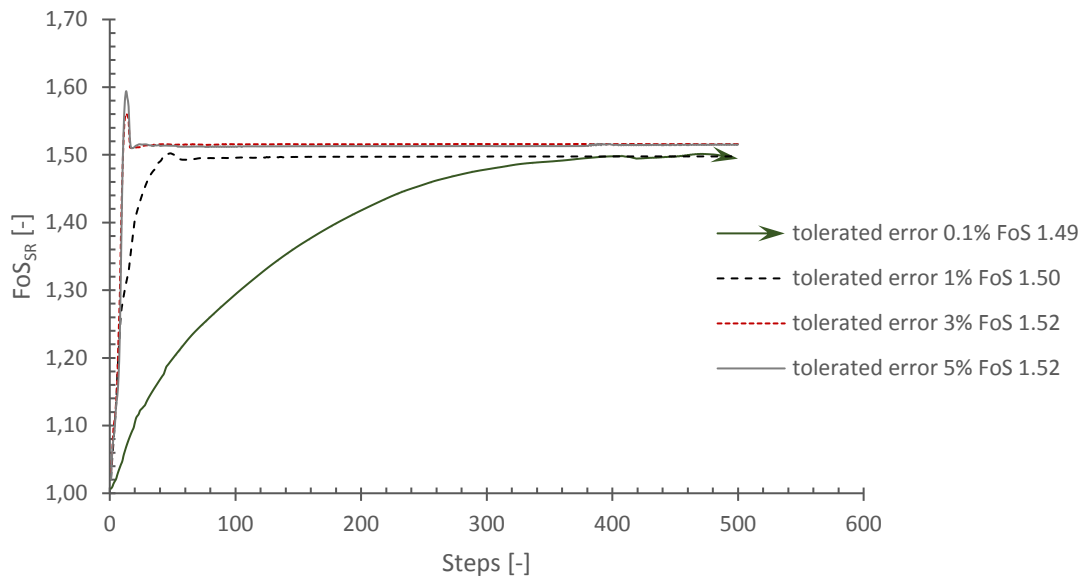   at FoS_{SR} 1.50 (HS model SRFEA 15-nod.)

Fig. 157   Influence of tolerated error 0.1% 1%, 3%, 5% for n.a. Davis A φ*=ψ'=29.84°
            at FoS_{SR} 2.00 (HS model SRFEA 15-nod.)

Fig. 158   Influence of tolerated error 1%, 3%, 5% for n.a. ψ'=11.7° at failure
            (HS model SRFEA 15-nod.)
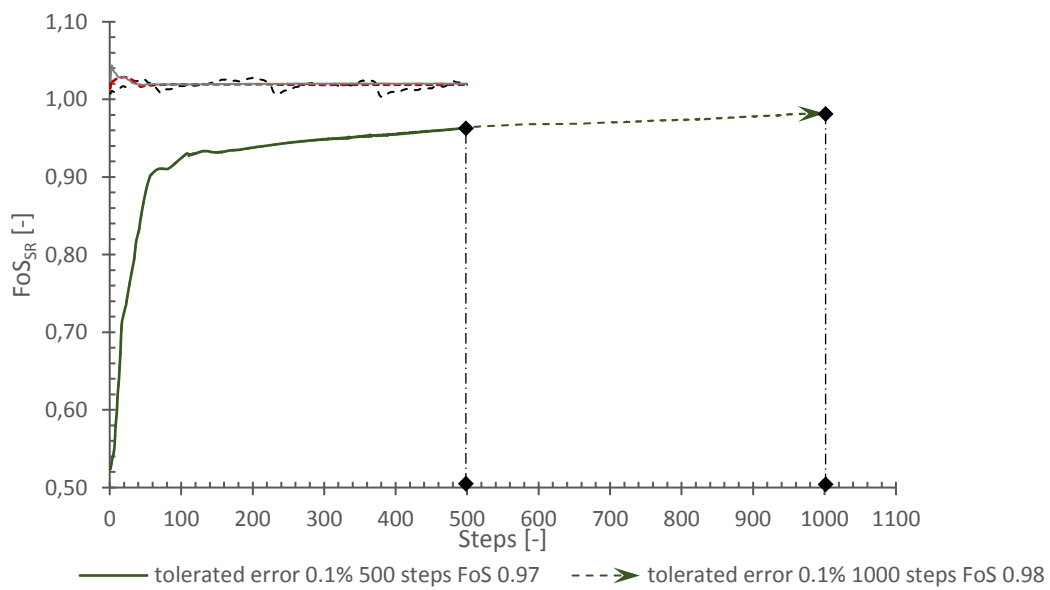
Fig. 159   Influence of tolerated error 0.1% for n.a. ψ'=11.7° at failure
            (HS model SRFEA 15-nod.)

Tab. 74   Comparison of the tolerated error 0.1%, 1%, 3%, 5% and the resulting FoS_{SR}
           at failure for n.a. ψ'=11.7° (HS model SRFEA 15-nod.)

	Tolerated error			
steps	0.1%	1%	3%	5%
500	FoS_{SR} 0.97	FoS_{SR} 1.02	FoS_{SR} 1.02	FoS_{SR} 1.02
1000	FoS_{SR} 0.98	-	-	-

Fig. 160   Influence of tolerated error 0.1%, 1%, 3%, 5% for n.a. ψ'= 11.7°
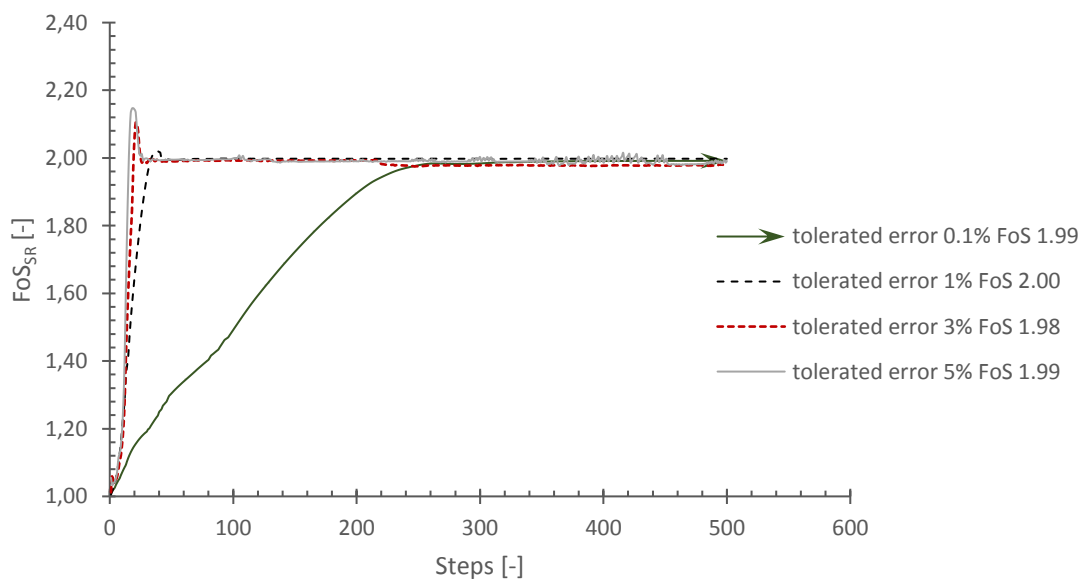at FoS$_{SR}$ 1.50 (HS model SRFEA 15-nod.)

Fig. 161   Influence of tolerated error 0.1%, 1%, 3%, 5% for n.a. ψ'= 11.7°
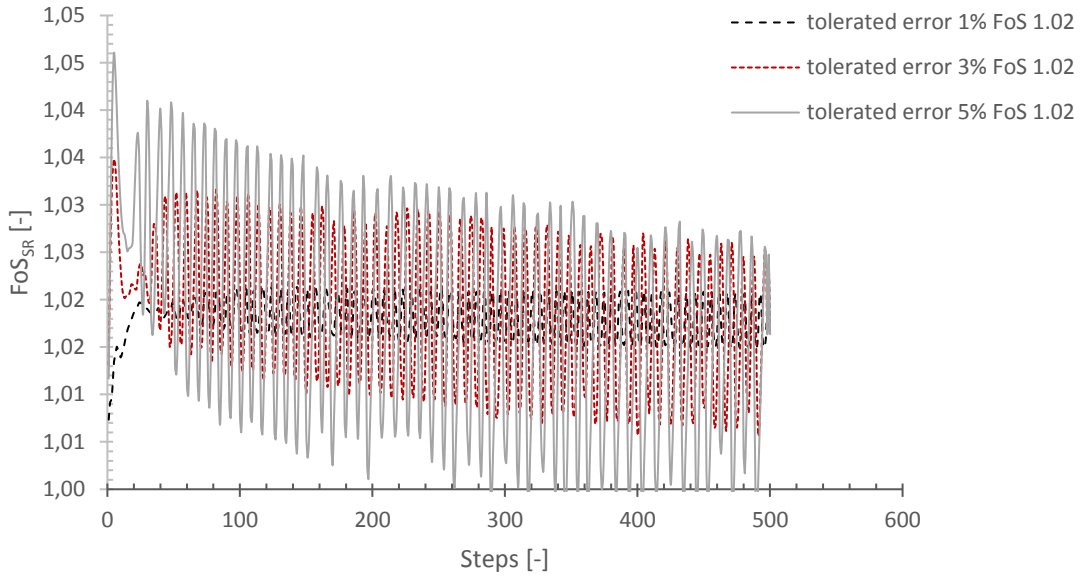at FoS$_{SR}$ 2.00 (HS model SRFEA 15-nod.)

Fig. 162   Influence of tolerated error 1%, 3%, 5% for n.a. Davis A φ*=ψ'=32.44° at failure (HS model SRFEA 15-nod.)
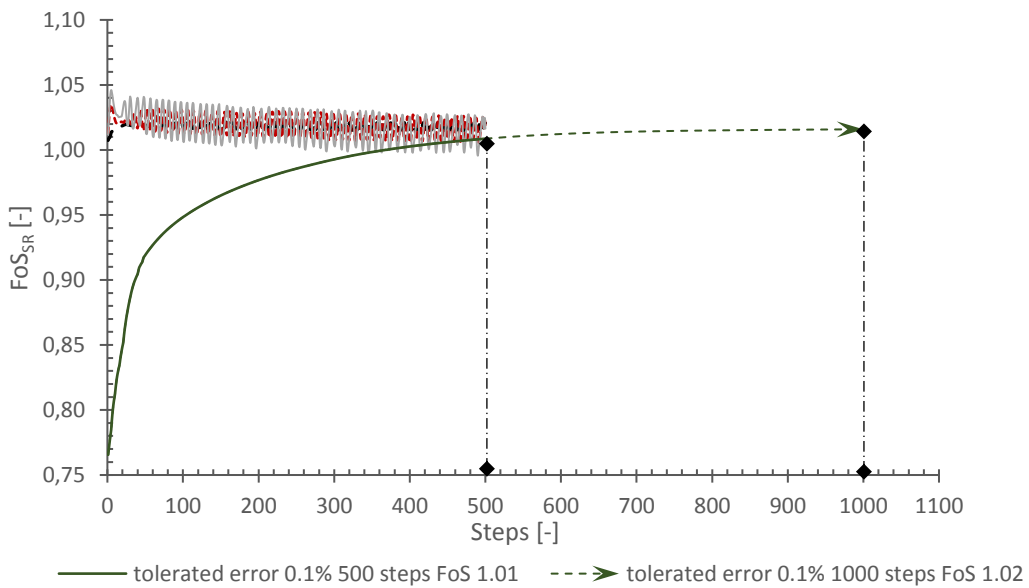

Fig. 163   Influence of tolerated error 0.1% for n.a. Davis A φ*=ψ'=32.44° at failure (HS model SRFEA 15-nod.)

Tab. 75   Comparison of the tolerated error 0.1%, 1%, 3%, 5% and the resulting FoS$_{SR}$ at failure for n.a. Davis A φ*=ψ'=32.44° (HS model SRFEA 15-nod.)

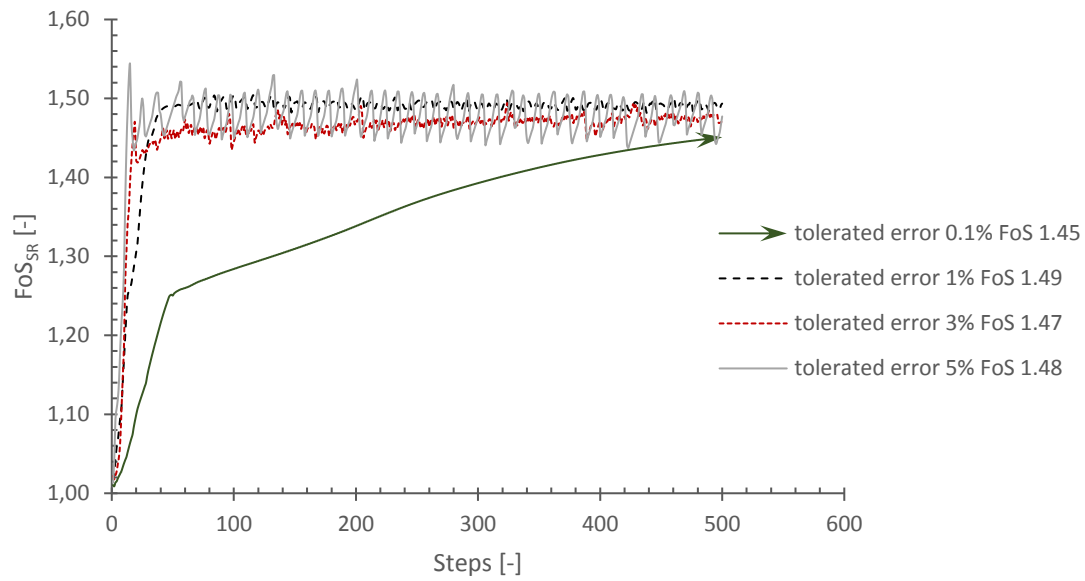|	Tolerated error			
steps	0.1%	1%	3%	5%
500	FoS$_{SR}$ 1.01	FoS$_{SR}$ 1.02	FoS$_{SR}$ 1.02	FoS$_{SR}$ 1.02
1000	FoS$_{SR}$ 1.02	-	-	-

Fig. 164   Influence of tolerated error 0.1%, 1%, 3%, 5% for n.a. Davis A φ*=ψ'=32.44°
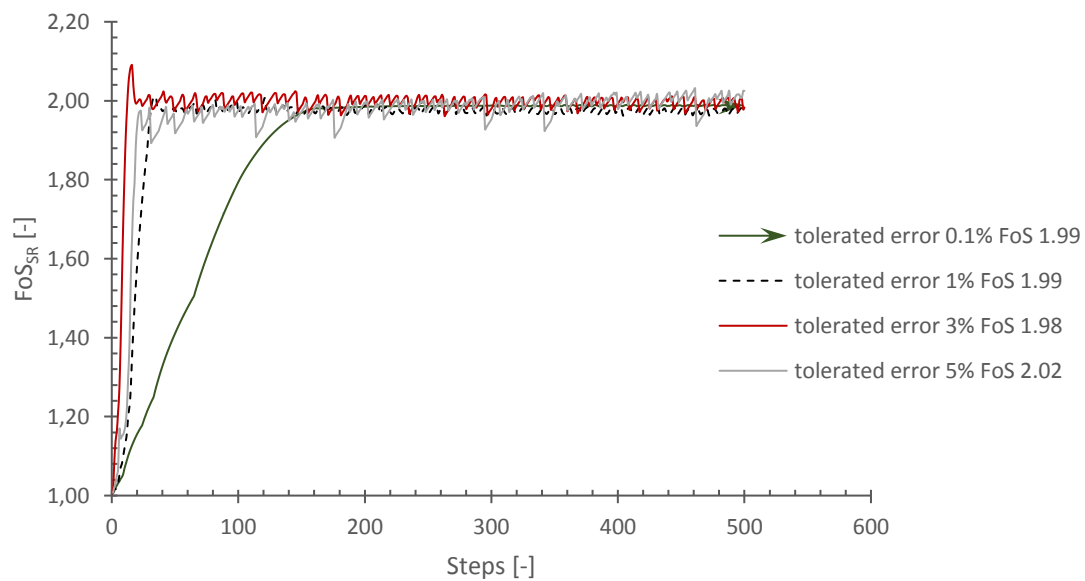at FoS$_{SR}$ 1.50 (HS model SRFEA 15-nod.)

Fig. 165   Influence of tolerated error 0.1%, 1%, 3%, 5% for n.a. Davis A φ*=ψ'=32.44°
at FoS$_{SR}$ 2.00 (HS model SRFEA 15-nod.)

9.4.2 D – K_0

Tab. 76   Influence of the K_0-value at the FoS_{SR}
               for Plaxis MC model SRFEA 15-nod. A. $\varphi'=\psi'=35°$

Plaxis MC model SRFEA 15-noded $\varphi'=\psi'=35°$					
$K_0 = 0.3$		$K_0 = 0.426$		$K_0 = 1.0$	
FoS_{SR}	load [kN/m]	FoS_{SR}	load [kN/m]	FoS_{SR}	load [kN/m]
3.00	203	2.99	204	3.01	203
2.01	430	2.01	427	2.01	430
1.51	835	1.50	850	1.51	835
1.00	3020	1.00	3020	1.00	3020

Tab. 77   Influence of the K_0-value at the FoS_{SR}
               for Plaxis MC model SRFEA 15-nod. n.a. $\psi'=0°$

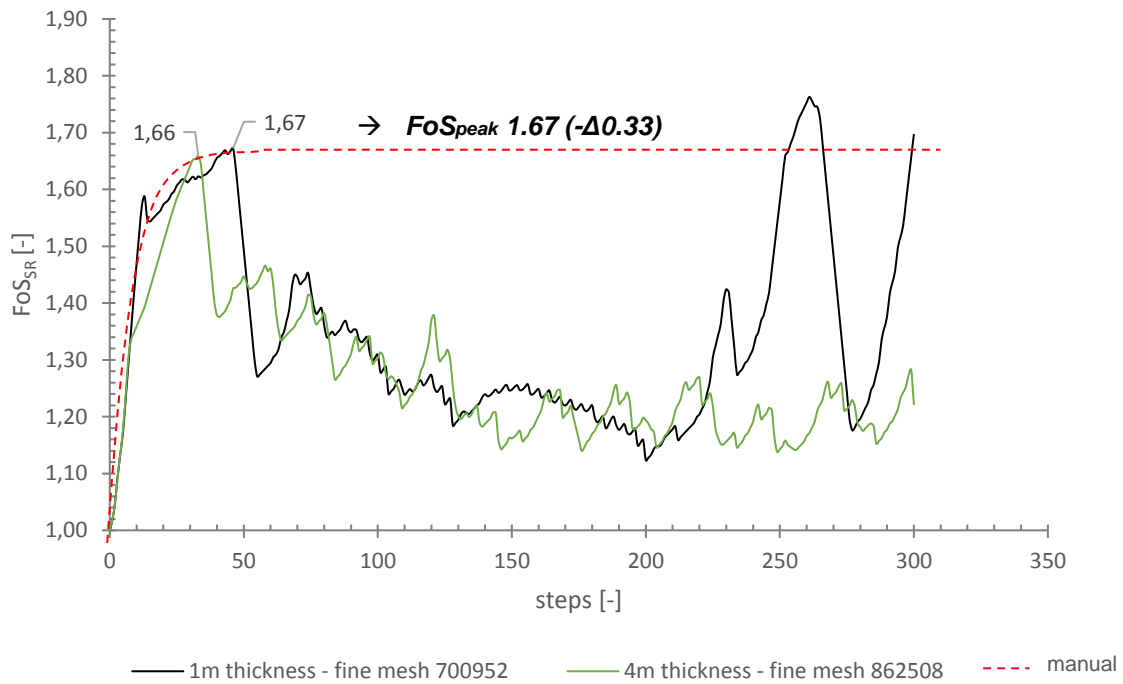| Plaxis MC model SRFEA 15-noded $\psi'=0°$					
$K_0 = 0.3$		$K_0 = 0.426$		$K_0 = 1.0$	
FoS_{SR}	load [kN/m]	FoS_{SR}	load [kN/m]	FoS_{SR}	load [kN/m]
3.01	200	3.01	198	2.99	200
2.01	400	2.00	400	2.01	400
1.50	735	1.50	730	1.50	735
1.00	1760	1.01	1760	1.02	1760

9.5 Comparison of 2D SR FoS with 3D SR FoS
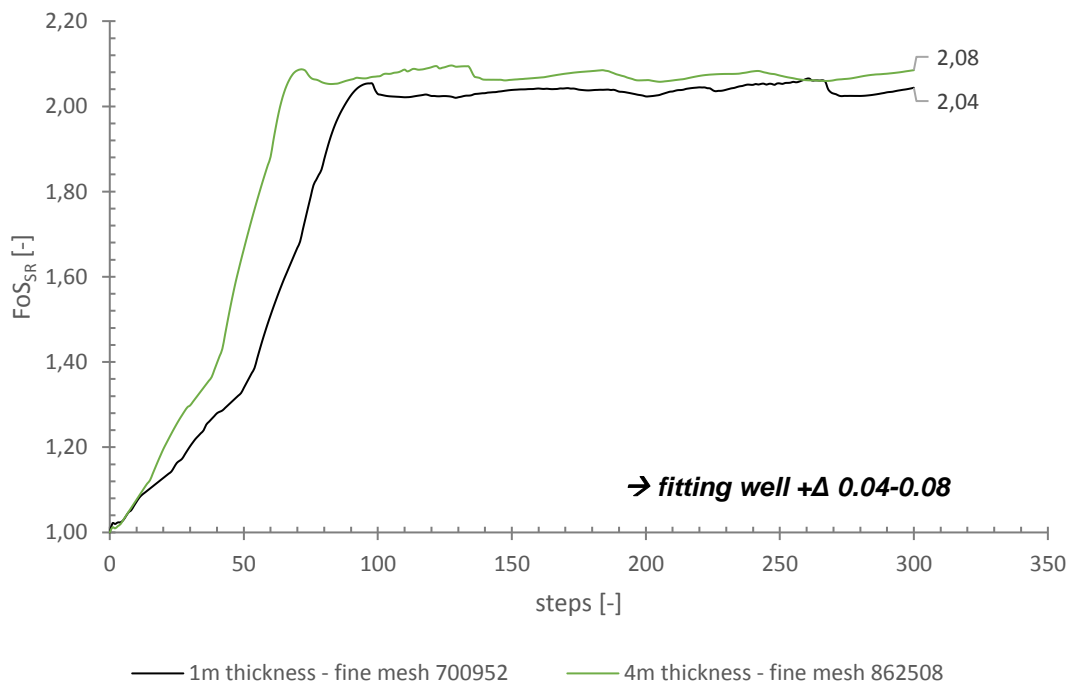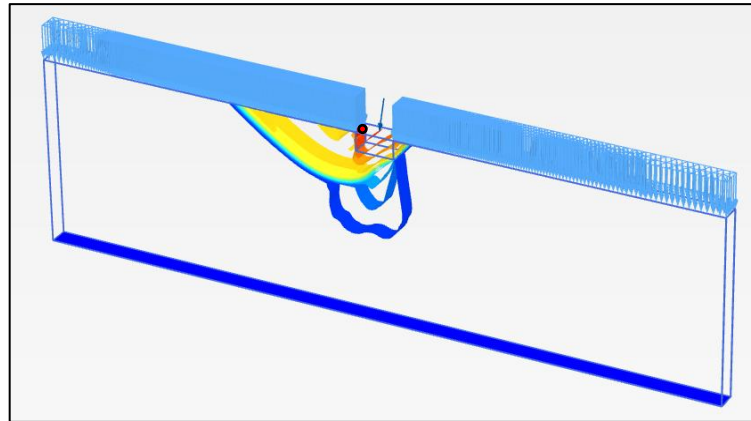

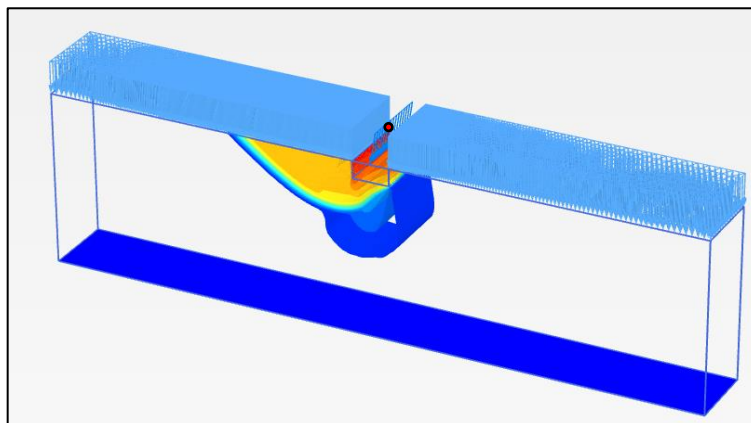Fig. 166 3D Plaxis MC model SRFEA 10-nod. at FoS$_{SR}$ 2.0 for a. φ'=ψ'=35°

Fig. 167 3D Plaxis MC model SRFEA 10-nod. at FoS$_{SR}$ 2.0 for n.a. ψ'=0°

max. lul at the left upper middle edge of the strip foundation

Fig. 168   3D Plaxis MC model SRFEA 10-nod. 1m thickness for n.a. ψ'=11.7°
              sliding surface at failure

max. lul at the left upper back corner of the strip foundation

Fig. 169   3D Plaxis MC model SRFEA 10-nod. 4m thickness for n.a. ψ'=11.7°
              sliding surface at failure
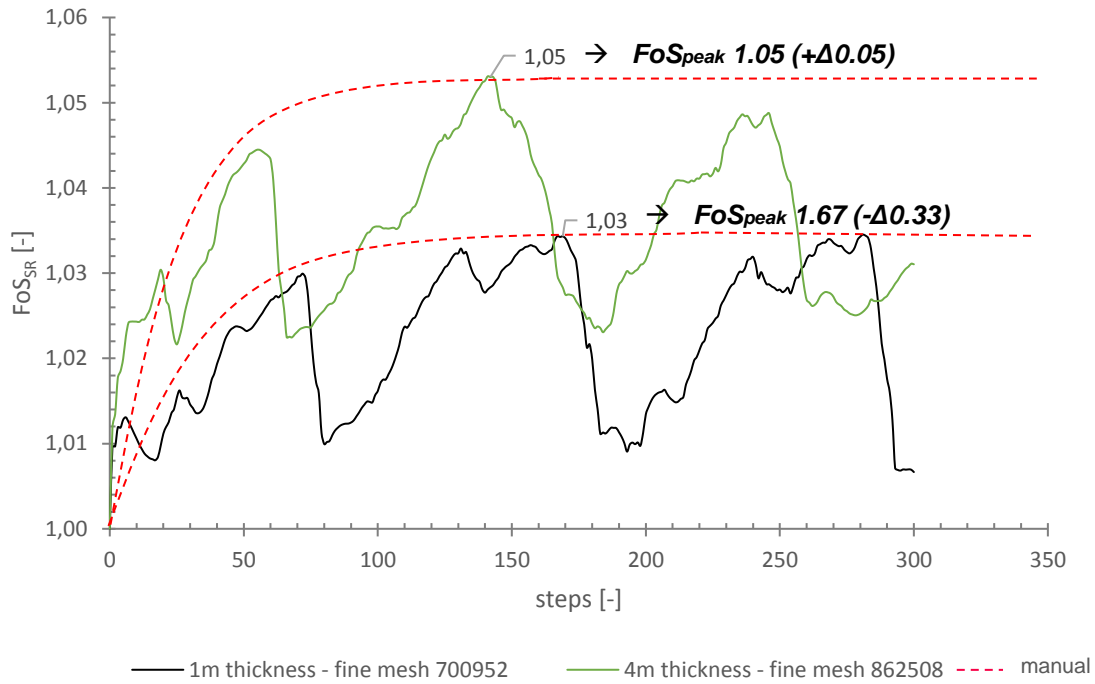
Fig. 170   3D Plaxis MC model SRFEA 10-nod. at failure for n.a. ψ'=11.7°
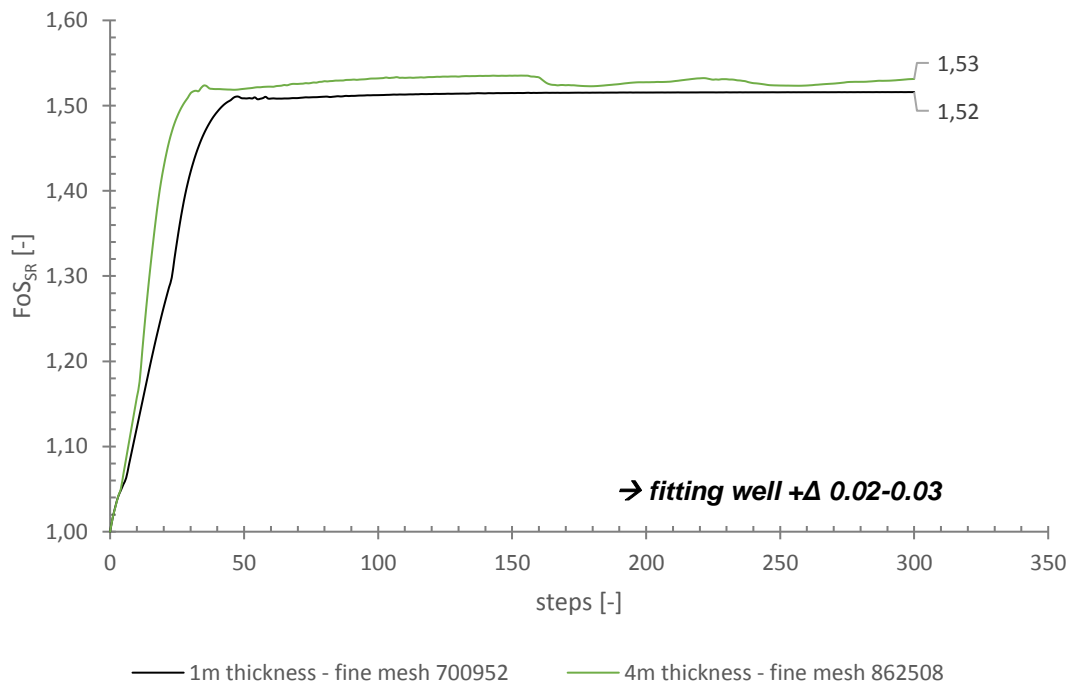

Fig. 171   3D Plaxis MC model SRFEA 10-nod. at FoS$_{SR}$ 1.5 for n.a. ψ'=11.7°